Ultrasound mediated microbubble cavitation for treatment and monitoring of cancer

Lance De Koninck

A dissertation

submitted in partial fulfillment of the

requirements for the degree of

Doctor of Philosophy

University of Washington
2025

Reading Committee:

Michalakis Averkiou, Chair

Matthew O'Donnell

Thomas Matula

Program Authorized to Offer Degree:
Bioengineering

University of Washington

Abstract

Ultrasound mediated microbubble cavitation for treatment and monitoring of cancer

Lance De Koninck

Chair of the Supervisory Committee:
Michalakis Averkiou
Department of Bioengineering

Microbubbles, typically used as a diagnostic ultrasound contrast agent to improve blood flow visualization, also holds great promise as a therapeutic agent for treatment of solid tumors. When insonified by an acoustic pulse, microbubbles undergo volumetric oscillations, providing both an acoustic signal for image contrast enhancement and localized microscale forces during cavitation. These microscale forces can induce several biological effects that overcome the barriers to treating solid tumors, including increased cell membrane permeability, enhanced drug delivery, and tumor-specific vascular changes. In this thesis, we present several investigations of how ultrasound and microbubbles can be applied as both a therapeutic and monitoring strategy for treating cancer. We begin with an introduction on microbubble cavitation and its capacity to monitor and modulate the tumor microenvironment (**Chapter 1**). First, we implement acoustic conditions suitable for generating mechanical forces with cavitation therapy on a clinical scanner and determine which acoustic conditions maximize cavitation activity *in vitro* (**Chapter 2**). We then investigate the mechanical effects of cavitation therapy *in vivo*, using real-time monitoring to elucidate mechanisms of changes to the tumor microenvironment and enhancement of drug delivery to solid tumors (**Chapter 3**). Next, we evaluate the enhanced heat deposition during cavitation therapy in an *ex vivo* machine perfused liver model, evaluating acoustic pressure and microbubble delivery methods to increase temperature and heated area (**Chapter 4**). We then implement subharmonic imaging on a clinical scanner for noninvasive estimation of interstitial fluid pressure in solid tumors and evaluate the mode's ambient pressure sensitivity in physiological ranges for a range of acoustic pressures and microbubble formulations (**Chapters 5 and 6**). We conclude with a summary of the accomplishments and future directions of this work (**Chapter 7**).

Table of Contents

LIST OF FIGURES

LIST OF TABLES

STATEMENT OF CONTRIBUTIONS

Chapters 2-5 have previously appeared as peer reviewed publications or are currently being prepared for submission where Lance De Koninck is the primary author or made significant contributions to the work, describe in detail below. A full list of publications and presentations that Lance De Koninck has contributed to are included at the end of this disseration.

Chapter 2 has appeared as "***De Koninck, LH.**, Vuong KS., Shin, S., Powers, JE., Averkiou MA. "Delivery of cavitation therapy with a modified clinical scanner: in vitro evaluation" IEEE Transactions on Ultrasonics, Ferroelectrics, and Frequency Control, 72 (3), 351-361 (2025)."* Lance De Koninck carried out experiments, developed cavitation analysis algorithm, analyzed results, and wrote the manuscript draft. Kaleb Vuong fabricated tissue-mimicking phantoms, Seonghun Shin assisted with data analysis, and Jeffry Powers implemented cavitation treatment mode on Philips EPIQ scanner. Mike Averkiou designed experiments, reviewed results, and edited the manuscript for final publication.

A version of the sections using a clinical scanner in **Chapter 3**, titled "*Ultrasound cavitation therapy: inducing tumor drug delivery and blood flow changes with clinical ultrasound tools*" has been submitted to *Journal of Controled Release* authored by Connor Krolak, **Lance De Koninck**, Sherry Gu, Yak-Nam Wang, Jeffry Powers, and Mike Averkiou. Lance De Koninck measured cavitation activity and interstitial fluid pressure, analyzed results, and assisted with the manuscript draft. Connor Krolak designed and performed animal experiments, performed histology and image analysis, and co-authored manuscript. Sherry Gu managed the animal colony and assisted with experiments, Yak-Nam Wang designed experiments and analyzed results, and Jeffry Powers implemented cavitation treatment mode on Philips EPIQ scanner. Mike Averkiou designed experiments, reviewed results, and edited the manuscript for final publication.

Chapter 4 has appeared as "*Juang, EK., **De Koninck, LH**., Vuong, KS., Gnanaskandan, A., Hsiao, CT., Averkiou, MA. "Controlled hyperthermia with high-intensity focused ultrasound and ultrasound contrast agent microbubbles in porcine liver" Ultrasound Med. Biol., 49 (8), 1852-1860 (2023)."* Lance De Koninck carried out the ex-vivo experiments, performed bioheat simulations, analyzed results and wrote the manuscript draft. Eric Juang carried out non-perfused

liver and ex-vivo experiments and assisted with the manuscript draft. Remaining authors reviewed the results, assisted with bioheat simulations, and edited the mansucript for final publication.

A version of **Chapter 5**, titled "*Implementation of subharmonic imaging on a clinical scanner for optimal ambient pressure sensitivity with SonoVue microbubbles*" has been submitted to *IEEE Transactions on Ultrasonics, Ferroelectics, and Frequency Control*, authored by **Lance De Koninck**, Gautam Babu, Jeffrey Powers, Nico de Jong, and Mike Averkiou. Lance De Koninck carried out experiments, analyzed results, wrote the manuscript draft. Gautam Babu assisted with experiment design and editing manuscript, Jeffry Powers implemented subharmonic imaging modes of Philips EPIQ scanner, and Nico de Jong reviewed results and edited the manuscript. Mike Averkiou designed experiments, reviewed results, and edited the manuscript for final publication. **Chapter 6** has also been prepared for future submission, with the same author and author contributions listed for **Chapter 5**.

ACKNOWLEDGEMENTS

Research was supported from the National Institute of Biomedical Imaging and Bioengineering of the National Institutes of Health under award number R01EB032655. All acknowledgements to individuals are included following their respective chapters.

First and foremost, I am grateful to my advisor, **Mike Averkiou**, for giving me the opportunity to explore the rich world of ultrasound and microbubbles and for inspiring me to be the best possible scientist I can be. I will be forever grateful for your mentorship and for being the example of scientific integreity I hope to emmulate. I would also like to thank my Supervisory Committee: **Matt O'Donnell**, **Tom Matula**, and **Mike Bailey** for their helpful insights throughout this process.

To my collaborator **Jeff Powers** for taking the time to teach me the ins and outs of the Philips system, and for assisting with the various iterations of therapy and subharmonic imaging modes implemented throughout this thesis. I am very grateful for your guidance and feel lucky to have had the opportunity to work with you over the past few years. Thank you also to **Nico de Jong** for guiding me through the world of subharmonic imaging and providing useful guidance.

To my lab mates **Connor Krolak**, **Kaleb Vuong**, and the rest of the **Averkiou lab** for your support and comradery throughout the years. You have all been wonderful scientists to work with, and I hope you'll forgive me for never opening the blinds in my office.

To my friend, **Tristan Oaks**, for the many phone calls, random road trips, and somehow always ending up the same place. I'm lucky to have had your support throughout all these years, and I look forward to seeing what we both do next.

To my mother, **Astrid** and my father **Guy** for their endless love and support througout my life. Your hard work and dedication has always inspired me to be the best I can be, and I hope to live up to your example.

Finally, to my wife, **Charlotte**, thank you does not do it justice. I would not be where I am today without you, and my life will be forever better with you in it.

CHAPTER 1. INTRODUCTION

Abstract

Cancer is among leading causes of death worldwide, accounting for 1 in 4 deaths in the United States. While major advancements into cancer therapeutics have been developed, the challenges posed by solid tumors due to abnormal vasculature and hostile tumor microenvironments prevent efficient, targeted treatments of the disease. Ultrasound and microbubble contrast agents are being investigated for their potential to enhance drug delivery and monitor perfusion changes in treated tumors. Microbubbles insonified by an ultrasound pulse oscillate, providing both an acoustic signal for image contrast enhancement as well as localized microscale forces during cavitation. These microscale forces can induce several biological effects and overcome the treatment barriers within solid tumors. In this chapter we introduce the challenges associated with treatment of solid tumors, how ultrasound and microbubbles can overcome these impediments, and describe the unique behavior microbubbles can exhibit in the tumor microenvironment. Additionally, the overall research aim of the project will be presented.

1.1 CHALLENGES OF CANCER THERAPY

1.1.1 Barriers to systemic drugs and the tumor microenvironment

Cancer is a major healthcare burden around the world and accounting for 1 in 4 deaths in the United States [1]. Nearly 85% of these cases are attributed to solid tumors [2], possessing a unique microenvironment that limits the penetration of anticancer drugs, exhibiting only modest effects [3, 4]. Most anticancer drugs are injected intravenously, and rely on a vascular network to carry the drug molecules to the target cells, then extravasate beyond the blood vessel walls, and finally cross the interstitial space to reach the cells of interest [5]. However, solid tumors often exhibit abnormal and poorly perfused vasculature, and for more developed tumors, avascular regions often at the center [6]. Additionally, the extracellular matrix in certain solid tumors is highly desmoplastic, characterized by fibrosis and excessive collagen formation [7]. This stiff matrix paired with the abnormal vasculature and poor lymphatic drainage results in elevated interstitial fluid pressure (IFP) as the rate of fluid entering the tumor is greater than the draining rate [8]. IFP is often greatest at the center of the tumor, creating a pressure gradient that can limit

diffusion of drug molecules to only the tumor periphery [9]. The combination of these factors creates a hostile environment for typical anticancer drugs and has encouraged investigation into new techniques for cancer treatments that reduce or eliminate these barriers.

1.1.2 Current cancer therapies

For most cancer patients, treatment recommendations usually follow surgery or systemic therapies such as chemotherapy, antiangiogenics and immune check point inhibitors [1]. While surgery is the preferred option, especially at early stages of the disease, it is often not possible due to the location, stage of cancer, or underlying diseases. Systemic therapies, comprising of a chemical substance for disease treatment, come in the form of an intravenous treatment typically used for late stage cancers [10]. Traditionally cytotoxic, chemotherapeutics target rapidly proliferating cells like cancer, but often require several rounds of treatment due to barriers in the solid tumor to drug penetration. These issues have led to discovery of new classes of anticancer drugs to target specific mechanisms in solid tumors. Anti-angiogenic therapies have been proposed to take advantage of the hypervascular nature of some tumors, inhibiting the formation of new blood vessels or reducing the tumoral blood supply, effectively starving the tumor [11]. However, if co-delivered with chemotherapeutics this introduces a new problem of removing vasculature network needed to deliver the drug, requiring special timing for effective treatment [12, 13]. Another approach is the use of immunotherapy which aims to enhance anti-tumor immunity by upregulating cytotoxic lymphocytes [14]. Recently, Chimeric Antigen Receptor (CAR)-T cell therapy has emerged as a promising immunotherapeutic approach to treating cancer by genetically engineering immune cells to target antigens present on cancer cells [15]. However, in the treatment of solid tumors, CAR-T cell therapy still suffers from the same penetration issues of other treatments in addition to the tumor microenvironment being immunosuppressant. Therefore, there is still a great need for a solution to alleviate the solid tumor barriers to drug penetration and enhance the efficacy of existing therapies.

1.2 MICROBUBBLE CAVITATION

1.2.1 Nonlinear oscillation of microbubbles

Microbubbles, such as those used as ultrasound contrast agents, insonified by ultrasound oscillate and provide both an acoustic signal for contrast enhancement as well as localized

microscale forces that can overcome the barriers within solid tumors [16], depending on the ultrasound parameters. The sinusoidal nature of an ultrasound waves create periods of high and low pressure, that results in microbubble compression and expansion respectively [17]. During this process, microbubbles will spherically scatter signal in all directions which can then be detected and used to construct images. A unique feature of microbubbles is their nonlinear oscillation, generating additional frequency components in the scattered signal that was not present in the frequency of the transmitted pulse [18]. These frequency components are typically monitored in 3 categories relative to the transmitted frequency (f_0): 1.) harmonics, identified as integer multiples ($n * f_0$, where n is an integer), 2.) sub- and ultraharmonics, identified as half-integer multiples ($\frac{n}{2} * f_0$) where n is an odd integer, and 3.) broadband noise, signal distributed to all frequencies. The emergence and relative magnitude of each of these frequency components are used to describe the specific type of microbubble oscillations. More importantly for this body of work, this also describes the likelihood of microbubbles inducing biological effects [19] such as ablation (mechanical and thermal) [20], cell membrane permeability (sonoporation) [21], and vascular disruption [22].

1.2.2 Cavitation dynamics of microbubbles during diagnostic ultrasound

Diagnostic ultrasound imaging typically utilizes low acoustic pressures (< 2 MPa) and short pulse durations. When insonified with pulses used in imaging modes, microbubbles scatter harmonic frequency components ($n * f_0$) that are distinct from those of the imaging pulse. To exploit these properties, nonlinear pulsing schemes have been developed to isolate the nonlinear frequency components specific to microbubbles [18]. The most used schemes on commercial imaging systems are pulse inversion [23], amplitude modulation [24], or amplitude-modulated pulse inversion [25]. At low acoustic pressure, tissue is unlikely to generate harmonic components that can be detected by ultrasound scanners, enabling nonlinear pulsing schemes to cancel out tissue signal and maintain nonlinear signal from microbubbles. However, improper dosing of microbubbles can produce imaging artifacts such as acoustic shadowing, where high concentrations of microbubbles attenuate sound and can shadow distal structures [18].

While conventional contrast-enhanced ultrasound forms images with signal from harmonic frequency components, another approach is to form images with subharmonic signal ($f_0/2$) that only microbubbles generate [26, 27]. Typically, microbubbles are driven near their average

resonance frequency, requiring high acoustic pressures to produce subharmonic signal in the scattered pulses [28]. However, by transmitting at twice the average resonance frequency of microbubbles, the acoustic pressure threshold for generating subharmonic signal is minimized, demonstrated first by Eller and Flynn [29] with free gas bubbles, and later Shankar, et al. [30] with shelled microbubbles. Additionally, tissue does not generate subharmonic signal, enabling image construction with microbubble-specific subharmonic signal that may be further improved with nonlinear pulsing schemes. In 1999, Shi, et al. [31] also demonstrated subharmonic signal from microbubbles is particularly sensitive to changes in ambient pressure, suggesting the use of subharmonic imaging for noninvasive pressure estimation. However, exact changes in subharmonic magnitude with ambient pressure depend on microbubble properties and ultrasound parameters. The mechanisms of subharmonic signal generation with microbubbles and the relationship between subharmonic signal and ambient pressure are further discussed in **Sections 1.3.3 and 1.3.4**.

1.2.3 Cavitation dynamics of microbubbles during therapeutic ultrasound

In therapeutic ultrasound much longer pulses than what is used in diagnostic ultrasound are used. As acoustic pressure increases, microbubble behavior is usually classified as stable or inertial cavitation. Stable cavitation is typically defined as the emergence of sub- and ultraharmonic components without a considerable increase in broadband noise [28]. The sub- and ultraharmonics represent large bubble oscillations that survive the full acoustic pulse duration. Studies by O'Reilly and Hynynen [32] and Sun, et al. [33] have demonstrated the utility microbubble oscillations during stable cavitation for opening of the blood-brain-barrier (BBB) and enhanced drug delivery. As acoustic pressure increases beyond a certain threshold, inertial cavitation can occur, described by lifting of the broadband noise in the frequency spectrum of the scattered sound [34]. Inertial cavitation is a violent process, where microbubbles rapidly expand and collapse, driven by the inertia of the surrounding medium and generating powerful localized effects such as shock waves [35], fluid jetting [36], and cellular damage [37]. The challenge of designing protocols for therapeutic ultrasound with microbubbles is carefully choosing the type of cavitation to elicit the desired biological response while minimizing unwanted adverse effects.

1.2.3.1 Cavitation resulting in mechanical effects

Microbubble cavitation can generate microscale mechanical forces, including microjetting, microstreaming, and inertial collapse, that can induce biological effects. Microjetting and microstreaming result from a microbubble changing conformation near a wall (i.e. a cell membrane), generating high velocity jetting or shear stresses [38]. This jetting or shear stress can increase cell membrane permeability, reversibly [39] or irreversibly [40], and facilitate intracellular drug uptake (sonoporation). Sufficiently high acoustic pressures may also cause inertial collapse, in which a microbubble implodes, generating high pressure shock waves that can increase cell membrane permeability or even damage the surrounding area [41]. These mechanical effects may also explain the transient loss of perfusion in solid tumors following cavitation treatments [22, 42]. It has been suggested that the immature neovessels which are prevalent in tumors [43] are more susceptible to mechanical damage from cavitation. This tumoral neovessel susceptibility enables preferential targeting of tumor vasculature while avoiding damage to the surrounding tissue [44, 45]. Together, these mechanical forces during microbubble cavitation can offer another successful strategy to eliminate barriers in solid tumors and has the potential to enhance drug delivery with appropriate timing. The relationship between mechanical forces from microbubble cavitation and changes to tumor perfusion are investigated in **Chapter 3**.

Beyond solid tumors, these mechanical effects have been successfully applied for other novel therapies. Using very short (μs-duration), extremely high pressure (> 28 MPa peak negative pressure in most soft tissues [46, 47]) pulses repeated at a low duty cycle can generate dense bubble clouds in tissue capable of mechanically disintegrating (liquefying) tissue to a subcellular level, referred to as histotripsy [20]. This is a highly localized effect, and has even been observed to bisect individual cells [48]. Microbubble cavitation has also been a useful method for opening of the BBB, enabling the passage of larger drug molecules that typically cannot cross the BBB [32, 33, 49]. Recent work has focused on determining the acoustic pressure threshold necessary for BBB opening and was found to be slightly lower than the inertial cavitation threshold [33].

1.2.3.2 Cavitation enhancing heat deposition

Microbubble cavitation may also elevate temperature within tissue beyond what it is possible with high intensity focused ultrasound (HIFU) alone, primarily through thermoviscous absorption of the acoustic emissions during inertial collapse [50]. The magnitude of acoustic

emissions during inertial collapse, and consequently the local elevation of temperature, is dependent on acoustic pressure. Therefore, careful selection of acoustic pressure can control temperature elevation from microbubble cavitation and has previously used for targeted thermal ablation [51-53] or drug delivery with thermosensitive liposomes [54]. Of interest for treating solid tumors is a small temperature elevation (3-8 ℃) referred to as mild hyperthermia. The transition temperature of collagen fibers is lower in solid tumors [55], so a small temperature increase is sufficient to denature the proteins and reduce the extracellular matrix density [56]. This can lead to increased hydraulic conductivity, enhancing fluid flow out of the tumor and reducing IFP [57]. Additionally, mild hyperthermia has been shown to enhance blood flow in tumors [58], which was correlated with a reduction of IFP [59].

Leveraging cavitation in ultrasound heating was first investigated without microbubbles, by using high acoustic pressures to first generate bubbles in the target medium (native cavitation) and then cavitate said bubbles to enhance temperature [60]. Later studies suggested that injected microbubbles act as cavitation nuclei that lower the cavitation threshold and enhance heating during high-intensity focused ultrasound [61, 62]. Microbubble heating relies on high intensity acoustic pulses, with many cycles or even continuous waves and high acoustic pressures sufficient for heat-enhancing cavitation. While microbubble heating can be performed during inertial cavitation, stable cavitation can also promote heat generation through the viscous losses in the boundary layer on the surface of oscillating bubbles [63]. However, the concentration of microbubbles in the treated medium can lead to prefocal heating and off target effects due to acoustic shadowing [64]. Therefore, a bubble-enhanced treatment regimen must balance microbubble delivery and acoustic pulse characteristics to generate the desired temperature elevation at the desired location. We will provide an in-depth investigation of microbubble enhanced heating in **Chapter 4**.

1.2.4 Cavitation detection methods

Considering the multiple therapeutic uses of cavitation, robust techniques for its detection are needed. Several techniques have been developed to monitor microbubble cavitation and its unique frequency components. A common technique is passive cavitation detection, where a device, typically a focused transducer (single element or array), is set to passively listen for scattered sound from microbubbles [34, 65]. These signals are then recorded and their spectrum is

evaluated for the presence of sub- and ultraharmonics and/or elevation of broadband noise. For most targeted cavitation therapies, these simple devices are sufficient for quantifying cavitation activity with excellent temporal resolution. Another approach is active cavitation detection, where the same transducer will both transmit an acoustic pulse and receive scattered signal. Diagnostic ultrasound relies on this principle. For example, B-mode imaging detects oscillating bubbles, which scatter strong signals and may appear as a hyperechoic region that can be distinguished from tissue speckle pattern [66, 67]. Recent work has also developed new techniques, such as passive acoustic mapping, that take advantage of ultrasound imaging and novel beamforming approaches that utilize very high frame rates to generate images of cavitation, providing spatial and temporal information [68, 69].

1.3 IMPACT OF INCREASED AMBIENT PRESSURE ON MICROBUBBLE OSCILLATIONS

1.3.1 Challenges of measuring IFP

IFP is typically measured with one of two invasive methods: wick-in-needle [70] or a transducer-tipped pressure catheter. These devices are designed to measure the hydrostatic pressure of excess fluid, either free-fluid (unbounded) or gel-bound fluid [71], in the tumor interstitium [72]. However, several challenges exist with these devices that limit their clinical utility. Both IFP measurement techniques involve the insertion of a needle into the tumor, resulting in complications such as hemorrhage and acute inflammation at the needle track site [73] that can artificially modify detected interstitial pressure [74]. For sufficiently large tumors, elevated IFP results in a pressure gradient, increasing from the tumor periphery to the center [9]. As a result, image guidance is required for accurate measurement of central tumor pressures (maximum IFP). Disagreement also exists over the sensitivity of these invasive techniques. DuFort, et al. [72] argue that only pressure catheter measurements can detect the ambient pressure of gel-bound fluid, while other groups claim that pressure catheter method are prone to solid stress artifacts (distinct from IFP) due to direct contact with tissue [75, 76]. The limitations of existing invasive IFP measurements and lack of a robust method have encouraged the development of new techniques such as ultrasound and microbubbles for noninvasive monitoring of ambient pressure.

1.3.2 Elevated IFP results in increased ambient pressure

In microvasculature, oncotic and hydrostatic pressures control the movement of fluid and large molecules across vessel walls [77]. As previously described, due to the "leaky" nature of abnormal tumor vasculature and defective lymphatic drainage, the volume of free fluid in the interstitial space of solid tumors is increased, resulting in elevated IFP. Due to this abnormal vasculature, pressure in the tumor microvasculature (where microbubbles are confined) has been shown to be equal to the interstitial pressure [77, 78]. Considering that IFP has been recorded at pressures as high as 100 mmHg (above atmospheric pressure) in solid tumors due to the overexpression of hyaluronan [72], this imparts a substantial increase in microvasculature pressure, acting to compress microbubbles as they travel through the vasculature of solid tumors. At ambient pressures greater than atmospheric, microbubbles favor what is referred to as a buckled state [79]. For lipid-shelled microbubbles, the buckled state can promote the generation of a subharmonic frequency component without necessarily inducing stable cavitation [80]. Additionally, the subharmonic signal produced by microbubble oscillations has been shown to be particularly sensitive to changes in ambient pressure [31]. We can take advantage of the relationship between subharmonic signal and ambient pressure and use microbubbles as sensors for changes in ambient pressure. Thus, the subharmonic component of the scattered ultrasound from microbubbles may be used to noninvasively measure changes in IFP.

1.3.3 Subharmonic signal dependence on acoustic parameters

Early works investigating subharmonic signals from free gas bubbles and encapsulated microbubbles explored the threshold at which these signals are generated at atmospheric pressure and the impact of acoustic conditions such as ultrasound frequency and acoustic pressure. In 1969, Eller and Flynn first described the threshold and frequency dependence of subharmonic generation from free gas bubbles [29]. Later, Shankar et al. [81] studied Optison (GE Healthcare, Chicago, IL, USA), a UCA with an albumin shell, and found the threshold for subharmonic signal generation to also be dependent on driving frequency. This threshold was minimized when the driving frequency was twice the average resonance frequency of the microbubble population, with subharmonic signal generated at acoustic pressures as low as 10 kPa in vitro. Shi et al. [27] also measured subharmonic signal generation with Optison near its resonance frequency, and introduced the development of subharmonic signal generation as a function of acoustic pressure

characterized by three stages: “occurrence” where subharmonic signals are minimal, “growth” where the magnitude of the subharmonic signal rapidly increases with acoustic pressure, and “saturation” where subharmonic signal magnitude remains relatively constant despite increasing acoustic pressure. Interestingly, the range of acoustic pressures used in this study (0.4-2.5 MPa) likely exceeds the level at which microbubble shell disruption (detectable signal deterioration in imaging) occurs, which has been estimated to be as low as 200 kPa depending on the microbubble size and driving frequency [82, 83]. Therefore, there are 2 main mechanisms for subharmonic signal generation: 1.) driving the bubble at its resonant frequency which often requires high acoustic pressures (> 200 kPa) to generate a subharmonic component [82], or 2.) driving the bubble at twice its resonance frequency, where subharmonic signal is detected at low acoustic pressures (< 200 kPa) but is dependent on microbubble shell properties [82-84].

1.3.4 Mechanisms of subharmonic signal generation

The relationship between subharmonic signal and acoustic pressure led several groups to further investigate the mechanisms of subharmonic signal generation from oscillations of lipid-coated microbubbles. Some encapsulated microbubbles at low acoustic pressures (5-100 kPa) driven at twice the resonant frequency exhibit compression-only behavior, which has been confirmed with optical measurements using a high-speed camera [84] and experiments monitoring scattered subharmonic signal [80]. The rapid change in the effective surface tension of the bubble’s shell can result in an asymmetric (compression-only) behavior [92] as it transitions from elastic and buckled states, as described by Marmottant et al. [79]. In general, as acoustic pressure increases (> 200 kPa) with long bursts (≥ 8 cycles), microbubble disruption and shell lipid shedding will occur, leaving a free gas bubble and shifting the asymmetry of bubble oscillations to favor expansion behavior [79, 92]. These increased acoustic pressures also exceed the destruction threshold of certain microbubbles that are resonant at the transmit frequency, indicating that subharmonic signal in this acoustic pressure regime is likely due to a combination of the destruction of resonant microbubbles and certain microbubbles oscillating at twice the resonance frequency [80, 82]. The work by Chomas et al. [82] shows that the subharmonic generation at twice the resonance frequency is dominant below the destruction threshold for microbubbles (for bubble radii > 2 μm, acoustic pressure ≤ 500 kPa), while subharmonic signal from bubbles driven at their resonant frequency are dominant above the destruction threshold (bubble radii ≤ 2 μm, acoustic pressures > 500 kPa). Since UCAs are polydisperse with an average bubble size, transmit

frequency and acoustic pressure must be carefully selected for appropriate subharmonic signal generation.

1.3.5 Subharmonic sensitivity to ambient pressure

Generally, as ambient pressure increases above atmospheric pressure, 3 major effects should take place: a.) increased compressive force on microbubbles, b.) increased dissolution rate of free bubbles, and c.) a shift in resonant frequency [95-97]. Further, the shift in resonance frequency may have two contributions depending on the condition of the microbubble shell: 1.) for free gas bubbles (after shell disruption) there is little to no change due to the weak dependence of the resonant frequency on hydrostatic pressure and initial radius, or 2.) lipid-shelled microbubbles shifting to a buckled, tensionless shell state with increased hydrostatic pressure. At low acoustic pressures where we only expect compression behavior for lipid-shelled microbubbles driven at twice the resonance frequency, only the dissolution rate and resonance shift need be considered, while utilizing high acoustic pressures all 3 effects must be considered. For lipid-shelled microbubbles insonified at low acoustic pressures, an increase in hydrostatic pressure should exaggerate compression behavior and increase the subharmonic signal [80, 84, 98]. In **Chapters 5 and 6**, we present an in-depth investigation of the subharmonic response of 2 clinically approved contrast agents (SonoVue and Sonazoid), with a special focus on subharmonic imaging at low acoustic pressures to minimize bubble destruction.

1.4 RESEARCH OBJECTIVES

The objective of this work is to study microbubble- and ultrasound-induced cavitation used in cancer treatment options that aim at impacting the tumor microenvironment. We separately investigate the mechanical forces and enhanced heat deposition generated by microbubble cavitation, and evaluate how microbubble cavitation can overcome the barriers to treating solid tumors, including abnormal vasculature, desmoplasia, and elevated IFP. We utilize passive cavitation detection (PCD) to confirm accurate targeting of cavitation treatments and evaluate microbubble cavitation activity both *in vitro* and animal tumor models *in vivo*. We develop new subharmonic imaging modes with clinically approved microbubbles as a noninvasive technique for monitoring IFP in solid tumors. Furthermore, we implement acoustic conditions suitable for generating mechanical forces with cavitation therapy on a clinical scanner, accelerating the translation of microbubble cavitation therapy to the clinic. An illustration of how we address the

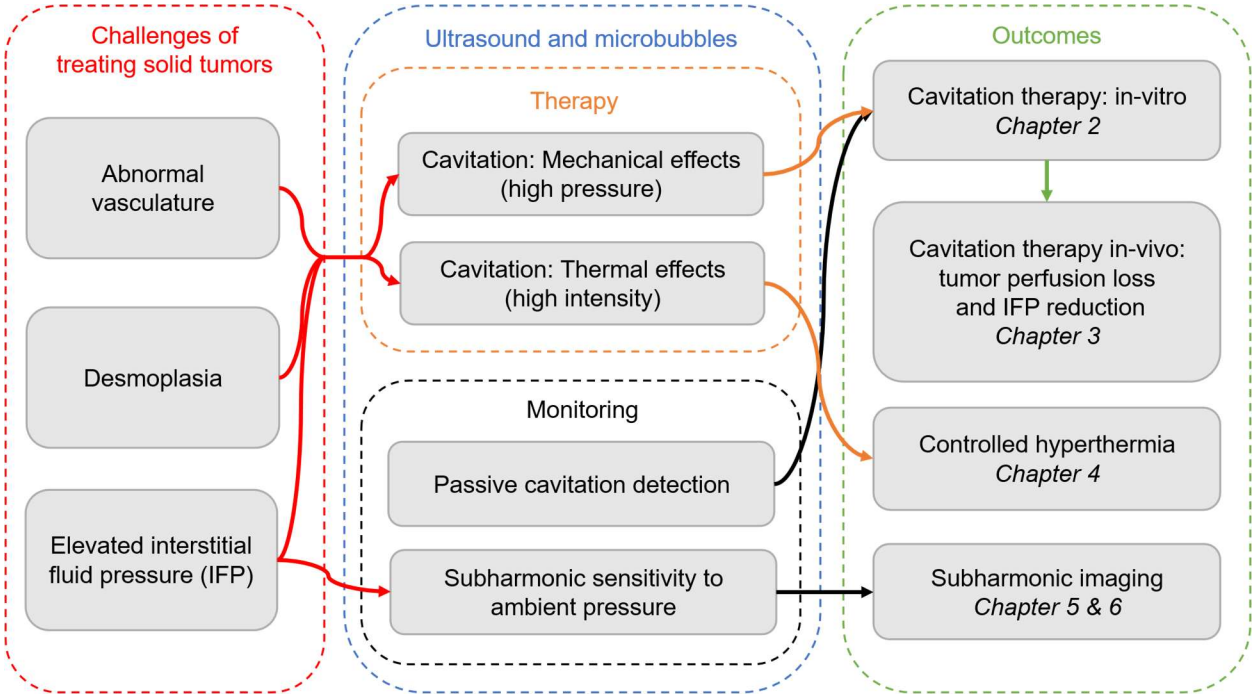

***Figure 1.1**: Flow chart of research objectives.*

challenges of treating solid tumors with ultrasound-mediated microbubble cavitation and monitor microbubble activity in this thesis is shown in **Figure 1.1**. In **Chapter 2**, we implement acoustic conditions suitable for generating mechanical forces with cavitation therapy on a clinical scanner. PCD measurements evaluate microbubble behavior during treatments and determine which acoustic conditions maximize cavitation activity *in vitro*, guiding acoustic parameter selection for the subsequent animal tumor model *in vivo* study. In **Chapter 3**, we investigate the mechanical effects of cavitation therapy *in vivo* such as transient tumor perfusion loss and reduction of IFP. PCD measurements confirm accurate targeting of cavitation treatments and furthermore the detected cavitation activity is a predictor of tumor perfusion loss. In **Chapter 4**, we evaluate the enhanced heat deposition during cavitation therapy in an ex vivo machine perfused liver model. We consider the effects of acoustic pressure, microbubble concentration, and microbubble delivery methods to elevate focal temperature and increase the heated area. In **Chapters 5 and 6**, we implement a new subharmonic imaging mode on a clinical scanner for noninvasive estimation of the ambient pressure in general and the interstitial fluid pressure in solid tumors. We measure the ambient pressure sensitivity of subharmonic imaging in physiological values for a range of acoustic pressures, imaging parameters, and 2 clinically approved microbubble formulations. We

conclude this thesis with a summary of the accomplishments and future directions of this work (**Chapter 7**).

1.5 REFERENCES

[1] D. Luo, K. A. Carter, D. Miranda, and J. F. Lovell, "Chemophototherapy: an emerging treatment option for solid tumors," *Advanced Science,* vol. 4, no. 1, p. 1600106, 2017. doi: 10.1002/advs.201600106.

[2] R. K. Jain, "Normalization of tumor vasculature: an emerging concept in antiangiogenic therapy," *Science,* vol. 307, no. 5706, pp. 58-62, 2005. doi: 10.1126/science.1104819.

[3] A. H. Kyle, L. A. Huxham, D. M. Yeoman, and A. I. Minchinton, "Limited tissue penetration of taxanes: a mechanism for resistance in solid tumors," *Clinical Cancer Research,* vol. 13, no. 9, pp. 2804-2810, 2007. doi: 10.1158/1078-0432.CCR-06-1941.

[4] O. Trédan, C. M. Galmarini, K. Patel, and I. F. Tannock, "Drug resistance and the solid tumor microenvironment," *Journal of the National Cancer Institute,* vol. 99, no. 19, pp. 1441-1454, 2007. doi: 10.1093/jnci/djm135.

[5] R. K. Jain and T. Stylianopoulos, "Delivering nanomedicine to solid tumors," *Nature reviews Clinical oncology,* vol. 7, no. 11, pp. 653-664, 2010. doi: 10.1038/nrclinonc.2010.139.

[6] V. P. Chauhan, T. Stylianopoulos, Y. Boucher, and R. K. Jain, "Delivery of molecular and nanoscale medicine to tumors: transport barriers and strategies," *Annual review of chemical and biomolecular engineering,* vol. 2, no. 1, pp. 281-298, 2011. doi: 10.1146/annurev-chembioeng-061010-114300.

[7] E. Henke, R. Nandigama, and S. Ergün, "Extracellular matrix in the tumor microenvironment and its impact on cancer therapy," *Frontiers in molecular biosciences,* vol. 6, p. 160, 2020. doi: 10.3389/fmolb.2019.00160.

[8] H. Kobayashi, R. Watanabe, and P. L. Choyke, "Improving conventional enhanced permeability and retention (EPR) effects; what is the appropriate target?," *Theranostics,* vol. 4, no. 1, p. 81, 2013. doi: 10.7150/thno.7193.

[9] A. Mohammadabadi *et al.*, "Pulsed focused ultrasound lowers interstitial fluid pressure and increases nanoparticle delivery and penetration in head and neck squamous cell carcinoma xenograft tumors," *Physics in Medicine & Biology,* vol. 65, no. 12, p. 125017, 2020. doi: 10.1088/1361-6560/ab9705.

[10] C. E. DeSantis *et al.*, "Cancer treatment and survivorship statistics, 2014," *CA: a cancer journal for clinicians,* vol. 64, no. 4, pp. 252-271, 2014. doi: 10.3322/caac.21235.

[11] K. Liu *et al.*, "Targeting the vasculature in hepatocellular carcinoma treatment: Starving versus normalizing blood supply," *Clinical and translational gastroenterology,* vol. 8, no. 6, p. e98, 2017. doi: 10.1038/ctg.2017.28.

[12] J. Ma, S. Pulfer, S. Li, J. Chu, K. Reed, and J. M. Gallo, "Pharmacodynamic-mediated reduction of temozolomide tumor concentrations by the angiogenesis inhibitor TNP-470," *Cancer research,* vol. 61, no. 14, pp. 5491-5498, 2001. doi:

[13] J. Ma and D. J. Waxman, "Combination of antiangiogenesis with chemotherapy for more effective cancer treatment," *Molecular cancer therapeutics,* vol. 7, no. 12, pp. 3670-3684, 2008. doi: 10.1158/1535-7163.MCT-08-0715.

[14] S. Menon, S. Shin, and G. Dy, "Advances in cancer immunotherapy in solid tumors," *Cancers,* vol. 8, no. 12, p. 106, 2016. doi: 10.3390/cancers8120106.

[15] K. M. Maalej *et al.*, "CAR-cell therapy in the era of solid tumor treatment: current challenges and emerging therapeutic advances," *Molecular cancer,* vol. 22, no. 1, p. 20, 2023. doi: 10.1186/s12943-023-01723-z.

[16] K. Ferrara, R. Pollard, and M. Borden, "Ultrasound microbubble contrast agents: fundamentals and application to gene and drug delivery," *Annu. Rev. Biomed. Eng.,* vol. 9, no. 1, pp. 415-447, 2007. doi: 10.1146/annurev.bioeng.8.061505.095852.

[17] E. Stride, "Physical principles of microbubbles for ultrasound imaging and therapy," *Cerebrovascular Diseases,* vol. 27, 2009. doi: 10.1159/000203122.

[18] M. A. Averkiou, M. F. Bruce, J. E. Powers, P. S. Sheeran, and P. N. Burns, "Imaging methods for ultrasound contrast agents," *Ultrasound in medicine & biology,* vol. 46, no. 3, pp. 498-517, 2020. doi: 10.1016/j.ultrasmedbio.2019.11.004.

[19] R. E. Apfel and C. K. Holland, "Gauging the likelihood of cavitation from short-pulse, low-duty cycle diagnostic ultrasound," *Ultrasound in medicine & biology,* vol. 17, no. 2, pp. 179-185, 1991. doi: 10.1016/0301-5629(91)90125-G.

[20] V. A. Khokhlova *et al.*, "Histotripsy methods in mechanical disintegration of tissue: Towards clinical applications," *International journal of hyperthermia,* vol. 31, no. 2, pp. 145-162, 2015. doi: 10.3109/02656736.2015.1007538.

[21] Y. Zhou, K. Yang, J. Cui, J. Ye, and C. Deng, "Controlled permeation of cell membrane by single bubble acoustic cavitation," *Journal of controlled release,* vol. 157, no. 1, pp. 103-111, 2012. doi: 10.1016/j.jconrel.2011.09.068.

[22] S. B. Keller, D. Suo, Y.-N. Wang, H. Kenerson, R. S. Yeung, and M. A. Averkiou, "Image-guided treatment of primary liver cancer in mice leads to vascular disruption and increased drug penetration," *Frontiers in Pharmacology,* vol. 11, p. 584344, 2020. doi: 10.3389/fphar.2020.584344.

[23] D. H. Simpson, C. Chien Ting, and P. N. Burns, "Pulse inversion Doppler: a new method for detecting nonlinear echoes from microbubble contrast agents," *IEEE Transactions on Ultrasonics, Ferroelectrics, and Frequency Control,* vol. 46, no. 2, pp. 372-382, 1999. doi: 10.1109/58.753026.

[24] V. Mor-Avi, E. G. Caiani, K. A. Collins, C. E. Korcarz, J. E. Bednarz, and R. M. Lang, "Combined Assessment of Myocardial Perfusion and Regional Left Ventricular Function by Analysis of Contrast-Enhanced Power Modulation Images," *Circulation,* vol. 104, no. 3, pp. 352-357, 2001/07/17 2001. doi: 10.1161/01.CIR.104.3.352.

[25] P. J. Phillips, "Contrast pulse sequences (CPS): imaging nonlinear microbubbles," in *2001 IEEE Ultrasonics Symposium. Proceedings. An International Symposium (Cat. No.01CH37263)*, 2001, vol. 2, pp. 1739-1745 vol.2. 10.1109/ULTSYM.2001.992057.

[26] P. M. Shankar, P. D. Krishna, and V. L. Newhouse, "Advantages of Subharmonic Over Second Harmonic Backscatter for Contrast-To-Tissue Echo Enhancement," *Ultrasound in Medicine & Biology,* vol. 24, no. 3, pp. 395-399, 1998/03/01/ 1998. doi: 10.1016/S0301-5629(97)00262-7.

[27] W. T. Shi *et al.*, "Subharmonic imaging with microbubble contrast agents: initial results," (in eng), *Ultrason Imaging,* vol. 21, no. 2, pp. 79-94, Apr 1999. doi: 10.1177/016173469902100201.

[28] K. B. Bader and C. K. Holland, "Gauging the likelihood of stable cavitation from ultrasound contrast agents," *Physics in Medicine & Biology,* vol. 58, no. 1, p. 127, 2012. doi: 10.1088/0031-9155/58/1/127.

[29] A. Eller and H. Flynn, "Generation of subharmonics of order one-half by bubbles in a sound field," *The Journal of the Acoustical Society of America,* vol. 46, no. 3B, pp. 722-727, 1969. doi: 10.1121/1.1911753.

[30] P. M. Shankar, P. D. Krishna, and V. L. Newhouse, "Subharmonic backscattering from ultrasound contrast agents," *The Journal of the Acoustical Society of America,* vol. 106, no. 4, pp. 2104-2110, 1999. doi: 10.1121/1.428142.

[31] W. Shi, F. Forsberg, J. Raichlen, L. Needleman, and B. Goldberg, "Pressure dependence of subharmonic signals from contrast microbubbles," *Ultrasound in Medicine & Biology,* vol. 25, no. 2, pp. 275-283, 1999/02/01/ 1999. doi: 10.1016/S0301-5629(98)00163-X.

[32] M. A. O'Reilly and K. Hynynen, "Blood-brain barrier: Real-time feedback-controlled focused ultrasound disruption by using an acoustic emissions–based controller," *Radiology,* vol. 263, no. 1, pp. 96-106, 2012. doi: 10.1148/radiol.11111417.

[33] T. Sun, G. Samiotaki, S. Wang, C. Acosta, C. C. Chen, and E. E. Konofagou, "Acoustic cavitation-based monitoring of the reversibility and permeability of ultrasound-induced blood-brain barrier opening," *Physics in Medicine & Biology,* vol. 60, no. 23, p. 9079, 2015. doi: 10.1088/0031-9155/60/23/9079.

[34] S. B. Keller, P. S. Sheeran, and M. A. Averkiou, "Cavitation therapy monitoring of commercial microbubbles with a clinical scanner," *IEEE Transactions on Ultrasonics, Ferroelectrics, and Frequency Control,* vol. 68, no. 4, pp. 1144-1154, 2020. doi: 10.1109/TUFFC.2020.3034532.

[35] J. Holzfuss, M. Rüggeberg, and A. Billo, "Shock wave emissions of a sonoluminescing bubble," *Physical review letters,* vol. 81, no. 24, p. 5434, 1998. doi: 10.1103/PhysRevLett.81.5434.

[36] A. Prosperetti, "Bubble phenomena in sound fields: part one," *Ultrasonics,* vol. 22, no. 2, pp. 69-77, 1984. doi: 10.1016/0041-624X(84)90024-6.

[37] W. W. Roberts, T. L. Hall, K. Ives, J. S. Wolf, J. B. Fowlkes, and C. A. Cain, "Pulsed cavitational ultrasound: a noninvasive technology for controlled tissue ablation (histotripsy) in the rabbit kidney," *The Journal of urology,* vol. 175, no. 2, pp. 734-738, 2006. doi: 10.1016/S0022-5347(05)00141-2.

[38] J. Collis *et al.*, "Cavitation microstreaming and stress fields created by microbubbles," *Ultrasonics,* vol. 50, no. 2, pp. 273-279, 2010/02/01/ 2010. doi: 10.1016/j.ultras.2009.10.002.

[39] J. Wu, J. P. Ross, and J.-F. Chiu, "Reparable sonoporation generated by microstreaming," *The Journal of the Acoustical Society of America,* vol. 111, no. 3, pp. 1460-1464, 2002. doi: 10.1121/1.1420389.

[40] T. van Rooij *et al.*, "Viability of endothelial cells after ultrasound-mediated sonoporation: Influence of targeting, oscillation, and displacement of microbubbles," *Journal of Controlled Release,* vol. 238, pp. 197-211, 2016/09/28/ 2016. doi: 10.1016/j.jconrel.2016.07.037.

[41] E. A. Brujan, T. Ikeda, and Y. Matsumoto, "On the pressure of cavitation bubbles," *Experimental Thermal and Fluid Science,* vol. 32, no. 5, pp. 1188-1191, 2008/04/01/ 2008. doi: 10.1016/j.expthermflusci.2008.01.006.

[42] X. Zhao, C. Pellow, and D. E. Goertz, "Intravital imaging and cavitation monitoring of antivascular ultrasound in tumor microvasculature," *Theranostics,* vol. 13, no. 1, p. 250, 2023. doi: 10.7150/thno.79186.

[43] D. Fukumura and R. K. Jain, "Tumor microvasculature and microenvironment: Targets for anti-angiogenesis and normalization," *Microvascular Research,* vol. 74, no. 2, pp. 72-84, 2007. doi: 10.1016/j.mvr.2007.05.003.

[44] J. Wang *et al.*, "Selective depletion of tumor neovasculature by microbubble destruction with appropriate ultrasound pressure," *International Journal of Cancer,* vol. 137, no. 10, pp. 2478-2491, 2015. doi: 10.1002/ijc.29597.

[45] S. B. Keller, Y.-N. Wang, S. Totten, R. S. Yeung, and M. A. Averkiou, "Safety of Image-Guided Treatment of the Liver with Ultrasound and Microbubbles in an in Vivo Porcine Model," *Ultrasound in Medicine & Biology,* vol. 47, no. 11, pp. 3211-3220, 2021. doi: 10.1016/j.ultrasmedbio.2021.07.003.

[46] A. D. Maxwell, C. A. Cain, T. L. Hall, J. B. Fowlkes, and Z. Xu, "Probability of Cavitation for Single Ultrasound Pulses Applied to Tissues and Tissue-Mimicking Materials," *Ultrasound in Medicine & Biology,* vol. 39, no. 3, pp. 449-465, 2013/03/01/ 2013. doi: 10.1016/j.ultrasmedbio.2012.09.004.

[47] K. W. Lin *et al.*, "Histotripsy beyond the intrinsic cavitation threshold using very short ultrasound pulses: microtripsy," *IEEE Transactions on Ultrasonics, Ferroelectrics, and Frequency Control,* vol. 61, no. 2, pp. 251-265, 2014. doi: 10.1109/TUFFC.2014.6722611.

[48] J. E. Parsons, C. A. Cain, G. D. Abrams, and J. B. Fowlkes, "Pulsed cavitational ultrasound therapy for controlled tissue homogenization," *Ultrasound in medicine & biology,* vol. 32, no. 1, pp. 115-129, 2006. doi: 10.1016/j.ultrasmedbio.2005.09.005.

[49] N. McDannold, N. Vykhodtseva, and K. Hynynen, "Targeted disruption of the blood–brain barrier with focused ultrasound: association with cavitation activity," *Physics in Medicine & Biology,* vol. 51, no. 4, p. 793, 2006. doi: 10.1088/0031-9155/51/4/003.

[50] C. H. Farny, R. G. Holt, and R. A. Roy, "The Correlation Between Bubble-Enhanced HIFU Heating and Cavitation Power," *IEEE Transactions on Biomedical Engineering,* vol. 57, no. 1, pp. 175-184, 2010. doi: 10.1109/TBME.2009.2028133.

[51] H. S. Kim, J.-H. Baik, L. D. Pham, and M. A. Jacobs, "MR-guided high-intensity focused ultrasound treatment for symptomatic uterine leiomyomata: long-term outcomes," *Academic radiology,* vol. 18, no. 8, pp. 970-976, 2011. doi: 10.1016/j.acra.2011.03.008.

[52] L. Poissonnier *et al.*, "Control of prostate cancer by transrectal HIFU in 227 patients," *European urology,* vol. 51, no. 2, pp. 381-387, 2007. doi: 10.1016/j.eururo.2006.04.012.

[53] J. Kennedy *et al.*, "High-intensity focused ultrasound for the treatment of liver tumours," *Ultrasonics,* vol. 42, no. 1-9, pp. 931-935, 2004. doi: 10.1016/j.ultras.2004.01.089.

[54] H. Grüll and S. Langereis, "Hyperthermia-triggered drug delivery from temperature-sensitive liposomes using MRI-guided high intensity focused ultrasound," *Journal of Controlled Release,* vol. 161, no. 2, pp. 317-327, 2012. doi: 10.1016/j.jconrel.2012.04.041.

[55] D. Fukumura and R. K. Jain, "Tumor microenvironment abnormalities: causes, consequences, and strategies to normalize," *Journal of cellular biochemistry,* vol. 101, no. 4, pp. 937-949, 2007. doi: 10.1002/jcb.21187.

[56] K. D. Watson *et al.*, "Ultrasound increases nanoparticle delivery by reducing intratumoral pressure and increasing transport in epithelial and epithelial–mesenchymal transition tumors," *Cancer research,* vol. 72, no. 6, pp. 1485-1493, 2012. doi: 10.1158/0008-5472.CAN-11-3232.

[57] L. Eikenes, Ø. S. Bruland, C. Brekken, and C. d. L. Davies, "Collagenase increases the transcapillary pressure gradient and improves the uptake and distribution of monoclonal antibodies in human osteosarcoma xenografts," *Cancer research,* vol. 64, no. 14, pp. 4768-4773, 2004. doi: 10.1158/0008-5472.CAN-03-1472.

[58] C. W. Song, "Effect of local hyperthermia on blood flow and microenvironment: a review," *Cancer research,* vol. 44, no. 10_Supplement, pp. 4721s-4730s, 1984. doi:

[59] A. Sen *et al.*, "Mild elevation of body temperature reduces tumor interstitial fluid pressure and hypoxia and enhances efficacy of radiotherapy in murine tumor models," *Cancer research,* vol. 71, no. 11, pp. 3872-3880, 2011. doi: 10.1158/0008-5472.CAN-10-4482.

[60] R. G. Holt and R. A. Roy, "Measurements of bubble-enhanced heating from focused, MHz-frequency ultrasound in a tissue-mimicking material," *Ultrasound in medicine & biology,* vol. 27, no. 10, pp. 1399-1412, 2001. doi: 10.1016/S0301-5629(01)00438-0.

[61] B. C. Tran, J. Seo, T. L. Hall, J. B. Fowlkes, and C. A. Cain, "Microbubble-enhanced cavitation for noninvasive ultrasound surgery," *IEEE transactions on ultrasonics, ferroelectrics, and frequency control,* vol. 50, no. 10, pp. 1296-1304, 2003. doi: 10.1109/TUFFC.2003.1244746.

[62] B. C. Tran, J. Seo, T. L. Hall, J. B. Fowlkes, and C. A. Cain, "Effects of contrast agent infusion rates on thresholds for tissue damage produced by single exposures of high-intensity ultrasound," *IEEE transactions on ultrasonics, ferroelectrics, and frequency control,* vol. 52, no. 7, pp. 1121-1130, 2005. doi: 10.1109/TUFFC.2005.1503998.

[63] C. C. Coussios, C. H. Farny, G. Ter Haar, and R. A. Roy, "Role of acoustic cavitation in the delivery and monitoring of cancer treatment by high-intensity focused ultrasound (HIFU)," *International Journal of Hyperthermia,* vol. 23, no. 2, pp. 105-120, 2007/01/01 2007. doi: 10.1080/02656730701194131.

[64] A. Clark, S. Bonilla, D. Suo, Y. Shapira, and M. Averkiou, "Microbubble-enhanced heating: exploring the effect of microbubble concentration and pressure amplitude on high-intensity focused ultrasound treatments," *Ultrasound in medicine & biology,* vol. 47, no. 8, pp. 2296-2309, 2021. doi: 10.1016/j.ultrasmedbio.2021.03.035.

[65] W.-S. Chen, A. A. Brayman, T. J. Matula, L. A. Crum, and M. W. Miller, "The pulse length-dependence of inertial cavitation dose and hemolysis," *Ultrasound in medicine & biology,* vol. 29, no. 5, pp. 739-748, 2003. doi: 10.1016/S0301-5629(03)00029-2.

[66] S. Vaezy *et al.*, "Real-time visualization of high-intensity focused ultrasound treatment using ultrasound imaging," *Ultrasound in medicine & biology,* vol. 27, no. 1, pp. 33-42, 2001. doi: 10.1016/S0301-5629(00)00279-9.

[67] B. A. Rabkin, V. Zderic, L. A. Crum, and S. Vaezy, "Biological and physical mechanisms of HIFU-induced hyperecho in ultrasound images," *Ultrasound in medicine & biology,* vol. 32, no. 11, pp. 1721-1729, 2006. doi: 10.1016/j.ultrasmedbio.2006.04.010.

[68] K. J. Haworth, K. B. Bader, K. T. Rich, C. K. Holland, and T. D. Mast, "Quantitative frequency-domain passive cavitation imaging," *IEEE transactions on ultrasonics, ferroelectrics, and frequency control,* vol. 64, no. 1, pp. 177-191, 2016. doi: 10.1109/TUFFC.2016.2620492.

[69] C. R. Jensen, R. W. Ritchie, M. Gyöngy, J. R. T. Collin, T. Leslie, and C.-C. Coussios, "Spatiotemporal Monitoring of High-Intensity Focused Ultrasound Therapy with Passive Acoustic Mapping," *Radiology,* vol. 262, no. 1, pp. 252-261, 2012. doi: 10.1148/radiol.11110670.

[70] H. O. Fadnes, R. K. Reed, and K. Aukland, "Interstitial fluid pressure in rats measured with a modified wick technique," *Microvascular Research,* vol. 14, no. 1, pp. 27-36, 1977/07/01/ 1977. doi: 10.1016/0026-2862(77)90138-8.

[71] R. A. Brace and A. C. Guyton, "Interstitial fluid pressure: Capsule, free fluid, gel fluid, and gel absorption pressure in subcutaneous tissue," *Microvascular Research,* vol. 18, no. 2, pp. 217-228, 1979/09/01/ 1979. doi: 10.1016/0026-2862(79)90030-X.

[72] Christopher C. DuFort *et al.*, "Interstitial Pressure in Pancreatic Ductal Adenocarcinoma Is Dominated by a Gel-Fluid Phase," *Biophysical Journal,* vol. 110, no. 9, pp. 2106-2119, 2016. doi: 10.1016/j.bpj.2016.03.040.

[73] A. Majewicz *et al.*, "Behavior of Tip-Steerable Needles in Ex Vivo and In Vivo Tissue," *IEEE Transactions on Biomedical Engineering,* vol. 59, no. 10, pp. 2705-2715, 2012. doi: 10.1109/TBME.2012.2204749.

[74] G. Griffon-Etienne, Y. Boucher, R. K. Jain, and H. D. Suit, "Effects of Needle Insertion in Tumors on Interstitial Fluid Pressure," *Microvascular Research,* vol. 54, no. 2, pp. 174-177, 1997/09/01/ 1997. doi: https://doi.org/10.1006/mvre.1997.2037.

[75] T. Stylianopoulos *et al.*, "Causes, consequences, and remedies for growth-induced solid stress in murine and human tumors," *Proceedings of the National Academy of Sciences,* vol. 109, no. 38, pp. 15101-15108, 2012/09/18 2012. doi: 10.1073/pnas.1213353109.

[76] Vikash P. Chauhan *et al.*, "Compression of Pancreatic Tumor Blood Vessels by Hyaluronan Is Caused by Solid Stress and Not Interstitial Fluid Pressure," *Cancer Cell,* vol. 26, no. 1, pp. 14-15, 2014. doi: 10.1016/j.ccr.2014.06.003.

[77] M. Stohrer, Y. Boucher, M. Stangassinger, and R. K. Jain, "Oncotic Pressure in Solid Tumors Is Elevated," *Cancer Research,* vol. 60, no. 15, pp. 4251-4255, 2000. doi:

[78] Y. Boucher and R. K. Jain, "Microvascular Pressure Is the Principal Driving Force for Interstitial Hypertension in Solid Tumors: Implications for Vascular Collapse," *Cancer Research,* vol. 52, no. 18, pp. 5110-5114, 1992. doi:

[79] P. Marmottant *et al.*, "A model for large amplitude oscillations of coated bubbles accounting for buckling and rupture," *The Journal of the Acoustical Society of America,* vol. 118, no. 6, pp. 3499-3505, 2005. doi: 10.1121/1.2109427.

[80] P. J. Frinking, J. Brochot, and M. Arditi, "Subharmonic scattering of phospholipid-shell microbubbles at low acoustic pressure amplitudes," (in eng), *IEEE Trans Ultrason Ferroelectr Freq Control,* vol. 57, no. 8, pp. 1762-71, Aug 2010. doi: 10.1109/tuffc.2010.1614.

[81] P. M. Shankar, P. D. Krishna, and V. L. Newhouse, "Subharmonic backscattering from ultrasound contrast agents," (in eng), *J Acoust Soc Am,* vol. 106, no. 4 Pt 1, pp. 2104-10, Oct 1999. doi: 10.1121/1.428142.

[82] J. Chomas, P. Dayton, D. May, and K. Ferrara, "Nondestructive subharmonic imaging," (in eng), *IEEE Trans Ultrason Ferroelectr Freq Control,* vol. 49, no. 7, pp. 883-92, Jul 2002. doi: 10.1109/tuffc.2002.1020158.

[83] P. J. A. Frinking, N. de Jong, and E. I. Céspedes, "Scattering properties of encapsulated gas bubbles at high ultrasound pressures," *The Journal of the Acoustical Society of America,* vol. 105, no. 3, pp. 1989-1996, 1999. doi: 10.1121/1.426732.

[84] N. de Jong *et al.*, ""Compression-only" behavior of phospholipid-coated contrast bubbles," (in eng), *Ultrasound Med Biol,* vol. 33, no. 4, pp. 653-6, Apr 2007. doi: 10.1016/j.ultrasmedbio.2006.09.016.

[85] G. Xu *et al.*, "Subharmonic Scattering of SonoVue Microbubbles Within 10-40-mmHg Overpressures In Vitro," (in eng), *IEEE Trans Ultrason Ferroelectr Freq Control,* vol. 68, no. 12, pp. 3583-3591, Dec 2021. doi: 10.1109/tuffc.2021.3101694.

[86] R. H. Azami, F. Forsberg, J. R. Eisenbrey, and K. Sarkar, "Acoustic response and ambient pressure sensitivity characterization of SonoVue for noninvasive pressure estimation," (in eng), *J Acoust Soc Am,* vol. 155, no. 4, pp. 2636-2645, Apr 1 2024. doi: 10.1121/10.0025690.

[87] E. A. Neppiras, "Acoustic cavitation," *Physics reports,* vol. 61, no. 3, pp. 159-251, 1980. doi: 10.1016/0370-1573(80)90115-5.

[88] Q. Wu *et al.*, "Challenges in classifying cavitation: Correlating high-speed optical imaging and passive acoustic mapping of cavitation dynamics," *The Journal of the Acoustical Society of America,* vol. 156, no. 5, pp. 3608-3620, 2024. doi: 10.1121/10.0034426.

[89] T. Sun, G. Samiotaki, S. Wang, C. Acosta, C. C. Chen, and E. E. Konofagou, "Acoustic cavitation-based monitoring of the reversibility and permeability of ultrasound-induced blood-brain barrier opening," (in eng), *Phys Med Biol,* vol. 60, no. 23, pp. 9079-94, Dec 7 2015. doi: 10.1088/0031-9155/60/23/9079.

[90] C. C. Coussios and R. A. Roy, "Applications of acoustics and cavitation to noninvasive therapy and drug delivery," *Annu. Rev. Fluid Mech.,* vol. 40, no. 1, pp. 395-420, 2008. doi: 10.1146/annurev.fluid.40.111406.102116.

[91] A. Eller and H. G. Flynn, "Generation of Subharmonics of Order One-Half by Bubbles in a Sound Field," *The Journal of the Acoustical Society of America,* vol. 46, no. 3B, p. 722, 3/11/2025 1969. doi: 10.1121/1.1911753.

[92] J. Sijl *et al.*, "Subharmonic behavior of phospholipid-coated ultrasound contrast agent microbubbles," (in eng), *J Acoust Soc Am,* vol. 128, no. 5, pp. 3239-52, Nov 2010. doi: 10.1121/1.3493443.

[93] S. B. Keller, P. S. Sheeran, and M. A. Averkiou, "Cavitation Therapy Monitoring of Commercial Microbubbles With a Clinical Scanner," (in eng), *IEEE Trans Ultrason Ferroelectr Freq Control,* vol. 68, no. 4, pp. 1144-1154, Apr 2021. doi: 10.1109/tuffc.2020.3034532.

[94] T. R. Porter, F. Xie, S. Li, A. D'Sa, and P. Rafter, "Increased ultrasound contrast and decreased microbubble destruction rates with triggered ultrasound imaging," (in eng), *J Am Soc Echocardiogr,* vol. 9, no. 5, pp. 599-605, Sep-Oct 1996. doi: 10.1016/s0894-7317(96)90054-1.

[95] C. Tremblay-Darveau, R. Williams, and P. N. Burns, "Measuring absolute blood pressure using microbubbles," (in eng), *Ultrasound Med Biol,* vol. 40, no. 4, pp. 775-87, Apr 2014. doi: 10.1016/j.ultrasmedbio.2013.10.017.

[96] X. Qiao, Y. Wen, J. Yu, A. Bouakaz, Y. Zong, and M. Wan, "Noninvasive Pressure Estimation Based on the Subharmonic Response of SonoVue: Application to Intracranial Blood Pressure Assessment," (in eng), *IEEE Trans Ultrason Ferroelectr Freq Control,* vol. 69, no. 3, pp. 957-966, Mar 2022. doi: 10.1109/tuffc.2021.3138100.

[97] A. Bouakaz, P. J. Frinking, N. de Jong, and N. Bom, "Noninvasive measurement of the hydrostatic pressure in a fluid-filled cavity based on the disappearance time of micrometer-sized free gas bubbles," (in eng), *Ultrasound Med Biol,* vol. 25, no. 9, pp. 1407-15, Nov 1999. doi: 10.1016/s0301-5629(99)00109-x.

[98] T. Faez, G. Renaud, M. Defontaine, S. Calle, and N. de Jong, "Dynamic manipulation of the subharmonic scattering of phospholipid-coated microbubbles," (in eng), *Phys Med Biol,* vol. 56, no. 19, pp. 6459-73, Oct 7 2011. doi: 10.1088/0031-9155/56/19/018.

CHAPTER 2. DELIVERY OF CAVITATION THERAPY WITH A MODIFIED CLINICAL SCANNER: IN VITRO EVALUATION[1]

Abstract

In this study we design and implement pulses (1.67 MHz, 20-1000 cycles, 0.8—2.5 MPa, 5-100 ms pulse repetition time) suitable for microbubble cavitation treatments with a phased array of a clinical ultrasound scanner. A range of acoustic parameters was evaluated in a tissue-mimicking phantom with suspended Sonazoid microbubbles. Hydrophone measurements were used to optimize the transmit beamforming. A passive cavitation detection system was designed to measure the microbubble scattered signals over a 1 s exposure. Postprocessing of the scattered signals evaluated frequency content to extract broadband energy and calculate the inertial cavitation dose (ICD). ICD was maximized at 1000 cycles (maximum pulse length), 5 ms (fastest firing rate), and 2.5 MPa peak negative pressure (maximum pressure). Inertial cavitation was only sustained for about 3 pulses (out of 100s fired) occurring within the first 100 ms of treatment. Temporal analysis of the first 1000 cycle pulse revealed that broadband energy is sustained for the entire pulse. We also demonstrate that while inertial cavitation is possible with clinically available pulse wave Doppler settings, ICD can be significantly increased using the new conditions suggested in this work. We have delivered successful image-guided cavitation treatment after modifying a clinical scanner and monitored the cavitation dose with a PCD system on a gel phantom with suspended microbubbles. We plan to apply this technique in vivo in animal tumor models next. This work demonstrates the first implementation of long, high-pressure pulses on a clinical scanner that users can optimize for cavitation treatments.

[1] *This chapter has appeared as:* ***De Koninck, LH.****, Vuong KS., Shin, S., Powers, JE., Averkiou MA. "Delivery of cavitation therapy with a modified clinical scanner: in vitro evaluation" IEEE Transactions on Ultrasonics, Ferroelectrics, and Frequency Control, 72 (3), 351-361 (2025).*

2.1 INTRODUCTION

Ultrasound-mediated microbubble cavitation is an emerging therapeutic technique where acoustic pulses produce microbubble oscillations to noninvasively induce targeted biological effects [1-3]. Microbubbles are conventionally used as a contrast agent in ultrasound imaging and are clinically approved for cardiac [4] and hepatic [5-7] applications. Under certain acoustic exposures, microbubbles may induce localized cellular and tissue changes and thus act as a therapeutic agent [8]. Since microbubbles are supplied as an intravenous injection, cavitation therapy enables targeted treatment of vascularized structures, such as organs and tumors, and has been studied in various animal cancer models [1, 3, 9]. Therapeutic outcomes such as blood brain barrier opening [10], sonoporation [11, 12], and cancer ablation [13], are highly dependent on acoustic parameters and the type of cavitation (stable versus inertial). Another outcome that was observed resulting from these treatments is a reduction in tumor blood flow and perfusion [1, 3]. It is hypothesized that the immature neovessels which are prevalent in tumors [14] are more susceptible to mechanical damage from cavitation. This tumoral neovessel susceptibility enables preferential targeting of tumor vasculature while avoiding damage to the surrounding tissue [9, 15].

While cavitation therapy has shown promising biological outcomes for treatment of tumors, a wide range of acoustic conditions employed for these treatments have been reported. Transmit parameters of interest include frequency (0.02 – 5 MHz), pulse length (1 μs – 100 ms, or continuous wave), peak negative pressure (0.2 – 9 MPa), pulse repetition time (2 μs – 10 s), and treatment duration (1 s – 31.5 min) [1, 9, 16-37]. As parameter optimization is an evolving problem, many of these studies were performed with custom single element transducers for their ultrasound treatment. Although flexible in transmit parameter selection, single element transducer systems usually require auxiliary components (for example function generators and amplifiers), are incapable of imaging for alignment and monitoring the treatment area, and they require regulatory approval before clinical use. This severely limits the clinical translation of cavitation therapy and has created a need for current clinical systems to deliver these treatments.

Several groups have begun work into delivering ultrasound-microbubble cavitation therapy with a clinical ultrasound system, but the lack of ability to modify a scanner pulsing parameters has limited progress. Dimcevski, et al. [36] used an unmodified LOGIQ 9 scanner (GE Healthcare,

Waukesha, WI, USA) and 4C curvilinear probe in a clinical study to enhance gemcitabine delivery. While they show a minimal increase in patient survival when treated with cavitation therapy, the authors admit that their previous work with a custom transducer utilizing a greater duty cycle (40%) that is not available on the scanner demonstrated greater therapeutic efficacy. Mason, et al. [37] used a Philips EPIQ scanner (Philips Healthcare, Bothell, WA, USA) and X5-1 matrix probe with unmodified pulsing parameters for treatment of peripheral artery disease. The authors evaluated different combinations of line density and pulse length (per line) to enhance blood flow and adenosine triphosphate release. However, their study was limited to the preset line densities and pulse lengths (only 5 and 40 cycles) and did not evaluate other parameters such as pressure and pulse repetition time (PRT). Cavitation therapy has also been implemented on research scanners, that while not clinically approved, demonstrates that diagnostic probes/scanners can generate sufficient acoustic pressure for microbubble cavitation and drug delivery enhancement [38]. This specific study considered much shorter pulses (2-20 cycles) that limit the total cavitation dose, as well as multiple beams per treatment area that may cause microbubble destruction in neighboring beams. In previous work from our lab [1, 15], we modified a Philips EPIQ scanner and S5-1 phased array to produce a 200-cycle pulse at a PRT of 20 ms and acoustic pressures between 2-3 MPa. This set of acoustic conditions demonstrated a selective disruption of tumor blood flow with enhanced uptake and penetration of doxorubicin, but we were unable to explore optimization of ultrasound exposure due to our selection of only one treatment condition. The S5-1 probe was also coupled directly to the animal model for treatment, which prevented us from imaging the tumors during treatment and evaluating beamforming that may have improved cavitation therapy efficacy.

In this study we implement a wide range of acoustic conditions (0.8—2.5 MPa, 20-1000 cycles, and 5-100 ms PRT) for cavitation treatments on a phased array of a clinical scanner. More importantly, we have implemented this therapeutic setting as part of the imaging workflow and provided the ability to interleave imaging and therapy for better image guidance. In addition, we redesigned the transmit beamforming to produce large beams that can cover a tumor of about 1 cm^3 with a single transmit event. Hydrophone measurements in water are used to characterize the sound field from different transmit beamforming configurations and to select an optimal condition that spatially covers the tumor. The various combinations of cavitation therapy are evaluated in a tissue-mimicking gel phantom where Sonazoid microbubbles at concentrations similar to those

used clinically are suspended to mimic the microcirculation of a tumor after a bolus injection. Passive cavitation detection is used to measure the scattered signal from each experimental condition over a 1 s exposure. The root mean square (RMS) and broadband energy of each signal is calculated to evaluate cavitation activity. The inertial cavitation dose (ICD) is then calculated over the treatment duration to compare the cavitation energy during different acoustic conditions.

2.2 Material and Methods

2.2.1 Modified Clinical System

Acoustic conditions suitable for cavitation therapy were implemented on a Philips EPIQ scanner and S5-1 phased array (Philips Healthcare, Bothell, WA, USA). We modified the standard B-mode setting to implement these conditions. Instead of forming a sector scan with multiple lines, the center line is repeatedly transmitted at a specified PRT. Pulses suitable for cavitation treatments were programmed with a frequency of 1.67 MHz (the lowest frequency that the S5-1 could efficiently transmit), duration of 20-1000 cycles and PRT of 5-100 ms. The number of cycles and the PRT were controlled by reprogrammed, existing knobs on the front panel (the 2D-Opt knob and the resolution-speed knob, respectively) of the scanner, enabling fast and real-time adjustment of therapeutic conditions. The produced acoustic pressure is selected by adjusting the output power on the front panel used in clinical imaging which in turn adjusts the transmitted voltage. The specific acoustic conditions were selected to be consistent with prior work studying ultrasound cavitation therapy with microbubbles [1, 9, 39, 40]. The 20-cycle pulse was used to investigate what an unmodified clinical scanner would be able to do since such a condition may be found in the pulse wave Doppler mode of clinical scanners. The user can freely switch to other imaging presets where B-mode and contrast imaging is available, enabling image-guidance before and after treatment. The present implementation allows interleaving treatment and imaging.

The transmit beamforming available to the S5-1 phased array was also modified to create a focused ultrasound beam with sufficient pressure for cavitation therapy and capable of treating the majority of a $1 cm^3$ tumor volume. While the focus of the elevation plane is fixed at 80.18 mm (defined by the fixed lens of the array), the focus of the azimuthal plane can be programed to any required depth by changing the element delays. We did not use the multi-zone (focus) feature of the scanner and all the transmit beamforming configurations included a single transmit event. The spatial extent of the sound field resulting from 8 focal lengths (**Table 2.1**) was measured in a water

Table 2.1: Modified transmit beamforming conditions per focal length

Azimuthal Focal Length (cm)	Number of Active Elements
3.2	40
4	40
5	64
6.3	64
8	80
10	80
13	80
17	80

tank with a 0.4 mm membrane hydrophone (UT1604-225; Precision Acoustics, Dorchester, UK) in both the azimuthal and elevation planes from which the effective treatment volume was estimated (continuous area with pressures within 6 dB of maximum pressure). An illustration of the S5-1 aperture is shown in **Figure 2.4**(a), showing the azimuthal and elevation planes, and the orientation of the individual elements (small number shown for demonstration here) represent an active element referred to in **Table 2.1**. The optimal beamforming setting was selected by maximizing 2 criteria: a.) effective treatment volume $\geq 1 cm^3$, and b.) average pressure within the treatment volume. Hydrophone measurements were then recorded at the center of the ideal treatment location to characterize output pressure at various transmit voltages. We note that all the implementation details described in the present section are new and were not available in our previous works [1, 15].

2.2.2 Passive Cavitation Detection

To evaluate the produced cavitation field from the selected acoustic conditions, we used a passive cavitation detection system. A schematic of this setup is shown in **Figure 2.1**(a), with the S5-1 phased array producing the acoustic conditions and a single element circular 1.91 cm diameter focused transducer (C308, Evident, Tokyo, Japan) with a center frequency of 5 MHz and 5.1 cm focal length as the receiver. A diagram of the treatment pulsing sequence is shown in **Figure 2.1**(b). To prevent the S5-1 directly transmitting to the C308, a 3D printed cylinder with an inner diameter of 2.5 cm and a length of 2 cm was attached to the C308. Measurements of the

signal detected by the C308 with and without the cylinder in the absence of any scatterer confirmed the blocking of the direct path. A comparison of the scattered signal from a wire target received by the C308 with and without the cylinder attachment confirmed that the cylinder does not affect the received amplitude. A tissue-mimicking phantom was positioned such that its geometric center was aligned with the overlapped focal regions of both transducers. Phantoms were made using an evaporated milk and porcine gelatin powder recipe as described by Farrer et al. [41] with an attenuation coefficient of 0.32 dB/cm (at 1 MHz), density of 1057 kg/m^3, and speed of sound of 1524 m/s. Prior to solidification, Sonazoid microbubbles (GE Healthcare, Amersham, UK), with base concentration of 1.79*10^8 MB/mL [42], were mixed into the liquid phantom at a concentration of 1000 microbubbles per mL of phantom. This concentration is similar to the clinical dose of Sonazoid for breast and liver imaging at 0.12 μL MB/kg mixed in 5 L of blood [43]. Phantoms were refrigerated for 1 hour before being removed from their mold and transferred to a plastic box with cutouts in each wall, allowing for direct coupling of the phantom to the water.

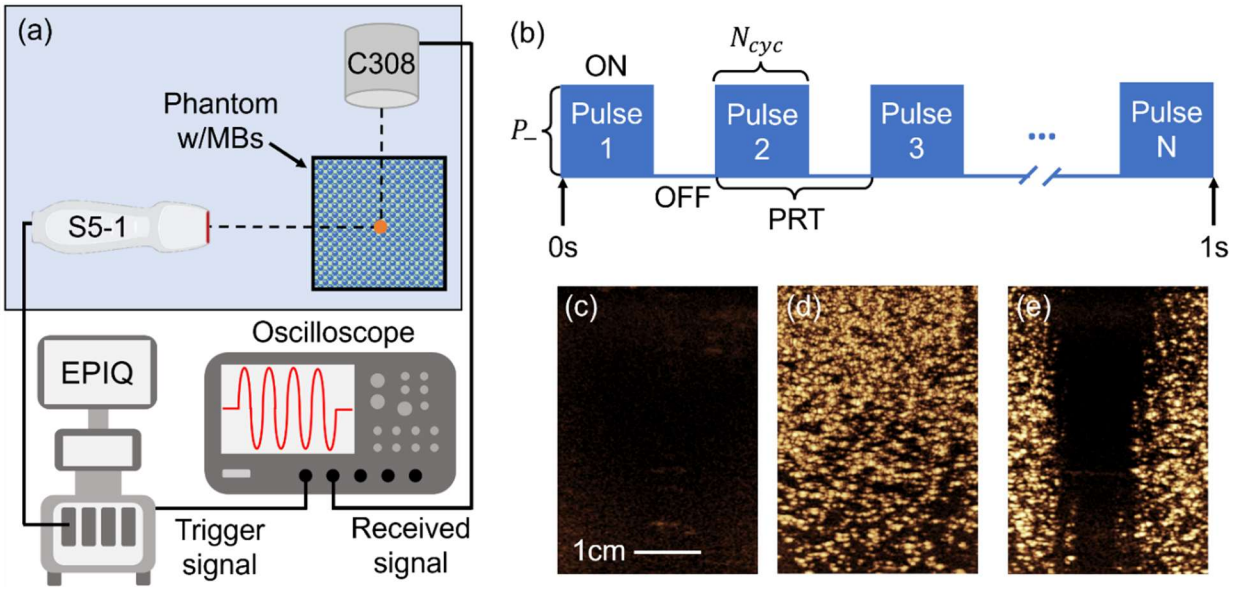

***Figure 2.1**: Schematic of passive cavitation detection, and example phantom images*

(a) Schematic of passive cavitation detection setup with the S5-1 clinical probe as transmit and the C308 single element transducer as receiver. Dashed lines indicate intended beam path, and the orange circle represents the overlapped focal regions of the S5-1 and C308. (b) Diagram of pulsing sequence for 1s treatment, demonstrating acoustic conditions (P_= peak negative pressure, N_{cyc} = number of cycles, PRT = pulse repetition time). Example ultrasound contrast images of the phantom without microbubbles (c), with microbubbles before ultrasound exposure (d) and after 1s treatment (e) with 200 cycles, 0.8 MPa, and 20 ms PRT.

Sonazoid was chosen because this contrast agent survives the phantom solidification process better than other commercially available microbubbles [44]. One phantom was used per trial, with each trial consisting of a 1 s treatment duration at fixed acoustic conditions. We performed 3 trials per condition (N = 33 total). A control group with no microbubbles was used to evaluate the baseline scattered signal for each acoustic condition. The presence of microbubbles in phantoms was confirmed with ultrasound imaging (L12-3 linear array of the EPIQ scanner while scanning in contrast mode) prior to each experiment and following exposure (**Figure 2.1**(c,d,e)). Contrast images were produced using a nonlinear technique (amplitude modulation at 4 MHz) and a low mechanical index (MI) of 0.06 to avoid bubble destruction [45]. The Pennes bioheat equation [46] was used to predict heat deposition during a 1s treatment of the gel phantom without microbubbles, and for our largest possible duty cycle (3%) at 2.5 MPa, 1.67 MHz we estimated little to no temperature increase ($\leq 0.1℃$) at the ideal treatment location.

Scattered pulses were recorded using an oscilloscope (DPO 7054C Tektronix, Beaverton, OR, USA) with a segmented memory technique ("FastFrame"). Prior to each sonication, the oscilloscope display was adjusted such that the anticipated pulse, based on time of flight, was centered in the viewing area. The user then defines the number of transmit events they wish to capture and at what resolution to record the data. An external trigger from the EPIQ scanner (**Figure 2.1**(a)) triggered the oscilloscope to capture the scattered sound from all pulses fired over the 1 s treatment duration. The scattered pulses were sampled at 100 MS/s. After each experiment the data was exported from the oscilloscope for post-processing using a custom MATLAB (MathWorks) script.

2.2.3 Cavitation Analysis

The processing of received scattered signals during cavitation treatments was performed following the algorithm outlined in **Figure 2.2**. This is adapted from existing techniques that calculate cavitation dose as an energy density derived from the summation of "inharmonic" (broadband) energy per pulse, but in this work, we omit the spatial extent of cavitation [47, 48]. First, each waveform is truncated to its respective original pulse length with a rectangular window and the RMS of the truncated waveform is calculated. The average value of the waveform is first removed (small offset of zero value of the oscilloscope), and the one-sided power spectrum (scaled by 2 divided by the number of samples squared) is taken of each truncated waveform. For each

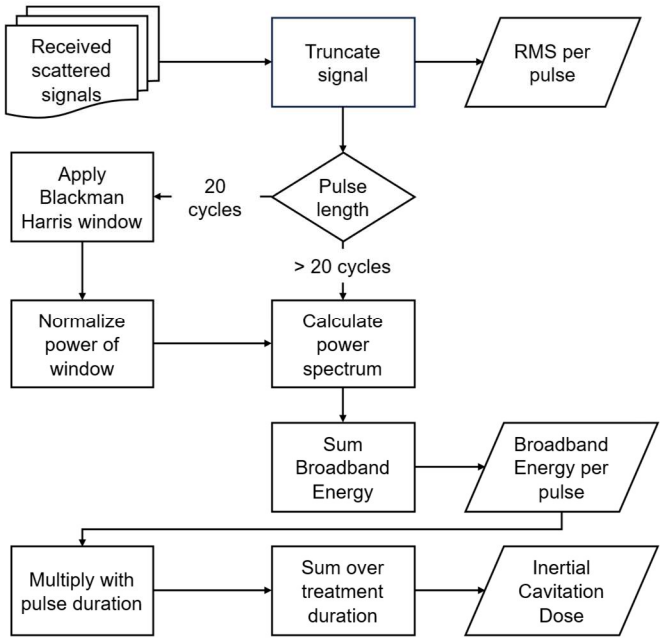

***Figure 2.2**: Cavitation analysis algorithm*

Post-processing algorithm of received scattered signals to evaluate RMS, broadband energy, and inertial cavitation dose. Parallelograms represent output data.

spectrum, broadband energy was collected above the third harmonic (to limit influence of transmitted pulse) in the frequency range of 5-10 MHz (roughly the upper limit of the receiver bandwidth) as shown in **Figure 2.3**. Within this range, frequency bands centered on each harmonic and ultraharmonic with a bandwidth of 0.3 MHz were excluded, while the remaining bands (green spaces, **Figure 2.3**) were summed resulting in the broadband energy per pulse. This process was

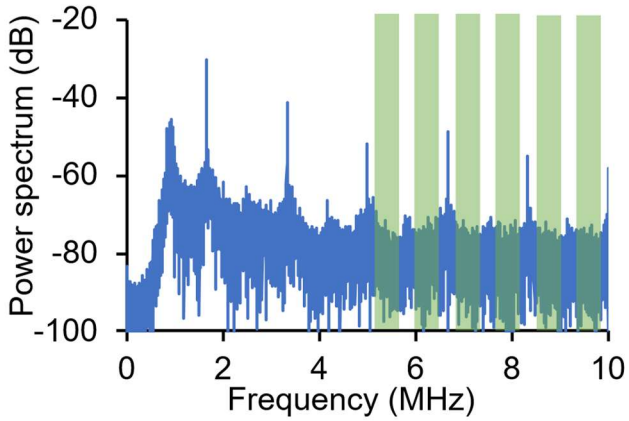

***Figure 2.3**: Example of power spectrum analysis*

Example power spectrum of pulse 1 using 1000 cycles, 2.2 MPa, and 20 ms pulse repetition time. Green bands indicate regions summed to find broadband energy per pulse.

repeated for all pulses. The inertial cavitation dose (ICD) was calculated as the summation over the treatment duration of the product of the broadband energy per pulse with the pulse duration. One exception to this method is the 20-cycle pulse, where the truncated pulse is multiplied by a Blackman-Harris window to reduce spectral leakage. For standardization, the power of the window is set equal to 1 by scaling the amplitude of the pulse by the square root of the number of samples divided by the summation of the window function squared. We also measured the temporal behavior of RMS and broadband energy within a single pulse by applying a rectangular window (40 cycle length at 1.67 MHz) to the first truncated pulse of the 1000 cycle condition. This window was then shifted by 20 cycles each iteration (50% overlap) through the entire pulse. For each window, the RMS and broadband energy is calculated in the same manner as described above.

2.3 RESULTS

2.3.1 Sound Field Characterization

The sound field at the 30 V setting produced by the beamforming selected for cavitation treatments (10 cm focal depth, **Table 2.1**) in the azimuthal and elevation planes is shown in **Figure 2.4**(b) and **Figure 2.4**(c), respectively. Using the full aperture (80 elements) and a similar focal

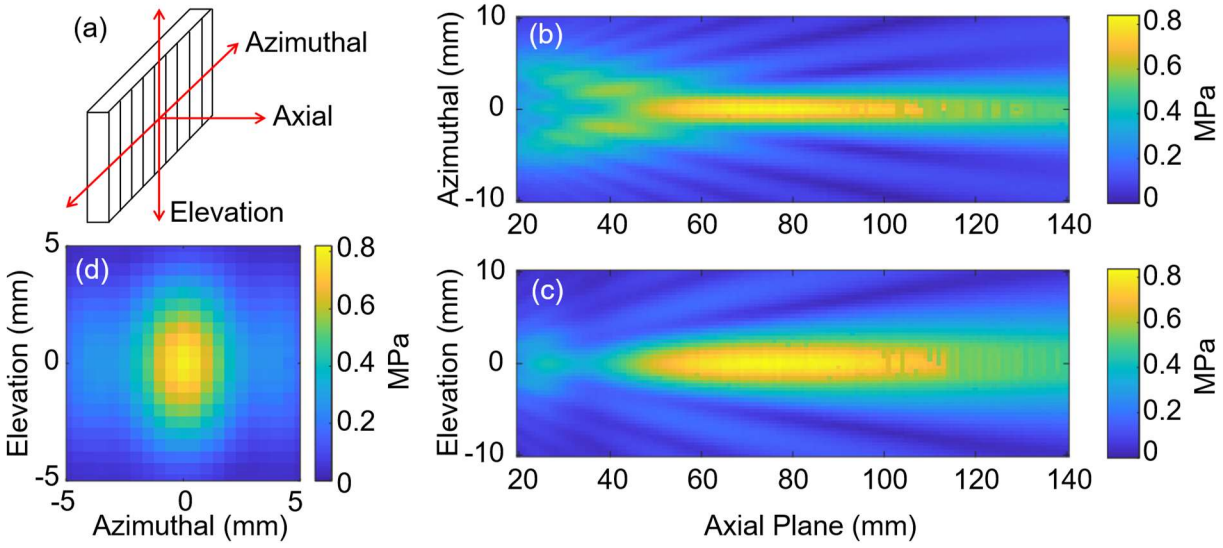

***Figure 2.4**: Sound field measurements of S5-1*

(a) Illustration of the S5-1 aperture showing the azimuthal, elevation, and axial planes, and columns on the aperture face representing active elements. Hydrophone measurement of the S5-1 acoustic pressure field with treatment beamforming in azimuthal (b) and elevation (c) planes, and focal plane measured 64 mm from the S5-1 (d). The azimuthal focus of this setting is 100 mm.

depth to the focus of the elevation plane resulted in the largest amplitude distributed over the largest focal region. The maximum pressure was measured at 6.4 cm axially from the S5-1 which we selected as the target location to deliver the cavitation treatment. **Figure 2.4**(d) shows the transverse sound field at an axial distance of 6.4 cm. From this plot we can estimate the 6 dB spot size of our treatment to be 6x4 mm in the elevation and azimuthal planes, respectively.

Waveforms measured on axis at 6.4 cm in the water tank at transmit voltages of 30 V (20, 200, 1000 cycles) and 120 V (20 cycles) and their corresponding frequency spectra (after truncation and applying Blackman-Harris window) are shown in **Figure 2.5**. These measurements confirm that the scanner and S5-1 phased array produce the required pulses at different pulse lengths and voltages. By scattering from a wire target and receiving with a small PZT transducer we also confirmed that the longer pulses sustained their amplitude over the duration of the entire pulse at the maximum transmit voltage with only a minimal ~5% amplitude drop during the last 50 μs of the 1000 cycle pulse. At 30 V, the peak positive and negative pressures (PPP and PNP, respectively) were 1.3 and 0.8 MPa, respectively. At 120 V, the PPP was 10 MPa, while the PNP was 2.2 MPa. Although the transmit voltage increased by a factor of 4, the PNP increased by a

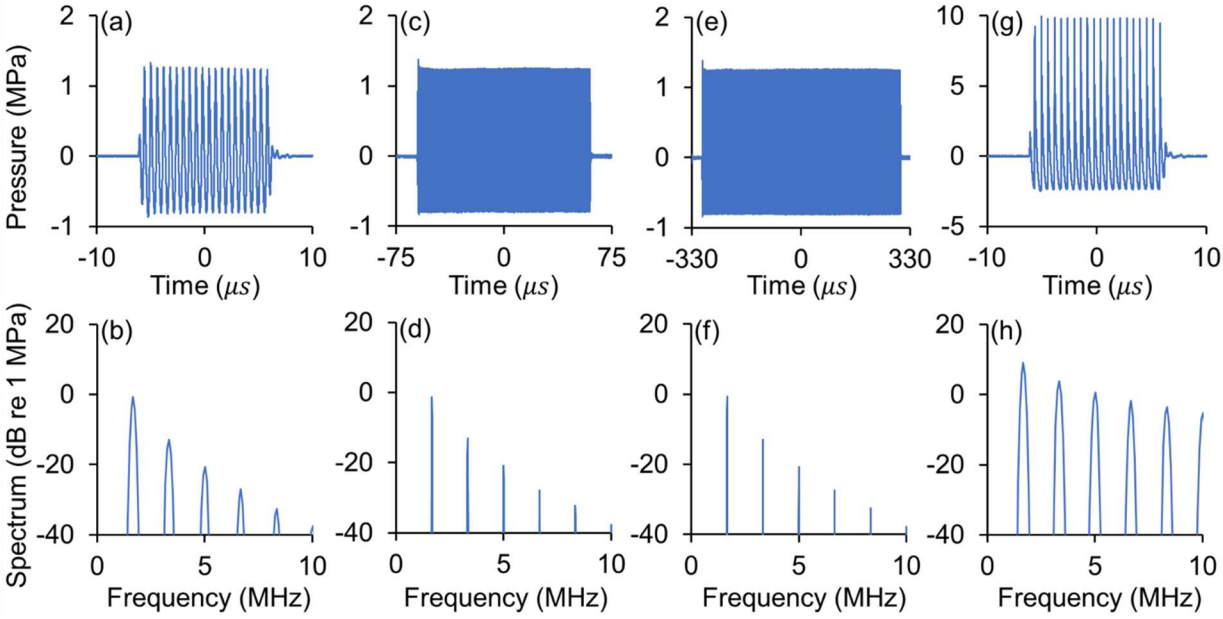

***Figure 2.5**: Waveform measurements of S5-1 with modified transmit*

Waveforms and corresponding frequency spectra of pulses produced with the S5-1 phased array measured in water at 30 V with 20 cycles [(a), (b)], 200 cycles [(c), (d)], 1000 cycles [(e), (f)] and 120 V with 20 cycles [(g), (h)] measured on-axis 64 mm from transducer.

factor of 2.8 and the peak positive pressure by a factor of 7.7. This asymmetry and the harmonics in the spectra indicate that nonlinear propagation through water significantly impacts the produced sound field at these amplitudes. When converting our maximum PNP (2.5 MPa) to MI without derating for attenuation through tissue (the sound path includes water and the gel phantom), this condition yields MI ~ 1.93 which barely exceeds the MI FDA limit. The spatial-peak temporal-average intensity (I_{SPTA}) was also calculated for the acoustic conditions in this study, with the maximum experimental acoustic conditions (1000 cycles, 2.2 MPa PNP, 10 MPa PPP, 20 ms PRT), producing an intensity of 37 W/cm^2. This intensity is well above the $I_{SPTA} \leq 0.72$ W/cm^2 limit set by the FDA for diagnostic ultrasound systems [49].

2.3.2 Produced Cavitation from Therapy Pulses

Figure 2.6(a) shows the RMS value (after subtracting the RMS baseline signal without microbubbles) of each pulse as a function of pulse number up to 12 pulses. Every point in this figure represents 1 scattered pulse. The different curves show different focal PNP (0.8, 1.5, 1.9, 2.2, and 2.5 MPa, not derated) and the 200-cycle pulse with 20 ms PRT was used. At the lowest measured pressure (0.8 MPa) the RMS stays constant and near a value of zero. However, higher pressures exhibit markedly greater RMS values for the first few pulses and then return to zero levels for the remainder of treatment. The 1.5 MPa pressure is the first pressure this sudden increase in RMS amplitude was observed, and higher pressures do not significantly increase RMS amplitude beyond the behavior at 1.5 MPa.

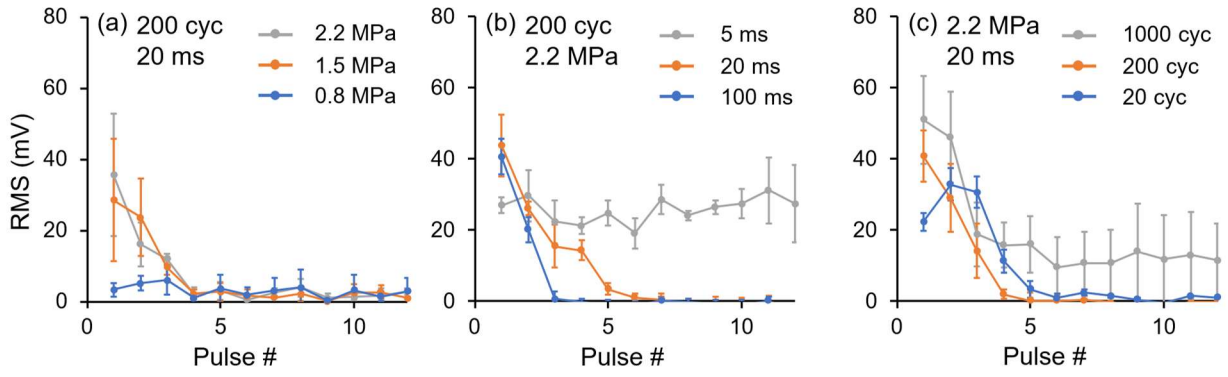

***Figure 2.6**: Average RMS of the scattered pulses as a function of pulse number.*

(a) The effect of different PNPs when using 200 cycles and PRT of 20 ms. (b) The effect of PRT when using 200 cycles and 2.2 MPa PNP. (c) The effect of number of cycles when using a PRT of 20 ms and 2.2 MPa PNP. Error bars indicate 1 standard deviation, and baseline signal was subtracted before averaging.

Figure 2.6(b) shows the RMS value of the first 12 scattered pulses after subtracting the baseline RMS value for 3 different PRT (5, 20, and 100 ms). Here we again used 200 cycles at 2.2 MPa PNP. We observe the only case of sustained RMS value for the entire treatment duration at the smallest PRT of 5 ms. This is likely due to the gas not having fully diffused from the bubbles with disrupted shells between pulses and continuing to scatter the pulses that follow. It is also possible that some coalescence takes place and larger gas pockets are formed. At greater PRTs (20, 100 ms), the RMS value reduces to zero within the first 3-5 pulses (~0.2 s) of treatment due to the longer time between pulses. We note that the 20 ms data in **Figure 2.6**(b) is the same condition as the 2.2 MPa line in **Figure 2.6**(a) but was remeasured hence a small difference. Similar trends are observed in **Figure 2.6**(c) where we evaluate the effect of the number of cycles on the scattered RMS signal after repeated firings over 12 scattered pulses and while using 20 ms PRT and 2.2 MPa PNP. For all pulse durations (number of cycles), the majority of RMS amplitude is reduced to zero level after the first few firings, with only minor differences in magnitude.

Figure 2.7 is similar to **Figure 2.6** with the exception that the y-axis is the net broadband energy (minus the baseline value) instead of the RMS value of the scattered pulse. All plots show similar behavior, where broadband energy quickly reduces to zero after a few firings (pulses). In **Figure 2.7**(a) where the pressure is varied, we see that at 0.8 MPa there is no broadband energy, while 1.5 MPa is the first setting with significant elevation of broadband energy (for first 3 pulses). This agrees with the RMS amplitude results, although further increases in pressure exhibit elevated

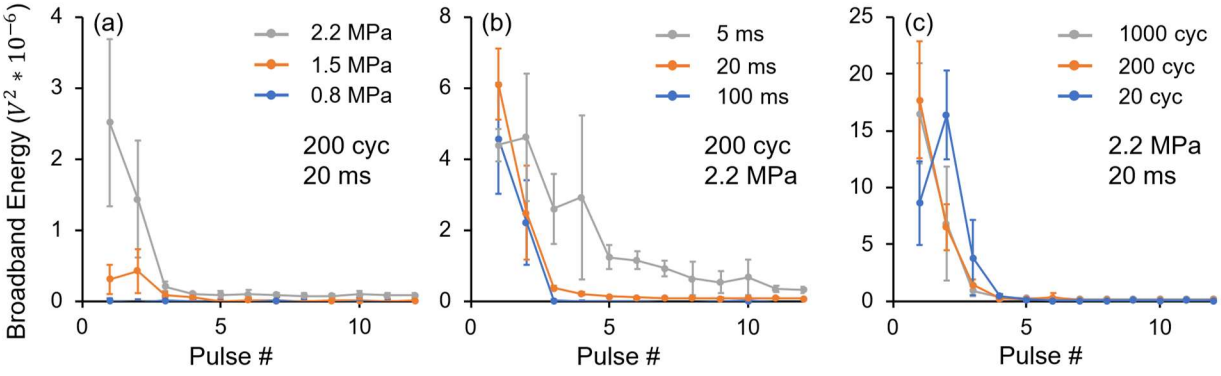

***Figure 2.7**: Average broadband energy of the scattered pulses as a function of pulse number.*

(a) The effect of different PNPs when using 200 cycles and PRT of 20 ms. (b) The effect of PRT when using 200 cycles and 2.2 MPa PNP. (c) The effect of number of cycles when using a PRT of 20 ms and 2.2 MPa PNP. Error bars indicate 1 standard deviation, and baseline signal was subtracted before averaging.

broadband noise which did not result in an increase in RMS in **Figure 2.6**(a). When PRT is varied in **Figure 2.7**(b), the number of pulses with elevated broadband energy increases as PRT decreases (more frequent firings). Both 100 ms and 20 ms PRT produce cavitation above zero-level for ~3 pulses, while the 5ms PRT maintains cavitation for up to 12 pulses. For the smaller PRTs (5 and 20 ms), although the number of pulses above zero-level is different, the decay of the broadband signal is similar in terms of time (~60 ms) and is probably driven by the diffusion time after shell disruption. Finally in **Figure 2.7**(c) where we evaluate the effect of the number of cycles on the scattered broadband energy, we observe that all 3 pulse durations had similar magnitude broadband energy per pulse which was only elevated above baseline for the first 3 firings (pulses). This agrees with the RMS amplitude results (**Figure 2.6**) where there are small differences between the pulse durations.

The average measured ICD (after baseline subtraction) over the entire treatment duration, both with and without microbubbles, as a function of each acoustic condition is shown in **Figure 2.8**. Similarly to **Figure 2.6** and **Figure 2.7**, we evaluated the effect of pressure, PRT and number of cycles in (a), (b) and (c), respectively. In **Figure 2.8**(a) the ICD as a function of PNP is shown for the 200-cycle pulse and PRT of 20 ms. As expected, ICD is increasing with PNP. The 1.5 MPa PNP is the first pressure to have ICD significantly greater than zero, in agreement with the RMS and broadband energy findings in **Figure 2.6** and **Figure 2.7**. No significant increase was observed in the baseline ICD (not shown), indicating that native cavitation did not occur in any of our

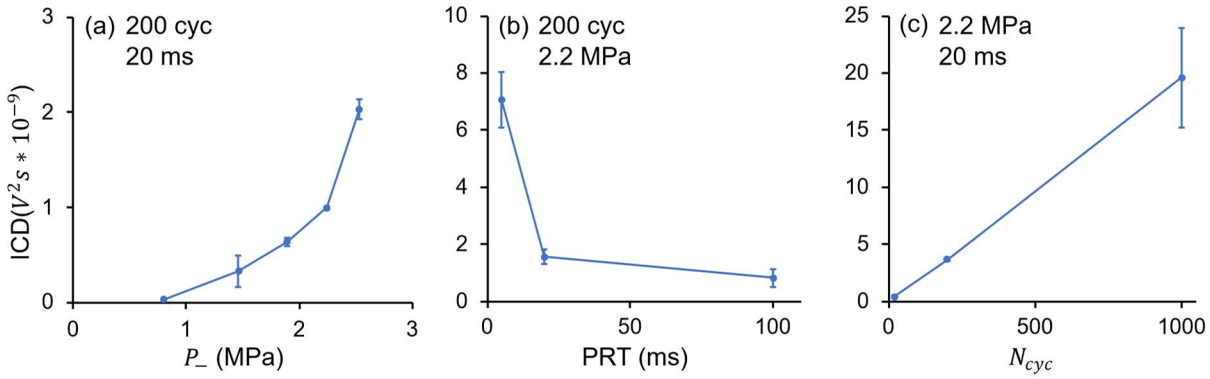

***Figure 2.8**: Inertial cavitation dose as a function of pressure, PRT, and number of cycles*

(a) Average inertial cavitation dose (ICD) as a function of PNP when using 200 cycles and 20 ms PRT. (b) ICD as a function of PRT when using 200 cycles and 2.2 MPa PNP. (c) ICD as a function of number of cycles when using a PRT of 20 ms and 2.2 MPa PNP. Error bars indicate 1 standard deviation and baseline signal was subtracted before averaging.

phantom experiments. In **Figure 2.8**(b) the ICD as a function of the PRT is shown for the 200-cycle pulse and PNP=2.2 MPa. The 5 ms PRT produces a significant increase in ICD. For the 20 and 100 ms PRT, the ICD is much lower. In **Figure 2.8**(c) the ICD as a function of the number of cycles in the pulse is plotted for PNP=2.2 MPa and PRT=20 ms. As pulse duration increases, we observe a linear increase in ICD. Since broadband energy magnitude was the same for all pulse lengths (**Figure 2.7**(c)), the observed linear slope represents increased cavitation duration, where the 1000 cycle pulses are 5 and 50 times longer than the 200 and 20 cycle pulses, respectively, and thus the ICD is 5 and 50 times greater.

To investigate whether the above cavitation behavior is representative of the entire pulse, we also evaluated the average measured RMS amplitude and broadband energy within the first 1000 cycle pulse (after removing baseline) at PNP=2.2 MPa, as shown in **Figure 2.9**. As described in Section II-C, we took 40 cycles at a time and advanced by 20 cycles until we processed the entire 1000 cycles pulse. Both the RMS value (**Figure 2.9**(a)) and broadband energy (**Figure 2.9**(b)) are relatively constant over the whole pulse duration. The average of this broadband energy is also consistent with our findings in **Figure 2.7**(c), specifically the magnitude of the first pulse for the 1000 cycle pulse.

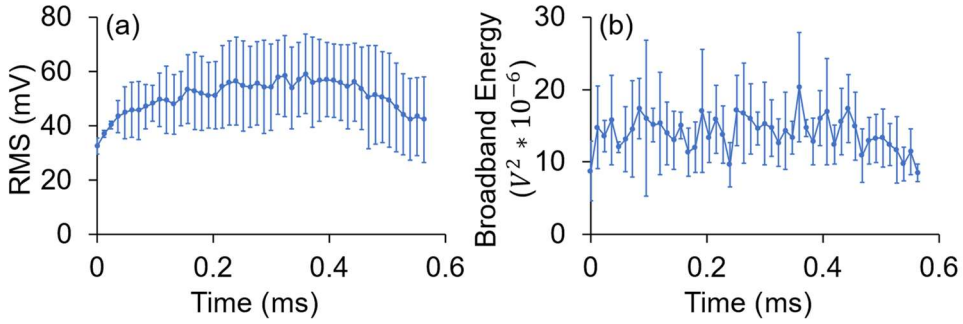

***Figure 2.9**: Temporal analysis of 1000 pulse: RMS and broadband energy*

Temporal analysis of the first 1000 cycle pulse at 2.2 MPa peak negative pressure. (a) Average (N = 3) RMS of scattered microbubble signal, and (b) the average broadband energy over the duration of the measured pulse. Error bars indicate 1 standard deviation, and baseline signal was subtracting before calculating average.

2.4 DISCUSSION

In this study we evaluated the effect of acoustic pressure, PRT, and pulse length on microbubble cavitation, each of which exhibited unique behavior at certain acoustic conditions.

We covered a more comprehensive range and number of parameters than previously studied. At the lowest PNP (0.8 MPa) there was no inertial cavitation dose measured (**Figure 2.8**(a)). At the PNP of 1.5 MPa is where we first measured a significant increase in ICD, which we can define as the detectable inertial cavitation threshold in our phantom model (with our pressure steps) and in agreement with other works performing threshold detection [50, 51]. While this PNP is greater than the inertial cavitation threshold of Sonazoid microbubbles simply diluted in water [42], it has previously been shown that entrapped microbubbles or those in the microcirculation require greater acoustic amplitudes before exhibiting the same cavitation activity measured by the elevation of broadband noise [44, 52]. The RMS value results (**Figure 2.6**(a)) also demonstrate this inertial cavitation threshold, indicating that RMS could be used as a simpler/qualitative metric for inertial cavitation (assuming a baseline value is known). ICD was found to be heavily dependent on PRT and increases exponentially with decreasing PRT. The 5 ms PRT produced 4-6X greater ICD than the 20 and 100 ms (**Figure 2.8**(b)). This is likely due to the diffusion time of microbubbles of this size, which has previously been shown to be 10-100 ms depending on size [53, 54]. By firing the ultrasound pulses faster than the diffusion time, gas from microbubbles is still present and can continue to cavitate, effectively prolonging the cavitation time of the ultrasound therapy. Interestingly, this diffusion time threshold is also evident in the RMS amplitude results (**Figure 2.6**(b)), where the 5 ms RMS is the only example of sustained amplitude. This microbubble behavior additionally may be a byproduct of the phantom environment, as Clark et al. [44] observed, in a similar phantom model, as gas from larger cavitating microbubbles (possibly due to coalescence) was unable to diffuse and generated hyperechoic regions in fundamental ultrasound images. While this behavior did not result in sustained broadband energy (**Figure 2.7**(b)) in our study, it could still be used as a simple detector of non-resonant microbubble behavior. Finally, when the pulse length was varied, we observed that the shortest pulse length of 20 cycles had the lowest ICD magnitude (**Figure 2.8**(c)), as expected. While still significantly greater than the zero level and generating broadband energy (**Figure 2.7**(c)), the short duration of this pulse is the major limiting factor in the delivered cavitation dose. As this pulse duration represents the condition available on all clinical scanners (as a pulsed wave Doppler mode), we have shown that while it is possible to produce inertial cavitation at this condition, the treatment effectiveness can be drastically increased by allowing for the conditions we have proposed and evaluated in this work.

The short duration of cavitation (1-3 pulses) due to rapid microbubble destruction and the broadband energy maximized during the first transmitted pulse suggests that cavitation treatments can be designed around firing a single pulse. From the results of ICD with variable pulse length (**Figure 2.8**(c)) we found that cavitation dose linearly increases with pulses length, and ICD could be further increased with a longer pulse. However, by increasing the pulse duration, we must then consider the thermal effects at the treatment location. The Pennes bioheat equation [46] was used to predict heat deposition in the gel phantom (accounting for water and gel phantom in beam path, **Figure 2.1**(a)) without microbubbles during a continuous treatment at 1.67 MHz, 10 MPa PPP, 2.2 MPa PNP. At the treatment location (64 mm), we calculated a temperature elevation of 0.023 ℃ per ms of exposure and an increase of 1 ℃ occurs after 43 ms, or ~71,000 cycles. For this specific probe and transmit conditions, a 43 ms pulse acts as the maximum setting for mechanical effects if the hardware allowed for such a pulse.

The choice of our in vitro model, a tissue-mimicking phantom with suspended microbubbles, may have impacted certain outcomes of our experiments but is still physiologically relevant. The suspended in gel microbubble model was selected to mimic the microvascular network (capillary bed) of a tumor during a bolus injection. At the capillary level, blood flow is extremely slow and can be modelled as stationary for the PRTs considered here. As microbubble cavitation therapy is highly dependent on microbubble concentration, and microbubbles are rapidly destroyed by these high-pressure pulses, the optimal time to begin ultrasound treatment would be during the peak intensity of a bolus injection where microbubble concentration is greatest [1, 45]. The entrapment of microbubbles allows our model to study this peak intensity event with long pulses at high amplitudes without acoustic streaming that would otherwise be present in a fluid solution and eliminates timing considerations between microbubble delivery and treatment start time. While our model lacks the ability for microbubbles to flow in and out of the target region, our results have also shown that the timescale of complete microbubble destruction (defined as the return of broadband energy to zero level, visualized in **Figure 2.1**(e)) is on the order of 100 ms for almost all acoustic conditions (**Figure 2.6**, **Figure 2.7**, **Figure 2.8**). These findings agree with a recent in vivo study of microbubble cavitation therapy in a murine model with similar treatment conditions to the ones we used here. Zhao et al. [3] found that most inertial cavitation energy subsided after the first 3 transmitted pulses, and when evaluating the duration of cavitation energy within a single 5 ms pulse (similar to our processing shown in **Figure 2.9**) inertial

cavitation subsided after the first 100 μs. Therefore, replenishment of the target area due to re-perfusion of microbubbles is only a diminished, secondary effect of ultrasound cavitation therapy, which is further exaggerated during bolus injections where reperfusion will always be with lower microbubble concentrations [45, 55].

Another consideration of our in vitro model is its fabrication reproducibility. A total of 36 phantoms were needed for the study (3 trials per acoustic condition, 11 conditions, and 3 controls) made as 3 different batches over 3 separate days, and while the phantom fabrication procedure was always the same, there seemed to be small differences in microbubble concentration on each day. This is evident in some small differences in terms of calculated ICD in **Figure 2.8** across the 3 plots. For example, the 2.2 MPa point in (a) should be the same as the 20 ms point in (b) and 200 cycles point in (c), but they are not. These small differences are attributed to microbubble concentration differences in the phantoms.

Another limitation of this study was the latent power threshold on the clinical scanner that dictated what combination of acoustic conditions was possible to transmit. In practice, we found that the upper limit of power delivery, PW, followed the relationship of $PW \propto V^2 * DC$, where V is the transmit voltage and DC is the duty cycle. Since duty cycle can be described as $N_{cyc}/(f_c * PRT)$ where N_{cyc} is the pulse duration in cycles, and f_c is the transmit frequency of the pulse, we can redefine the power relationship in the context of this work as $PW \propto V^2 * N_{cyc} * PRT^{-1}$ for a fixed transmit frequency. As demonstrated in this work, there is still a wide range of parameter combinations that can result in significant cavitation activity with a clinical system. However, certain maximum settings (selected from the results of **Figure 2.8**), such as PNP=2.5 MPa, 1000 cycle pulse duration, and 5 ms PRT are not possible with the current hardware on the system and were therefore not evaluated in this work. The upper (hardware) intensity limit of clinical scanners is even more limiting in other therapeutic applications of ultrasound such as thermal ablation [44, 56]. At the present time it is not possible to perform heat-based treatments with the clinical scanner we used in this study.

2.5 CONCLUSION

In this study we demonstrated that a clinical scanner, programmed to transmit long pulses (up to 1000 cycles), at high acoustic pressures (up to 2.5 MPa PNP) and variable pulse repetition

time (5-100 ms), can induce inertial cavitation in a tissue mimicking gel phantom with microbubbles while still maintaining imaging capabilities and providing image guidance. We were able to evaluate a comprehensive range of the important parameters (PNP, PRT and cycles) not previously covered to this extent by utilizing a novel perfusion phantom. Passive cavitation measurements were used to calculate the inertial cavitation dose (ICD) for all acoustic conditions and we determined an inertial cavitation threshold of 1.5 MPa in our tissue phantom. We found that ICD was maximized at 1000 cycles (maximum pulse length), 5 ms (fastest firing rate), and 2.5 MPa peak negative pressure (maximum pressure). The duration of inertial cavitation was usually 3-5 transmit pulses occurring within the first 100 ms of treatment. Temporal analysis of the first 1000 cycle pulse revealed that broadband energy is sustained for the entire pulse suggesting that the microbubbles inertially cavitated for the entire pulse duration. We also demonstrated that while inertial cavitation is possible with clinically available settings (~20 cycle pulse), ICD can be significantly increased when using much longer pulses and smaller PRTs that can still be programmed on a clinical scanner. We plan to use these acoustic conditions for image-guided cavitation treatments in vivo next.

2.6 REFERENCES

[1] S. B. Keller, D. Suo, Y.-N. Wang, H. Kenerson, R. S. Yeung, and M. A. Averkiou, "Image-Guided Treatment of Primary Liver Cancer in Mice Leads to Vascular Disruption and Increased Drug Penetration," *Frontiers in Pharmacology,* vol. 11, 2020. doi: 10.3389/fphar.2020.584344.

[2] S. B. Keller and M. A. Averkiou, "The role of ultrasound in modulating interstitial fluid pressure in solid tumors for improved drug delivery," *Bioconjugate Chemistry,* vol. 33, no. 6, pp. 1049-1056, 2021. doi: 10.1021/acs.bioconjchem.1c00422.

[3] X. Zhao, C. Pellow, and D. E. Goertz, "Intravital imaging and cavitation monitoring of antivascular ultrasound in tumor microvasculature," *Theranostics,* Research Paper vol. 13, no. 1, pp. 250-266, 2023. doi: 10.7150/thno.79186.

[4] S. L. Mulvagh *et al.*, "Contrast echocardiography: current and future applications," *Journal of the American Society of Echocardiography,* vol. 13, no. 4, pp. 331-342, 2000. doi: 10.1067/mje.2000.105462.

[5] Y. Kono *et al.*, "Gray-scale second harmonic imaging of the liver with galactose-based microbubbles," *Investigative radiology,* vol. 32, no. 2, pp. 120-125, 1997. doi:

[6] S. R. Wilson, P. N. Burns, D. Muradali, J. A. Wilson, and X. Lai, "Harmonic hepatic US with microbubble contrast agent: initial experience showing improved characterization of

hemangioma, hepatocellular carcinoma, and metastasis," *Radiology,* vol. 215, no. 1, pp. 153-161, 2000. doi: 10.1148/radiology.215.1.r00ap081.

[7] K. Darge *et al.*, "Safety of contrast-enhanced ultrasound in children for non-cardiac applications: a review by the Society for Pediatric Radiology (SPR) and the International Contrast Ultrasound Society (ICUS)," *Pediatric radiology,* vol. 43, pp. 1063-1073, 2013. doi: 10.1007/s00247-013-2746-6.

[8] D. L. Miller and R. M. Thomas, "Ultrasound contrast agents nucleate inertial cavitation in vitro," *Ultrasound in medicine & biology,* vol. 21, no. 8, pp. 1059-1065, 1995. doi: 10.1016/0301-5629(95)93252-U.

[9] J. Wang *et al.*, "Selective depletion of tumor neovasculature by microbubble destruction with appropriate ultrasound pressure," *International Journal of Cancer,* vol. 137, no. 10, pp. 2478-2491, 2015. doi: 10.1002/ijc.29597.

[10] T. Sun, G. Samiotaki, S. Wang, C. Acosta, C. C. Chen, and E. E. Konofagou, "Acoustic cavitation-based monitoring of the reversibility and permeability of ultrasound-induced blood-brain barrier opening," *Physics in Medicine & Biology,* vol. 60, no. 23, p. 9079, 2015. doi: 10.1088/0031-9155/60/23/9079.

[11] T. van Rooij *et al.*, "Viability of endothelial cells after ultrasound-mediated sonoporation: Influence of targeting, oscillation, and displacement of microbubbles," *Journal of Controlled Release,* vol. 238, pp. 197-211, 2016. doi: 10.1016/j.jconrel.2016.07.037.

[12] S. Keller, M. Bruce, and M. A. Averkiou, "Ultrasound imaging of microbubble activity during sonoporation pulse sequences," *Ultrasound in medicine & biology,* vol. 45, no. 3, pp. 833-845, 2019. doi: 10.1016/j.ultrasmedbio.2018.11.011.

[13] D. R. Mittelstein *et al.*, "Selective ablation of cancer cells with low intensity pulsed ultrasound," *Applied Physics Letters,* vol. 116, no. 1, 2020. doi: 10.1063/1.5128627.

[14] D. Fukumura and R. K. Jain, "Tumor microvasculature and microenvironment: Targets for anti-angiogenesis and normalization," *Microvascular Research,* vol. 74, no. 2, pp. 72-84, 2007. doi: 10.1016/j.mvr.2007.05.003.

[15] S. B. Keller, Y.-N. Wang, S. Totten, R. S. Yeung, and M. A. Averkiou, "Safety of Image-Guided Treatment of the Liver with Ultrasound and Microbubbles in an in Vivo Porcine Model," *Ultrasound in Medicine & Biology,* vol. 47, no. 11, pp. 3211-3220, 2021. doi: 10.1016/j.ultrasmedbio.2021.07.003.

[16] A. K. W. Wood, S. Ansaloni, L. S. Ziemer, W. M. F. Lee, M. D. Feldman, and C. M. Sehgal, "The antivascular action of physiotherapy ultrasound on murine tumors," *Ultrasound in Medicine & Biology,* vol. 31, no. 10, pp. 1403-1410, 2005. doi: 10.1016/j.ultrasmedbio.2005.06.008.

[17] J. H. Hwang, A. A. Brayman, M. A. Reidy, T. J. Matula, M. B. Kimmey, and L. A. Crum, "Vascular effects induced by combined 1-MHz ultrasound and microbubble contrast agent treatments in vivo," *Ultrasound in Medicine & Biology,* vol. 31, no. 4, pp. 553-564, 2005. doi: 10.1016/j.ultrasmedbio.2004.12.014.

[18] J. H. Hwang, J. Tu, A. A. Brayman, T. J. Matula, and L. A. Crum, "Correlation between inertial cavitation dose and endothelial cell damage in vivo," *Ultrasound in Medicine & Biology,* vol. 32, no. 10, pp. 1611-1619, 2006/10/01/ 2006. doi: 10.1016/j.ultrasmedbio.2006.07.016.

[19] A. K. W. Wood *et al.*, "The Disruption of Murine Tumor Neovasculature by Low-intensity Ultrasound—Comparison Between 1- and 3-MHz Sonication Frequencies," *Academic Radiology,* vol. 15, no. 9, pp. 1133-1141, 2008. doi: 10.1016/j.acra.2008.04.012.

[20] C. Chien Ting, B. I. Raju, T. Shevchenko, and A. L. Klibanov, "Control and reversal of tumor growth by ultrasound activated microbubbles," in *2009 IEEE International Ultrasonics Symposium*, 2009, pp. 77-80. 10.1109/ULTSYM.2009.5441604.

[21] A. K. W. Wood, S. M. Schultz, W. M. F. Lee, R. M. Bunte, and C. M. Sehgal, "Antivascular Ultrasound Therapy Extends Survival of Mice With Implanted Melanomas," *Ultrasound in Medicine & Biology,* vol. 36, no. 5, pp. 853-857, 2010. doi: 10.1016/j.ultrasmedbio.2010.02.001.

[22] C. W. Burke, A. L. Klibanov, J. P. Sheehan, and R. J. Price, "Inhibition of glioma growth by microbubble activation in a subcutaneous model using low duty cycle ultrasound without significant heating: Laboratory investigation," *Journal of Neurosurgery JNS,* vol. 114, no. 6, pp. 1654-1661, 2011. doi: 10.3171/2010.11.JNS101201.

[23] H.-L. Liu, H.-Y. Hsieh, L.-A. Lu, C.-W. Kang, M.-F. Wu, and C.-Y. Lin, "Low-pressure pulsed focused ultrasound with microbubbles promotes an anticancer immunological response," *Journal of Translational Medicine,* vol. 10, no. 1, p. 221, 2012. doi: 10.1186/1479-5876-10-221.

[24] X. Hu *et al.*, "Insonation of targeted microbubbles produces regions of reduced blood flow within tumor vasculature," *Invest Radiol.,* vol. 47, no. 7, pp. 398-405, 2012. doi: 10.1097/RLI.0b013e31824bd237.

[25] P. Huang *et al.*, "Enhanced antitumor efficacy of ultrasonic cavitation with up-sized microbubbles in pancreatic cancer," *Oncotarget,* vol. 6, no. 24, pp. 20241-20251, 2015. doi: 10.18632/oncotarget.4048.

[26] Y. Yang, W. Bai, Y. Chen, Y. Lin, and B. Hu, "Optimization of low-frequency low-intensity ultrasound-mediated microvessel disruption on prostate cancer xenografts in nude mice using an orthogonal experimental design," *Oncol Lett,* vol. 10, no. 5, pp. 2999-3007, 2015. doi: 10.3892/ol.2015.3716.

[27] S. J. Hunt, T. Gade, M. C. Soulen, S. Pickup, and C. M. Sehgal, "Antivascular Ultrasound Therapy," *Journal of Ultrasound in Medicine,* vol. 34, no. 2, pp. 275-287, 2015. doi: 10.7863/ultra.34.2.275.

[28] C. P. Keravnou, I. De Cock, I. Lentacker, M.-L. Izamis, and M. A. Averkiou, "Microvascular Injury and Perfusion Changes Induced by Ultrasound and Microbubbles in a Machine-Perfused Pig Liver," *Ultrasound in Medicine & Biology,* vol. 42, no. 11, pp. 2676-2686, 2016. doi: 10.1016/j.ultrasmedbio.2016.06.025.

[29] Y.-J. Ho, T.-C. Wang, C.-H. Fan, and C.-K. Yeh, "Spatially Uniform Tumor Treatment and Drug Penetration by Regulating Ultrasound with Microbubbles," *ACS Applied Materials & Interfaces,* vol. 10, no. 21, pp. 17784-17791, 2018/05/30 2018. doi: 10.1021/acsami.8b05508.

[30] Y. Sun, J. Luo, J. Chen, F. Xu, X. Ding, and P. Huang, "Ultrasound-mediated microbubbles destruction for treatment of rabbit VX2 orthotopic hepatic tumors," *Applied Acoustics,* vol. 138, pp. 216-225, 2018. doi: 10.1016/j.apacoust.2018.04.007.

[31] Y. Jing *et al.*, "Ultrasound-targeted microbubble destruction improved the antiangiogenic effect of Endostar in triple-negative breast carcinoma xenografts," *Journal of Cancer Research and Clinical Oncology,* vol. 145, no. 5, pp. 1191-1200, 2019. doi: 10.1007/s00432-019-02866-7.

[32] P. T. Yemane *et al.*, "Effect of Ultrasound on the Vasculature and Extravasation of Nanoscale Particles Imaged in Real Time," *Ultrasound in Medicine & Biology,* vol. 45, no. 11, pp. 3028-3041, 2019. doi: 10.1016/j.ultrasmedbio.2019.07.683.

[33] J. C. D'Souza *et al.*, "Microbubble-enhanced ultrasound for the antivascular treatment and monitoring of hepatocellular carcinoma," *Nanotheranostics,* vol. 3, no. 4, pp. 331-341, 2019. doi: 10.7150/ntno.39514.

[34] Y. He *et al.*, "Improving the Therapeutic Effect of Ultrasound Combined With Microbubbles on Muscular Tumor Xenografts With Appropriate Acoustic Pressure," *Frontiers in Pharmacology,* Original Research vol. 11, 2020. doi: 10.3389/fphar.2020.01057.

[35] X. Zhao, A. Wright, and D. E. Goertz, "An optical and acoustic investigation of microbubble cavitation in small channels under therapeutic ultrasound conditions," *Ultrasonics Sonochemistry,* vol. 93, p. 106291, 2023. doi: 10.1016/j.ultsonch.2023.106291.

[36] G. Dimcevski *et al.*, "A human clinical trial using ultrasound and microbubbles to enhance gemcitabine treatment of inoperable pancreatic cancer," *Journal of Controlled Release,* vol. 243, pp. 172-181, 2016. doi: 10.1016/j.jconrel.2016.10.007.

[37] O. N. R. Mason *et al.*, "Augmentation of Tissue Perfusion in Patients With Peripheral Artery Disease Using Microbubble Cavitation," *JACC: Cardiovascular Imaging,* vol. 13, no. 3, pp. 641-651, 2020. doi: 10.1016/j.jcmg.2019.06.012.

[38] T. Di Ianni *et al.*, "Ultrasound/microbubble-mediated targeted delivery of anticancer microRNA-loaded nanoparticles to deep tissues in pigs," *Journal of Controlled Release,* vol. 309, pp. 1-10, 2019/09/10/ 2019. doi: 10.1016/j.jconrel.2019.07.024.

[39] D. E. Goertz *et al.*, "Antitumor Effects of Combining Docetaxel (Taxotere) with the Antivascular Action of Ultrasound Stimulated Microbubbles," *PLOS ONE,* vol. 7, no. 12, p. e52307, 2012. doi: 10.1371/journal.pone.0052307.

[40] Z. Liu *et al.*, "Disruption of Tumor Neovasculature by Microbubble Enhanced Ultrasound: A Potential New Physical Therapy of Anti-Angiogenesis," *Ultrasound in Medicine & Biology,* vol. 38, no. 2, pp. 253-261, 2012/02/01/ 2012. doi: 10.1016/j.ultrasmedbio.2011.11.007.

[41] A. I. Farrer *et al.*, "Characterization and evaluation of tissue-mimicking gelatin phantoms for use with MRgFUS," *Journal of Therapeutic Ultrasound,* vol. 3, no. 1, p. 9, 2015. doi: 10.1186/s40349-015-0030-y.

[42] S. B. Keller, P. S. Sheeran, and M. A. Averkiou, "Cavitation therapy monitoring of commercial microbubbles with a clinical scanner," *IEEE Transactions on Ultrasonics,*

Ferroelectrics, and Frequency Control, vol. 68, no. 4, pp. 1144-1154, 2020. doi: 10.1109/TUFFC.2020.3034532.

[43] P. Li *et al.*, "Pharmacokinetics of Perfluorobutane after Intra-Venous Bolus Injection of Sonazoid in Healthy Chinese Volunteers," *Ultrasound in Medicine & Biology,* vol. 43, no. 5, pp. 1031-1039, 2017/05/01/ 2017. doi: 10.1016/j.ultrasmedbio.2017.01.003.

[44] A. Clark, S. Bonilla, D. Suo, Y. Shapira, and M. Averkiou, "Microbubble-enhanced heating: exploring the effect of microbubble concentration and pressure amplitude on high-intensity focused ultrasound treatments," *Ultrasound in medicine & biology,* vol. 47, no. 8, pp. 2296-2309, 2021. doi: 10.1016/j.ultrasmedbio.2021.03.035.

[45] M. A. Averkiou, M. F. Bruce, J. E. Powers, P. S. Sheeran, and P. N. Burns, "Imaging methods for ultrasound contrast agents," *Ultrasound in medicine & biology,* vol. 46, no. 3, pp. 498-517, 2020. doi: 10.1016/j.ultrasmedbio.2019.11.004.

[46] H. H. Pennes, "Analysis of tissue and arterial blood temperatures in the resting human forearm," *Journal of applied physiology,* vol. 1, no. 2, pp. 93-122, 1948. doi: 10.1152/jappl.1948.1.2.93.

[47] D. Suarez Escudero, K. J. Haworth, C. Genstler, and C. K. Holland, "Quantifying the Effect of Acoustic Parameters on Temporal and Spatial Cavitation Activity: Gauging Cavitation Dose," *Ultrasound in Medicine & Biology,* vol. 49, no. 11, pp. 2388-2397, 2023/11/01/ 2023. doi: 10.1016/j.ultrasmedbio.2023.08.002.

[48] M. Lafond *et al.*, "Cavitation Emissions Nucleated by Definity Infused through an EkoSonic Catheter in a Flow Phantom," *Ultrasound in Medicine & Biology,* vol. 47, no. 3, pp. 693-709, 2021/03/01/ 2021. doi: 10.1016/j.ultrasmedbio.2020.10.010.

[49] United States Food and Drug Administration. (2023). *Marketing Clearance of Diagnostic*

Ultrasound Systems and

Transducers: Guidance for Industry and Food and

Drug Administration Staff.

[50] W.-S. Chen, T. J. Matula, A. A. Brayman, and L. A. Crum, "A comparison of the fragmentation thresholds and inertial cavitation doses of different ultrasound contrast agents," *The Journal of the Acoustical Society of America,* vol. 113, no. 1, pp. 643-651, 2003. doi:

[51] X. Guo, Q. Li, Z. Zhang, D. Zhang, and J. Tu, "Investigation on the inertial cavitation threshold and shell properties of commercialized ultrasound contrast agent microbubbles," *The Journal of the Acoustical Society of America,* vol. 134, no. 2, pp. 1622-1631, 2013. doi: 10.1121/1.4812887.

[52] X. Yang and C. C. Church, "A model for the dynamics of gas bubbles in soft tissue," *The Journal of the Acoustical Society of America,* vol. 118, no. 6, pp. 3595-3606, 2005. doi: 10.1121/1.2118307.

[53] W.-S. Chen, T. J. Matula, and L. A. Crum, "The disappearance of ultrasound contrast bubbles: observations of bubble dissolution and cavitation nucleation," *Ultrasound in Medicine & Biology,* vol. 28, no. 6, pp. 793-803, 2002. doi: 10.1016/S0301-5629(02)00517-3.

[54] E. C. James, A. D. Paul, J. M. Donovan, and W. F. Katherine, "Threshold of fragmentation for ultrasonic contrast agents," *Journal of Biomedical Optics,* vol. 6, no. 2, pp. 141-150, 2001. doi: 10.1117/1.1352752.

[55] C. Strouthos, M. Lampaskis, V. Sboros, A. Mcneilly, and M. Averkiou, "Indicator dilution models for the quantification of microvascular blood flow with bolus administration of ultrasound contrast agents," *IEEE Transactions on Ultrasonics, Ferroelectrics, and Frequency Control,* vol. 57, no. 6, pp. 1296-1310, 2010. doi: 10.1109/TUFFC.2010.1550.

[56] E. K. Juang, L. H. De Koninck, K. S. Vuong, A. Gnanaskandan, C.-T. Hsiao, and M. A. Averkiou, "Controlled hyperthermia with high-intensity focused ultrasound and ultrasound contrast agent microbubbles in porcine liver," *Ultrasound in Medicine & Biology,* vol. 49, no. 8, pp. 1852-1860, 2023. doi: 10.1016/j.ultrasmedbio.2023.04.015.

CHAPTER 3. MICROBUBBLE INDUCED CAVITATION: IMPACT ON TUMOR INTERSTITIAL FLUID PRESSURE AND TRANSIENT PERFUSION LOSS[2]

Abstract

Most solid tumors exhibit abnormal vasculature that limits the effectiveness of anticancer drugs. Ultrasound-mediated microbubble cavitation is an emerging therapeutic technique that can induce localized vascular changes in the solid tumors and enhance drug delivery. However, the relationship between microbubble cavitation activity and changes to tumor blood flow are not well understood. In this work we utilized simultaneous passive cavitation detection (PCD) and contrast-enhanced ultrasound imaging (CEUS) in tumor-bearing mice during cavitation therapy to provide comprehensive information of both cavitation activity and its impact on tumor blood flow. The outcomes of cavitation therapy were investigated in 2 studies: 1) treatment delivered by a modified clinical scanner (long pulses, high pressures) to demonstrate clinical translation of cavitation therapy, and 2) treatment delivered by a single element transducer for better control of cavitation activity during treatments. CEUS images were acquired before, during, and after each treatment and quantified to measure vascular changes. PCD confirmed accurate targeting by monitoring microbubble activity during treatment and classified the type of cavitation activity. Pressure catheter measurements confirmed a significant reduction in IFP resulting from cavitation treatments. All ultrasound conditions induced transient tumor perfusion loss (TTPL) without significant tissue damage or hemorrhage. The high-pressure treatments (> 2 MPa) caused more TTPL in terms of its spatial extent and duration. PCD measurements showed that cavitation activity rapidly diminished during the first few (1-20) treatment pulses. These results demonstrate the complimentary information PCD and CEUS can provide for detecting TTPL and the feasibility of tumor cavitation treatment with a clinical scanner.

[2] *Sections using cavitation treatment with a clinical scanner have appeared as part of: Krolak C., **De Koninck LH.**, Gu S., Wang YN., Powers JE., Averkiou M. "Ultrasound cavitation therapy: inducing tumor drug delivery and blood flow changes with clinical ultrasound tools" J. Control. Release (in review).*

3.1 INTRODUCTION

Cancer is a global healthcare burden, accounting for millions of deaths each year, with 85% of cases classified as solid tumors [1]. Of particular interest is hepatocellular carcinoma (HCC) a form of liver cancer that is increasing in prevalence around the world, attributed as the fourth leading cause of cancer-related deaths [2]. Treatment of these tumors is often difficult, as surgical resection is often not available for patients with advanced disease, with systemic treatments such as chemotherapy being the only viable option [3]. Unfortunately, hypervascular solid tumors like HCC also exhibit abnormal vasculature and elevated interstitial fluid pressure (IFP) that limits the effectiveness of the majority of anticancer drugs [4, 5]. Therefore, there is a great need for techniques to eliminate these barriers within solid tumors and enhance existing therapeutics.

Ultrasound- and microbubble-mediated cavitation is an emerging therapeutic technique where acoustic pulses produce microbubble oscillations to noninvasively induce targeted biological effects [6-8]. Microbubbles are also used as a contrast agent in contrast-enhanced ultrasound (CEUS) and are clinically approved for cardiac [9] and hepatic [10-12] applications. Under certain acoustic exposures different from those used in imaging, microbubbles may induce localized cellular, vascular and tissue changes and thus act as a therapeutic agent [13]. Since microbubbles are a blood pool agent and are supplied with an intravenous injection, cavitation therapy enables targeted treatment of any vascularized structures, such as organs and tumors, and has been studied in various animal cancer models [6, 8, 14]. For well-perfused solid tumors, such as HCC, cavitation therapy can induce a tumor transient perfusion loss (TTPL) [6, 8]. It is hypothesized that the immature neovessels which are prevalent in tumors [15] are more susceptible to mechanical forces and thus damage from cavitation. This tumoral neovessel susceptibility enables preferential targeting of tumor vasculature while avoiding damage to the surrounding tissue [14, 16]. However, the heterogeneity of vascular patterns in HCCs [17] can limit the delivery of microbubbles within the tumor and impact the effectiveness of cavitation treatments. As a result, techniques such as CEUS that provide spatial information of microbubble delivery to tumors are necessary for accurate targeting of cavitation therapy and monitoring TTPL. Additionally, therapeutic outcomes of cavitation therapy such as reduced blood flow, blood brain barrier opening [18], sonoporation [19, 20], and ablation via histotripsy [21], are all highly dependent on acoustic parameters and the type of generated cavitation (stable versus inertial) [22, 23]. While certain transmit parameters, such as acoustic pressure and pulse duration, are known to heavily influence

cavitation activity, no robust treatment protocol yet exists for in-vivo cavitation therapy. Monitoring microbubble behavior during treatment would reveal the relative magnitude and duration of cavitation activity and could be used to optimize treatment protocols for maximizing cavitation activity.

Passive cavitation detection (PCD) is a useful tool during cavitation therapy to characterize cavitation activity. Typically, a focused transducer (single element or array), is set to passively receive scattered signals from microbubbles insonified with a separate transducer [22, 24]. These signals are then recorded, their frequency spectrum analyzed and evaluated for the presence of sub- and ultraharmonics and/or elevation of broadband energy. Of relevance to this study is the elevation of broadband energy, indicating the occurrence of inertial cavitation [22] where microbubbles rapidly expand and collapse, driven by the inertia of the surrounding medium and generating powerful localized effects such as shock waves [25], fluid jetting [26], and cellular damage [27]. For most targeted cavitation therapies, simple PCD setups are sufficient for quantifying cavitation activity with excellent temporal resolution. PCD measurements are generally reported as the amplitude (or energy) of relevant frequency content per transmitted pulse, describing the detected average cavitation activity during treatment [8, 24, 28-31]. Since differences in transmit parameters (acoustic pressure, pulse length, pulse repetition time-PRT) can impact cavitation activity [32], PCD measurements may also be used to calculate a cavitation dose to describe the average cavitation activity of the entire treatment [24, 29-31]. Cavitation dose has been correlated with erythrocyte hemolysis [24, 30] and endothelial cell damage [31] and may be used as an indicator of vessel disruption in tumors treated with cavitation therapy [28]. While PCD measurements can offer valuable insights into cavitation activity, this information can only be collected during treatments, requiring additional monitoring techniques such as CEUS to fully describe changes to the tumor microenvironment. Consequently, the combination of CEUS and PCD monitoring during cavitation therapy offers the most complete measurement of changes to tumor blood flow.

In this work we performed simultaneous PCD and CEUS measurements of tumor-bearing mice during cavitation therapy to provide comprehensive information of both cavitation activity and changes to tumor blood flow, specifically TTPL. The outcomes of cavitation therapy were investigated in 2 studies: 1.) microbubble cavitation treatment delivered by a modified clinical scanner (transmit long pulses, high pressures) to enable in the future clinical translation of

cavitation therapy, and 2.) treatment delivered by a single element transducer for a short duration (1 s) to provide more control of the parameters and improve understanding of cavitation activity during treatments. A PCD system was used to measure the scattered signal from cavitation treatments and confirm accurate targeting. Broadband energy of each signal was calculated to describe cavitation activity within each scattered pulse. The ICD was calculated over the treatment duration to compare cavitation activity during different acoustic conditions. CEUS was used to guide the procedures and evaluate outcomes such as TTPL. Finally, pressure catheter measurements were used to evaluate changes in tumor IFP resulting from cavitation treatments, aiming to further understand cavitation induced changes of the tumor microenvironment.

3.2 MATERIAL AND METHODS

3.2.1 Tumor cell line and mouse model preparation

All animal protocols performed were approved by the Institutional Animal Care and Use Committee (IACUC) at the University of Washington, Seattle. This study used a human hepatocellular carcinoma line (HCC), specially HEPG2 (American Type Culture Collection, HB-8065), as a means of relating this work to previous and projected studies evaluating HCCs. Cells were cultured at 37°C at 5% CO2, in Eagle's Minimum Essential Medium supplemented with 10% fetal bovine serum and 1% antibiotic/antimycotic.

In eight- to twelve-week-old athymic nude mice (Charles River Laboratories, Wilmington, MA), $2 * 10^6$ HEPG2 cells suspended in 50 μL of phosphate buffered saline mixed with 50 μL of Matrigel was implanted in the hind flank with a 23G needle. Tumors were measured twice a week with a GE LogicBook XP (General Electric HealthCare, Chicago, IL, USA), and animals were recruited to the study once the maximum tumor diameter was between 8-10 mm, or an approximate tumor volume of 80 mm^3 from an ellipsoidal estimation.

3.2.2 Microbubble contrast agent

SonoVue® microbubbles (Bracco Suisse SA, Geneva, Switzerland) were utilized in this study due to its clinical approval for the characterization of focal liver lesions in the United States and in several countries across Europe and Asia. Microbubble dosing of 50 μL per injection was determined based upon previous work [6, 20] to provide adequate signal without inducing acoustic shadowing, and this dosing scheme was employed for all microbubble injections. We note that this

microbubble dose (approximately 2 mL/kg) is considerably greater than the clinical dose of SonoVue in humans (approximately 0.03 mL/kg) [33] but still similar to what has been done in previous similar studies. Bolus injections were selected over infusion to eliminate the added complexity of infusions, navigate the small volumes allowed in small animals, and provide the most concentrated bubble delivery.

3.2.3 Ultrasound parameters

3.2.3.1 Modified clinical scanner

Acoustic conditions suitable for cavitation treatments were implemented on a Philips EPIQ scanner and S5-1 phased array (Philips Healthcare, Bothell, WA, USA). The treatment conditions in this work are a modified version of the scanner settings previously described [34]. Briefly, we modified the standard B-mode setting where instead of forming a sector scan with multiple lines, the center line is repeatedly transmitted at a specified PRT. Pulses were programmed with a frequency of 1.67 MHz (the lowest frequency that the S5-1 could efficiently transmit), duration of 1000 cycles, and PRT of 5-100 ms. Peak negative pressures in the range of 0.3-2.5 MPa could be selected with the output knob. Two cavitation treatments were explored in this study: “moderate” (1.6 MPa, 5 ms PRT) and “high” (2.2 MPa, 100 ms PRT) to be consistent with prior work investigating ultrasound and microbubble cavitation treatments in vivo [28, 35-41]. We assumed that frequent firing (lower PRT) is more beneficial in cavitation treatments. We also wanted to evaluate 2 acoustic pressures. Thus, we chose the lowest possible PRT for those two pressures that were possible to implement on the specific scanner and while considering its hardware limitations. A deep azimuthal focus (z = 13 cm) was selected to create a large focal region 65 mm from the probe, such that a majority of the tumor received the same acoustic pressure. High acoustic pressures, greatest number of cycles, and shortest pulse repetition times were employed in this study to maximize inertial cavitation dose based on its relationship with drug extravasation distance [28] and to explore cavitation-induced mechanical changes such as reduction of tumor IFP, which have primarily been observed at acoustic pressures at or above 1 MPa [42, 43]. Bioheat simulations (without microbubbles) estimated only a 0.35°C and 0.07°C temperature rise in the moderate and high cavitation treatment conditions, respectively, suggesting the absence of any thermal effects of these treatments.

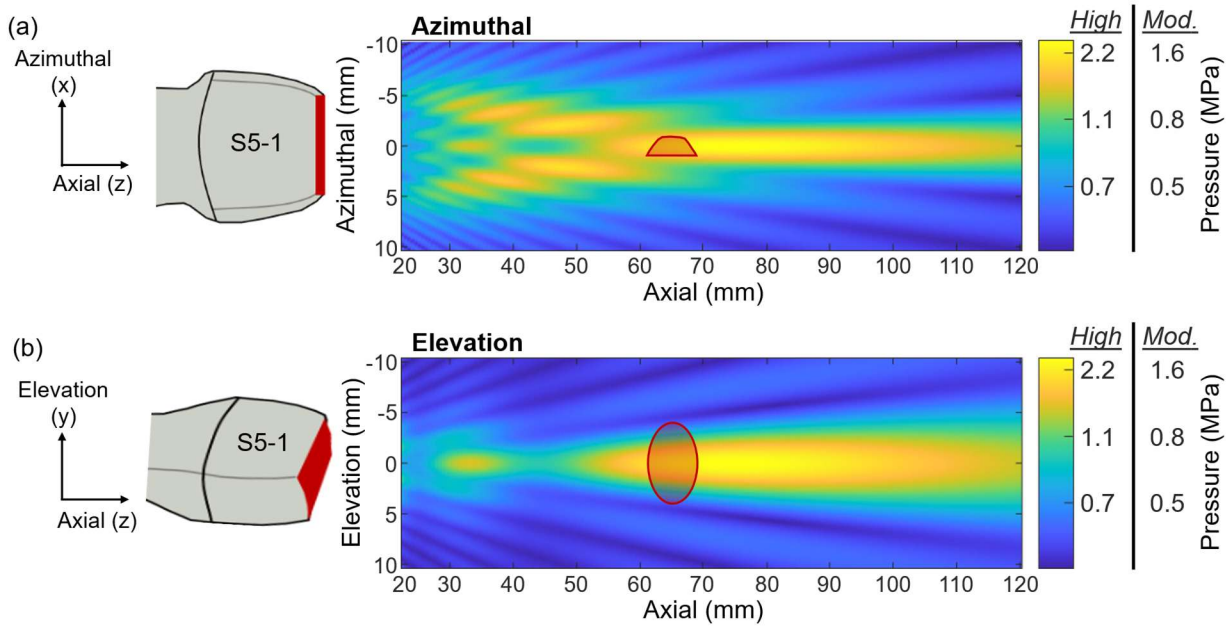

***Figure 3.1**: Simulations for treatment beamforming from the S5-1 phased array.*

(a) The 2-D azimuthal beam field with a representative 8 mm diameter tumor at 65 mm from the probe. Theoretical peak negative pressures for the high and moderate cavitation treatment condition are listed. (b) The 2-D elevation beam field with a representative 8 mm diameter tumor at 65 mm from the probe. Theoretical peak negative pressures for the high and moderate cavitation treatment condition are listed.

Simulated acoustic fields for the azimuthal and elevation planes of the S5-1 with a representative tumor are shown in **Figure 3.1**. The field simulations are based on the angular spectrum method of the Fresnel diffraction approximation with 2D Fast Fourier Transforms.

3.2.3.2 Single element transducer

A focused, single element transducer (1.19 MHz, 4.7 cm dia., 5.1 cm focal length) driven by an RF amplifier (2200L, Electronics and Innovation, Rochester, NY, USA) was selected to generate all required conditions in the second in-depth study of TTPL. Transmit pulses were programmed on an arbitrary function generator (AFG3102C, Tektronix, Beaverton, OR, USA) with 1000 cycles at 1.19 MHz and a pulse repetition time (PRT) of 10 ms. Three acoustic pressures, 1.2, 2.5, and 4.0 MPa (peak negative), were explored in this study, consistent with prior work investigating ultrasound and microbubble cavitation treatments in vivo [28, 35-41]. The simulated acoustic field of the axial plane of the focused transducer with a representative tumor (red circle, 8 mm diameter) is shown in **Figure 3.2**. The field simulation is a numerical solution of the Rayleigh integral for a circular piston transmitting through water (linear field). The maximum

pressure is generated at 50 mm axially from the transducer; however, we selected an axial distance of 55 mm as the treatment location to increase the 6-dB spot size (length = 13 mm, width = 2 mm) with minimal loss in delivered peak acoustic pressure. The white, dashed oval represents the cross-section of the detection area of the PCD transducer, defined as the 6-dB spot size of the transducer (length = 20 mm, width = 1 mm, volume = 80 mm^3). The PCD detection area is also centered at 55 mm and angled at 45° relative to the orientation of focused transducer, consistent with the experimental setup in **Figure 3.3**. Due to the small overlap between the 6-dB spot sizes of the focused transducer and the PCD transducer, microbubble cavitation activity reported in this work is specific to the tumor.

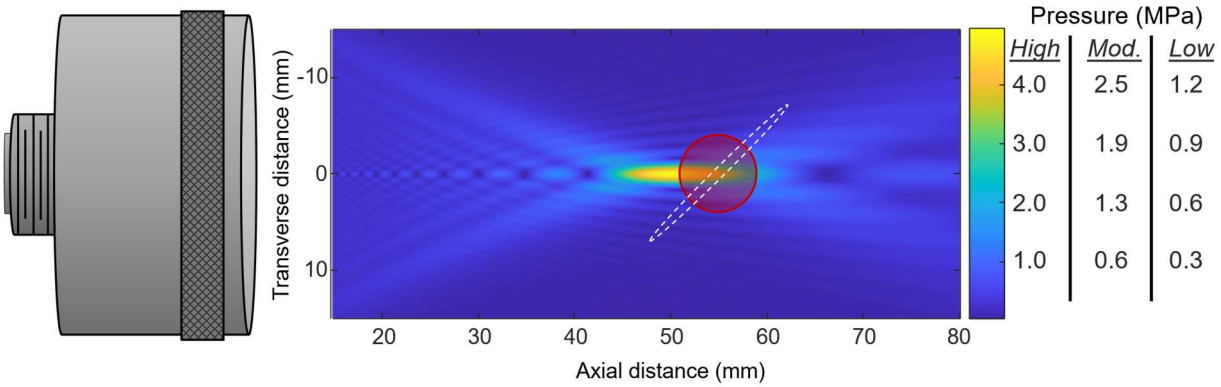

***Figure 3.2**: Simulation of the focused transducer acoustic pressure field in the axial plane.*

Theoretical peak negative pressures for the high (4.0 MPa), moderate (2.5 MPa), and low (1.2 MPa) cavitation treatment conditions are listed. The red circle represents an 8 mm diameter tumor centered 55 mm axially from the transducer. The white dashed oval represents the cross-section of the passive cavitation detection 6 dB spot size (length = 20 mm, width = 1 mm), centered 55 mm axially from focused transducer and at a 45° angle consistent with the transducer configuration in the experimental setup.

3.2.4 Experimental setup and alignment

To simultaneously treat and monitor mice, a heated (37℃), degassed water tank setup was developed where transducers and animals could be submerged and co-aligned. A schematic of the setup is depicted in **Figure 3.3**. Cavitation treatments were delivered with either a focused, single element transducer or a Philips ultrasound probe (EPIQ, S5-1). A 5 MHz single element transducer (C308, 5 MHz, 1.9 cm diameter, 5.1 cm focal length; Evident Scientific, Waltham, MA) was used to perform passive cavitation detection (PCD) and evaluate cavitation in vivo. A clinical imaging probe (L12-5) connected to a clinical scanner (iU22, Philips Healthcare, Bothell, WA) was also

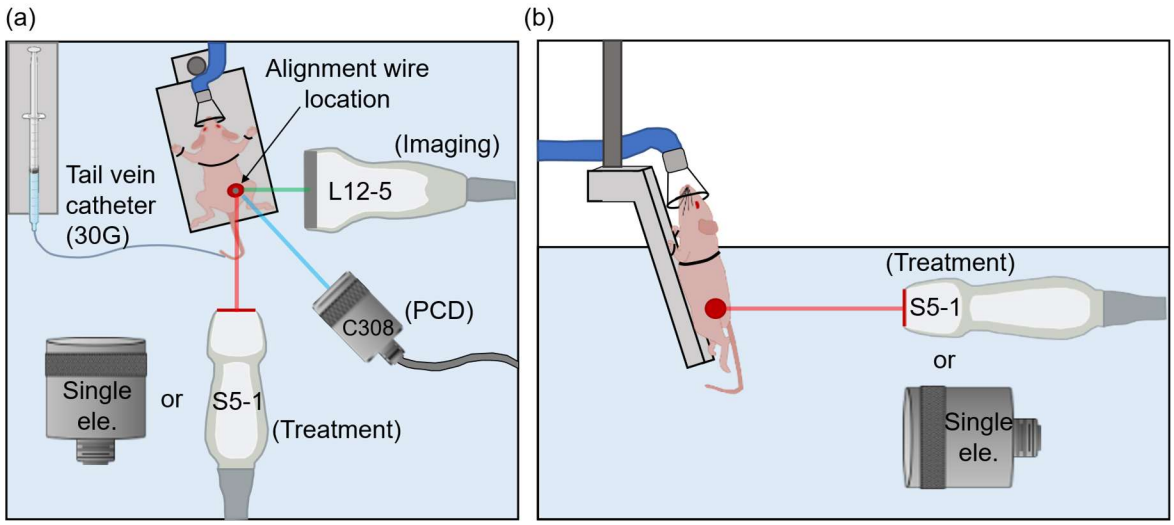

***Figure 3.3**: Schematic of heated water tank experimental setup.*

(a) A top-down view, illustrating the co-alignment of the treatment, imaging, and passive cavitation detecting probes. The red dot represents the subcutaneous tumor on the mouse. A black dot within the tumor indicates the location of the wire used to align the probes before the mouse was place with the center of the tumor in the same location. (b) A side view of the setup, illustrating the partial submersion of the mouse, and the alignment of the treatment device to the exact depth of the tumor.

used for small animal imaging. To align to the tumor, the imaging probe, PCD, and treatment transducers (S5-1 or single element) were co-aligned to the same 3-D position using a thin vertical wire target. First, the PCD transducer was aligned 5.1 cm (geometric focus) from the wire using a pulse-echo technique. The PCD transducer was then used as a receiver to align the treatment transducer, either 6.5 cm (S5-1) or 5.5 cm (single element) from the wire, and L12-5 probe 2 cm from the wire, respectively, and to the same vertical position as the PCD transducer. The position of the wire on the L12-5 image was recorded, after which the wire target was removed from the water tank. Mice were then anesthetized under 1.5-2% isoflurane and prepared with a 30G needle tail vein catheter. The mice were secured to a custom restraining board before being partially submerged in the water tank and positioned such that the center of the tumor coincided with the wire position on the L12-5 image.

3.2.5 Treatment protocol delivered with clinical scanner for the IFP and general TTPL study

For treatments with the S5-1, three groups of 8 mice (4 male, 4 female, total n = 24) were randomly divided into one of the following conditions: control, moderate cavitation, and high

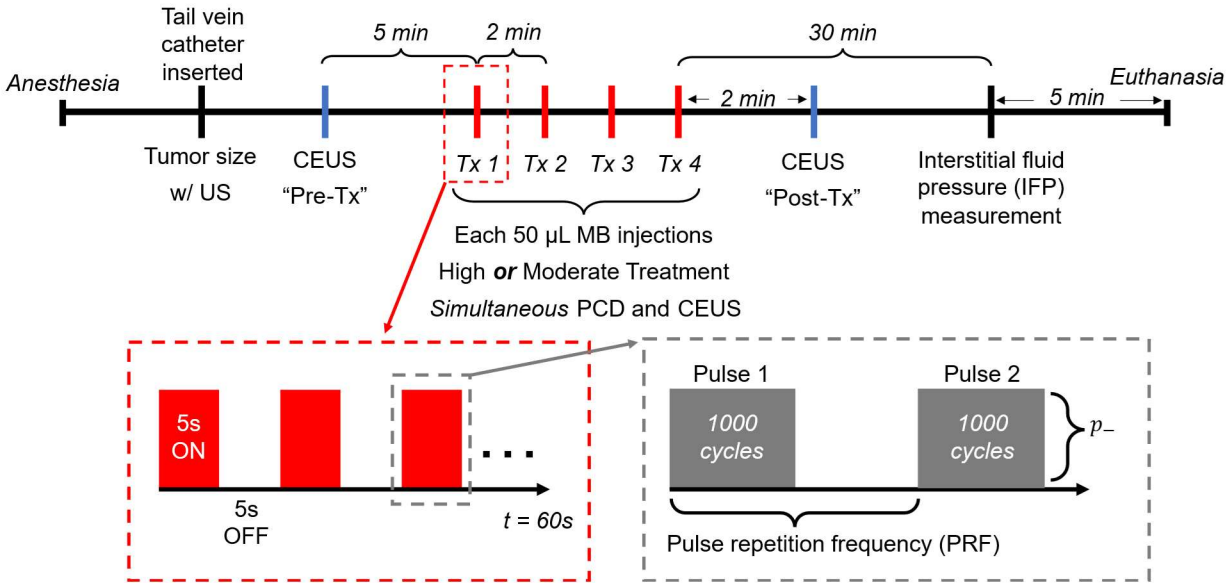

***Figure 3.4**: Experimental protocol for treatments with clinical scanner.*

MB = microbubble, US = ultrasound, CEUS = contrast-enhanced ultrasound, Tx = treatment, PCD = passive cavitation detection.

cavitation. An overview of the experimental timeline is shown in **Figure 3.4**. A 50 µL bolus of microbubbles was delivered before cavitation treatments while the tumor was continuously scanned with CEUS (amplitude modulation, 4.1 MHz, mechanical index = 0.06) to establish baseline tumor vascularity, titled "pre-Tx". A time-intensity curve, illustrated in **Figure 3.5**, was formed from a freeform polygon region of interest of the tumor to determine when peak microbubble concentration within it had occurred. Treatments were performed for a total of 30 seconds at the determined peak of the bolus, in alternating 5 second "on" and "off" periods, and repeated for a total of 4 treatments in each tumor. The rationale for the 5 second "on" duration is to ensure all microbubbles within the tumor are insonified long enough and destroyed. Complete microbubble destruction potentially occurs within 100 milliseconds but we selected 5 seconds to be overly conservative. The rationale for the 5 second "off" period is to allow time for surrounding circulating microbubbles to re-perfuse the tumor and be insonified based on our prior knowledge of the rise time of TICs from murine tumors being approximately 5 seconds. A 50 µL bolus of microbubbles was also delivered after the cavitation treatments while CEUS was performed to evaluate the immediate tumor blood flow changes resulting from the treatment, titled "post-treatment". For a subset of mice (4 moderate, 4 high, total n = 8), PCD measurements were recorded using an oscilloscope (DPO 7054C Tektronix, Beaverton, OR, USA) with a segmented

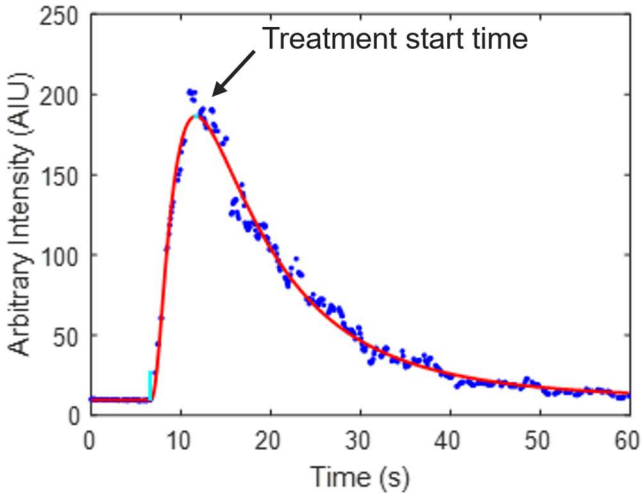

Figure 3.5*: Example time-intensity curve of bolus injection in mice before cavitation treatment. The data points come from a CEUS image loop collected before treatment, performed to determine microbubble timing.*

memory technique ("Fast Frame"). An external trigger from the EPIQ scanner triggered the oscilloscope to capture the scattered sound from all pulses within the first second of each treatment, sampled at 100 MS/s. Before injecting microbubbles, PCD was recorded in each animal to establish a baseline signal.

3.2.6 Treatment protocol delivered with single element transducer for the in-depth study of TTPL

For treatments with the single element transducer, a set of 15 mice were randomly divided into 3 treatment groups (N = 5): 1.2 MPa, 2.5 MPa, and 4 MPa peak negative acoustic pressure. An overview of the experimental timeline is shown in **Figure 3.6**. Similar to the S5-1 treatment protocol, a 50 µL bolus of microbubbles was delivered before cavitation treatments while the tumor was continuously scanned with CEUS to generate a time-intensity curve and determine the time of peak image intensity in the tumor (**Figure 3.5**). A single 1 s treatment was then performed, where ultrasound pulses were transmitted at the PRT (10 ms) for a total of 1 second at the predetermined peak of the bolus. CEUS was performed at 5 time points after treatments, titled "post-Tx" to evaluate immediate tumor blood flow changes (1 min, immediately after) and time-dependent vascular changes (5, 15, 30, and 60 min after treatment), with a separate 50 µL bolus injection of microbubbles per CEUS evaluation. Scattered pulses received by the PCD transducer were recorded using an oscilloscope (DPO 7054C Tektronix Beaverton, OR, USA) with a

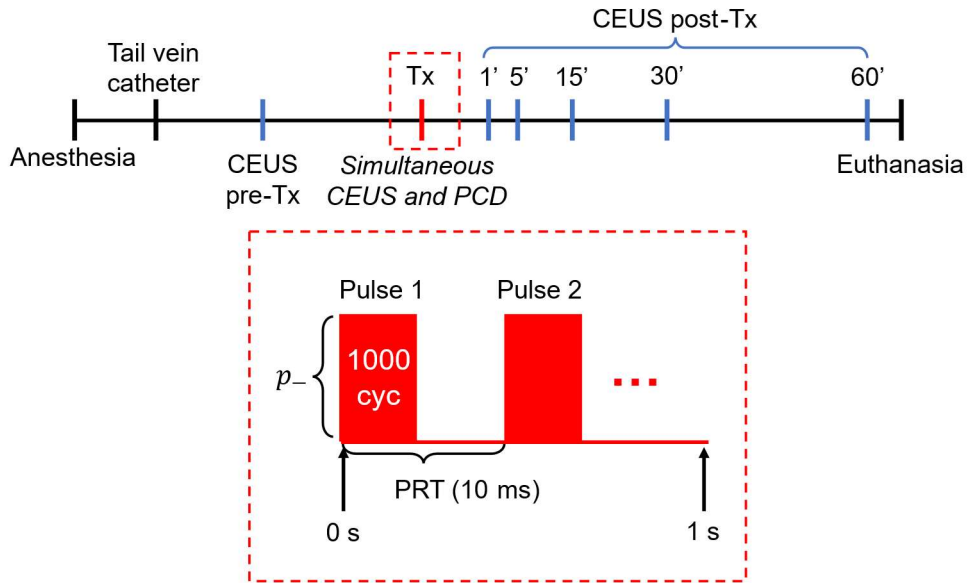

***Figure 3.6**: Experimental protocol for treatments with single element transducer.*

CEUS = contrast-enhanced ultrasound, Tx = treatment, PCD = passive cavitation detection, p_- = peak negative pressure, PRT = pulse repetition time.

segmented memory technique ("FastFrame") as described in our previous work [32]. An external trigger from the arbitrary function generation triggered the oscilloscope to capture the scattered sound from the first 50 transmitted pulses (0.5 s treatment time), sampled at 200 MS/s. After each experiment, the data were exported from the oscilloscope for postprocessing using a custom MATLAB (MathWorks) script.

3.2.7 Interstitial fluid pressure measurements

After cavitation treatments with the S5-1 (**Figure 3.4**), mice were removed from the water tank and 30 minutes after the last treatment, tumor IFP was measured. A pressure catheter (SPR-671, ADInstruments Inc., Colorado Springs, CO, USA) was threaded through a thin-walled 19G needle and soaked in deionized water for 30 min before calibrating the baseline zero to be equal to atmospheric pressure (sensor held just below water surface). The catheter is then retracted into the needle and inserted into the center of the tumor with the help of ultrasound imaging. The needle was then removed from the tumor and the catheter measured the pressure for 30 seconds before being removed.

3.2.8 Passive cavitation analysis

Processing of received scattered signals during cavitation treatments was performed similar to the technique presented in our previous work [32]. Briefly, each waveform is first truncated to its respective original pulse length with a rectangular window and the rms of the truncated window is calculated. The average value of the waveform is then removed (small offset of zero value of the oscilloscope), and the one-sided power spectrum (scaled by 2 divided by the number of samples squared) is taken of each truncated waveform. For each spectrum, broadband energy was collected between the third harmonic (to limit influence of transmitted pulse) and 10 MHz (roughly the upper limit of the receiver bandwidth). Within this range, frequency bands centered on each harmonic and ultraharmonic with a bandwidth of 0.3 MHz were excluded, while the remaining bands were summed resulting in the broadband energy per pulse. This process was repeated for all pulses. The inertial cavitation dose (ICD) was calculated as the summation over the treatment duration of the product of the broadband energy per pulse with the pulse duration.

3.2.9 CEUS quantification

To quantitatively determine changes in perfusion loss within the tumor resulting from the cavitation treatment, we used a perfusion quantification algorithm titled "Maximum Intensity Projection Time Area Curve" analysis (MIP-TAC)[3]. Briefly Pre- and post-Tx CEUS loops were extracted from the ultrasound scanner, processed with Philips QLAB's super-resolution technique which performs maximum intensity projection in combination with advanced motion compensation techniques and proprietary image processing that leads to higher spatial resolution [44], and then fed into a custom MATLAB algorithm. This algorithm calculated the percentage of the tumor area with microbubble signal (or perfused regions of the tumor) for all frames and generates MIP-TAC curves. To derive these curves, all pixels within the tumor ROI with signal above baseline noise, established by the average non-zero signal within the tumor ROI prior to contrast arrival, in each processed CEUS image were considered to be perfused, and the percentage of pixels in the ROI which satisfied this condition were calculated for each frame of the loop. The transient tumor perfusion loss, evaluated as the difference in MIP-TAC values 15 seconds after contrast arrival (pre-Tx minus post-Tx), was then calculated for all mice and for each of the 5 post-

[3] MIP-TAC analysis was developed by Connor Krolak, presented in greater detail in: *Krolak C., **De Koninck LH.**, Gu S., Wang YN., Powers JE., Averkiou M. "Ultrasound cavitation therapy: inducing tumor drug delivery and blood flow changes with clinical ultrasound tools" J. Control. Release (in review).*

Tx CEUS scans during single element transducer treatments (**Figure 3.6**). The 15 second timepoint was selected as it is the approximate one-pass circulation time of blood in a mouse [45] to mitigate potential confounding of these metrics from differences in recirculating bubbles across mice, and to minimize smearing of contrast signal from maximum intensity projection over time due to respiratory motion.

3.2.10 Statistical analysis

For cavitation treatments delivered with the S5-1, a two-sided Welch's t-test was used to evaluate statistical differences between the resulting tumor perfusion loss from the moderate and high cavitation treatment groups. A repeated measures ANOVA was utilized to identify statistically significant differences in tumor perfusion loss during treatment between the moderate and high cavitation groups. A Kruskal-Wallis with Dunn's post-hoc test was used for interstitial fluid pressure measurements. For all analysis, the significance levels were set to 0.05.

3.3 RESULTS

3.3.1 Cavitation activity versus TTPL during repeated treatments with a clinical scanner

3.3.1.1 Quantification of TTPL from CEUS

Figure 3.7 depicts tumoral perfusion loss throughout the treatment regime following treatment with the clinical scanner. In the moderate cavitation treatment (**Figure 3.7**(a)), tumor vascularity persisted throughout all four treatments, with a gradual decrease observed in the center of the tumor. For the high cavitation treatment (**Figure 3.7**(b)), nearly complete tumor perfusion loss was observed after the first cavitation treatment, and persisted throughout the following three treatments. Tumor perfusion loss throughout treatment in the high cavitation and moderate cavitation groups was quantified in **Figure 3.8**. MIP-TAC perfused area was calculated for each treatment injection at the time of the peak of the bolus, as determined by the pre-treatment injection. These percentages were then subtracted from the pre-treatment value and averaged by group to generate the curves shown in **Figure 3.8**. Significant reduction of tumor blood volume was observed after the first treatment in the high cavitation condition and sustained for the remaining treatments as compared to the moderate cavitation condition ($p = 0.002$, repeated measures ANOVA).

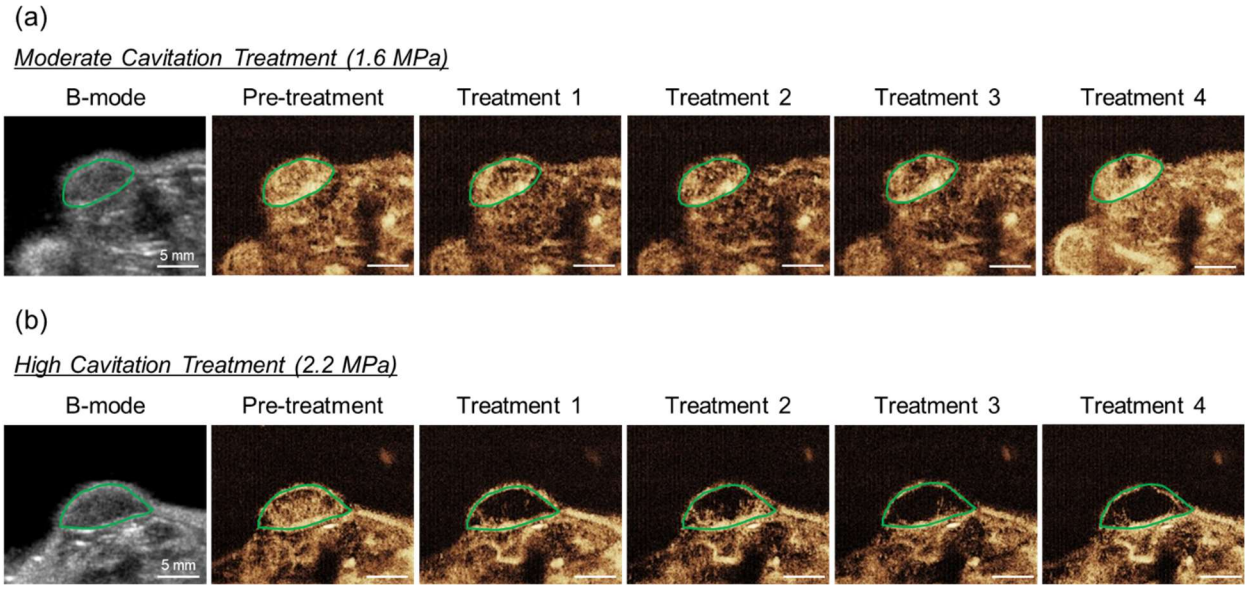

***Figure 3.7**: B-mode and contrast images during cavitation treatments.*

Contrast-enhanced ultrasound (CEUS) images during treatment for the (a) moderate cavitation and (b) high cavitation group.

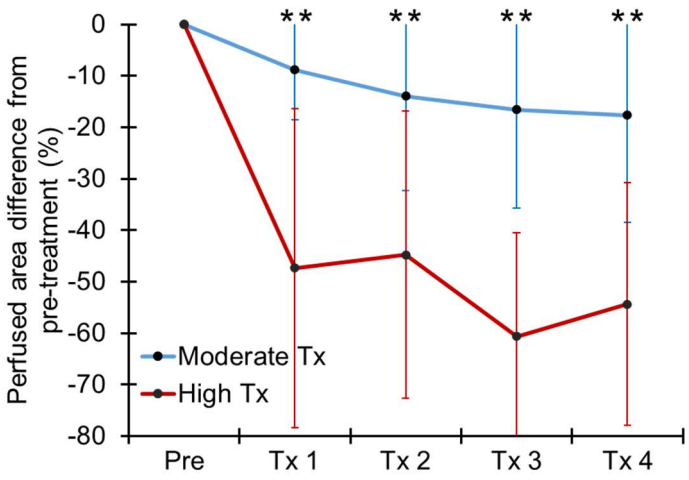

Figure 3.8*: Quantitative tumor perfusion loss across treatment injections.*

*Average and standard deviation values exhibit the significant reduction in tumor blood volume in the high condition as opposed to the moderate condition (2-way repeated measures ANOVA, p = 0.002, 95% confidence interval of mean differences: [21.98, 53.71], Cohen's d effect size: 1.71, n = 7 per group). **p < 0.01.*

3.3.1.2 Evaluation of cavitation activity

Figure 3.9 shows the cavitation activity measured by PCD during treatments delivered with the clinical scanner. **Figure 3.9**(a) is an example spectrum of the first transmitted pulse of a high cavitation treatment where elevation of broadband energy is observed. The average (n = 4) broadband energy of the first 5 pulses during the high cavitation treatments is shown in **Figure 3.9**(b). Only the first few pulses generated broadband energy significantly greater than the zero level (baseline, no microbubbles), and by the third pulse broadband energy had returned to the zero level. The cavitation activity of the first pulse is further analyzed in **Figure 3.9**(c), which shows the average (n = 3) broadband energy of the first pulse of treatments 1 and 4 (see **Figure 3.4**) for both the moderate and high cavitation conditions. In treatment 1, both moderate and high conditions generate elevated broadband energy above baseline, indicating cavitation treatments produced spectral components consistent with what is often referred to as inertial cavitation as we

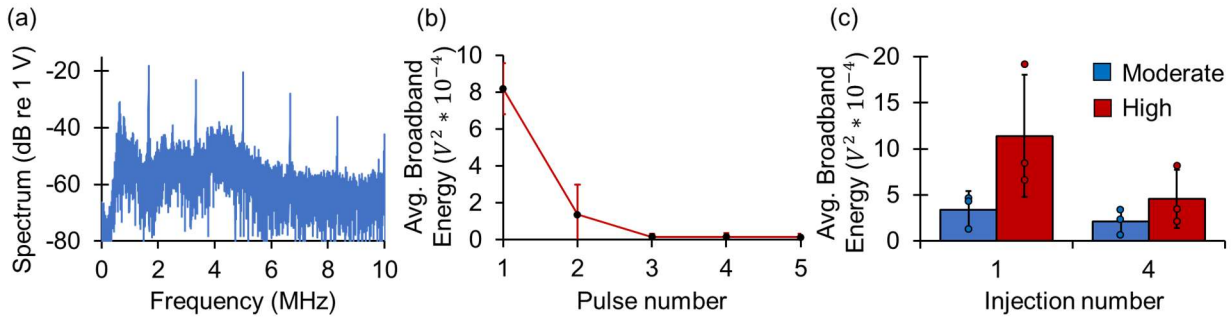

***Figure 3.9**: PCD measurements during cavitation treatments with clinical scanner.*

(A) An example frequency spectrum of microbubble cavitation from passive cavitation detection. (B) Mean and standard deviation of average broadband energy in the first 5 treatment pulses for a subset of mice in the high cavitation treatment condition (n = 4). (C) Mean and standard deviation of average broadband energy for the first treatment pulse of injection 1 and 4 for both cavitation treatment groups (n = 3 per group).

intended when selecting these conditions. The high cavitation condition produced an average broadband energy level 3.4 times greater than the broadband energy from the moderate condition. By treatment 4 the broadband energy is reduced, with the moderate condition reduced by an average of 1.6 times, and the high condition reduced by an average of 2.5 times. This is likely due to the reduced number of scatterers in the tumor center (see **Figure 3.7**), indicating PCD is also sensitive to blood flow disruption. However, PCD measurements may be sensitive to scattered signal from the tumor periphery, since broadband energy is still elevated in the high cavitation condition despite no microbubbles being present in the tumor center.

3.3.2 Cavitation activity versus time evolution of TTPL with a single element focused transducer

3.3.2.1 Quantification of TTPL from CEUS

Figure 3.10 shows representative super-resolution processed CEUS images recorded before cavitation treatments (pre-Tx) and during 0 to 60 minutes following cavitation (post-Tx) treatments. Before treatment (pre-Tx), all tumors (green outline) are well perfused. Immediately after treatment with 1.2 MPa (post-Tx, 1 min), a minor and heterogenous reduction in blood flow was observed. Five minutes after the 1.2 MPa treatment, blood flow appears to return to pre-Tx levels and slightly reduces at each subsequent CEUS scans. Immediately after the 2.5 MPa treatment (post-Tx, 1 min), tumors exhibit significant perfusion loss in the tumor center, with some blood flow maintain in the tumor periphery. Partial recovery of blood flow is observed on subsequent CEUS scans, but tumors cannot recover to pre-Tx appearance by 60 minutes post-Tx.

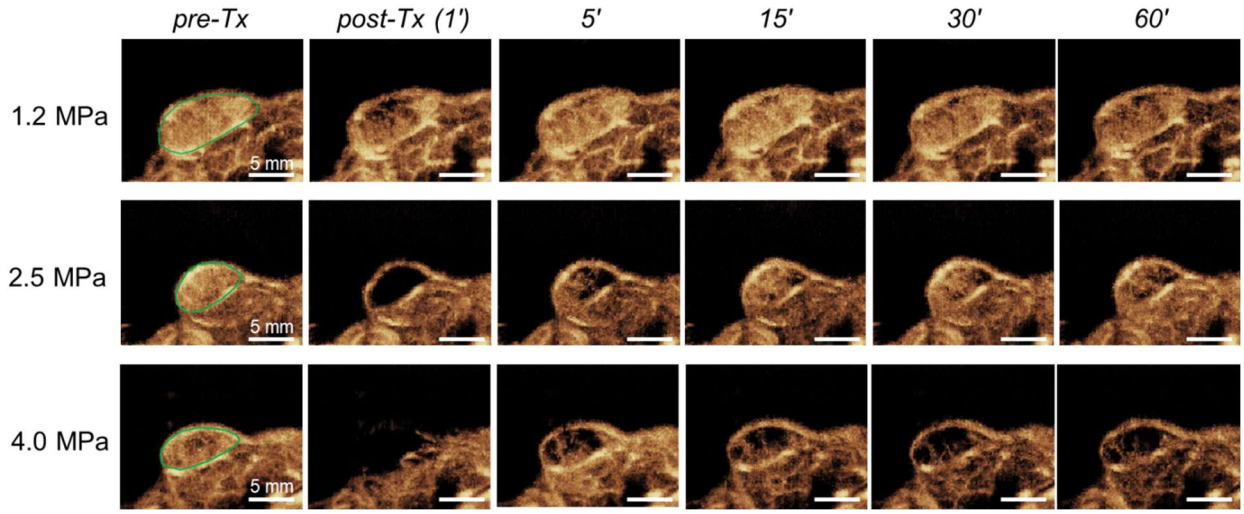

***Figure 3.10**: CEUS qualitative tumor vascular changes in response to single element cavitation treatments.*

Representative maximum intensity projection-processed contrast-enhanced ultrasound images before (pre-Tx) and after (post-Tx) each cavitation treatment. Each tumor was evaluated at 5 time points after treatment (1, 5-, 15-, 30-, and 60-minutes post-Tx). Green circle in pre-Tx outlines the tumor region and represents the region of interest used during image quantification.

Immediately after treatment with 4.0 MPa (post-Tx, 1 min), cessation of blood flow in a large area of the tumor and the tumor periphery is observed. CEUS scans 5 minutes after treatment show recovery of blood flow in the tumor periphery and like the 2.5 MPa treatments a partial recovery of blood flow in some areas of the tumor.

To further investigate the changes to tumor perfusion following cavitation treatments, **Figure 3.11** shows the average change in perfused area calculated from each post-Tx CEUS scan. Before treatment (0 min), tumors exhibit 100% perfused area, in agreement with the pre-Tx images in **Figure 3.10**. After treatment with 1.2 MPa, perfused area is initially reduced by 40% (1 min) but fully recovers to 100% perfused area as soon as 5 minutes after treatment. A significant reduction in perfused areas is observed immediately after treatments with 2.5 MPa, exhibiting an average reduction of 80% of the perfused area. Five minutes after 2.5 MPa treatments, tumors recover to 70% perfused area which is then maintained for the remainder of the observation time (60 minutes). Tumors treated with 4.0 MPa also show a significant reduction in blood flow immediately after treatment (1 min), exhibiting a 98% average reduction in perfused area. We note

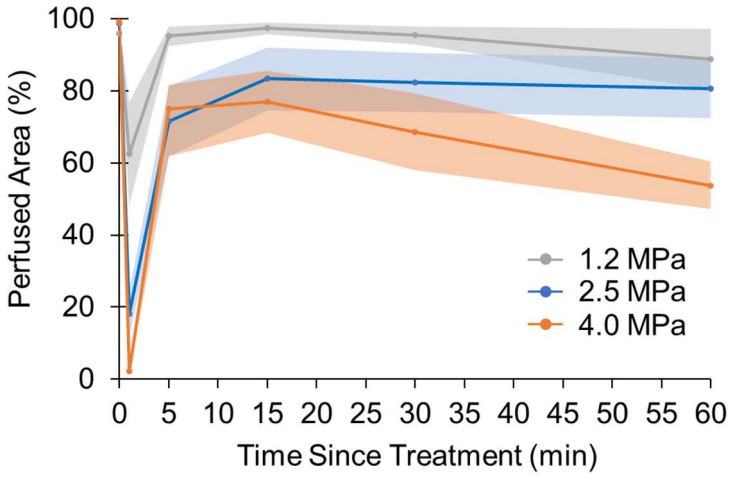

***Figure 3.11**: CEUS quantitative tumor vascular changes in response to cavitation treatments with single element transducer.*

Average change in perfused area of tumors quantified from post-Tx CEUS and monitored up to 60 minutes following cavitation treatments. Shaded regions represent standard error of each cavitation treatment.

that 4.0 MPa shows a greater reduction of perfused area due to the inclusion of part of the tumor periphery in the region of interest. At 5 minutes post-Tx with 4.0 MPa, perfused area again recovers to 70%, however, from 15-60 minutes post-Tx perfused area gradually reduces to 60% perfused area at 60 minutes. The changes to perfused area reflect the qualitative observations (**Figure 3.10**) and the unique reduction of perfused area from 15-60 minutes following treatments with 4.0 MPa indicates a difference in tumor response between 2.5 and 4.0 MPa despite similar reductions in perfused area immediately after treatment.

3.3.2.2 Evaluation of cavitation activity

Figure 3.12 shows the cavitation activity (rms) measured by PCD during treatments delivered with the single element focused transducer. Every point in the figure represents one scattered pulse. The different curves show different focal peak negative pressures (1.2, 2.5, and 4.0 MPa). **Figure 3.12**(a) shows the average rms value of baseline signal (without microbubbles) of each pulse as a function of pulse number up to 50 pulses. During low (1.2 MPa) and moderate (2.5 MPa) acoustic pressures, the rms value is constant for all 50 pulses, and slightly increases in magnitude with increasing acoustic pressure. During the high acoustic pressure (4.0 MPa), rms is no longer constant, increasing from pulses 5-7 to a rms value much greater (3.75 times) than rms during 2.5 MPa. The substantial increase in rms at 4.0 MPa is likely due to cavitation in the water

tank (despite degassing) that was observed with CEUS and may have impacted PCD measurements of the 4.0 MPa treatments.

Figure 3.12(b) shows the average net rms value (after subtracting the rms baseline signal) of each pulse as a function of pulse number up to 50 pulses. At the lowest acoustic pressure (1.2 MPa), the rms stays constant and near a value of zero (baseline). During the moderate acoustic pressure (2.5 MPa), rms is elevated above zero level at the start of treatment, gradually reducing to zero level by the 20th pulse. However, the highest acoustic pressure (4.0 MPa) exhibits markedly greater rms values (3 times greater than rms during 2.5 MPa) that is sustained for all 50 pulses. Similar to **Figure 3.12**(a), the unique rms behavior during 4.0 MPa (high magnitude, sustained activity) is most likely evidence of off-target cavitation in the water tank being detected by the PCD system.

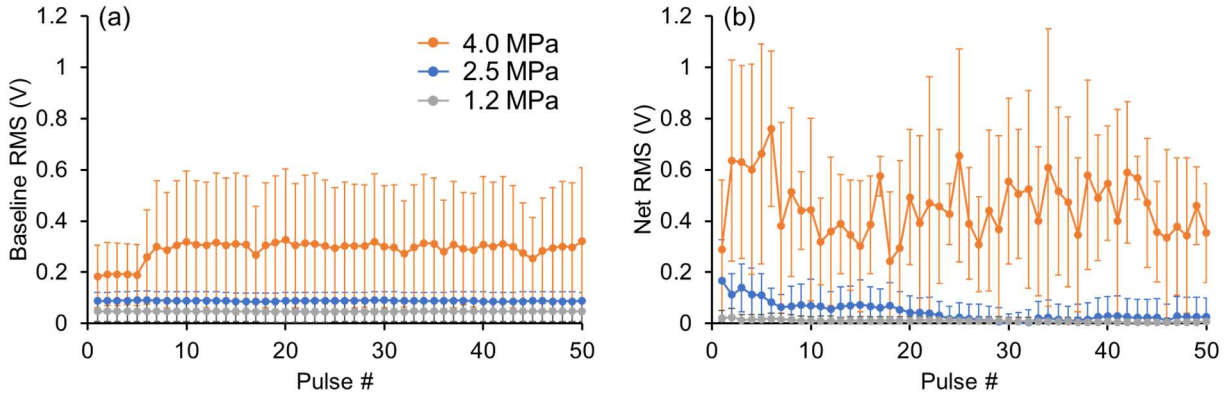

***Figure 3.12**: Average rms of scattered pulses during treatments with single element transducer as a function of pulse number.*

(a) Average baseline rms (no microbubbles) during 1.2, 2.5, and 4.0 MPa treatments. (b) Average net rms (subtract baseline rms from treatment rms) during 1.2, 2.5, and 4.0 MPa treatments. Error bars indicate one standard deviation.

Figure 3.13 is similar to **Figure 3.12** with the exception that the y-axis is the broadband energy instead of the rms value of the scattered pulse. **Figure 3.13**(a) shows the broadband energy of baseline signal exhibits similar trends to the rms values per pulse (**Figure 3.12**), where broadband energy is constant during 1.2 and 2.5 MPa treatments and significantly increased in magnitude during 4.0 MPa. **Figure 3.13**(b) shows the average net broadband energy (minus the baseline value) of each scattered pulse as a function of pulse number up to 50 pulses. At the lowest acoustic pressure of 1.2 MPa, broadband energy is elevated above the zero level (baseline) for the first 2 pulses. Increasing the acoustic pressure to 2.5 MPa resulted in elevation of broadband energy

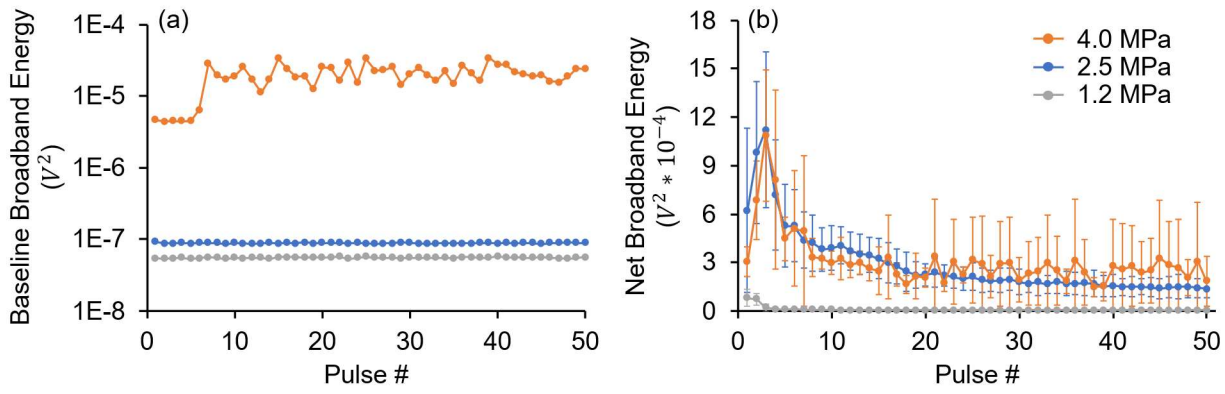

***Figure 3.13**: Average broadband energy of scattered pulses during treatments with single element transducer as a function of pulse number.*

(a) Average broadband energy of baseline signal (no microbubbles) during 1.2, 2.5, and 4.0 MPa treatments. Magnitudes are displayed on logarithmic scale. (b) Average net broadband energy (subtract baseline broadband energy from treatment broadband energy) during 1.2, 2.5, and 4.0 MPa treatments. Error bars indicate one standard deviation.

at the start of treatment and was maximized during the 3rd transmitted pulse. Broadband energy gradually decreases over the subsequent pulses, achieving a steady state around the 20th transmitted pulse, which agrees with the similar rate of reduction of the rms value observed in **Figure 3.12**(b). Broadband energy remains slightly elevated above zero level from pulses 20-50, possibly due to detection of microbubble cavitation in the tumor periphery which is not disrupted after 2.5 MPa treatments (see **Figure 3.10**). As acoustic pressure increases to 4 MPa, similar broadband energy is detected as the 2.5 MPa treatment, most likely due to off-target cavitation in the water tank preventing accurate PCD monitoring of 4.0 MPa treatment. We note that magnitude of broadband energy during 4.0 MPa with microbubbles (average maximum of $11 * 10^{-4}\ V^2$) is at least an order magnitude greater than baseline (average of $2 * 10^{-5}\ V^2$), indicating some microbubble cavitation in the tumor may still be detected. However, due to the lack of spatial information with our PCD system we are unable to separate the cavitation signatures of microbubbles in the tumor from off-target cavitation in the water tank.

The ICD of the first 50 transmitted pulses for each 1 s cavitation treatment is shown in **Figure 3.14**. The ICD during 1.2 MPa treatments was the lowest due to the relatively low broadband energy generated, and only being sustained for 2 pulses [see **Figure 3.13**(b)]. During 2.5 MPa, ICD is significantly increased (33 times greater than ICD at 1.2 MPa) due to the relatively high magnitude of broadband energy being sustained up to 20 pulses. The ICD was the same for

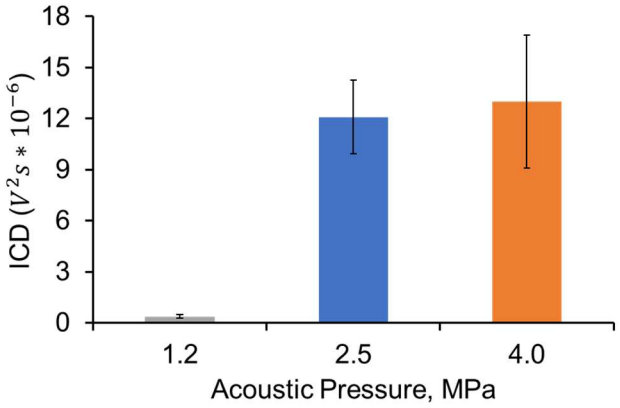

***Figure 3.14**: Average inertial cavitation dose (ICD) of each cavitation treatment over a 1 s duration.*

Error bars indicate standard error, and baseline signal was subtracted before averaging.

the 2.5 and 4.0 MPa treatments due to similar detected broadband energy both in terms of magnitude and sustained activity over several pulses. The increase in ICD with acoustic pressure also agrees with the enhanced reduction of tumor perfusion with increasing acoustic pressure observed with CEUS immediately after treatment (see post-Tx 1 min, **Figure 3.10**).

3.3.3 Interstitial fluid pressure measurements

Figure 3.15 shows average IFP measurements by treatment condition during cavitation therapy with the clinical scanner. There was a significant reduction ($p = 0.001$ and $p = 0.015$ for the moderate condition and high condition respectively) in IFP in both ultrasound cavitation conditions relative to the controls, despite all IFPs measured being very low, <10 mmHg. However, despite the vascular differences between the ultrasound treatment conditions, no significant differences in IFP were recorded between the moderate and high conditions.

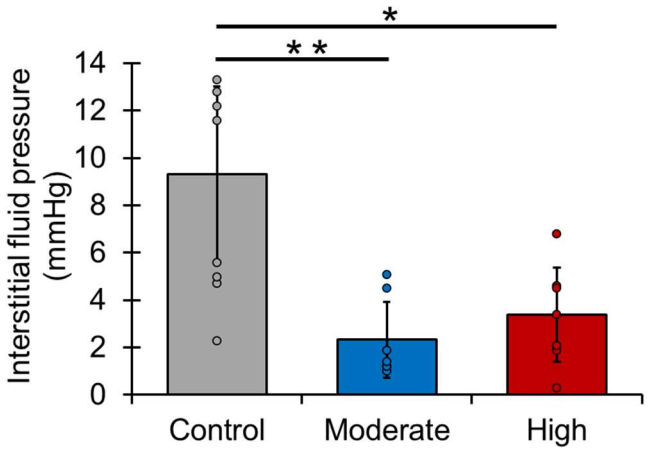

***Figure 3.15**: Average and standard deviation of interstitial fluid pressure measurements by treatment condition.*

*A significant decrease in interstitial fluid pressure was observed in both the moderate ($p = 0.001$) and high ($p = 0.015$) cavitation treatment groups relative to the control group (Kruskal-Wallis with Dunn's post-hoc, ranked ε^2 effect size: 0.57, $n = 7$ per group). *$p < 0.05$, **$p < 0.01$.*

3.4 Discussion

In this study we delivered ultrasound cavitation treatments with clinically approved microbubbles and either a modified clinical scanner or a single element 1 MHz focused transducer to evaluate the effect of acoustic pressure on tumor transient perfusion loss and interstitial fluid pressure. PCD confirmed accurate targeting by monitoring microbubble activity during treatments. CEUS was used to evaluate qualitative and quantitative tumor perfusion outcomes. We investigated ultrasound pulses that cause inertial cavitation in vivo and observed transient tumor perfusion loss--TTPL. Pressure catheter measurements confirmed a significant reduction in IFP resulting from cavitation treatments. CEUS evaluation showed that all cavitation treatments resulted in reduction in tumor blood flow immediately after treatment that increased in severity with acoustic pressure. PCD measurements showed that cavitation activity rapidly diminished during the first few (1-20) treatment pulses. Cavitation activity measured during treatment agreed with TTPL observed immediately after treatment, indicating PCD may be used to predict TTPL severity.

3.4.1 Microbubble cavitation-induced transient tumor perfusion loss

Through inclusion of two ultrasound cavitation treatment protocols, we were able to initially investigate the relationship between these tumor blood flow disruption events and acoustic

parameters. Importantly, this study uniquely incorporates CEUS imaging during treatment, allowing for the evaluation of microbubble presence during and between treatments, enabling future optimization of cavitation treatments. We observed how the extent of tumor perfusion loss scaled with acoustic pressure, as suggested in previous similar works [8, 28, 37, 46], and our comparison of cavitation therapy with single or repeated treatments paired with PCD measurements of cavitation activity offers new insights on optimizing cavitation treatment protocols for inducing TTPL. We observed that all ultrasound conditions, regardless of the protocol, induced TTPL that increased in severity with acoustic pressure. At the start of each treatment, PCD measurements also detected elevation of broadband energy [see **Figure 3.9**(b) and **Figure 3.13**(b)] indicating the occurrence of inertial cavitation [22]. While inertial cavitation of microbubbles may generate both localized mechanical forces [25-27] and enhanced heat deposition [47], our selection of acoustic parameters (low intensity) and brief treatment durations (1 s or 5 s of continuous sonication) promotes the mechanical effects of microbubble cavitation. Therefore, the presence of inertial cavitation indicates TTPL likely resulted from the mechanical forces of cavitating microbubbles. However, exact changes to tumor vasculature depended on the acoustic conditions and microbubble delivery specific to each treatment protocol.

During cavitation therapy delivered with the clinical scanner, we performed four consecutive cavitation treatments with alternating five second “on” and “off” periods with simultaneous PCD and CEUS to provide feedback about our treatment regime. The purpose of the five second off periods was to allow for residual microbubbles to recirculate into the tumor, to then cavitate to further treatment efficacy. However, we observed through both CEUS and PCD that very few microbubbles re-entered the tumor after the first five-second treatment, and that nearly all the effect of the cavitation treatment occurred during the first sonication period (**Figure 3.16**). Insonifying the tumor for 60 seconds with the 5 second on/off scheme was a conservative approach to leverage recirculating microbubbles, but the limited number of residual microbubbles in this

small animal model after the first exposure was confirmed by both PCD and CEUS. Based on our readouts from PCD and CEUS, a more optimal treatment protocol could utilize a much shorter "on" period with no repeated firings, such as a single 1 second exposure. Additionally, the four repeated injections were intended to each induce the same biological effect for increased drug penetration, compounding upon one another to allow for greater treatment efficacy. However, as depicted in **Figure 3.7** and **Figure 3.8**, the high cavitation treatment (2.2 MPa) caused a nearly complete cessation of flow within the tumor immediately after the first treatment. Meanwhile the moderate cavitation treatment (1.6 MPa) gradually decreased tumor perfusion, particularly in the center of the tumor. These results suggest that the efficacy of repeated cavitation treatments is diminished when significant blood flow disruption occurs. Despite its limited influence in this study, the relevance of recirculating microbubbles would likely be more significant in humans. However, increasing the time between cavitation treatments may allow for recovery of tumor perfusion, which we further investigated during our treatments with the single element transducer.

During cavitation therapy delivered with a focused, single element transducer we investigated performing cavitation therapy as a single, 1 s treatment and CEUS monitored the time

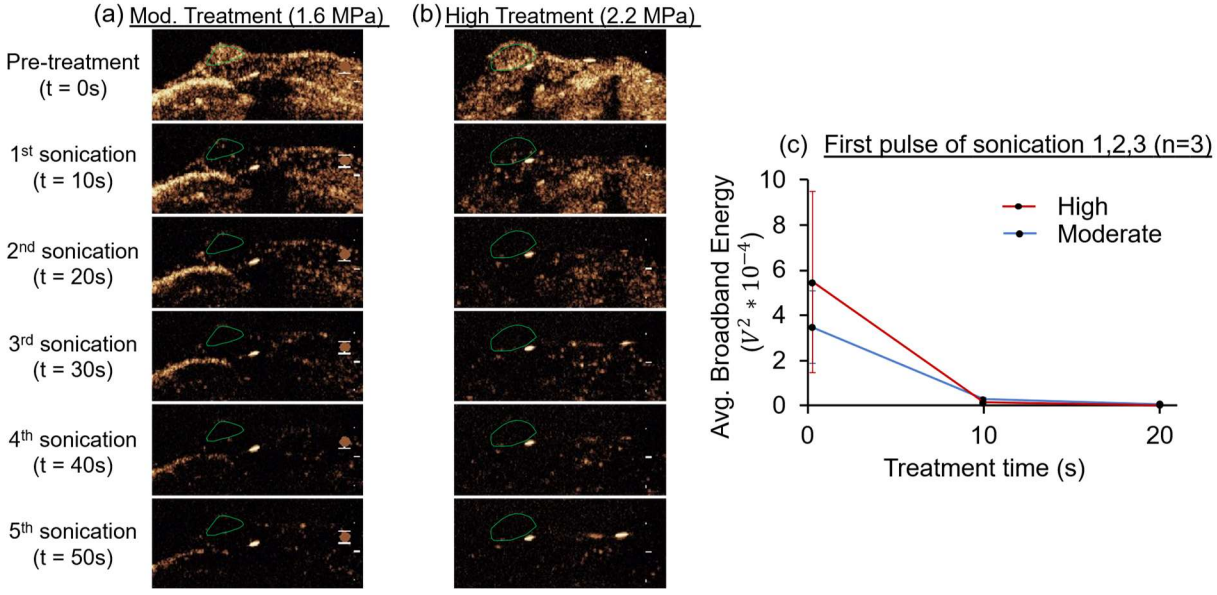

***Figure 3.16**: CEUS and PCD measurements during the first cavitation treatment with S5-1.*

CEUS images recorded during a single microbubble injection immediately before each 5 s "ON" period of (a) the moderate cavitation treatment (1.6 MPa) or (b) the high cavitation treatment (2.2 MPa). (c) Mean and standard deviation of average broadband energy of the first transmitted pulse of the first 3 5 s "ON" treatment periods during high and moderate cavitation treatments (n = 3).

evolution of TTPL up to 60 minutes after each treatment. Despite the short treatment duration (1 s), significant disruption of tumor blood flow was still observed immediately after cavitation treatments (post Tx, 1 min, **Figure 3.10**) with partial disruption of tumor perfusion at low acoustic pressure (1.2 MPa) and near-complete cessation of flow at higher acoustic pressures (2.5, 4.0 MPa). PCD measurements were also sensitive to tumor perfusion changes, where ICD increased from 1.2 MPa to 2.5 MPa [see **Figure 3.14**] corresponding with enhanced reduction of tumor perfusion from 1.2 to 2.5 MPa (**Figure 3.11)**. The significant reduction of tumor perfusion and cavitation activity generated with the single, 1 s treatment protocol supports our initial conclusion that effective cavitation treatments may still be delivered with short treatment durations. Monitoring TTPL after the 1 s cavitation treatments also revealed that the majority of tumor perfusion (> 50% perfused area) recovered 5 minutes after treatment (**Figure 3.10**) at all acoustic pressures. While the recovery of tumor vasculature following cavitation therapy has been reported in previous similar studies using CEUS [14, 40, 48], this is typically reported on larger time scales (hours, days). Our measurements of TTPL within the first hour after cavitation treatments indicate that delaying subsequent cavitation treatments by at least 5 minutes in this tumor model can increase the efficacy of treatments and may be used to further enhance systemic drug delivery.

These tumor blood flow disruption events could be utilized synergistically with other treatment techniques beyond drug extravasation. One such application is thermal ablation where perfusion within a lesion acts a heat-sink effect, extending the required treatment time and efficacy. Another is with immune-based therapies, where sensitization of the immune system has been initially explored in relation to ultrasound cavitation treatments [35, 39, 49, 50], and could assist in overcoming the immune-silencing properties of these solid tumors. A greater understanding of how the blood flow disruption events explored in this study influence tumor progression has yet to be studied but will be addressed in future work.

3.4.2 Microbubble cavitation impacts tumor interstitial fluid pressure

Highly arterialized tumors like HCC experience enhanced permeability and retention which increases interstitial fluid pressure, generating a pressure gradient that limits drug penetration within the tumor [51]. As demonstrated in **Figure 3.15**, we observed a significant reduction in IFP with both cavitation treatments (albeit these are small pressures), indicating that these conditions are able to mechanically alter the tumor microenvironment and relieve this pressure gradient. The relationship between the reduction in tumor IFP and cavitation treatments

is still not well understood and has been attributed to various cavitation-induced bioeffects such as widening of endothelial cell junctions, deformation of collagen fibers, dilation of lymphatic vessels, and the reduction of tumor blood perfusion [52, 53]. Despite lacking a comprehensive understanding of this mechanism, cavitation treatments have displayed a relationship with tumor IFP scaling with acoustic pressure [42], and suggest a means for improved therapeutic payload delivery through enhanced vascular permeability and removal of this pressure gradient acting as a barrier to diffusion [42, 54]. Other studies have also attributed similar changes in tumor IFP as observed in this study (5-10 mmHg) to enhanced drug uptake [43].

3.4.3 Acoustic pressure threshold for significant TTPL

Our evaluations with CEUS and PCD both indicate that TTPL is highly dependent on acoustic pressure. The measured tumor perfusion changes resulting from cavitation treatments delivered with the clinical scanner [see **Figure 3.8**, **Figure 3.10**] were clustered into 2 regimes: partial disruption (< 50% reduction in perfused area) observed after the first (Tx 1) 1.6 MPa acoustic pressure treatment, and significant disruption (> 50% reduction in perfused area) observed after the first 2.2 MPa treatment. Similar regimes were observed after 1 s cavitation treatments delivered with the single element transducer [see **Figure 3.11**], where partial disruption occurred immediately after 1.2 MPa treatments and significant disruption occurred immediately after the 2.5 and 4.0 MPa treatments. Additionally, PCD measurements during treatments with the single element transducer demonstrated that ICD significantly increased from 1.2 to 2.5 MPa [see **Figure 3.14**], in agreement with the partial and significant disruption thresholds of tumor perfusion. Our findings indicate an acoustic pressure threshold near 2 MPa may exist above which most of the tumor blood flow is temporarily eliminated. Similar evaluations of tumor perfusion changes after cavitation therapy have also observed partial disruption at acoustic pressures equal to or below 2 MPa [8, 14, 36, 37, 40, 48, 55, 56] and significant disruption at acoustic pressures greater than 2 MPa [8, 14, 28, 37, 56-58] despite differences in ultrasound parameters such as pulse duration, transmit frequency, and treatment time. The dependence of transient tumor perfusion loss on acoustic pressure could be due to the increased susceptibility of immature neovessels (prevalent in tumors) to mechanical damage from microbubble cavitation [15].. Zhao, et al. [8] demonstrated that small vessels (< 50 μm), are predominantly disrupted at low acoustic pressures (1 MPa), with larger vessels shutdown as acoustic pressure increases ($\geq$ 2 MPa). The heterogeneity of vessel sizes in tumors [8] can also influence the acoustic pressure threshold for inertial cavitation [59],

requiring high acoustic pressures (> 2 MPa) to generate inertial cavitation in all vessels sizes present in solid tumors. While the mechanism for TTPL is still unclear, our findings demonstrate that careful selection of acoustic pressure is needed to elicit desired tumor perfusion changes.

3.4.4 Limitations

Despite the advances in cavitation treatments made in this study, there are limitations which should be addressed. Although many components of this study were clinically relevant, treatments were performed in a subcutaneous murine model. This is unlike HCCs, where the tumor microenvironment is derived from and surrounded by the host organ, particularly impacted by disease. Subcutaneous lesions also lack some of the complex physiological composition that is unique to HCC, and further considerations of targeting, cavitation dynamics, and therapeutic efficacy would need to be addressed prior to clinical translation. Implementation of this technique to human tumors and other complex lesion types, particularly poorly perfused ones, may be limited by low microbubble concentrations. This potential barrier could be mitigated with other tumor sensitizing therapies to improve blood flow employed in similar studies such as mild hyperthermia [60] or nitric oxide therapy [61, 62]. In addition, even though ultrasound conditions were consistent with ranges established in existing literature, we were unable to explore a greater parameter space (for example pulse repetition time and numbers of cycles) due to study limitations. Acoustic pressure has been described as a primary driver of cavitation-induced bioeffects, particularly tumor vascular changes [41, 63]. However, pulse length and PRT also play a very important role in the produced cavitation and can impact drug penetration. These three acoustic parameters – peak negative pressure, pulse length, and PRT – still require a more extensive investigation to determine their unique contributions to cavitation induced tumor microenvironment changes.

Another consideration for this work was the water tank used for the experimental setup possibly influencing the delivery and measurement of cavitation treatments. The quality of degassing of the water tank was limited due to the configuration of the setup. As a result, native cavitation (without microbubbles) was observed in the water tank just outside the tumor during 4.0 MPa treatments, coinciding with the axial position of maximum acoustic pressure of the focused, single element transducer [see **Figure 3.2**]. We observed a significant increase of both average rms and broadband energy during baseline measurements of the 4.0 MPa condition [see **Figure 3.12**(a) and **Figure 3.13**(a)], indicating cavitation in the water tank impacted PCD measurements. Intense cavitation in the water tank could have briefly shielded the tumor from receiving the full

acoustic amplitude [64], which may have reduced the delivered acoustic pressure below 4.0 MPa . This shielding may further explain why the detected magnitude of broadband energy was similar between the 2.5 and 4.0 MPa treatments. As significant TTPL was observed at 2.5 and 4.0 MPa, in agreement with other cavitation therapy studies [8, 14, 28, 37, 56-58], this potential acoustic shielding did not significantly impact delivery of treatment pulses. To avoid the generation of off-target cavitation, a possible solution is to use a cone filled with heavily degassed water as an attachment to the treatment device.

This study, while in-part aiming to be highly translatable, was unable to attend to several considerations that would need to be addressed prior to clinical translation. Although we introduced IFP measurements to further understand the mechanical effects of these treatment conditions, the scope of this study was unable to clearly answer the mechanistic question of how cavitation treatments induce transient tumor perfusion loss. Due to the complex nature of microbubble interactions with surrounding tissues in a very small temporal window, the exact mechanism is very challenging to evaluate but could be explored further in future experiments. While we found good agreement between cavitation activity and TTPL in this tumor model, it may be possible to transmit a low acoustic pressure without leading to TTPL but still producing elevation of broadband energy detectable with PCD, limiting the effectiveness of broadband energy as a universal metric for TTPL. Mechanical alterations to the tumor microenvironment were also the only effect studied here, but thermal changes produced by ultrasound treatments and their possible synergistic nature with tumor drug penetration could be explored further. Finally, although the murine model used in this study is intended to act as an analog to human tumors, the question remains whether tumor perfusion disruption may be caused in humans with our acoustic conditions.

3.5 CONCLUSION

In this work we utilized simultaneous passive cavitation detection (PCD) and contrast-enhanced ultrasound imaging (CEUS) in tumor-bearing mice during cavitation therapy to provide comprehensive information of both cavitation activity and its impact on tumor perfusion. CEUS can be used to quantify the spatial and temporal extent of transient tumor perfusion loss (TTPL). PCD confirmed targeting of cavitation treatments and predicted the extent of TTPL immediately after treatment. Pressure catheter measurements confirmed that cavitation treatments resulted in a

significant reduction of interstitial fluid pressure. All ultrasound conditions induced transient tumor perfusion loss (TTPL) that increased in severity with acoustic pressure, confirmed with CEUS and PCD. At low acoustic pressures (< 2 MPa), tumor perfusion is partially disrupted (< 50% reduction in perfused area), while high acoustic pressures (> 2 MPa) induced significant disruption of perfusion (> 50% reduction in perfused area). PCD measurements showed that cavitation activity rapidly diminished during the first few (1-20) treatment pulses. Cavitation treatment using a single, 1 second treatment induced significant TTPL at 2.5 and 4.0 MPa, demonstrating effective cavitation treatments may still be delivered with short treatment durations. Monitoring TTPL after 1 s duration cavitation treatments revealed that after the complete cessation of flow, the majority of tumor perfusion (70%) can recover as soon as 5 minutes after treatment. The findings in this work demonstrate the complimentary information PCD and CEUS can provide for detecting TTPL, the changes cavitation therapy can induce within the tumor microenvironment, and the feasibility of tumor cavitation treatment with a clinical scanner.

3.6 ACKNOWLEDGEMENTS

This work was supported by NIH grant R01EB032655. SonoVue was generously supplied by Bracco (Bracco Suisse SA, Geneva, Switzerland).

3.7 REFERENCES

[1] R. K. Jain, "Normalization of tumor vasculature: an emerging concept in antiangiogenic therapy," *Science,* vol. 307, no. 5706, pp. 58-62, 2005. doi: 10.1126/science.1104819.

[2] H. B. El–Serag and K. L. Rudolph, "Hepatocellular carcinoma: epidemiology and molecular carcinogenesis," *Gastroenterology,* vol. 132, no. 7, pp. 2557-2576, 2007. doi: 10.1053/j.gastro.2007.04.061.

[3] D. Luo, K. A. Carter, D. Miranda, and J. F. Lovell, "Chemophototherapy: an emerging treatment option for solid tumors," *Advanced Science,* vol. 4, no. 1, p. 1600106, 2017. doi: 10.1002/advs.201600106.

[4] R. K. Jain and T. Stylianopoulos, "Delivering nanomedicine to solid tumors," *Nature reviews Clinical oncology,* vol. 7, no. 11, pp. 653-664, 2010. doi: 10.1038/nrclinonc.2010.139.

[5] D. Semela and J.-F. Dufour, "Angiogenesis and hepatocellular carcinoma," *Journal of hepatology,* vol. 41, no. 5, pp. 864-880, 2004. doi: 10.1016/j.jhep.2004.09.006.

[6] S. B. Keller, D. Suo, Y.-N. Wang, H. Kenerson, R. S. Yeung, and M. A. Averkiou, "Image-Guided Treatment of Primary Liver Cancer in Mice Leads to Vascular Disruption and Increased Drug Penetration," *Frontiers in Pharmacology,* vol. 11, 2020. doi: 10.3389/fphar.2020.584344.

[7] S. B. Keller and M. A. Averkiou, "The role of ultrasound in modulating interstitial fluid pressure in solid tumors for improved drug delivery," *Bioconjugate Chemistry,* vol. 33, no. 6, pp. 1049-1056, 2021. doi: 10.1021/acs.bioconjchem.1c00422.

[8] X. Zhao, C. Pellow, and D. E. Goertz, "Intravital imaging and cavitation monitoring of antivascular ultrasound in tumor microvasculature," *Theranostics,* Research Paper vol. 13, no. 1, pp. 250-266, 2023. doi: 10.7150/thno.79186.

[9] S. L. Mulvagh *et al.*, "Contrast echocardiography: current and future applications," *Journal of the American Society of Echocardiography,* vol. 13, no. 4, pp. 331-342, 2000. doi: 10.1067/mje.2000.105462.

[10] Y. Kono *et al.*, "Gray-scale second harmonic imaging of the liver with galactose-based microbubbles," *Investigative radiology,* vol. 32, no. 2, pp. 120-125, 1997. doi:

[11] S. R. Wilson, P. N. Burns, D. Muradali, J. A. Wilson, and X. Lai, "Harmonic hepatic US with microbubble contrast agent: initial experience showing improved characterization of hemangioma, hepatocellular carcinoma, and metastasis," *Radiology,* vol. 215, no. 1, pp. 153-161, 2000. doi: 10.1148/radiology.215.1.r00ap08153.

[12] K. Darge *et al.*, "Safety of contrast-enhanced ultrasound in children for non-cardiac applications: a review by the Society for Pediatric Radiology (SPR) and the International Contrast Ultrasound Society (ICUS)," *Pediatric radiology,* vol. 43, pp. 1063-1073, 2013. doi: 10.1007/s00247-013-2746-6.

[13] D. L. Miller and R. M. Thomas, "Ultrasound contrast agents nucleate inertial cavitation in vitro," *Ultrasound in medicine & biology,* vol. 21, no. 8, pp. 1059-1065, 1995. doi: 10.1016/0301-5629(95)93252-U.

[14] J. Wang *et al.*, "Selective depletion of tumor neovasculature by microbubble destruction with appropriate ultrasound pressure," *International Journal of Cancer,* vol. 137, no. 10, pp. 2478-2491, 2015. doi: 10.1002/ijc.29597.

[15] D. Fukumura and R. K. Jain, "Tumor microvasculature and microenvironment: Targets for anti-angiogenesis and normalization," *Microvascular Research,* vol. 74, no. 2, pp. 72-84, 2007. doi: 10.1016/j.mvr.2007.05.003.

[16] S. B. Keller, Y.-N. Wang, S. Totten, R. S. Yeung, and M. A. Averkiou, "Safety of Image-Guided Treatment of the Liver with Ultrasound and Microbubbles in an in Vivo Porcine Model," *Ultrasound in Medicine & Biology,* vol. 47, no. 11, pp. 3211-3220, 2021. doi: 10.1016/j.ultrasmedbio.2021.07.003.

[17] C. Krolak *et al.*, "Quantification of hepatocellular carcinoma vascular dynamics with contrast-enhanced ultrasound for LI-RADS implementation," *Investigative radiology,* vol. 59, no. 4, pp. 337-344, 2024. doi: 10.1097/RLI.0000000000001022.

[18] T. Sun, G. Samiotaki, S. Wang, C. Acosta, C. C. Chen, and E. E. Konofagou, "Acoustic cavitation-based monitoring of the reversibility and permeability of ultrasound-induced blood-brain barrier opening," *Physics in Medicine & Biology,* vol. 60, no. 23, p. 9079, 2015. doi: 10.1088/0031-9155/60/23/9079.

[19] T. van Rooij *et al.*, "Viability of endothelial cells after ultrasound-mediated sonoporation: Influence of targeting, oscillation, and displacement of microbubbles," *Journal of Controlled Release,* vol. 238, pp. 197-211, 2016. doi: 10.1016/j.jconrel.2016.07.037.

[20] S. Keller, M. Bruce, and M. A. Averkiou, "Ultrasound imaging of microbubble activity during sonoporation pulse sequences," *Ultrasound in medicine & biology,* vol. 45, no. 3, pp. 833-845, 2019. doi: 10.1016/j.ultrasmedbio.2018.11.011.

[21] V. A. Khokhlova *et al.*, "Histotripsy methods in mechanical disintegration of tissue: Towards clinical applications," *International journal of hyperthermia,* vol. 31, no. 2, pp. 145-162, 2015. doi: 10.3109/02656736.2015.1007538.

[22] S. B. Keller, D. Suo, Y.-N. Wang, H. Kenerson, R. S. Yeung, and M. A. Averkiou, "Image-guided treatment of primary liver cancer in mice leads to vascular disruption and increased drug penetration," *Frontiers in Pharmacology,* vol. 11, p. 584344, 2020. doi: 10.3389/fphar.2020.584344.

[23] K. B. Bader and C. K. Holland, "Gauging the likelihood of stable cavitation from ultrasound contrast agents," *Physics in Medicine & Biology,* vol. 58, no. 1, p. 127, 2012. doi: 10.1088/0031-9155/58/1/127.

[24] W.-S. Chen, A. A. Brayman, T. J. Matula, L. A. Crum, and M. W. Miller, "The pulse length-dependence of inertial cavitation dose and hemolysis," *Ultrasound in medicine & biology,* vol. 29, no. 5, pp. 739-748, 2003. doi: 10.1016/S0301-5629(03)00029-2.

[25] J. Holzfuss, M. Rüggeberg, and A. Billo, "Shock wave emissions of a sonoluminescing bubble," *Physical review letters,* vol. 81, no. 24, p. 5434, 1998. doi: 10.1103/PhysRevLett.81.5434.

[26] A. Prosperetti, "Bubble phenomena in sound fields: part one," *Ultrasonics,* vol. 22, no. 2, pp. 69-77, 1984. doi: 10.1016/0041-624X(84)90024-6.

[27] W. W. Roberts, T. L. Hall, K. Ives, J. S. Wolf, J. B. Fowlkes, and C. A. Cain, "Pulsed cavitational ultrasound: a noninvasive technology for controlled tissue ablation (histotripsy) in the rabbit kidney," *The Journal of urology,* vol. 175, no. 2, pp. 734-738, 2006. doi: 10.1016/S0022-5347(05)00141-2.

[28] Y.-J. Ho, T.-C. Wang, C.-H. Fan, and C.-K. Yeh, "Spatially Uniform Tumor Treatment and Drug Penetration by Regulating Ultrasound with Microbubbles," *ACS Applied Materials & Interfaces,* vol. 10, no. 21, pp. 17784-17791, 2018/05/30 2018. doi: 10.1021/acsami.8b05508.

[29] W.-S. Chen, T. J. Matula, A. A. Brayman, and L. A. Crum, "A comparison of the fragmentation thresholds and inertial cavitation doses of different ultrasound contrast agents," *The Journal of the Acoustical Society of America,* vol. 113, no. 1, pp. 643-651, 2003. doi: 10.1121/1.1529667.

[30] W.-S. Chen, A. A. Brayman, T. J. Matula, and L. A. Crum, "Inertial cavitation dose and hemolysis produced in vitro with or without Optison®," *Ultrasound in medicine & biology,* vol. 29, no. 5, pp. 725-737, 2003. doi: 10.1016/S0301-5629(03)00013-9.

[31] J. H. Hwang, J. Tu, A. A. Brayman, T. J. Matula, and L. A. Crum, "Correlation between inertial cavitation dose and endothelial cell damage in vivo," *Ultrasound in Medicine & Biology,* vol. 32, no. 10, pp. 1611-1619, 2006/10/01/ 2006. doi: 10.1016/j.ultrasmedbio.2006.07.016.

[32] L. H. D. Koninck, K. S. Vuong, S. Shin, J. E. Powers, and M. A. Averkiou, "Delivery of Cavitation Therapy With a Modified Clinical Scanner: In Vitro Evaluation," *IEEE Transactions on Ultrasonics, Ferroelectrics, and Frequency Control,* vol. 72, no. 3, pp. 351-361, 2025. doi: 10.1109/TUFFC.2025.3536932.

[33] D. R. Morel *et al.*, "Human pharmacokinetics and safety evaluation of SonoVue™, a new contrast agent for ultrasound imaging," *Investigative radiology,* vol. 35, no. 1, p. 80, 2000. doi:

[34] L. H. De Koninck, K. S. Vuong, S. Shin, J. E. Powers, and M. A. Averkiou, "Delivery of Cavitation Therapy With a Modified Clinical Scanner: In Vitro Evaluation," (in eng), *IEEE Trans Ultrason Ferroelectr Freq Control,* vol. 72, no. 3, pp. 351-361, Mar 2025. doi: 10.1109/tuffc.2025.3536932.

[35] S. Bulner, A. Prodeus, J. Gariepy, K. Hynynen, and D. E. Goertz, "Enhancing Checkpoint Inhibitor Therapy with Ultrasound Stimulated Microbubbles," (in eng), *Ultrasound Med Biol,* vol. 45, no. 2, pp. 500-512, Feb 2019. doi: 10.1016/j.ultrasmedbio.2018.10.002.

[36] D. E. Goertz *et al.*, "Antitumor effects of combining docetaxel (taxotere) with the antivascular action of ultrasound stimulated microbubbles," (in eng), *PLoS One,* vol. 7, no. 12, p. e52307, 2012. doi: 10.1371/journal.pone.0052307.

[37] X. Hu *et al.*, "Insonation of targeted microbubbles produces regions of reduced blood flow within tumor vasculature," (in eng), *Invest Radiol,* vol. 47, no. 7, pp. 398-405, Jul 2012. doi: 10.1097/RLI.0b013e31824bd237.

[38] S. B. Keller, D. Suo, Y. N. Wang, H. Kenerson, R. S. Yeung, and M. A. Averkiou, "Image-Guided Treatment of Primary Liver Cancer in Mice Leads to Vascular Disruption and Increased Drug Penetration," (in eng), *Front Pharmacol,* vol. 11, p. 584344, 2020. doi: 10.3389/fphar.2020.584344.

[39] H. L. Liu, H. Y. Hsieh, L. A. Lu, C. W. Kang, M. F. Wu, and C. Y. Lin, "Low-pressure pulsed focused ultrasound with microbubbles promotes an anticancer immunological response," (in eng), *J Transl Med,* vol. 10, p. 221, Nov 11 2012. doi: 10.1186/1479-5876-10-221.

[40] M. Todorova *et al.*, "Antitumor effects of combining metronomic chemotherapy with the antivascular action of ultrasound stimulated microbubbles," (in eng), *Int J Cancer,* vol. 132, no. 12, pp. 2956-66, Jun 15 2013. doi: 10.1002/ijc.27977.

[41] J. Wang *et al.*, "Selective depletion of tumor neovasculature by microbubble destruction with appropriate ultrasound pressure," (in eng), *Int J Cancer,* vol. 137, no. 10, pp. 2478-91, Nov 15 2015. doi: 10.1002/ijc.29597.

[42] Y. He *et al.*, "Regulation of IFP in solid tumours through acoustic pressure to enhance infiltration of nanoparticles of various sizes," (in eng), *J Drug Target,* vol. 32, no. 8, pp. 964-976, Sep 2024. doi: 10.1080/1061186x.2024.2367579.

[43] N. Xiao, J. Liu, L. Liao, J. Sun, W. Jin, and X. Shu, "Ultrasound Combined With Microbubbles Increase the Delivery of Doxorubicin by Reducing the Interstitial Fluid Pressure," *Ultrasound Quarterly,* vol. 35, no. 2, pp. 103-109, 2019. doi: 10.1097/ruq.0000000000000381.

[44] M. Apfelbeck, T. Loupas, M. Chaloupka, and D.-A. Clevert, "Improved diagnostic confidence using Super Resolution CEUS imaging in testicular lesions," *Clinical Hemorheology and Microcirculation,* vol. 88, no. s1, pp. S113-S125, 2024. doi: 10.3233/ch-248109.

[45] K. Welsher, S. P. Sherlock, and H. Dai, "Deep-tissue anatomical imaging of mice using carbon nanotube fluorophores in the second near-infrared window," (in eng), *Proc Natl Acad Sci U S A,* vol. 108, no. 22, pp. 8943-8, May 31 2011. doi: 10.1073/pnas.1014501108.

[46] P. T. Yemane *et al.*, "Effect of Ultrasound on the Vasculature and Extravasation of Nanoscale Particles Imaged in Real Time," (in eng), *Ultrasound Med Biol,* vol. 45, no. 11, pp. 3028-3041, Nov 2019. doi: 10.1016/j.ultrasmedbio.2019.07.683.

[47] C. H. Farny, R. G. Holt, and R. A. Roy, "The Correlation Between Bubble-Enhanced HIFU Heating and Cavitation Power," *IEEE Transactions on Biomedical Engineering,* vol. 57, no. 1, pp. 175-184, 2010. doi: 10.1109/TBME.2009.2028133.

[48] P. Huang *et al.*, "Enhanced antitumor efficacy of ultrasonic cavitation with up-sized microbubbles in pancreatic cancer," *Oncotarget,* vol. 6, no. 24, p. 20241, 2015. doi: 10.18632/oncotarget.4048.

[49] P. Lai *et al.*, "Breast tumor response to ultrasound mediated excitation of microbubbles and radiation therapy in vivo," (in eng), *Oncoscience,* vol. 3, no. 3-4, pp. 98-108, 2016. doi: 10.18632/oncoscience.299.

[50] Y. Wu, J. Li, L. Shu, Z. Tian, S. Wu, and Z. Wu, "Ultrasound combined with microbubble mediated immunotherapy for tumor microenvironment," (in eng), *Front Pharmacol,* vol. 15, p. 1304502, 2024. doi: 10.3389/fphar.2024.1304502.

[51] D. Semela and J. F. Dufour, "Angiogenesis and hepatocellular carcinoma," (in eng), *J Hepatol,* vol. 41, no. 5, pp. 864-80, Nov 2004. doi: 10.1016/j.jhep.2004.09.006.

[52] S. B. Keller and M. A. Averkiou, "The Role of Ultrasound in Modulating Interstitial Fluid Pressure in Solid Tumors for Improved Drug Delivery," (in eng), *Bioconjug Chem,* vol. 33, no. 6, pp. 1049-1056, Jun 15 2022. doi: 10.1021/acs.bioconjchem.1c00422.

[53] A. Mohammadabadi *et al.*, "Pulsed focused ultrasound lowers interstitial fluid pressure and increases nanoparticle delivery and penetration in head and neck squamous cell carcinoma xenograft tumors," (in eng), *Phys Med Biol,* vol. 65, no. 12, p. 125017, Jun 22 2020. doi: 10.1088/1361-6560/ab9705.

[54] F. Xi, Y. Feng, Q. Chen, L. Chen, and J. Liu, "Microbubbles Ultrasonic Cavitation Regulates Tumor Interstitial Fluid Pressure and Enhances Sonodynamic Therapy," (in eng), *Front Oncol,* vol. 12, p. 852454, 2022. doi: 10.3389/fonc.2022.852454.

[55] C. W. Burke, A. L. Klibanov, J. P. Sheehan, and R. J. Price, "Inhibition of glioma growth by microbubble activation in a subcutaneous model using low duty cycle ultrasound without significant heating," *Journal of neurosurgery,* vol. 114, no. 6, pp. 1654-1661, 2011. doi: 10.3171/2010.11.JNS101201.

[56] Y. He *et al.*, "Improving the Therapeutic Effect of Ultrasound Combined With Microbubbles on Muscular Tumor Xenografts With Appropriate Acoustic Pressure," (in English), *Frontiers in Pharmacology,* Original Research vol. Volume 11 - 2020, 2020-July-15 2020. doi: 10.3389/fphar.2020.01057.

[57] Z. Liu *et al.*, "Disruption of Tumor Neovasculature by Microbubble Enhanced Ultrasound: A Potential New Physical Therapy of Anti-Angiogenesis," *Ultrasound in Medicine & Biology,* vol. 38, no. 2, pp. 253-261, 2012/02/01/ 2012. doi: 10.1016/j.ultrasmedbio.2011.11.007.

[58] C. Chien Ting, B. I. Raju, T. Shevchenko, and A. L. Klibanov, "Control and reversal of tumor growth by ultrasound activated microbubbles," in *2009 IEEE International Ultrasonics Symposium*, 2009, pp. 77-80. 10.1109/ULTSYM.2009.5441604.

[59] X. Zhao, A. Wright, and D. E. Goertz, "An optical and acoustic investigation of microbubble cavitation in small channels under therapeutic ultrasound conditions," *Ultrasonics Sonochemistry,* vol. 93, p. 106291, 2023. doi: 10.1016/j.ultsonch.2023.106291.

[60] Y. Xiang *et al.*, "Ultrasound -Induced Thermal Effect Enhances the Efficacy of Chemotherapy and Immunotherapy in Tumor Treatment," (in eng), *Int J Nanomedicine,* vol. 19, pp. 6677-6692, 2024. doi: 10.2147/ijn.S464830.

[61] T. Luo *et al.*, "Ultrasound-Stimulated Microbubbles Cavitation Combined with Nitric Oxide Signaling Pathway to Alleviate Tumor Hypoperfusion and Hypoxia in MC38 Tumor Model," (in eng), *Acad Radiol,* vol. 32, no. 7, pp. 4121-4133, Jul 2025. doi: 10.1016/j.acra.2025.03.034.

[62] Y. Zhao *et al.*, "Ultrasound targeted microbubble destruction-triggered nitric oxide release via nanoscale ultrasound contrast agent for sensitizing chemoimmunotherapy," (in eng), *J Nanobiotechnology,* vol. 21, no. 1, p. 35, Jan 30 2023. doi: 10.1186/s12951-023-01776-8.

[63] Y. He *et al.*, "Improving the Therapeutic Effect of Ultrasound Combined With Microbubbles on Muscular Tumor Xenografts With Appropriate Acoustic Pressure," (in eng), *Front Pharmacol,* vol. 11, p. 1057, 2020. doi: 10.3389/fphar.2020.01057.

[64] K. Maeda and T. Colonius, "Bubble cloud dynamics in an ultrasound field," *Journal of Fluid Mechanics,* vol. 862, pp. 1105-1134, 2019. doi: 10.1017/jfm.2018.968.

CHAPTER 4. CONTROLLED HYPERTHERMIA WITH HIGH-INTENSITY FOCUSED ULTRASOUND AND ULTRASOUND CONTRAST AGENT MICROBUBBLES IN PORCINE LIVER[4]

Abstract

The objective of this work was to study microbubble-enhanced temperature elevation with high-intensity focused ultrasound (HIFU) at different acoustic pressures and under image guidance. The microbubbles were administered with either local or vascular injections (that mimic systemic injections) in perfused and non-perfused ex vivo porcine liver under ultrasound image guidance. Porcine liver was insonified for 30 s with a single-element HIFU transducer (0.9 MHz, 0.413 ms, 82% duty cycle, focal pressures of 0.6−3.5 MPa). Contrast microbubbles were injected either locally or through the vasculature. A needle thermocouple at the focus measured temperature elevation. Diagnostic ultrasound (Philips iU22, C5-1 probe) guided placement of the thermocouple and delivery of microbubbles and monitored the procedure in real time. At lower acoustic pressures (0.6 and 1.2 MPa) in non-perfused liver, inertial cavitation of the injected microbubbles led to greater temperatures at the focus compared with HIFU-only treatments. At higher pressures (2.4 and 3.5 MPa) native inertial cavitation in the tissue (without injecting microbubbles) resulted in temperature elevations similar to those after injecting microbubbles. The heated area was larger when using microbubbles at all pressures. In the presence of perfusion, only local injections provided a sufficiently high concentration of microbubbles necessary for significant temperature enhancement. Local injections of microbubbles provide a higher concentration of microbubbles in a smaller area, avoiding acoustic shadowing, and can lead to higher temperature elevation at lower pressures and increase the size of the heated area at all pressures.

[4] *This chapter has appeared as: Juang, EK., **De Koninck, LH**., Vuong, KS., Gnanaskandan, A., Hsiao, CT., Averkiou, MA. "Controlled hyperthermia with high-intensity focused ultrasound and ultrasound contrast agent microbubbles in porcine liver" Ultrasound Med. Biol., 49 (8), 1852-1860 (2023).*

4.1 INTRODUCTION

High-intensity focused ultrasound (HIFU) is an emerging therapeutic modality currently used for targeted ablation of benign tumors, such as uterine fibroids [1-3], and malignant tumors in the prostate [4-6], liver [7, 8], kidney [9], pancreas [9, 10], or bone [11]. The noninvasive nature of HIFU has also made it an attractive complement to conventional treatment options such as transarterial chemoembolization (TACE), where studies have reported improved short-term and long-term outcomes in patients with liver cancer when combining HIFU with TACE [12-18]. However, delivering sufficient acoustic energy through hard tissues (e.g., the skull or dense fibrous tissue) or anatomical barriers (e.g., intraabdominal fat) to the intended target has been a challenge that prevented HIFU from being more widely applicable [19]. For instance, the use of magnetic resonance-guided HIFU for the treatment of essential tremor requires high acoustic intensities to overcome the amount of sound that is absorbed or reflected by the skull [20]. This increase in acoustic energy input may be complicated by unwanted heat deposition outside the focus or intended target, potentially leading to burns in the skin and subcutaneous fat [21]. Therefore, there exists a need for a method to elevate temperature locally with HIFU at lower acoustic intensities without causing significant collateral damage.

The difficulties associated with accurate energy deposition can be mitigated by administering microbubbles during HIFU, which are conventionally used as ultrasound contrast agents (UCA). UCA are clinically approved for use in cardiology applications such as the assessment of coronary artery disease via left ventricular opacification in contrast echocardiography [22] and liver applications such as the evaluation of liver masses in both adult and pediatric patients [23-25]. While ultrasound imaging with UCA, commonly known as contrast-enhanced ultrasound (CEUS), does not increase the temperature of the surrounding tissue, several studies have explored the potential of heating enhancement when combining microbubbles (either exogenous UCA or microbubbles generated in situ due to cavitation) with HIFU, which operates at much higher focal intensities than CEUS. Holt and Roy [26] investigated cavitation-enhanced heating at various acoustic pressure amplitudes and insonation durations in two types of tissue-mimicking phantoms (i.e., polyvinyl alcohol and agar), using thermocouples to monitor temperature elevation at various distances away from the acoustic axis. While they did not introduce UCA in their work, they generated small bubbles in situ through acoustic cavitation and

observed a marked enhanced heating when the inertial cavitation threshold was exceeded. Later studies done by Tran et al. [27, 28] demonstrated that the injection of UCA microbubbles during HIFU can act as cavitation nuclei and lower the energy threshold for HIFU-based thermal ablation. Tung et al. [29] studied bubble-enhanced heating by embedding Definity microbubbles of various concentrations in polyacrylamide phantoms. They reported a reduction in required energy input for a fixed temperature elevation and an increase in the size and a shift of the location (proximal to the transducer focus) of thermal lesions. Clark et al. [30] further investigated the concentration-dependent effect of microbubble-enhanced heating using egg white gel phantoms with diluted UCAs and real-time ultrasound imaging. They suggested that sustained microbubble cavitation by way of an optimal combination of acoustic pressure input and microbubble concentration is the key to effective ultrasound heating. Interestingly, at high concentrations the diluted UCAs which are interspersed inside the egg white gel phantoms introduced nonlinear attenuation of pre-focal microbubbles that modified the HIFU pressure field through acoustic shadowing. These changes can make the temperature elevation and the location of thermal lesions unpredictable and complicate the use of HIFU. Administering microbubbles to a specific location in the phantom or tissue via local injection was suggested as a method to mitigate this issue, but it has not been investigated previously.

Although tissue-mimicking phantoms dosed with microbubbles offer a controlled environment to study HIFU, it is still a departure from the physiological environment of the human body where microbubbles travel with blood in the vasculature. The use of tissue models that are more representative of the human body, such as animal models or ex vivo perfused organs, is important for the study of HIFU-induced local hyperthermia. McDannold et al. [31] used contrast-enhanced magnetic resonance imaging to evaluate the effects of HIFU-microbubble combined heating and observed greater local energy absorption in rabbit brain tissue when compared with HIFU-only treatment. Yu et al. [32, 33] reported higher rates of HIFU-induced necrosis in rabbit and goat liver models when microbubbles were used. Hanajiri et al. [34] treated induced tumors in rat livers with HIFU and Levovist (Schering, Berlin) microbubbles and reported significantly greater tissue coagulation in the HIFU-microbubble treatment group when compared to HIFU-saline treatment. Kaneko et al. [35] also observed similar effects in a rabbit liver model. However, the aforementioned studies have not investigated the effect of microbubble concentration coupled with the acoustic pressure or the method of microbubble delivery (dilution, vascular/systemic or

local injections) and consequently any advantages of controlled bubble-enhanced heating remain unknown.

The goal of this work was to quantitatively assess local hyperthermia when using HIFU and commercial UCA microbubbles concurrently in non-perfused porcine liver and ex vivo machine-perfused porcine liver [36, 37]. The use of machine-perfused ex vivo porcine livers enabled us to study the effect of heat convection due to blood flow and perfusion. Special emphasis was placed on microbubble concentration and the method of delivery in relation to the acoustic pressure. Vascular injections that mimic systemic in vivo injections and local injections were considered. We investigated the extent of focal temperature elevation in porcine liver tissues as a result of HIFU application, with and without microbubbles, at different acoustic pressures and a range of temperature elevation including mild hyperthermia. Ultrasound-guidance via a clinical ultrasound scanner was used to direct HIFU to predetermined targets in the porcine liver tissue and align the thermocouple. Computer simulations were utilized to predict and validate the observed temperature elevation in perfused and non-perfused porcine liver when using HIFU alone.

4.2 METHODS

4.2.1 Experimental setup

The experimental setup consisted of a porcine liver (preparation described in a later section) partially submerged in a container filled with either degassed, deionized water or blood mimicking fluid (perfusate) (**Figure 4.1**). The liver was insonified from above using a single element focused transducer (H116; Sonic Concepts, Bothell, WA, USA) operating at 0.9 MHz. The transducer was mounted on a metal cage and attached to a manual 3-axis micro-positioner (Newport Corporation, Irvine, CA, USA). A custom 4-cm long acrylic coupling cone (C-101; Sonic Concepts) filled with degassed water was fitted to the HIFU transducer to couple it to the liver. The end of the cone has a thin elastic membrane and it was coupled to the liver with ultrasound gel. The purpose of the cone was to provide an adjustable offset between the transducer's surface and the entry plane since the liver sample was thinner than the actual focal length. The cone provides a fixed distance of degassed water to guide ultrasound to the sample and avoid any form of cavitation before entering the liver. Ultrasound pulses were generated with an arbitrary function generator (AFG3102C; Tektronix, Beaverton, OR, USA) and amplified by a linear power amplifier (2200L; Electronics & Innovation, Rochester, NY, USA), before being

transmitted by the transducer. HIFU was delivered as 372000 cycle pulses fired at a pulse repetition frequency of 2 Hz (82% duty cycle) for 30 seconds. The 2 Hz frame rate was selected to allow for interleaving of the HIFU exposure as described by Clark et al. [30] The focal acoustic pressures selected for our experiments were 0.63, 1.25, 2.50, and 3.75 MPa, as measured in water with a hydrophone. Each measurement was averaged 128 times and the peak-to-peak amplitude divided by 2 was recorded as the amplitude. Because of nonlinear propagation in the water, the peak positive and peak negative values for the aforementioned pressures were 0.67 and -0.59, 1.38 and -1.12, 3.0 and -2.0, 4.81 and -2.69 MPa, respectively. The uncertainty of the membrane hydrophone was 13%. Taking into consideration the liver tissue attenuation (see materials and methods) the in-situ pressures in the liver were estimated to be 0.6, 1.2, 2.4, and 3.5 MPa. As it was not possible to measure the in-situ pressures in the liver and most propagation takes place in the water-filled cone, we assume that the peak positive and negative values in situ would be analogous to those reported for water above. In-situ pressures are used in the rest of the manuscript and the figures. A C5-1 curved array transducer connected to a Philips iU-22 scanner (Philips

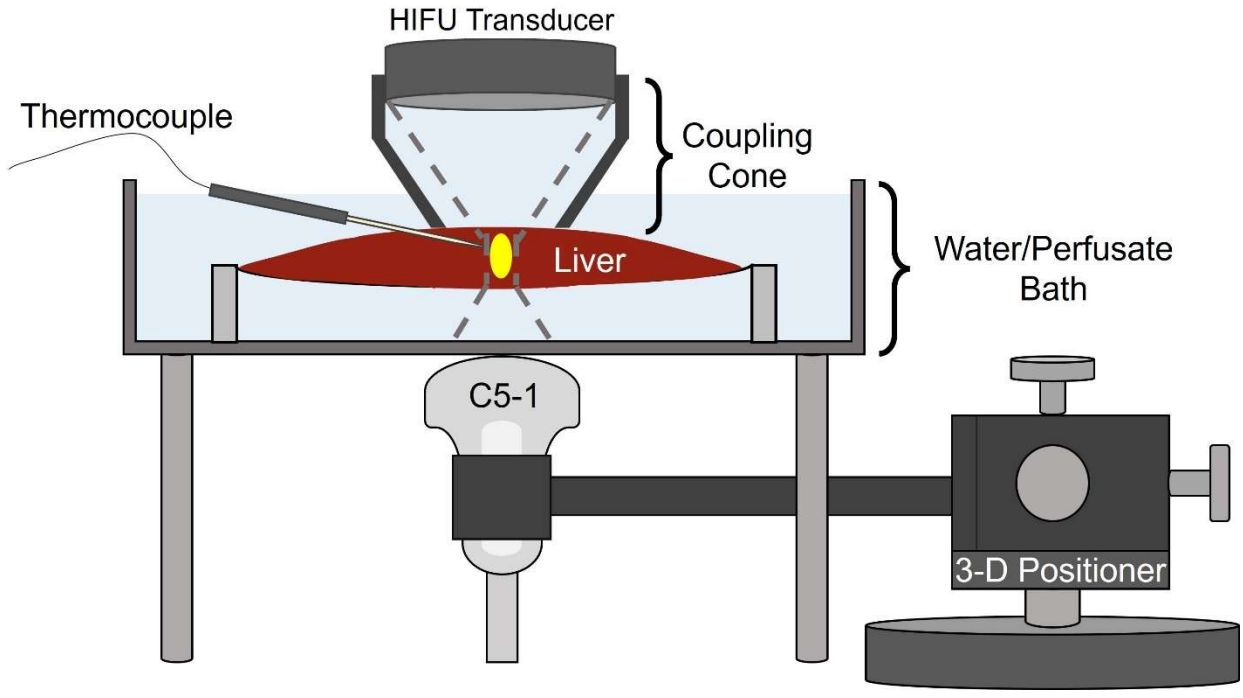

***Figure 4.1**: Experimental setup of HIFU treatment of ex vivo porcine liver.*

Experimental setup of high-intensity focused ultrasound (HIFU) treatment of ex vivo porcine liver. A three-axis micropositioner allows alignment of the imaging transducer (placed below the liver) with the HIFU transducer and thermocouple. A plastic cone filled with de-gassed water couples the transducer to the liver surface. The liver is submerged in perfusate liquid.

Healthcare, Bothell, WA, USA) was placed below the liver to provide real-time ultrasound images and to guide the placement of a thermocouple (MT-26/6HT; Physitemp Instruments, Clifton, NJ, USA) which is a needle microprobe. The needle thermocouple was positioned in the liver such that its tip was at the focus of the HIFU transducer. In addition to temperature measurements at the focus, we also measured the temperature at locations away from the focus by translating the HIFU transducer. The alignment procedure of the needle thermocouple with the HIFU transducer and the imaging plane is further described in a later section.

4.2.2 Acoustic pressure measurement

The transverse and axial pressure fields of the HIFU transducer were measured in an ultrasonic water tank with a 0.4 mm sensor diameter polyvinylidene fluoride membrane hydrophone (UT1604-225; Precision Acoustics, Dorchester, UK) calibrated in the 1-30 MHz range. Hydrophone measurements were compared with theoretical predictions based on the Rayleigh integral to find more accurate estimates of the transducer radius and focal length [30]. The focal depth and diameter were found to be 62.1 mm and 58.2 mm respectively. The half amplitude distances in the axial and transverse directions were ~15.8 and ~2.5 mm, respectively. We can model the focal volume as a prolate spheroid with the above half amplitude distances as its semi-axes:

$$V = \frac{4}{3}\pi\left(\frac{R}{2}\right)^2\left(\frac{Z}{2}\right), \tag{1}$$

where R and Z are the transverse and axial half amplitude distances respectively, resulting in an estimated volume, V, of 51.71 mm^3. To evaluate the influence, if any, of the C-101 coupling cone on the acoustic field, hydrophone measurements at the focus were taken with and without the cone attached and no differences were noted. Also, since the acoustic impedance of water and liver tissue are very similar, the reflection coefficient is 0.02 suggesting very little, if any, energy reflecting at the interface.

4.2.3 Liver tissue preparation

The sources of porcine livers used in this work include local commercial farms, slaughterhouses, and affiliated research groups that used porcine research models for other research purposes. Use of ex-vivo perfused livers in this study did not require an Institutional Animal Care and Use Committee approval, as verified by our academic institution. Our machine-

perfused porcine liver setup is a modified version of the procedure previously described [36, 38]. Briefly, a porcine liver was resected from a deceased pig with the portal vein and the hepatic artery largely preserved. The resection was completed within 30 minutes of the animal's death to limit ischemic necrosis as well as stenotic and thrombotic changes to the hepatic tissue, which would otherwise severely compromise the ex vivo perfusion of the liver in the laboratory. Once the liver is outside the body, the portal vein and hepatic artery of the liver were cannulated and flushed, first with 8 liters of lactated ringer's solution (6 liters at room temperature and 2 liters ice-cold) then with 3 liters of ice-cold histidine-tryptophan-ketoglutarate (HTK) solution (prepared in-house). Subsequently, the liver was submerged in 2 liters of HTK solution in static cold storage and transported back to the laboratory, where it was connected to a normothermic machine-perfusion system. The liver was then perfused with 8 liters of blood mimicking fluid that consisted of Powdered Williams Medium E (Sigma-Aldrich, St. Louis, MO, USA), sodium bicarbonate (Sigma-Aldrich, St. Louis, MO, USA), heparin (Fisher Scientific, Waltham, MA, USA), insulin (Lantus SoloStar Pen, Sanofi, Paris, France), and dexamethasone (Sigma-Aldrich, St. Louis, MO, USA). The liver was also supplied with 95% oxygen/5% carbon dioxide via an oxygenator (Affinity NT Oxygenation System; Medtronic, Dublin, Ireland) in a custom-made machine-perfusion system to maintain the viability of the liver. Two flowmeters (EW-32461-44 and EW-32460-40, Cole-Parmer) were used to regulate perfusion to the portal venous system and hepatic arterial system. Finally, the liver was submerged in blood mimicking fluid using the setup seen in **Figure 4.1**. For the non-perfused livers, we used untreated segments of the machine-perfused livers after they were removed from the machine-perfusion system.

4.2.4 Microbubble injection and temperature measurement

Alignment of the HIFU transducer and the needle thermocouple was done with ultrasound guidance by the method described by Keravnou et al. [38] (**Figure 4.2**). First, the needle thermocouple was inserted into a 19G needle, which acted as a sound-reflective sheath for identifying the location of the thermocouple as well as a stationary channel for local injections. This thermocouple-needle combination was then inserted into the porcine liver and spatially manipulated until maximal echogenicity was visualized on the iU-22 ultrasound scanner (**Figure 4.2**(a)). Visualization of the thermocouple-needle combination was possible due to incomplete linear signal cancellation in the nonlinear amplitude modulation mode [39] of the imaging probe. The HIFU transducer with the coupling cone was then placed on the liver tissue from above, and

the amplifier was activated while the function generator remained off. This produced a radio frequency interference signal (**Figure 4.2**b) in the ultrasound image where the focus of the HIFU beam could be visualized and aligned with the tip of the needle. The precision of the alignment technique is +/-0.5 mm. Another option for aligning the thermocouple was the use of small temperature increases with low amplitude exposures. However, this technique can still cause some microbubble disruption and we opted not to use it.

Sonazoid microbubbles (GE Healthcare, Amersham, UK) were introduced to the liver via local injections with a 19G needle at the HIFU focus (which is also at the tip of the thermocouple as previously described) or vascular injections (mimicking systemic in vivo injections) to the portal vein and hepatic artery also with a 19G needle and through an inline rubber port. When using local injections of microbubbles, the thermocouple was briefly removed from the guide needle and 0.05 ml of Sonazoid (estimated concentration: 2×10^8 MB/ml) was injected through the same guide needle directly in the tissue (not the vessels) in a similar method to how percutaneous ethanol injections are performed for clinically treating some liver tumors. The presence of the injected microbubbles was confirmed with the C5-1 imaging probe while scanning in contrast mode (**Figure 4.2**(c)). Contrast images were collected using a nonlinear technique (amplitude modulation at 1.7 MHz) at a low mechanical index (0.05) to avoid bubble destruction and in a contrast-side-by-side format with nonlinear imaging on one side and fundamental imaging on the other [39]. The thermocouple was immediately reinserted through the guide needle after the bubble

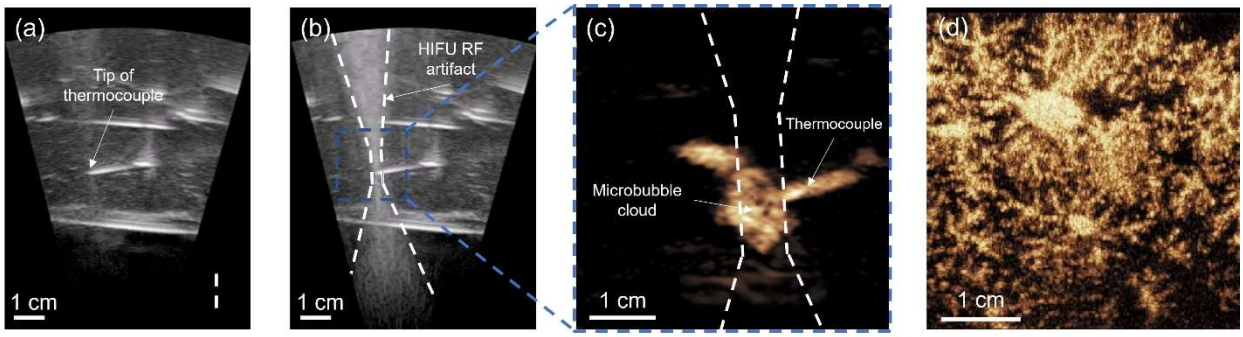

***Figure 4.2**: HIFU and thermocouple alignment.*

(a) B-mode (fundamental) images of the liver revealing placement of the thermocouple in the target area. (b) By use of a radiofrequency (RF) artifact, the focus of the high-intensity focused ultrasound (HIFU) transducer is shown in the liver image and aids the placement of the tip of the thermocouple at the focus. (c) Contrast image of the liver revealing microbubbles after a local injection collecting at the tip of the thermocouple. (d) Contrast image of the liver revealing the vessel structure of a liver area after a systemic microbubble injection in a perfused pig liver.

injection. Realignment was performed where necessary. When using vascular/systemic injections of microbubbles, simultaneous injections of 0.3 ml of Sonazoid into the portal vein and/or hepatic artery were performed. The microbubbles then flow to the area of interest with the blood flow in the same way that systemic intravenous injections arrive in the liver of patients. The time between injection of the microbubbles and the arrival at the site of interest, as confirmed with contrast imaging (**Figure 4.2**(d)), was about 30 seconds.

The sequences of HIFU application were identical regardless of local or vascular/systemic injection of the microbubbles. First, baseline temperature measurements at the HIFU focus were recorded prior to HIFU application. All experiments took place at room temperature, 23 ℃. Previous studies have shown that microbubble response at room temperature has only slight differences to responses at body temperature (37 ℃) and can be offset by using slightly higher concentrations [40]. After HIFU was switched on, focal temperature measurements were recorded. To make off-axis temperature measurements, the 3-axis micropositioner was used to adjust the lateral position of the HIFU transducer while the thermocouple remained fixed.

4.2.5 Bioheat simulations

Temperature elevation is defined as $\Delta T = T - T_0$, where T and T_0 are the current and initial temperatures, respectively. In the absence of microbubbles, ΔT was modeled using the bioheat transfer equation described by Pennes [41]. The bioheat equation is a linear parabolic heat equation that assumes tissue can be modeled as a continuum, where heating effects from vessels are uniformly accounted for to avoid localized inhomogeneities. The equation addresses two mechanisms of heat transfer in the body: conduction within the tissue, and convection due to blood flow and three methods of heat generation: absorption of energy, blood perfusion, and metabolic activity. In this study, we are using ex-vivo tissue, so we ignore the metabolic energy term in the equation. To address both tissue types, we used the following bioheat equation to predict change in temperature per unit volume:

$$\rho c_p \frac{\partial T}{\partial t} = \kappa \nabla^2 T + Q + Q_p, \tag{2}$$

where ρ is the density of the medium (water: 1000, liver: 1060 kg m^{-3}), c_p is the specific heat capacity of the medium (water: 4180, non-perfused liver: 3500 J $kg^{-1}K^{-1}$, perfused liver: 3500 J $kg^{-1}K^{-1}$), κ is the thermal conductivity of the medium (water: 0.610, liver: 0.534 W $m^{-1}K^{-1}$), and T

represents temperature in degrees Kelvin (K). The final two terms, Q and Q_p, are the rate of heat generation from the acoustic field and the rate of heat transfer due to blood perfusion per unit volume, respectively. For monochromatic sound waves, the rate of energy generation per unit volume in tissue can be expressed as:

$$Q = 2\alpha I, \tag{3}$$

where α is the absorption coefficient of the medium (water: 0.025, non-perfused liver: 8.19 Np m^{-1} MHz^{-1}, perfused liver: 4 Np m^{-1} MHz^{-1}), and I (Pa^2) is the intensity of the radiated waves. Since this equation assumes monochromatic waves, it does not apply when there is nonlinear propagation and harmonic generation. For the higher pressures used in the present work there may be some nonlinear distortion that was not modeled with our theoretical simulations since we assumed monochromatic waves at the amplitudes that we have measured in water and then derated for tissue attenuation. The transfer of thermal energy from blood flow per unit volume is given as:

$$Q_p = c_B W_B (T - T_B), \tag{4}$$

where c_B, W_B, and T_B are the specific heat capacity (3770 J $kg^{-1}K^{-1}$), perfusion rate (kg $m^{-3}s^{-1}$) and ambient temperature (K) of blood respectively [42]. In this study, the perfusate solution flowed through the machine-perfused model mimics the properties of blood and was maintained at room temperature such that T_B ~23℃. Since the rate of perfusion was limited by the flow rate of the machine-perfusion system, the perfusion rate was estimated from an average flow rate of 200 mL min^{-1} for 10 L of perfusate with density 1060 kg m^{-3} to yield $W_B = 0.3533$ kg $m^{-3}s^{-1}$. For modeling machine-perfused tissue, all terms are used to predict temperature, while non-perfused modeling sets $Q_p = 0$.

4.3 RESULTS

4.3.1 Non-perfused ex vivo tissue

The measured change in focal temperature (ΔT) in non-perfused ex-vivo liver tissue (N = 8) as a function of time for different pressures is shown in **Figure 4.3**. The blue curves show the measured (dashed line) and simulated (dotted line) ΔT in the absence of microbubbles. The green lines show ΔT when microbubbles are used. The shaded regions represent one standard deviation.

At low pressures, 0.6 MPa (**Figure 4.3**(a)) and 1.2 MPa (**Figure 4.3**(b)), with no microbubbles injected there is a gradual temperature increase when HIFU is active from 10 s to 40 s, followed by a gradual temperature decrease as the liver tissue cools. Measurements and simulations are in good agreement at these low pressures. When microbubbles are introduced at these pressures, two prominent indicators of tissue heating are seen: an initial rapid temperature rise within the first second of HIFU activation, and a significant difference in peak temperature compared to HIFU-only treatments. At 0.6 MPa there was a 3.5℃ increase in ΔT during the first second of heating and a 7℃ difference in peak ΔT. The same trend with an initial 4.9℃ ΔT increase during the first second of heating and a 12℃ difference in peak ΔT was observed at 1.2 MPa. However, at higher pressures, 2.4 MPa (**Figure 4.3**(c)) and 3.5 MPa (**Figure 4.3**(d)), we see that the temperature profiles with or without microbubbles are similar. This result was assumed to be due to cavitation of residual air micro pockets in the liver tissue, an effect confirmed with imaging during the procedure. At these higher pressures, cavitation is nucleated in both cases, either from UCAs or

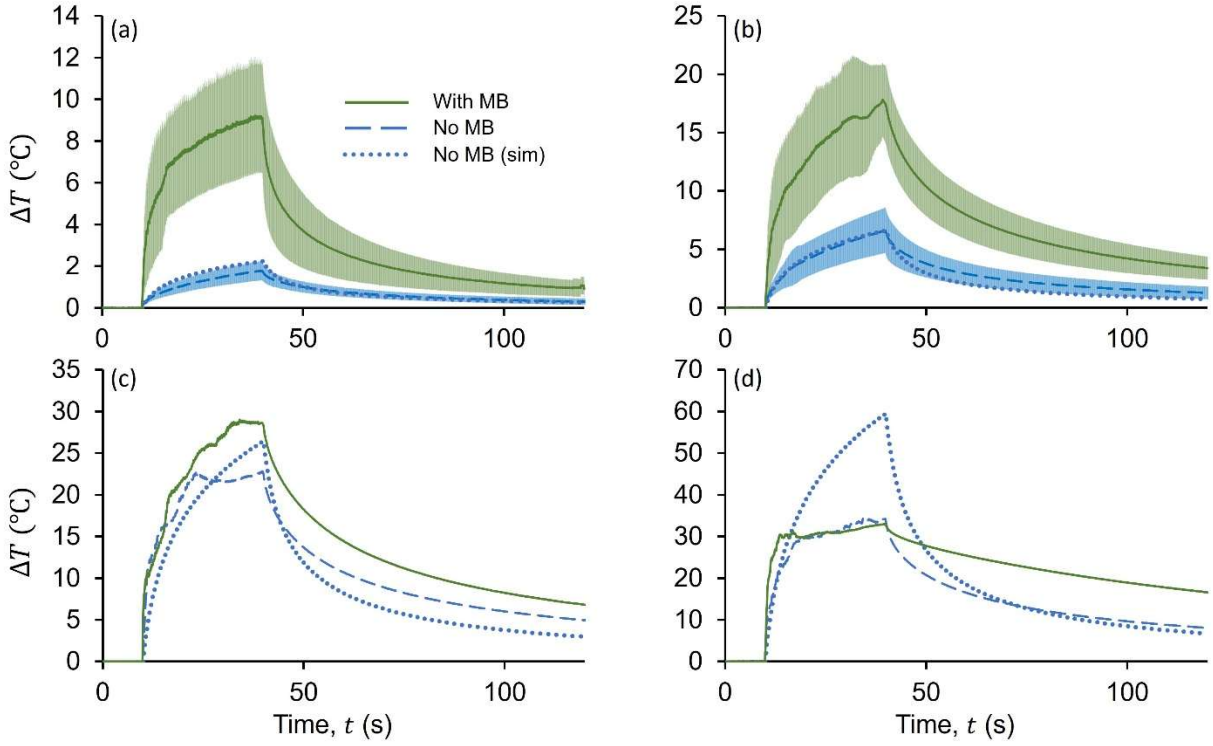

***Figure 4.3**: Temperature elevation in non-perfused liver tissue.*

Measured and simulated temperature elevation (ΔT) with and without microbubbles during 30 s of high-intensity focused ultrasound (HIFU) exposure and 80 s after exposure at four focal acoustic pressures: (a) 0.6 MPa, (b) 1.2 MPa, (c) 2.4 MPa, and (d) 3.55 MPa. Shaded areas indicate one standard deviation. MB, microbubbles; sim, simulation.

trapped gas pockets in the tissue, and we observe similar ΔT regardless of whether microbubbles had been injected. For clarity, the shaded region representing a standard deviation has been removed from the higher pressures since error behavior was consistent with the corresponding shaded regions of the lower pressures. Simulations of HIFU with no microbubbles at these higher pressures (2.4 and 3.5 MPa) show a similar or slower temperature rise compared to our measurements. Interestingly, the cooling behavior at 3.5 MPa was much slower with microbubbles than without. One reason for this might be the irregular shape of the UCA bolus (see for example **Figure 4.2**(c)) which may have caused the place of the maximum heating to take place slightly away from the tip of the thermocouple. The slow cooling may also be attributed to a larger area being heated and requiring a longer time to cool down. These two points will be further discussed in the next section.

The ΔT for all pressures is further summarized in **Figure 4.4**(a), which shows the peak measured focal ΔT at each non-derated (water) focal pressure in the presence and in the absence of microbubbles. The temperature gain due to microbubbles is the difference between the green (with bubbles) and the blue (without bubbles) lines. At lower pressures (0.6 and 1.2 MPa) there is a greater temperature gain, and at higher pressures this effect is reduced mainly due to cavitation in the tissue due to air pockets and other native cavitation nuclei. At the highest pressure setting (3.5 MPa) the maximum ΔT was the same with and without microbubbles. Native cavitation also increased the variability of peak temperature measurements at higher pressures, shown by larger error bars at 2.4 and 3.5 MPa. Another time of interest was 35 s after heating had concluded (at 75

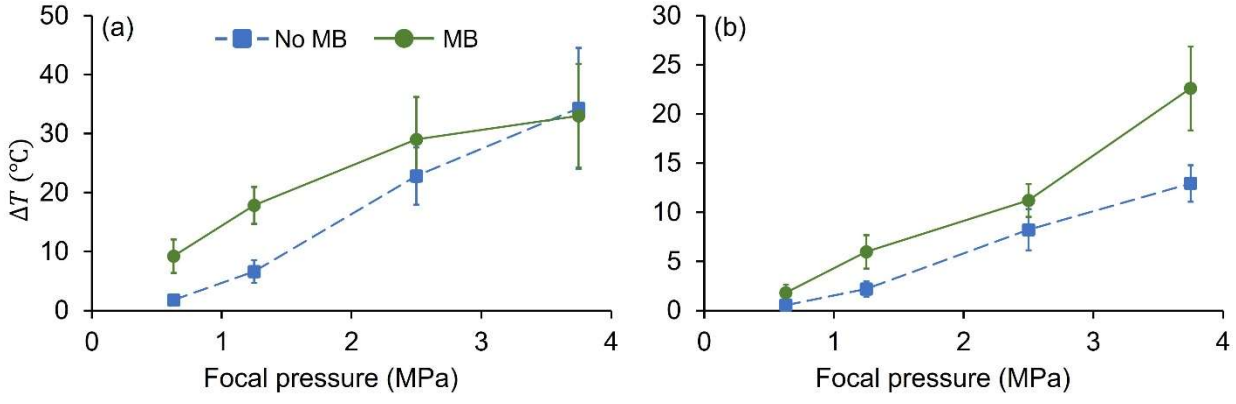

***Figure 4.4**: Temperature elevation during heating and cooling of tissue.*

Measured temperature elevation as a function of acoustic pressure (a) after 30 s of heating and (b) 35 s after end of heating. Error bars indicate one standard deviation.

s total time according to **Figure 4.3**) to investigate the cooling of the medium and is shown in **Figure 4.4**(b). ΔT was consistently greater at this time point for all focal pressures when microbubbles were injected in the tissue (the green line is above the blue line), and it continued to increase with increasing focal pressure. Given the ΔT saturation observed in **Figure 4.4**(a) at 3.5MPa and the increased retention of heat for all focal pressures with microbubbles in **Figure 4.4**(b), heating with microbubbles leads to similar temperature but slower cooling rates compared to HIFU-only, which in turn suggests a larger heated area has been formed at higher pressures (2.5, 3.5 MPa). The heated area is defined as the area where the temperature during HIFU exposure is greater than half the maximum temperature reached. A positive outcome from using microbubbles is when the relative ΔT with injected microbubbles is greater than the ΔT without microbubbles and/or the heated area with microbubbles is greater than the heated area without microbubbles. The results for 3.5 MPa will be further discussed in the next section.

In **Figure 4.5** we show ΔT with (green) and without (blue dashed) microbubbles measured at 1 mm radially away from the axis at the focus for all the pressures considered. At this location,

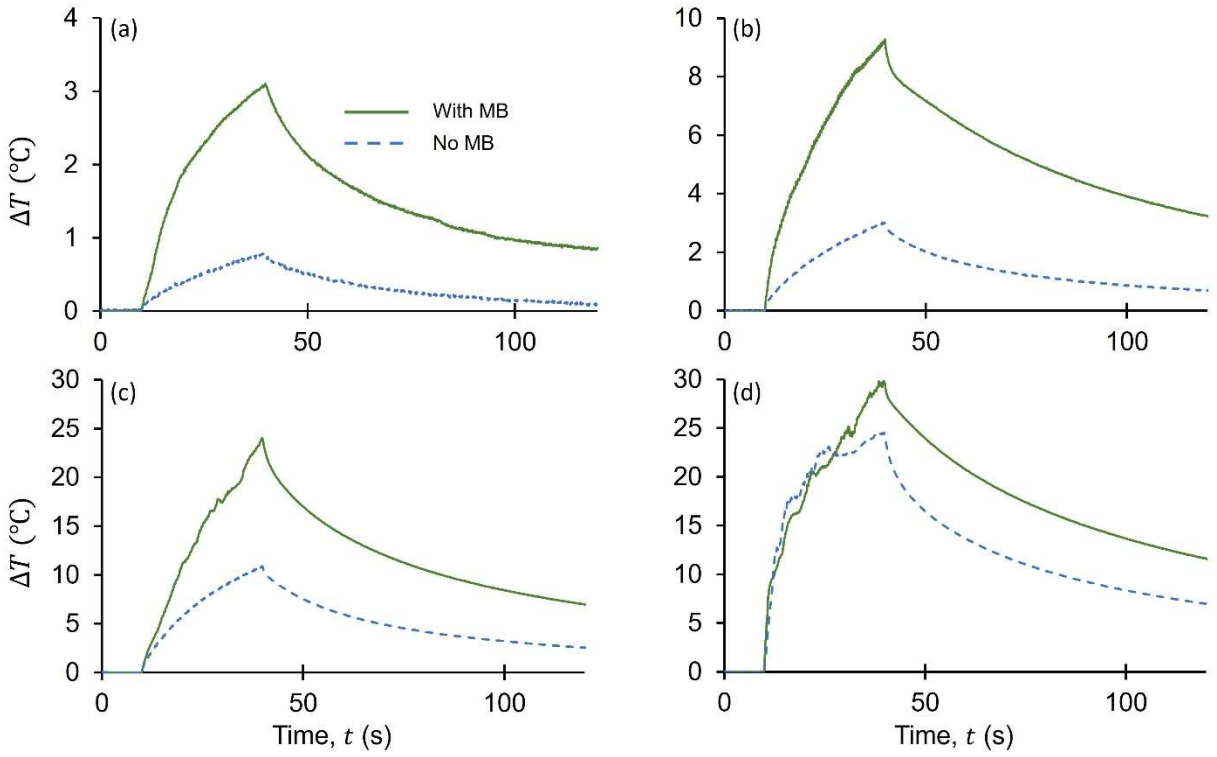

***Figure 4.5**: Temperature elevation 1 mm off axis in non-perfused tissue.*

Measured temperature elevation 1 mm radially off axis with and without microbubbles for four non-derated focal pressures: (a) 0.6 MPa, (b) 1.2 MPa, (c) 2.4 MPa, and (d) 3.5 MPa.

the measurements show significant ΔT enhancement when using microbubbles at all pressures. Native cavitation described above that reduced the temperature enhancement at the higher pressures on axis (**Figure 4.3**(c) and **Figure 4.3**(d)) is less pronounced off axis. To be able to clearly distinguish the differences between the curves, we did not include a shaded region representing a standard deviation. The recorded standard deviation was similar to that of the axial measurements in **Figure 4.3** and **Figure 4.4**.

4.3.2 Machine-perfused tissue

In **Figure 4.6**, ΔT measurements and predictions from Eq. (2) in both perfused and non-perfused liver when not using microbubbles at an acoustic pressure of 1.2 MPa are shown to evaluate the effect of blood flow and perfusion. Measurements were repeated 6 times, and the shaded area shows the standard deviation (spread of our measurements). The use of machine perfusion (physiological flow in the liver) adds convection due to the flow, also modeled by Eq. (2). For the same acoustic input energy, ΔT in the machine-perfused liver was lower compared to that of the non-perfused liver. Tissue cooling was faster in machine-perfused liver once HIFU is turned off. Heat was dissipated by the circulating perfusate which acted as a heat sink due to its larger volume and lower relative temperature. Our simulations with perfusion mostly agree with

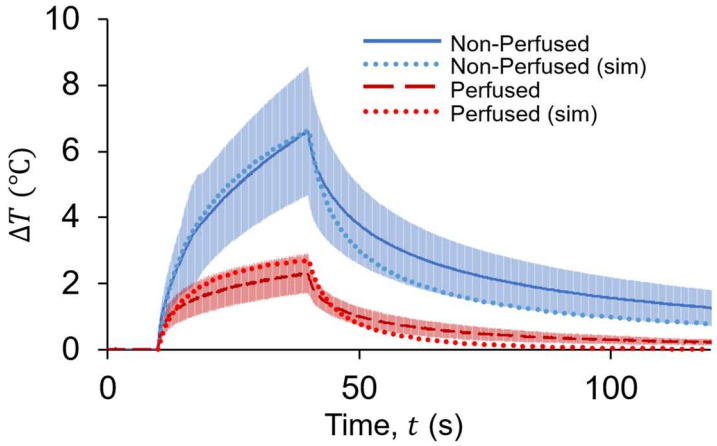

***Figure 4.6**: Comparison of temperature elevation in perfused and non-perfused tissue.*

Focal temperature elevation (ΔT) in perfused and non-perfused porcine liver with no microbubbles at an acoustic pressure of 1.2 MPa (non-derated). Solid and dashed lines represent average measured temperature of perfused and non-perfused liver respectively, with a shaded region indicating one standard deviation. The dotted lines represent predicted focal temperatures in perfused and non-perfused liver with no microbubbles. sim, simulation.

the measured data but predict a faster cooling rate which may indicate a reduced quality of expected perfusion in the ex-vivo experiments.

In **Figure 4.7**, we show ΔT in a perfused liver (N = 4) with and without microbubbles supplied either systemically (injected into the main feeding vessels) or locally (injected directly at the focus under image guidance) at pressures 1.2 (**Figure 4.7**(a)) and 2.4 MPa (**Figure 4.7**(b)). Again, the shaded areas have been removed for clarity, with error trends with and without microbubbles established in **Figure 4.3** and **Figure 4.6**, respectively. A prediction of ΔT in the perfused liver without microbubbles (dotted red line) was also included for both pressures. At the lowest pressure (0.6 MPa, not shown here) there was no ΔT due to perfusion-related heat dissipation. At the highest pressure (3.5 MPa, also not shown here) intense cavitation activity confirmed with imaging resulted in no ΔT difference between using and not using microbubbles. At pressures 1.2 MPa (**Figure 4.7**(a)) and 2.4 MPa (**Figure 4.7**(b)) we observe that the local injections result in markedly higher ΔT as seen previously with the non-perfused liver. Vascular/systemic injections led to similar ΔT to that observed without microbubbles at both pressures. Like the non-perfused liver temperature measurements in **Figure 4.3**, local injections in **Figure 4.7** show a temperature profile at 1.2 MPa with a steep initial slope followed by a smooth temperature increase. At 2.4 MPa the local injection temperature profile has an even steeper initial

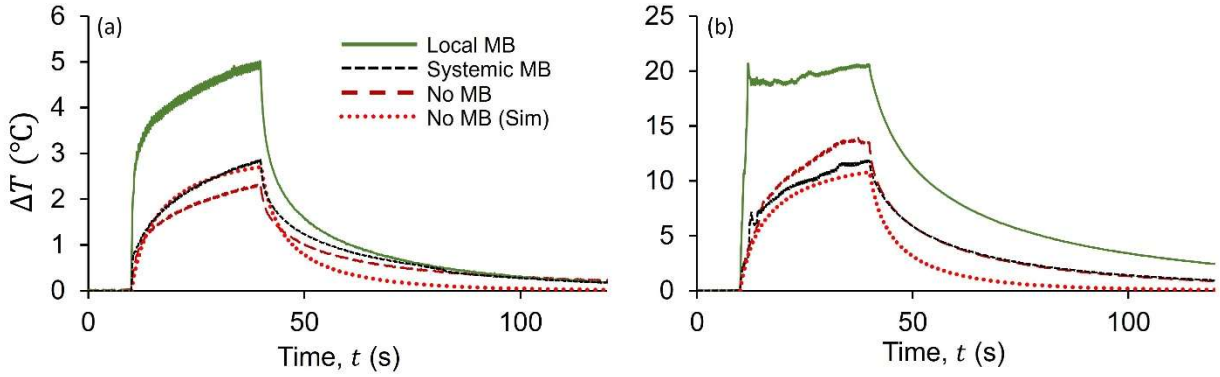

***Figure 4.7**: Temperature elevation during local vs systemic microbubble injection.*

Measured focal temperature elevation (ΔT) in machine-perfused porcine liver with and without microbubbles (MB) for two focal pressures: (a) 1.2 MPa, (b) 2.4 MPa. Two microbubble delivery methods were used: local injection (solid line) and systemic injection (short dash line). Theoretical predictions of focal temperature elevation in perfused porcine with no microbubbles are represented as dotted lines. MB, microbubbles; sim, simulation.

slope followed by temperature saturation due to excessive cavitation. In summary, at these pressures there is a significant heating enhancement only with local injections.

4.4 DISCUSSION

The objective of this work was to investigate temperature elevation with HIFU (noting that HIFU does not always imply thermal ablation) in the presence of UCA microbubbles in an ex-vivo porcine liver, with and without machine perfusion, which we consider to be very close to the physiologic environment in human tissue. The use of machine perfusion allowed for the evaluation of the effect of blood flow and perfusion on heat transfer in the liver. We compared HIFU with local microbubble injections at the focal region to HIFU with vascular/systemic microbubble injections via the portal vein and/or hepatic artery in terms of tissue ΔT they induce. Heating enhancement was confirmed with needle thermocouple measurements (a) at the focus and 1 mm laterally away from the focus after 30 s of heating, and (b) 35 s after turning off HIFU and while the tissue was cooling down.

Our results showed that, in both perfused and non-perfused porcine livers, HIFU with local microbubble injections led to greater tissue temperature elevation (ΔT) relative to HIFU-only treatment. In contrast, HIFU with systemic microbubble injections caused little to no enhancement in tissue temperature elevation compared to HIFU without microbubbles. We attribute this result to a need for a high concentration of microbubbles at the target area of the HIFU treatment but not everywhere else in the path of the beam. Clark et al. [30] reported a similar observation. They varied the concentration of uniformly diluted microbubbles in an egg white phantom and studied its effects on temperature elevation and lesion formation after HIFU exposure. They found that as the microbubble concentration increased the heating enhancement from microbubbles also increased. However, since the microbubbles were evenly diluted throughout the phantom, their highest microbubble concentrations led to excess attenuation (acoustic shadowing) along the path of ultrasound. This shadowing shifted the maximum temperature and the treatment area away from their thermocouple and closer to the HIFU transducer. They used both optical images and pre-focal temperature measurements to confirm the shift of the heated area. In our study, local injections of microbubbles provided sufficient concentration only around the focal area, and led to significant heating enhancement without encountering acoustic shadowing and the shift of the heated area observed by Clark et al. [30] as there are no microbubbles along the HIFU beam path

to attenuate the sound. In our study, although vascular/systemic injections utilized a larger initial concentration of microbubbles compared to local injections, these microbubbles were diluted and distributed throughout the porcine liver vasculatures, resulting in low effective microbubble concentrations at the treatment site. In addition, the quality of perfusion in the ex-vivo livers was moderate and some areas were not fully perfused. Compromised perfusion in some tissue areas further reduced the number of available microbubbles for heating enhancement when using systemic injections. We suspect that these are the most prominent factors that led to the lack of enhanced tissue temperature elevation in HIFU with systemic microbubble injections. While it may still be possible to enhance the heating with systemic injections of microbubbles in a more perfused tissue, we suspect that the higher concentrations of microbubbles will introduce acoustic shadowing as it was also observed in a previous study [30]. As such, we hypothesize that, in order to enhance heat deposition with HIFU with systemic administration of microbubbles, a fine balance must be struck between delivering sufficient microbubbles to the treatment site while preventing acoustic shadowing. An added complication is that the acoustic shadowing due to high microbubble concentration is also amplitude-dependent [43, 44].

Our experimental results indicated that the acoustic pressure amplitude plays an important role. The ΔT increase at the focus resulting from the use of microbubbles was more pronounced at the two lower pressures (0.6 and 1.2 MPa) than the two higher pressures (2.4-3.5 MPa). However, there was overall heating enhancement at all pressures as confirmed with the focal temperatures during the cooling process (**Figure 4.4**(b)) and the off-axis measurements (**Figure 4.5**) which also suggest an increase of the heated area. The increased cavitation activity around the focus (with injected UCAs or due to native cavitation in tissue at higher pressures) can scatter the ultrasound in the neighboring tissue and increase the heated area.

We attribute the heating enhancement due to microbubbles to two kinds of cavitation activity: cavitation of the injected UCA microbubbles and native cavitation within the medium without injecting microbubbles. Keller et al. [45] have previously studied cavitation of microbubbles, specifically the inertial cavitation threshold (evidenced by the onset of broadband noise in scattered frequency spectrum) of various clinical microbubbles. For Sonazoid which we used in the present study, they found its cavitation threshold to be approximately 0.3 MPa in a water tank where microbubbles were able to freely move. We suspect that in a physiological

environment such as our porcine liver models, where Sonazoid microbubbles are spatially confined, the cavitation threshold is likely to be at a higher acoustic pressure. Using Sonazoid diluted in egg white gel phantoms, Clark et al. [30] found that sustained microbubble activity, which was assumed to be inertial cavitation, occurred above a critical pressure threshold of 0.5 MPa. Given the similar HIFU source and acoustic pressures, we can assume that cavitation of microbubbles observed in this work was inertial at all focal pressures (0.6-3.5 MPa). Holt and Roy [26] studied native cavitation with microbubbles generated in situ in agar phantoms and found that surpassing the inertial cavitation threshold of these media led to enhanced focal temperatures. For longer pulse durations like the 30 s heating of this study, they found an inertial cavitation threshold of ~2 MPa, considerably larger than the threshold of clinical microbubbles. At these pressure settings, temperature measurements deviate from the bioheat equation when cavitation is not included in the model and exhibit a greater heating rate. Holt and Roy also noted a saturation of peak temperature as acoustic pressure increased beyond the inertial cavitation threshold, which they attributed to bubbles shielding the focal area by scattering the acoustic wave and diffusing energy deposition. Although we did not directly measure inertial cavitation in this study, our temperature elevation measurements and the points raised above suggest that inertial cavitation was likely present in all the conditions evaluated. Specifically, the temperature measurements for higher focal pressures (2.4 and 3.5 MPa) in the absence of UCA microbubbles (**Figure 4.3**(c) and **Figure 4.3**(d)), where both pressure settings led to temperature saturation and a similar or greater heating rate in the experiment compared to what simulations predicted, suggesting that inertial cavitation of the residual air micropockets and other cavitation nuclei within the liver occurs. Therefore, when UCA microbubbles are present, the two lower pressures (0.6 and 1.2 MPa) are above the inertial cavitation range of the UCA microbubbles but below the inertial cavitation threshold of residual air pockets in the medium. We refer to this pressure range as “controlled” bubble-enhanced heating. This is shown in **Figure 4.4**(a) for 0.6 and 1.2 MPa where cavitation of the UCA microbubbles leads to significant ΔT enhancement. However, as pressure increases (e.g., 2.4 and 3.5 MPa) beyond the inertial cavitation threshold of both the injected UCA microbubbles and residual air micropockets in the medium, intense cavitation shields the focal area from further energy deposition and ΔT reaches a plateau. We refer to this pressure range as “uncontrolled” bubble-enhanced heating. There is still some added benefit from using UCA microbubbles even at

these higher pressures evidenced by the tissue temperature during cooling (**Figure 4.4**(b)) and the off-axis measurements (**Figure 4.5**).

One main limitation of this work was the accuracy of our needle thermocouple alignment, especially with microbubbles present. Another thermocouple-related limitation was that we were only able to measure the temperature at one point in space at a time. Although done under image guidance, the needle thermocouple was inserted by hand and had an estimated placement accuracy of 0.5 mm. The inaccuracy in placement is due largely to microbubbles obscuring the tip of the thermocouple, as seen in **Figure 4.2**(c). As our thermocouple was initially aligned to the focus of the HIFU transducer, reinsertion of the thermocouple tip following microbubble injection may have caused it to shift away from the presumed HIFU focus per alignment. The irregular bolus shape of the microbubble cloud in **Figure 4.2**(c) may have also resulted in the ΔT saturation (green line plateaus at 3.5 MPa in **Figure 4.3**(d)). At this high pressure, the microbubble cloud shape caused the maximum temperature elevation to occur slightly in front of the thermocouple. Thus, the actual maximum temperature in the tissue would likely have been much higher than 70 degrees and this would explain the much slower cooling rate observed. Given our setup, it was also not possible to align our thermocouple parallel to the acoustic axis (to limit the viscous heating artifact) as suggested by Holt and Roy [26] and also discussed in depth by Morris et al. [46] As stated in the Morris et al. work, needle thermocouples (the type of thermocouple we used) generate less viscous heating artifact or there is a second systematic effect, likely to be thermal conduction along the wire, which acts to reduce the effect of this heating. Also, our temperature measurements without microbubbles were in good agreement with our simulations, indicating that the viscous heating artifact did not significantly impact our measurements. Yet another limitation to our study is the use of only one thermocouple to take temperature measurements, which compromised our ability to directly probe the full size of heated area created. This could be alleviated by using volumetric temperature measurement techniques such as thermal camera imaging [47] and magnetic resonance temperature measurements [48]. However, these potential workarounds introduce new challenges such as thermal imaging being limited to surface measurements and magnetic resonance having lower spatial and temporal resolution besides from being very costly and introducing compatibility complexities. Despite the aforementioned limitations to utilizing a thermocouple, our approach proved to be simple and effective and to provide reliable temperature elevation measurements in tissue in the presence of microbubbles.

The clinical applicability of our findings is left to be determined due to the reliance on local injections of microbubbles as a means of enhancing temperature rise in a small target area. While local injections are not a clinically approved method for UCA administration (only intravenous injection which we have been referring to as systemic is allowed), there have been research works reported where local microbubble injections in-vivo were used [49].

It still seems possible that systemic injections can significantly enhance the heating during HIFU in vivo only if an adequately high concentration of microbubbles is successfully delivered to the target area. Treatment of hypervascular tumors (not only for ablation but also for mild hyperthermia for enhanced drug delivery) may be a suitable target application for microbubble-enhanced HIFU. One example is hepatocellular carcinoma, which is a primary liver malignancy characterized by an early hypervascular arterial enhancement relative to the normal liver parenchyma in CEUS scans [50]. This could indicate an early diversion of blood flow to the tumor, which would increase microbubble concentration in the tumor and enhance heating during HIFU. Pending further investigation, a possibility remains that the microbubble concentration in vivo would not reach the optimal level required for significant heating enhancement with HIFU. The option to perform local bubble injections in a manner similar to that used to perform percutaneous ethanol injections clinically performed is still available and according to the work presented here might lead to more efficient local heating. Although in vivo work presents many new challenges, the insights into microbubble-enhanced heating from our work here may provide useful initial guidance towards the development and success of such treatments.

The methods proposed with the present work are not specifically targeted to HIFU ablation; they could be also utilized for drug uptake enhancement with local mild hyperthermia where a temperature elevation of 5-10 ℃ is required. This would allow for a larger treatment area and transducers with lower focusing gains operating at of lower amplitudes than HIFU ablation. Ultrasound cavitation treatments for enhanced drug delivery [38, 51] that use long ultrasound pulses could be modified to deliver higher intensities (not necessarily amplitudes) and thus combine mechanical and thermal effects for treating the tumor microenvironment. We envision such a technique to be performed with either a few intravenous boluses or multiple small local injections of microbubbles and the treatment procedure to last 10-20 min. It may also be possible that a clinical imaging transducer could generate these conditions.

4.5 CONCLUSION

In this study we showed that adjunctive use of HIFU with UCA microbubbles can lead to greater temperature elevations compared to HIFU alone. We identified the acoustic pressure and the microbubble concentration as the two important parameters. In non-perfused porcine liver, low acoustic pressures (< 2 MPa) with local injections of microbubbles led to greater temperature elevation at the focus than when no microbubbles were used. Higher pressures (>2 MPa) produced cavitation in the tissue even without injecting microbubbles and offered reduced gain in focal temperature elevation when injecting microbubbles. At all pressures the heated area was larger when microbubbles were injected.

In the perfused porcine liver where blood flow affects heat dissipation, we observed that only local injections of microbubbles had a sufficient microbubble concentration to enhance the heating during HIFU. There is a threshold microbubble concentration required for enhanced heating that the systemic injections were unable to provide. Overall, local injections of microbubbles can induce temperature increase and heated area enhancement in HIFU treatments.

4.6 REFERENCES

[1] H. S. Kim, J.-H. Baik, L. D. Pham, and M. A. Jacobs, "MR-guided high-intensity focused ultrasound treatment for symptomatic uterine leiomyomata: long-term outcomes," *Academic radiology,* vol. 18, no. 8, pp. 970-976, 2011.

[2] M. Z. Mahmoud, M. Alkhorayef, K. S. Alzimami, M. S. Aljuhani, and A. Sulieman, "High-intensity focused ultrasound (HIFU) in uterine fibroid treatment: review study," *Polish journal of radiology,* vol. 79, p. 384, 2014. doi: 10.12659/PJR.891110.

[3] I. M. Verpalen *et al.*, "The Focused Ultrasound Myoma Outcome Study (FUMOS); a retrospective cohort study on long-term outcomes of MR-HIFU therapy," *European Radiology,* vol. 30, no. 5, pp. 2473-2482, 2020/05/01 2020. doi: 10.1007/s00330-019-06641-7.

[4] L. Poissonnier *et al.*, "Control of prostate cancer by transrectal HIFU in 227 patients," *European urology,* vol. 51, no. 2, pp. 381-387, 2007.

[5] S. Crouzet, F. J. Murat, G. Pasticier, P. Cassier, J. Y. Chapelon, and A. Gelet, "High intensity focused ultrasound (HIFU) for prostate cancer: current clinical status, outcomes and future perspectives," *International Journal of Hyperthermia,* vol. 26, no. 8, pp. 796-803, 2010. doi: 10.3109/02656736.2010.498803.

[6] A. Stabile *et al.*, "Medium-term oncological outcomes in a large cohort of men treated with either focal or hemi-ablation using high-intensity focused ultrasonography for primary localized prostate cancer," *BJU International,* vol. 124, no. 3, pp. 431-440, 2019. doi: 10.1111/bju.14710.

[7] C.-X. Li *et al.*, "Analysis of clinical effect of high-intensity focused ultrasound on liver cancer," *World Journal of Gastroenterology,* vol. 10, no. 15, p. 2201, 2004. doi: 10.3748/wjg.v10.i15.2201.

[8] J. Kennedy *et al.*, "High-intensity focused ultrasound for the treatment of liver tumours," *Ultrasonics,* vol. 42, no. 1-9, pp. 931-935, 2004.

[9] F. Wu *et al.*, "Extracorporeal focused ultrasound surgery for treatment of human solid carcinomas: early Chinese clinical experience," *Ultrasound in Medicine & Biology,* vol. 30, no. 2, pp. 245-260, 2004/02/01/ 2004. doi: 10.1016/j.ultrasmedbio.2003.10.010.

[10] T. D. Khokhlova and J. H. Hwang, "HIFU for Palliative Treatment of Pancreatic Cancer," in *Therapeutic Ultrasound*, J.-M. Escoffre and A. Bouakaz, Eds. Cham: Springer International Publishing, 2016, pp. 83-95.

[11] W. Chen *et al.*, "Primary bone malignancy: effective treatment with high-intensity focused ultrasound ablation," *Radiology,* vol. 255, no. 3, p. 967, 2010. doi: 10.1148/radiol.1009037.

[12] F. Wu *et al.*, "Advanced Hepatocellular Carcinoma: Treatment with High-Intensity Focused Ultrasound Ablation Combined with Transcatheter Arterial Embolization," *Radiology,* vol. 235, no. 2, pp. 659-667, 2005. doi: 10.1148/radiol.2352030916.

[13] C. Li, W. Zhang, R. Zhang, L. Zhang, P. Wu, and F. Zhang, "Therapeutic effects and prognostic factors in high-intensity focused ultrasound combined with chemoembolisation for larger hepatocellular carcinoma," *European journal of cancer,* vol. 46, no. 13, pp. 2513-2521, 2010. doi: 10.1016/j.ejca.2010.06.015.

[14] C. Jin *et al.*, "High-intensity focused ultrasound combined with transarterial chemoembolization for unresectable hepatocellular carcinoma: long-term follow-up and clinical analysis," *European journal of radiology,* vol. 80, no. 3, pp. 662-669, 2011. doi: 10.1016/j.ejrad.2010.08.042.

[15] G. Xu *et al.*, "Follow-Up of High-Intensity Focused Ultrasound Treatment for Patients with Hepatocellular Carcinoma," *Ultrasound in Medicine & Biology,* vol. 37, no. 12, pp. 1993-1999, 2011/12/01/ 2011. doi: 10.1016/j.ultrasmedbio.2011.08.011.

[16] L. Cui *et al.*, "Comparative study on transcatheter arterial chemoembolization, portal vein embolization and high intensity focused ultrasound sequential therapy for patients," *Asian Pacific Journal of Cancer Prevention,* vol. 13, no. 12, pp. 6257-6261, 2012.

[17] J. Kim, D. Chung, S. Jung, S. Cho, S. Hahn, and J. Lee, "Therapeutic effect of high-intensity focused ultrasound combined with transarterial chemoembolisation for hepatocellular carcinoma< 5 cm: comparison with transarterial chemoembolisation monotherapy—preliminary observations," *The British journal of radiology,* vol. 85, no. 1018, pp. e940-e946, 2012. doi: 10.1259/bjr/32750755.

[18] K. S. Chok *et al.*, "Pilot study of high-intensity focused ultrasound ablation as a bridging therapy for hepatocellular carcinoma patients wait-listed for liver transplantation," *Liver Transplantation,* vol. 20, no. 8, pp. 912-921, 2014. doi: 10.1002/lt.23892.

[19] R. Illing *et al.*, "The safety and feasibility of extracorporeal high-intensity focused ultrasound (HIFU) for the treatment of liver and kidney tumours in a Western population," *British journal of cancer,* vol. 93, no. 8, pp. 890-895, 2005. doi: 10.1038/sj.bjc.6602803.

[20] M. Rohani and A. Fasano, "Focused Ultrasound for Essential Tremor: Review of the Evidence and Discussion of Current Hurdles," (in eng), *Tremor Other Hyperkinet Mov (N Y),* vol. 7, p. 462, 2017. doi: 10.7916/d8z89jn1.

[21] C. Mougenot, M. Köhler, J. Enholm, B. Quesson, and C. Moonen, "Quantification of near-field heating during volumetric MR-HIFU ablation," *Medical physics,* vol. 38, no. 1, pp. 272-282, 2011. doi: 10.1118/1.3518083.

[22] S. L. Mulvagh *et al.*, "Contrast echocardiography: current and future applications," *Journal of the American Society of Echocardiography,* vol. 13, no. 4, pp. 331-342, 2000. doi: 10.1067/mje.2000.105462.

[23] Y. Kono *et al.*, "Gray-scale second harmonic imaging of the liver with galactose-based microbubbles," *Investigative radiology,* vol. 32, no. 2, pp. 120-125, 1997.

[24] S. R. Wilson, P. N. Burns, D. Muradali, J. A. Wilson, and X. Lai, "Harmonic Hepatic US with Microbubble Contrast Agent: Initial Experience Showing Improved Characterization of Hemangioma, Hepatocellular Carcinoma, and Metastasis," *Radiology,* vol. 215, no. 1, pp. 153-161, 2000. doi: 10.1148/radiology.215.1.r00ap08153.

[25] K. Darge *et al.*, "Safety of contrast-enhanced ultrasound in children for non-cardiac applications: a review by the Society for Pediatric Radiology (SPR) and the International Contrast Ultrasound Society (ICUS)," *Pediatric radiology,* vol. 43, no. 9, pp. 1063-1073, 2013.

[26] R. G. Holt and R. A. Roy, "Measurements of bubble-enhanced heating from focused, MHz-frequency ultrasound in a tissue-mimicking material," *Ultrasound in medicine & biology,* vol. 27, no. 10, pp. 1399-1412, 2001.

[27] B. C. Tran, S. Jongbum, T. L. Hall, J. B. Fowlkes, and C. A. Cain, "Microbubble-enhanced cavitation for noninvasive ultrasound surgery," *IEEE Transactions on Ultrasonics, Ferroelectrics, and Frequency Control,* vol. 50, no. 10, pp. 1296-1304, 2003. doi: 10.1109/TUFFC.2003.1244746.

[28] B. C. Tran, S. Jongbum, T. L. Hall, J. B. Fowlkes, and C. A. Cain, "Effects of contrast agent infusion rates on thresholds for tissue damage produced by single exposures of high-intensity ultrasound," *IEEE Transactions on Ultrasonics, Ferroelectrics, and Frequency Control,* vol. 52, no. 7, pp. 1121-1130, 2005. doi: 10.1109/TUFFC.2005.1503998.

[29] Y.-S. Tung, H.-L. Liu, C.-C. Wu, K.-C. Ju, W.-S. Chen, and W.-L. Lin, "Contrast-agent-enhanced ultrasound thermal ablation," *Ultrasound in Medicine & Biology,* vol. 32, no. 7, pp. 1103-1110, 2006/07/01/ 2006. doi: 10.1016/j.ultrasmedbio.2006.04.005.

[30] A. Clark, S. Bonilla, D. Suo, Y. Shapira, and M. Averkiou, "Microbubble-enhanced heating: exploring the effect of microbubble concentration and pressure amplitude on high-intensity focused ultrasound treatments," *Ultrasound in medicine & biology,* vol. 47, no. 8, pp. 2296-2309, 2021. doi: 10.1016/j.ultrasmedbio.2021.03.035.

[31] N. J. McDannold, N. I. Vykhodtseva, and K. Hynynen, "Microbubble contrast agent with focused ultrasound to create brain lesions at low power levels: MR imaging and histologic study in rabbits," *Radiology,* vol. 241, no. 1, pp. 95-106, 2006. doi: 10.1148/radiol.241105117.

[32] T. Yu, X. Fan, S. Xiong, K. Hu, and Z. Wang, "Microbubbles assist goat liver ablation by high intensity focused ultrasound," *European Radiology,* vol. 16, no. 7, pp. 1557-1563, 2006/07/01 2006a. doi: 10.1007/s00330-006-0176-7.

[33] T. Yu, S. Xiong, T. J. Mason, and Z. Wang, "The use of a microbubble agent to enhance rabbit liver destruction using high intensity focused ultrasound," *Ultrasonics Sonochemistry,* vol. 13, no. 2, pp. 143-149, 2006/02/01/ 2006b. doi: 10.1016/j.ultsonch.2005.02.001.

[34] K. Hanajiri *et al.*, "Microbubble-induced increase in ablation of liver tumors by high-intensity focused ultrasound," *Hepatology Research,* vol. 36, no. 4, pp. 308-314, 2006. doi: 10.1016/j.hepres.2006.08.013.

[35] Y. Kaneko *et al.*, "Use of a microbubble agent to increase the effects of high intensity focused ultrasound on liver tissue," *European radiology,* vol. 15, no. 7, pp. 1415-1420, 2005. doi: 10.1007/s00330-005-2663-7.

[36] M.-L. Izamis, A. Efstathiades, C. Keravnou, E. L. Leen, and M. A. Averkiou, "Dynamic contrast-enhanced ultrasound of slaughterhouse porcine livers in machine perfusion," *Ultrasound in medicine & biology,* vol. 40, no. 9, pp. 2217-2230, 2014. doi: 10.1016/j.ultrasmedbio.2014.03.031.

[37] M.-L. Izamis, A. Efstathiades, C. Keravnou, S. Georgiadou, P. N. Martins, and M. A. Averkiou, "Effects of air embolism size and location on porcine hepatic microcirculation in machine perfusion," *Liver Transplantation,* vol. 20, no. 5, pp. 601-611, 2014. doi: 10.1002/lt.23838.

[38] C. P. Keravnou, I. De Cock, I. Lentacker, M.-L. Izamis, and M. A. Averkiou, "Microvascular injury and perfusion changes induced by ultrasound and microbubbles in a machine-perfused pig liver," *Ultrasound in medicine & biology,* vol. 42, no. 11, pp. 2676-2686, 2016. doi: 10.1016/j.ultrasmedbio.2016.06.025.

[39] M. A. Averkiou, M. F. Bruce, J. E. Powers, P. S. Sheeran, and P. N. Burns, "Imaging methods for ultrasound contrast agents," *Ultrasound in medicine & biology,* vol. 46, no. 3, pp. 498-517, 2020. doi: 10.1016/j.ultrasmedbio.2019.11.004.

[40] H. Mulvana, E. Stride, M. Tang, J. V. Hajnal, and R. Eckersley, "Temperature-Dependent Differences in the Nonlinear Acoustic Behavior of Ultrasound Contrast Agents Revealed by High-Speed Imaging and Bulk Acoustics," *Ultrasound in Medicine & Biology,* vol. 37, no. 9, pp. 1509-1517, 2011/09/01/ 2011. doi: 10.1016/j.ultrasmedbio.2011.05.020.

[41] H. H. Pennes, "Analysis of Tissue and Arterial Blood Temperatures in the Resting Human Forearm," *Journal of Applied Physiology,* vol. 1, no. 2, pp. 93-122, 1948. doi: 10.1152/jappl.1948.1.2.93.

[42] T. Drizdal, P. Togni, L. Visek, and J. Vrba, "Comparison of constant and temperature dependent blood perfusion in temperature prediction for superficial hyperthermia," *Radioengineering,* vol. 19, no. 2, pp. 281-289, 2010.

[43] S. Keller, M. Bruce, and M. A. Averkiou, "Ultrasound Imaging of Microbubble Activity during Sonoporation Pulse Sequences," *Ultrasound in Medicine & Biology,* vol. 45, no. 3, pp. 833-845, 2019/03/01/ 2019. doi: 10.1016/j.ultrasmedbio.2018.11.011.

[44] Y. Matsumoto, J. S. Allen, S. Yoshizawa, T. Ikeda, and Y. Kaneko, "Medical ultrasound with microbubbles," *Experimental Thermal and Fluid Science,* vol. 29, no. 3, pp. 255-265, 2005/03/01/ 2005. doi: 10.1016/j.expthermflusci.2004.05.008.

[45] S. B. Keller, P. S. Sheeran, and M. A. Averkiou, "Cavitation therapy monitoring of commercial microbubbles with a clinical scanner," *IEEE Transactions on Ultrasonics, Ferroelectrics, and Frequency Control,* vol. 68, no. 4, pp. 1144-1154, 2020. doi: 10.1109/TUFFC.2020.3034532.

[46] H. Morris, I. Rivens, A. Shaw, and G. t. Haar, "Investigation of the viscous heating artefact arising from the use of thermocouples in a focused ultrasound field," *Physics in Medicine & Biology,* vol. 53, no. 17, p. 4759, 2008/08/13 2008. doi: 10.1088/0031-9155/53/17/020.

[47] C. Song *et al.*, "Thermographic Investigation of The Heating Effect of High Intensity Focused Ultrasound," in *2005 IEEE Engineering in Medicine and Biology 27th Annual Conference*, 2005, pp. 3456-3458. doi: 10.1109/IEMBS.2005.1617222.

[48] B. Quesson, J. A. de Zwart, and C. T. W. Moonen, "Magnetic resonance temperature imaging for guidance of thermotherapy," *Journal of Magnetic Resonance Imaging,* vol. 12, no. 4, pp. 525-533, 2000. doi: https://doi.org/10.1002/1522-2586(200010)12:4<525::AID-JMRI3>3.0.CO;2-V.

[49] L. Qiu *et al.*, "Ultrasound-targeted microbubble destruction enhances naked plasmid DNA transfection in rabbit Achilles tendons in vivo," *Gene Therapy,* vol. 19, no. 7, pp. 703-710, 2012/07/01 2012. doi: 10.1038/gt.2011.165.

[50] S. R. Wilson, P. N. Burns, and Y. Kono, "Contrast-Enhanced Ultrasound of Focal Liver Masses: A Success Story," *Ultrasound in Medicine & Biology,* vol. 46, no. 5, pp. 1059-1070, 2020/05/01/ 2020. doi: 10.1016/j.ultrasmedbio.2019.12.021.

[51] S. B. Keller, D. Suo, Y.-N. Wang, H. Kenerson, R. S. Yeung, and M. A. Averkiou, "Image-Guided Treatment of Primary Liver Cancer in Mice Leads to Vascular Disruption and Increased Drug Penetration," *Frontiers in Pharmacology,* vol. 11, 2020. doi: 10.3389/fphar.2020.584344.

CHAPTER 5. IMPLEMENTATION OF SUBHARMONIC IMAGING ON A CLINICAL SCANNER FOR OPTIMAL AMBIENT PRESSURE SENSITIVITY WITH SONOVUE MICROBUBBLES[5]

Abstract

Subharmonic imaging for ambient pressure estimation is a noninvasive alternative to direct pressure catheter measurements that are currently used to diagnose multiple disease processes and monitor interstitial fluid pressure (IFP). However, clinical implementations of subharmonic imaging lack important attributes necessary for accurate generation and detection of the subharmonic component. Some implementations employ frequencies near the resonance frequency of microbubbles, requiring high acoustic pressure to generate subharmonic signals. Others utilize short pulses (2-6 cycles) which result in scattered spectra where the fundamental and subharmonic frequencies overlap. We investigated longer pulses at twice the resonance frequency of SonoVue microbubbles and detected the subharmonic component with a narrow receive bandwidth in a pulse inversion scheme as a sensitive method to detect ambient pressure. We used an in-vitro pressure chamber with transparent acoustic windows and filled with SonoVue microbubbles to vary the ambient pressure (0-140 mmHg) while collecting subharmonic images. We considered multiple frequencies, pulse lengths, acoustic pressures (0-900 kPa), pulsing schemes and imaging array types. Native linearized image data and radiofrequency data were used to accurately measure the subharmonic signal in the images. Transmitting at twice the resonance frequency (4.2 MHz) results in the greatest change in subharmonic signal with ambient pressure, a 16 dB increase from 0-80 mmHg (+0.2 dB/mmHg) at 70 kPa acoustic pressure. SonoVue is particularly sensitive to low ambient pressures (0-40 mmHg), relevant for monitoring IFP in solid tumors. Higher ambient pressures (> 100 mmHg) resulted in microbubble destruction that reduced image intensity without a change in subharmonic sensitivity. The findings in this work provide evidence of the utility of SonoVue for ambient pressure sensing at low acoustic pressures.

[5] *This chapter has appeared as:* ***De Koninck LH****., Babu G., Powers JE., de Jong N., Averkiou, MA. "Implementation of subharmonic imaging on a clinical scanner for optimal ambient pressure sensitivity with SonoVue microbubbles" IEEE Transactions on Ultrasonics, Ferroelectrics, and Frequency Control (in review).*

5.1 INTRODUCTION

Measurement of physiological pressures is a vital element in the management and diagnosis of multiple disease processes, such as heart failure [11, 12], cirrhosis [13, 14], pulmonary hypertension [15, 16] and traumatic brain injury [17, 18]. Assessment of physiological pressures within the body is generally performed by either direct invasive measurement using a pressure catheter or non-invasive estimation using various modalities such as ultrasound or pressure cuffs. However, catheterization carries procedural risks and is costly [14, 17, 19-22], while non-invasive pressure estimation techniques presently have a narrow scope of assessment and limited degree of accuracy [14, 17, 23-27]. One potential solution that addresses these shortcomings involves the use of ultrasound contrast agents (UCAs) as ambient pressure sensors. When insonified, UCAs produce a nonlinear response that can be separated from the linear signal derived from tissue [28]. Contrast-enhanced ultrasound (CEUS) typically uses a nonlinear pulsing scheme to eliminate the linear, fundamental component of the signal (equal to transmit frequency) and form images with the remaining nonlinear signal (whole harmonics of the transmit frequency) to further isolate microbubble echoes [28]. Another approach is to form contrast images with the subharmonic signal (half the transmit frequency [29]. We note that while tissue can generate harmonics due to nonlinear propagation of ultrasound, only microbubbles generate a subharmonic signal. The subharmonic signal of UCAs has also been shown to be more sensitive to ambient pressure changes than other harmonic components [30, 31]. However, disagreement over optimal acoustic parameters, specifically transmit frequency and acoustic pressure, and even microbubble choice has led to conflicting information on subharmonic signal change with ambient pressure and delayed clinical translation.

Several in-vitro studies, using scattering experimental set ups and optical measurements, have determined the subharmonic response of microbubbles to be dependent on two acoustic parameters: transmit frequency and incident acoustic pressure. The presence of subharmonic signals has historically been used as an indicator for stable cavitation, sustained oscillations around an equilibrium size, but may not be representative of the complete diversity of cavitation dynamics [32, 33]. However, this type of cavitation requires the use of acoustic pressures (> 200 kPa) that can compromise the microbubble shell and result in the oscillation of a free gas bubble [34, 35]. For lipid-coated microbubbles, the acoustic pressure threshold for subharmonic signal generation is minimized when the driving frequency is twice the average resonance frequency of the

microbubble population [36], limiting bubble destruction. Since UCAs are polydisperse with a variety of microbubble sizes typically around 1-10 μm [37, 38], the average resonance frequency refers to the resonance frequency of the average microbubble size of the UCA. In this regime, microbubbles at low acoustic pressures (5-100 kPa) exhibit a rapid change in effective surface tension of the bubble's shell [39] as it transitions from elastic and buckled states [40], resulting in compression-only behavior [41, 42]. In general, as the acoustic pressure increases (> 200 kPa) with long bursts (> 8 cycles), microbubble shell disruption and lipid shedding will occur, leaving a free gas bubble and shifting the asymmetry of bubble oscillations to favor expansion behavior [39, 40]. These increased pressures also exceed the destruction threshold of certain microbubbles that are resonant at the transmit frequency, indicating that subharmonic signal in this pressure regime is likely due to a combination of collapsing resonant microbubbles and microbubbles oscillating at twice the resonance frequency [34, 42]. As a side note, when using acoustic pressures that result in microbubbles destruction, CEUS becomes more challenging because slow frame rates (typically controlled by triggering, e.g., electrocardiogram triggering) must be used to allow for replenishment of microbubbles [43, 44]. As ambient pressure increases above atmospheric pressure, 3 new effects should take place: a.) inhibition of expansion behavior, b.) increased dissolution rate of free bubbles, and c.) a shift in resonant frequency [45-47]. At low acoustic pressures where we only expect compression behavior with no shell rupture, only the resonance shift need be considered, while high acoustic pressures must consider all 3 effects. When microbubbles are insonified at low acoustic pressures, an increase in ambient pressure will exaggerate compression behavior due to the low initial surface tension and increase the subharmonic signal [41, 42, 48, 49]. When microbubbles are insonified at high acoustic pressures, increased ambient pressure will dampen the expansion behavior of larger amplitude oscillations and exaggerate dissolution of bubbles with ruptured shells, reducing the number of scatterers. Depending on the balance of these effects, the subharmonic signal will exhibit no change with ambient pressure or even an inverse relationship [50]. Therefore, it is difficult to assign a single value of subharmonic signal change with ambient pressure (dB/mmHg) to a microbubble formulation, leading to the wide range of sensitivities reported in literature.

While subharmonic imaging has been investigated by many groups and has already been commercially released, several questions remain on how to use it, which microbubbles are suited for this mode and why it is not yet clinically used. **Table 5.1** presents the clinical systems currently

known to have (or had) subharmonic imaging capability and used to evaluate ambient pressure in-vivo, their transmit parameters, and the contrast agents used in the listed studies. The clinical systems include the Sonix RP scanner with a PA4-2 phased array (Ultrasonix Medical Corp., Richmond BC, Canada), SonixTablet (BK Ultrasound, Peabody, MA, USA) with a SA4-2 phased array, and the LOGIQ 9 scanner with a 4C curved array (GE HealthCare, Chicago, IL, USA). All listed studies used transmit frequencies near the average resonance frequency (2.5 MHz) with short pulses. In addition, subharmonic imaging with SonoVue has not yet been evaluated in-vivo. A more recent release of subharmonic imaging is available on the LOGIQ E10 scanner (GE HealthCare, Chicago, IL, USA) with the C1-6 curvilinear array (implemented with a transmit frequency of 2.5 MHz, receive frequency of 1.25 MHz, 4 cycles, and amplitude modulation) [51], but recent in-vivo studies with this scanner use different probes (C2-9, C1-6-D) where not all transmit parameters are specified, so we excluded this system from **Table 5.1** [52, 53]. Although shorter pulses improve the axial resolution of images, these pulses exhibit a wide bandwidth that may result in overlapping fundamental and subharmonic frequencies that cannot be separated. Dave, et al. [7] directly compared 4, 8, and 16 cycle subharmonic imaging pulses in a canine model

Table 5.1: Clinical systems, associated transmit parameters, and contrast agents of in-vivo subharmonic imaging studies

Clinical System	Probe	Transmit Frequency (MHz)	Transmit pulse length (cycles)	Acoustic pressure range (kPa)[a]	Contrast agents	Reference
Sonix RP	PA4-2	2.5	2[b]	300-900	Definity Sonazoid	[1-3]
SonixTablet	SA4-2[b]	2.5, 3	4, 6[b]	300-600	Definity Sonazoid	[4, 5]
LOGIQ 9	4C	2.5	4[c]	200-900	Definity Sonazoid	[6-10]

[a]Estimated from acoustic pressure range (reported as percentage of maximum acoustic output) used in listed manuscripts after incident acoustic output algorithm. [b]Parameter not specified in all listed manuscripts but assumed to be unchanged based on prior studies by the same research group using the same clinical system. [c]Pulse lengths of 2-16 were evaluated in earlier studies, but only the 4-cycle pulse was implemented for later clinical studies.

and found the shortest pulse length (4 cycles) to provide the best correlation of subharmonic amplitudes with portal vein pressures, but spectra of radiofrequency data was not provided so the effect of bandwidth could not be directly observed. Another consideration is by transmitting at 2.5 MHz (and receiving around 1.25 MHz), high acoustic pressures are needed to generate subharmonic signals as this is near the average resonance frequency of UCAs [34]. **Table 5.1** lists the range of acoustic pressures (peak-to-peak) used to evaluate subharmonic amplitude of UCAs in-vivo, estimated from the typical evaluation range of 10-40% of maximum acoustic output as selected by the incident acoustic pressure algorithm [7]. These acoustic pressures generally exceed the acoustic pressure threshold for shell disruption (> 200 kPa) [39, 40]. Consequently, clinical implementation of subharmonic imaging has yet to explore ambient pressure sensing at low acoustic pressures (< 200 kPa) and taking advantage of transmitting at twice the resonant frequency to reduce the subharmonic threshold.

In this study, we implement subharmonic imaging on a clinical scanner and investigate the optimal parameters for noninvasive ambient pressure sensing with SonoVue microbubbles. We considered frequency, number of cycles, acoustic amplitude and nonlinear pulsing schemes. We investigated transmitting acoustic pulses at twice the average resonance frequency to increase the ambient pressure sensitivity. This frequency minimizes the acoustic pressure threshold for subharmonic signal generation. Subharmonic imaging was implemented on a curvilinear and linear array of a clinical scanner at 3 frequencies: 2.5 MHz (around resonance) 4.2 MHz (at 2x resonance) and 7.0 MHz (greater than 2x resonance). The acoustic pulses used were longer than conventional fundamental or nonlinear imaging pulses (18 cycles) to better segment and detect the subharmonic signals. Three nonlinear pulsing schemes (amplitude modulation-AM, pulse inversion-PI, and amplitude-modulated pulse inversion-AMPI) and single pulses with simple receive filtering were evaluated for producing subharmonic images and maximum ambient pressure sensing. Hydrophone measurements in water are used to characterize the sound field from different subharmonic imaging modes and measure if sound is directly transmitted at the subharmonic frequency. A custom-built chamber pressurized to physiologically relevant static ambient pressures (0-140 mmHg) was used to evaluate change in subharmonic signal with ambient pressure. We used a clinically approved microbubble contrast agent, SonoVue (Bracco, Milan, Italy), diluted to concentrations equivalent to clinical doses. The microbubble solutions were constantly stirred and imaged at a slow frame rate (0.33 Hz) to minimize microbubble destruction

during the experiments. Both native linearized image data (with the logarithmic compression removed) and radiofrequency (RF) data were recorded and post-processed to measure changes in image intensity and subharmonic signal magnitude. The subharmonic signal change per unit ambient pressure is the key metric used to evaluate all the ultrasound parameters and select the optimal ones for ambient pressure sensing.

5.2 Materials and Methods

5.2.1 Implementation of subharmonic imaging on a clinical scanner

Subharmonic imaging was implemented on a Philips EPIQ scanner, C5-1 curvilinear array, and eL18-4 linear array (Philips Healthcare, Bothell, WA, USA). Various combinations of acoustic parameters were programmed (shown in **Table 5.2**), including transmit frequency, receive frequency, number of cycles, nonlinear pulsing schemes and our naming convention. We investigated that transmitting acoustic pulses at twice the average resonance frequency will result in the greatest change in subharmonic signal with ambient pressure compared to other frequencies. Three transmit frequencies were implemented: 2.5 MHz (around resonance), 4.2 MHz (at 2x resonance) and 7.0 MHz (greater than 2x resonance). Due to the available bandwidths in different

Table 5.2: Modified transmit and receive settings for subharmonic imaging modes

Probe	Transmit / Receive Frequency (MHz)	Tx pulse length (cycles)	Pulsing scheme	Mode Name
C5-1	2.5 / 1.25	6	Single AM	$SHI_{2.5}$ $SHI_{AM2.5}$
C5-1	4.2 / 2.1	18	Single AM PI AMPI	$SHI_{4.2}$ $SHI_{AM\ .2}$ $SHI_{PI4.2}$ $SHI_{AMPI4.2}$
eL18-4	7.0 / 3.5	18	Single PI	$SHI_{7.0}$ $SHI_{PI7.0}$

probes, 2.5 and 4.2 MHz transmit frequencies were implemented on the C5-1 probe, while 7 MHz was implemented on the eL18-4 probe. Receive filters were centered at the corresponding half transmit frequency component for the 3 settings (1.25, 2.1, 3.5 MHz,) with a narrow bandwidth to extract only the subharmonic signal. Acoustic pulses were also programmed with 2 pulse lengths multiplied by a Hamming window, 6 cycles representative of conventional CEUS imaging pulse lengths, and windowed 18 cycles to further separate subharmonic and fundamental components. Three standard nonlinear pulsing schemes were implemented to enhance the segmentation of the linear and nonlinear signals : (a) amplitude modulation (AM, transmitting 3 pulses per line, 2 half amplitude and 1 full amplitude, and combining the scattered signal of each pulse at 1/3 amplitude by subtracting the full amplitude from the sum of the half amplitude), (b) pulse inversion (PI, transmitting 2 pulses per line, 1 full amplitude and 1 inverted full amplitude, and adding the scattered signal of each pulse at half amplitude), and (c) amplitude-modulated pulse inversion (AMPI, transmitting 3 pulses per line, 2 half amplitude and 1 inverted full amplitude, and adding the scattered signal of each pulse at 1/3 amplitude). A fourth technique of transmitting a single pulse per line at full amplitude was also evaluated. The produced acoustic pressure is selected by adjusting the output power on the front panel used in clinical imaging, which in turn adjusts the transmitted voltage. We note that the $SHI_{AM2.5}$ mode is a standard CEUS setting on the scanner with only the receive filter modified to be centered at the half transmit frequency component with a narrow bandwidth, and is similar to the commercial releases of subharmonic imaging (transmit frequency of 2.5 MHz, receive frequency of 1.25 MHz, 4 cycles, AM pulsing scheme) described in **Table 5.1**. We wanted to have a setting with a small number of cycles to be able to evaluate the effect of pulse length.

The pulse of each subharmonic mode was measured in a water tank with a 0.4 mm membrane hydrophone (UT1604-225; Precision Acoustics, Dorchester U.K.) to evaluate the spectrum of the transmitted sound wave, especially the components at the subharmonic frequency, and map the axial field. **Fig. 1** shows hydrophone measurements with $SHI_{2.5}$ (**Figure 5.1**(a-c)), $SHI_{4.2}$ (**Figure 5.1**(d-f)), and $SHI_{7.0}$ (**Figure 5.1**(g-i)). The left column (**Figure 5.1**(a), **Figure 5.1**(d)**, Figure 5.1**(g)) shows the transmitted acoustic pulse measured at the axial location of maximum pressure per subharmonic mode (61 mm for $SHI_{2.5}$, 73 mm for $SHI_{4.2}$, 60 mm for $SHI_{7.0}$). **Figure 5.1**(b) shows the overlap of fundamental and subharmonic with $SHI_{2.5}$. The amplitude at the subharmonic component is 20dB below the fundamental and it is not possible to

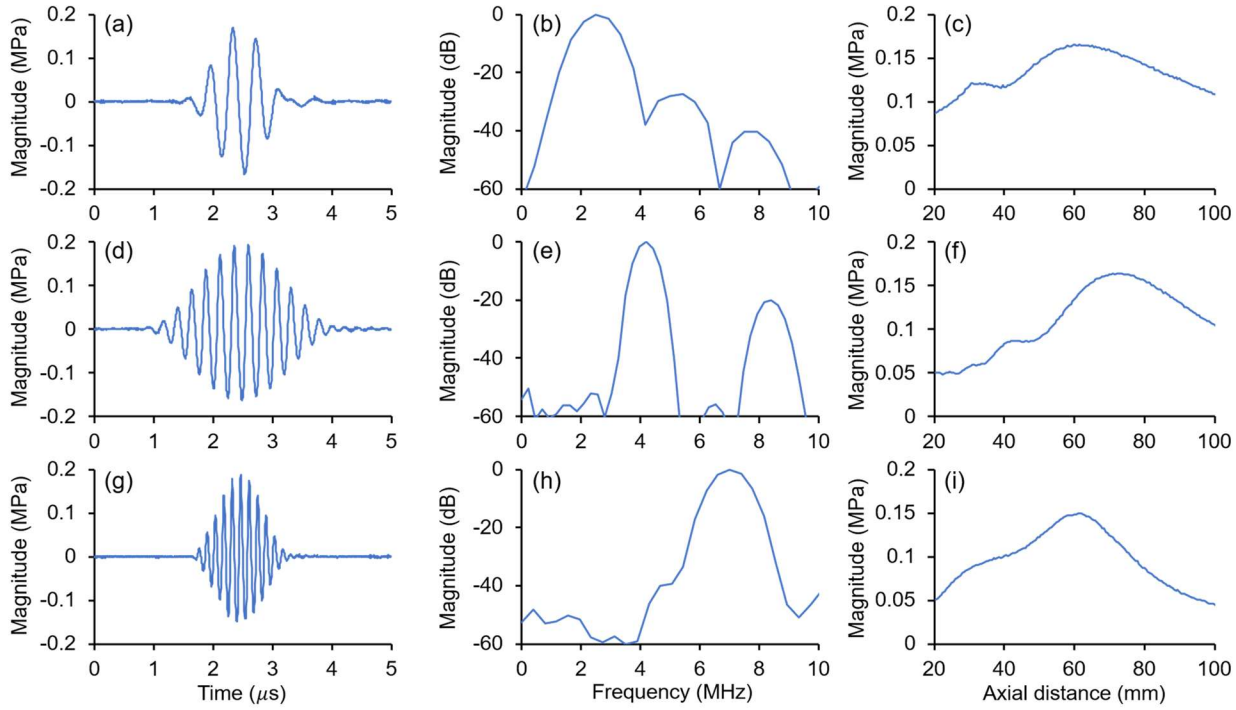

Figure 5.1*: Hydrophone measurements of subharmonic imaging modes.*

Hydrophone measurements of pulses used in subharmonic imaging modes with the C5-1 probe at 2.5 MHz (top row), 4.2 MHz (center row), and eL18-4 probe at 7 MHz (bottom row). Left column is the transmitted pulse measured at axial distances of (a) 61 mm, (d) 73 mm, and (g) 60 mm. Center column (b, e, h) is the corresponding frequency spectra of time waveforms normalized to the magnitude of the fundamental component. Right column (c, f, i) is the axial pressure variation along the center transmitted line.

know what part of it belongs to the fundamental and what to the subharmonic. No appreciable acoustic amplitude was measured at the subharmonic component with $SHI_{4.2}$ (**Figure 5.1**(e)) and $SHI_{7.0}$ (**Figure 5.1**(h)). The right column (**Figure 5.1**(c), **Figure 5.1**(f)**, Figure 5.1**(j)) shows the axial pressure distribution measured along the center transmitted line. The azimuthal focus of each subharmonic mode was selected such that the maximum acoustic pressure was delivered 6-7 cm axially from the selected probe. The acoustic pressures reported in this study correspond to the peak negative pressure measured at the axial location of maximum pressure in water during the full amplitude pulse of each pulsing scheme.

5.2.2 Experimental setup

To evaluate the effect of the ambient pressure on the subharmonic signal, we used a custom air-tight chamber capable of pressurizing to 140 mmHg above atmospheric pressure (0 mmHg). A schematic of this setup is shown in **Figure 5.2**(a). The chamber (length = 10 cm, width = 10 cm,

height = 10 cm) is submerged in a water tank, with the outer wall positioned 2 cm away from the imaging probe. The ambient pressure was manually controlled in the range of 0-140 mmHg with an air-filled syringe and confirmed with a pressure gauge (± 1 mmHg). Circular holes of 5 cm diameter were cut through each wall of the chamber and sealed with a thin polycarbonate sheet (0.13 mm thickness), which was measured to result in negligible transmission loss. A magnetic stir bar placed inside the chamber was used to continuously stir the microbubble solution during experiments. To minimize reflections, the imaging probe was rotated a small angle (5°) relative to the orthogonal position with the chamber wall. **Figure 5.2**(b) shows an example subharmonic image (set to the maximum dynamic range of 70 dB) without microbubbles, where the dashed lines represent the walls of the chamber demonstrating no reflections inside the chamber.

5.2.3 Microbubble preparation

SonoVue (Bracco Suisse SA, Geneva, Switzerland), a clinically approved contrast agent, was reconstituted according to manufacturer instructions, resulting in a base concentration of ~10^8 microbubbles/mL [54], and all measurements were completed within 3 hours of preparing the vial. Prior to each experiment, a new microbubble dilution was prepared by extracting a small volume from the vial, mixing in deionized water for 30 s, and then injecting into the chamber, resulting in

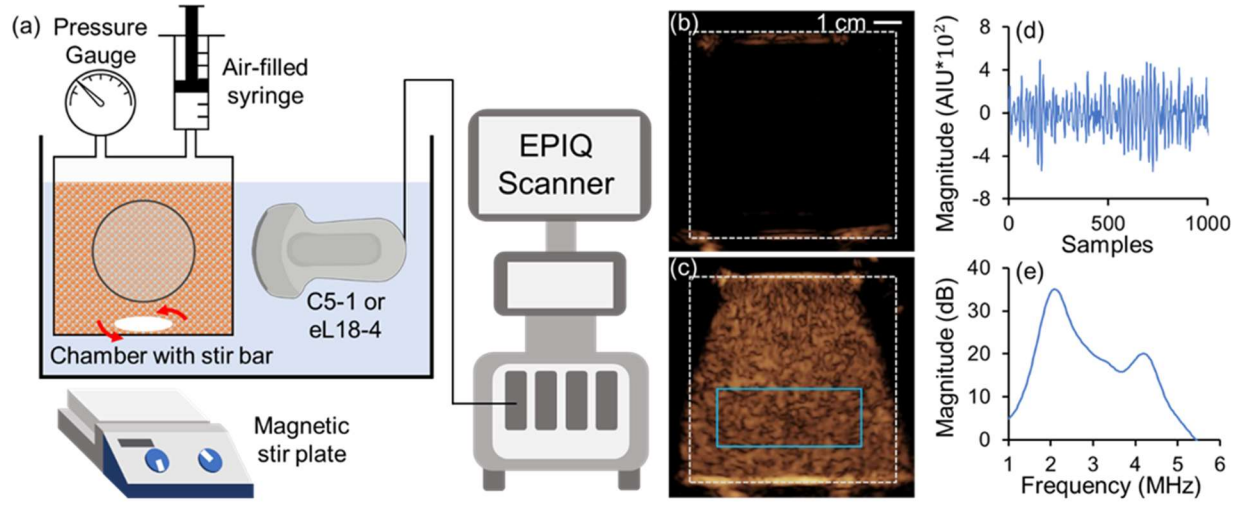

***Figure 5.2**: Schematic of ambient pressure experiments and examples of image and RF analysis.*

(a) Schematic of the experimental setup. Example subharmonic images (4.2 MHz) of the pressure chamber with (b) no microbubbles, and (c) with SonoVue. The white dashed line outlines the chamber walls and the blue box the region of interest used for image and RF analysis. (d) Example radiofrequency time-series data from a single line after pulse inversion. (e) Example spectra from pulse inversion RF data averaged from 100 transmit lines.

a concentration of ~10^4 microbubbles/mL. The microbubble concentration was selected to be representative of clinical concentrations [55] when mixed in 5 L blood. To control for variation from different dilution times observed in literature [56], all experiments began 2 minutes from when agent was extracted from the starting vial.

5.2.4 Experimental protocol

To measure subharmonic signal change with ambient pressure, two different approaches were utilized. First, the chamber was set to a static ambient pressure between 0-100 mmHg, allowed to mix for 30s, and then the acoustic pressure was gradually increased. At each acoustic pressure, an image loop was recorded consisting of 5 frames captured at a frame rate of 0.33 Hz (once every 3 seconds) to minimize bubble destruction when evaluating the higher acoustic pressures. To avoid signal saturation at high acoustic pressures (> 400 kPa), the 2D analog gain of the scanner was reduced by 8 dB relative to the gain selected for subharmonic imaging at acoustic pressures < 400 kPa according to the procedure described in Keravnou, et al. [57]. We believe this is a very important point when considering signals with large dynamic range from clinical scanners. During data analysis, image intensity values acquired with high acoustic pressures were adjusted by 8 dB to compensate for the difference in gain. A new microbubble dilution was used for each ambient pressure, with each experiment being completed within 10 minutes of extracting contrast agent from the starting vial. The second approach was to acquire subharmonic images while the ambient pressure varied at a fixed acoustic pressure. This approach allows evaluating any permanent effects of the increased ambient pressure on the microbubble behavior. A single microbubble dilution is imaged during 3 static ambient pressures: 1.) atmospheric pressure (0 mmHg), 2.) increased ambient pressure between 0-140 mmHg (p_{amb}), and 3.) after depressurizing the chamber to return to atmospheric pressure. Image intensities measured when the chamber is not pressurized (p_{amb} = 0 mmHg) are used as a reference to calculate changes in image intensity from ambient pressure-induced microbubble destruction. Each image loop consisted of 5 frames captured at 0.33 Hz frame rate, with loops set 1 minute apart to allow for enough time to record each loop, apply ambient pressure changes, and 30 s of stirring time. RF data was also captured (sampled at 40 MHz) during each p_{amb} image loop, where the RF data from individual pulses that form pulsing schemes is preserved, and saved for post-processing.

5.2.5 Image quantification and RF analysis

Native DICOM (linearized image data) were collected and post-processed with QLAB (Philips Healthcare, Bothell, WA, USA) using a region of interest (**Figure 5.2**(c)) spanning an image depth of 5-7 cm to measure linearized image intensity per frame. The average image intensity over 5 frames was calculated. RF data recorded during each p_{amb} image loop was analyzed in MATLAB using a custom script. First, an image is reconstructed from the RF data, and a region of interest (similar to **Figure 5.2**(c)) selects data from the center 100 lines. Example of RF data from the center line is shown in **Figure 5.2**(d). The frequency spectrum (dB relative to 1 arbitrary intensity unit-AIU) is then calculated for each line. Finally, all 100 spectra are averaged together to generate a single average spectra per region of interest, an example of which (after PI processing) is shown in **Figure 5.2**(e). To measure subharmonic magnitude from RF data, the average signal within a 0.2 MHz bandwidth centered on the subharmonic component was recorded per spectra.

5.3 RESULTS

5.3.1 The effect of frequency and bandwidth on subharmonic imaging

Figure 5.3 shows subharmonic images at low acoustic pressures (< 200 kPa) during ambient pressures of 0 (atmospheric pressure), 40, and 80 mmHg. In the top row where a short (windowed 6-cycle) pulse at 2.5 MHz in AM mode at 170 kPa is used ($SHI_{AM2.5}$) the image intensity slightly decreases as ambient pressure increases. In the middle row where a longer (windowed 18-cycle amplitude-shaded) pulse at 4.2 MHz in PI mode at 70 kPa is used ($SHI_{PI\ .2}$), the image intensity increases with ambient pressure. The same behavior is observed in the bottom row where a similar longer pulse is used at 7 MHz in PI mode at 110 kPa. The average spectra of RF data of these subharmonic images are shown in **Figure 5.4** for the full amplitude pulse (left column) and the combined pulses according to the pulsing scheme (right column). With $SHI_{2.5}$ at 170 kPa, the spectra (**Figure 5.4**(a)) exhibit a peak at the transmit frequency (2.5 MHz), and no distinct peak is observed at the subharmonic frequency (1.25 MHz). Additionally, there is no difference between the spectra measured at ambient pressures of 0 and 80 mmHg. The spectra

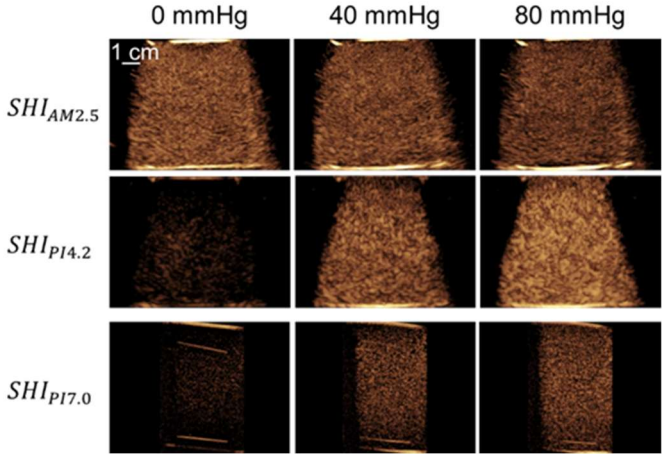

Figure 5.3*: Subharmonic images of SonoVue at low acoustic pressures for 3 ambient pressures.*

Top row is subharmonic imaging at 170 kPa acoustic pressure with the C5-1 probe ($SHI_{AM\ .5}$, 6 cycles at 2.5 MHz transmit and 1.25 MHz receive). Center row is subharmonic imaging at 70 kPa acoustic pressure with the C5-1 probe ($SHI_{PI4.2}$, 18 cycles at 4.2 MHz transmit and 2.1 MHz receive). Bottom row is subharmonic imaging at 110 kPa acoustic pressure with the eL18-4 probe ($SHI_{PI7.0}$, 18 cycles at 7.0 MHz transmit and 3.5 MHz receive).

from the AM processing ($SHI_{AM2.5}$) in **Figure 5.4**(b) shows a slight reduction (~ 2dB) in magnitude for signal at frequencies between 1 - 4 MHz as ambient pressure increases from 0 to 80 mmHg. Again, no distinct peak is observed at the subharmonic frequency. Conversely, the spectra from $SHI_{4.2}$ (**Figure 5.4**(c)) shows distinct peaks at both the transmit frequency (4.2 MHz) and the subharmonic frequency (2.1 MHz). Increasing ambient pressure from 0 to 80 mmHg results in a 10 dB increase in subharmonic magnitude and no change to the fundamental magnitude. This subharmonic increase with ambient pressure is further increased in the spectra from the PI processing ($SHI_{PI4.2}$, **Figure 5.4**(d)), which shows a 14 dB increase in subharmonic magnitude due to the significant reduction in the fundamental magnitude. Similarly, spectra of the $SHI_{7.0}$ pulse at 110 kPa (**Figure 5.4**(e)) and the combined pulse ($SHI_{PI7.0}$, **Figure 5.4**(f)) exhibit peaks at the transmit frequency (7 MHz) and the subharmonic frequency (3.5 MHz) that increases with

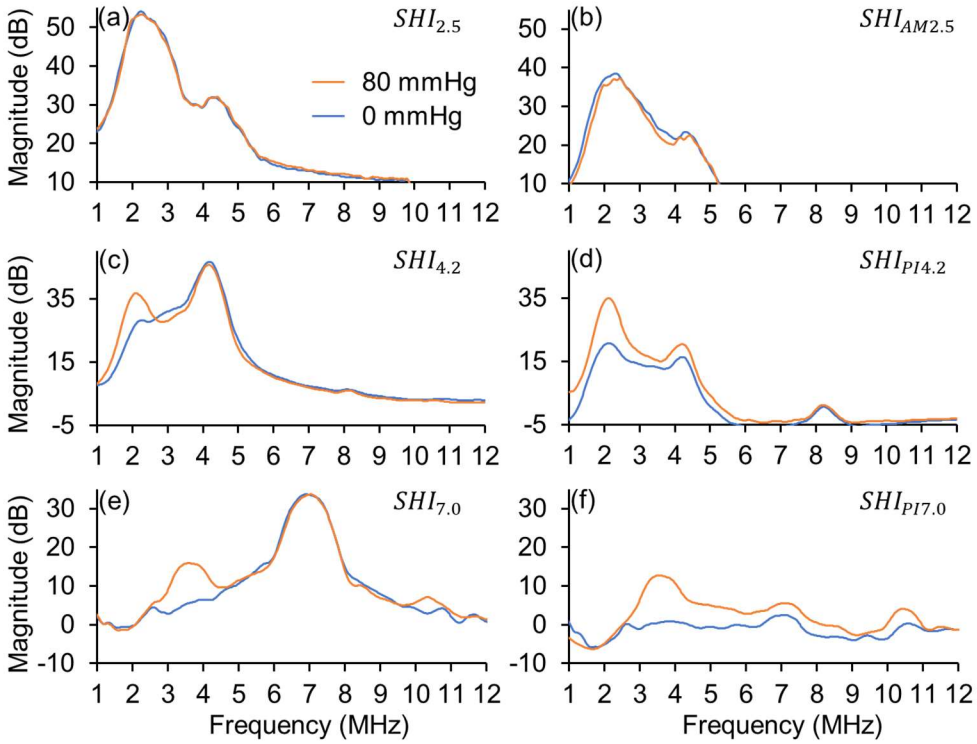

***Figure 5.4**: Average spectra of RF data measured during subharmonic imaging of SonoVue.*

Left column shows spectra of a single pulse and right column shows spectra after applying a pulsing scheme, both at ambient pressures of 0 mmHg (atmospheric) and 80 mmHg. Top row (a-b) uses C5-1 at 2.5 MHz, 6 cycles, amplitude modulation to demonstrate the impact of the transmitted pulse bandwidth. Center row (c-d) uses C5-1 at 4.2 MHz, 18 cycles, pulse inversion with our preferred transmitted bandwidth. Bottom row (e-f) is measured with eL18-4 at 7 MHz, 18 cycles, pulse inversion.

ambient pressure. Interestingly, we also observe an ultraharmonic component at 10.5 MHz that increases by 4 dB as ambient pressure increases.

Next, we consider the produced subharmonic images with SonoVue microbubbles and evaluate the image (subharmonic) intensity at various ambient and acoustic pressures. **Figure 5.5** shows subharmonic images with $SHI_{PI\ .2}$ at acoustic pressures of 70, 430, and 700 kPa (rows) and ambient pressures of 0, 40, and 80 mmHg (columns). We note that the images at an acoustic pressure of 70 kPa have an extra gain of 8 dB compared to the images at 430 and 700 kPa. At 70 kPa a significant increase in subharmonic intensity with ambient pressure is observed. At 430 kPa a smaller increase in subharmonic intensity is observed. Finally at 700 kPa a brighter region appears at an imaging depth of 6-9 cm which does not change with ambient pressure changes. The image brightness at shallower imaging depths (3-5 cm) at 700 kPa still increases slightly with ambient pressure.

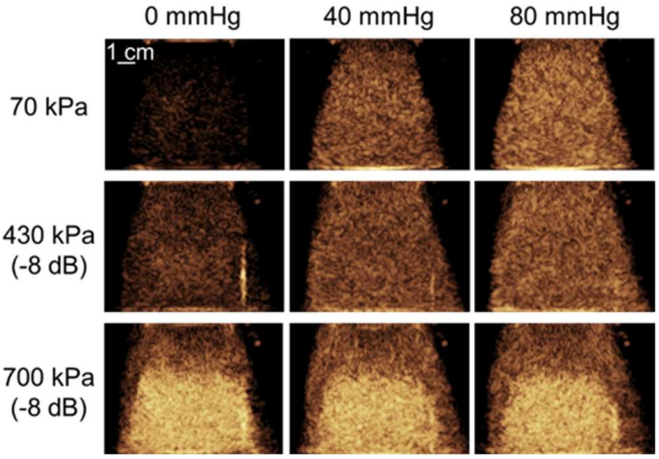

Figure 5.5*: Subharmonic images of SonoVue at 3 ambient pressures and 3 acoustic pressures. Images acquired with C5-1, 4.2 MHz, 18 cycles, pulse inversion.*

Figure 5.6 shows the average subharmonic intensity as a function of acoustic pressure for ambient pressures of 0 – 100 mmHg. **Figure 5.6**(a) shows measurements with $SHI_{AM\ .5}$, where the subharmonic intensity generally increases almost linearly with acoustic pressure. At low acoustic pressures (< 200 kPa), the subharmonic intensity is slightly reduced with increasing ambient pressure, and at acoustic pressures greater than 400 kPa subharmonic intensity does not change with ambient pressure. **Figure 5.6**(b) shows measurements with $SHI_{PI\ .2}$, where the subharmonic intensity changes at different rates with acoustic pressure. From 0-160 kPa, the subharmonic intensity rapidly increases, followed by a plateau of subharmonic intensity from 160-350 kPa, and changing again at acoustic pressures greater than 400 kPa where subharmonic intensity increases with acoustic pressure. When the acoustic pressure is less than 350 kPa, an increase in ambient pressure results in a significant increase in subharmonic intensity, but for acoustic pressures greater than 500 kPa the subharmonic intensity does not change with ambient pressure. Interestingly, at the lowest acoustic pressure of 35 kPa, the measurements at 0 and 20 mmHg did not detect subharmonic signal, while measurements at ambient pressures greater than 40 mmHg detected a subharmonic response. The reason for this is that the intensity measured under 0 and 20 mmHg are below the noise floor. **Figure 5.6**(c) shows measurements collected with $SHI_{PI7.0}$ where, like $SHI_{PI4.2}$, the subharmonic intensity increases from 0-200 kPa, then plateaus from 200-350 kPa. The subharmonic intensity is also observed to increase with ambient

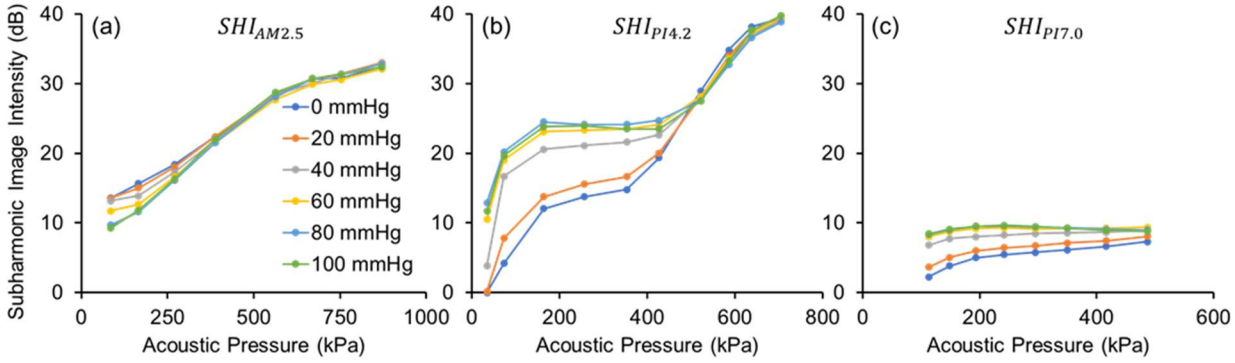

Figure 5.6*: Average image intensity of SonoVue as a function of acoustic pressure for 6 ambient pressures.*

(a) C5-1 probe, transmit frequency 2.5 MHz, receive frequency 1.25 MHz), 6 cycles, amplitude modulation. (b) C5-1 probe, transmit frequency 4.2 MHz, receive frequency 2.1 MHz, 18 cycles, pulse inversion. (c) eL18-4 probe, transmit frequency 7 MHz, receive frequency 3.5 MHz, 18 cycles, pulse inversion.

pressure in this acoustic pressure range, with a smaller increase relative to measurements with $SHI_{PI4.2}$.

To quantify the subharmonic signal change with ambient pressure of each subharmonic imaging mode, **Figure 5.7** shows the subharmonic intensity as a function of ambient pressure, normalized to the subharmonic intensity at 0 mmHg. For $SHI_{AM\ .5}$ (**Figure 5.7**(a)), low acoustic pressures (< 200 kPa) exhibit a sensitivity of -0.05 dB/mmHg from 0-80 mmHg. Increasing acoustic pressure reduces this subharmonic signal change, such that no change in subharmonic intensity with ambient pressure is observed at acoustic pressures greater than 400 kPa. For $SHI_{PI4.2}$ (**Figure 5.7**(b)), the subharmonic intensity increases with ambient pressure, maximized at an acoustic pressure of 70 kPa with a 16 dB increase and ambient pressure sensitivity of 0.2 dB/mmHg from 0-80 mmHg. As acoustic pressure increases, this sensitivity gradually decreases until no change in subharmonic intensity is observed at 500 kPa. Measurements with SHI_{PI7} (**Figure 5.7**(c)) were also maximized at the lowest acoustic pressure (110 kPa) with a 6 dB increase at 80 mmHg and a sensitivity of 0.08 dB/mmHg from 0-80 mmHg. Like $SHI_{AM2.5}$ and $SHI_{PI4.2}$, increasing acoustic pressure decreases the subharmonic sensitivity to ambient pressure.

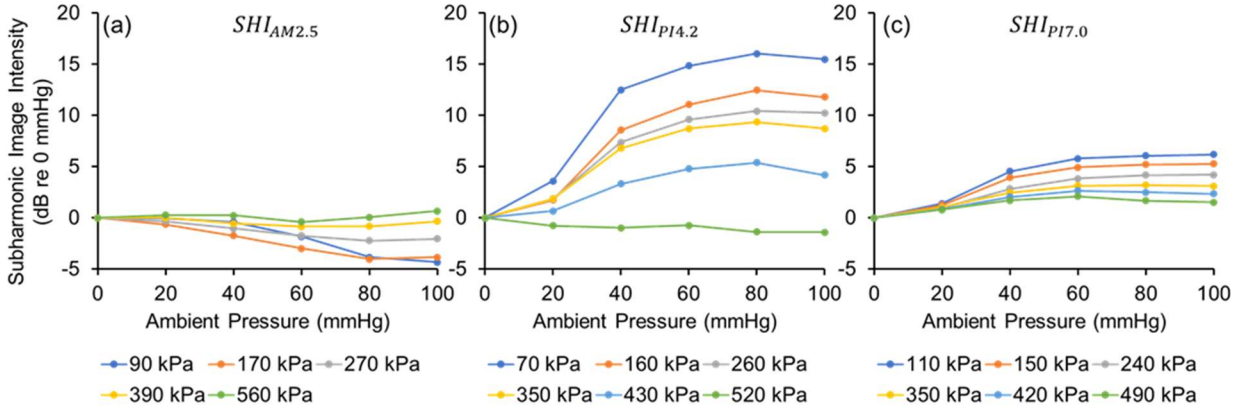

***Figure 5.7**: Average image intensity of SonoVue as a function of ambient pressure at different acoustic pressures.*

(a) C5-1 probe, transmit frequency 2.5 MHz, receive frequency 1.25 MHz), 6 cycles, amplitude modulation. (b) C5-1 probe, transmit frequency 4.2 MHz, receive frequency 2.1 MHz, 18 cycles, pulse inversion. (c) eL18-4 probe, transmit frequency 7 MHz, receive frequency 3.5 MHz, 18 cycles, pulse inversion. Intensity values were normalized with respect to the value at atmospheric pressure (0 mmHg).

5.3.2 *The effect of pulsing schemes on subharmonic signal extraction*

Using subharmonic imaging at 4.2 MHz, 4 pulsing schemes (**Table 5.2**) were evaluated at a range of acoustic pressures and ambient pressure with SonoVue. The subharmonic magnitude detected with each pulsing scheme is highlighted in **Figure 5.8**, which shows the average subharmonic intensity as a function of ambient pressure normalized to the subharmonic intensity at 0 mmHg. We note that all pulsing schemes exhibit the same behavior of subharmonic intensity increasing with acoustic pressure as demonstrated with $SHI_{PI\ .2}$ in **Figure 5.6**(b). At an acoustic pressure of 70 kPa (**Figure 5.8**(a)) all pulsing schemes increase with ambient pressure, maximized at 80 mmHg with a 16 dB increase and sensitivity of 0.2 dB/mmHg from 0-80 mmHg. Small to negligible differences between the pulsing schemes are observed in the 20-60 mmHg ambient pressure range, possibly due to experimental error or noise. PI offers a slightly greater change in subharmonic intensity from 20-40 mmHg, exhibiting a sensitivity of 0.45 dB/mmHg. At the highest acoustic pressure of 700 kPa (**Figure 5.8**(b)), all pulsing schemes show no sensitivity to changes in ambient pressure.

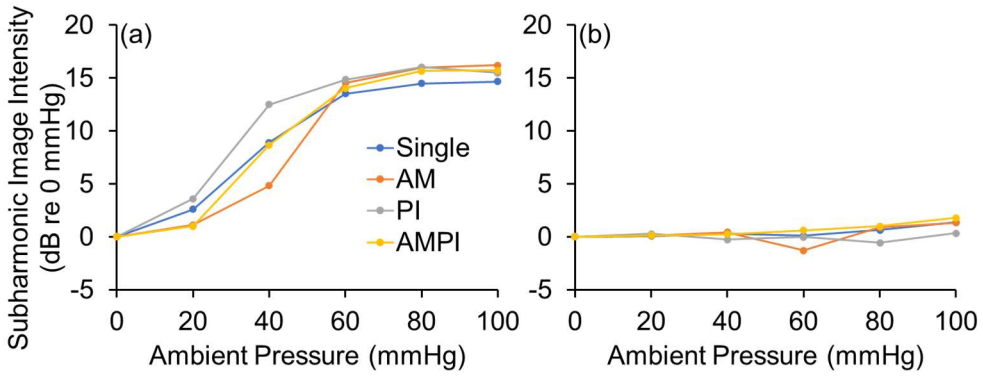

Figure 5.8*: Average image intensity of SonoVue as a function of ambient pressure during different pulsing schemes.*

Subharmonic images recorded with the C5-1 probe (transmit frequency 4.2 MHz, receive frequency 2.1 MHz, 18 cycles) with different pulsing schemes at acoustic pressures of (a) 70 kPa and (b) 700 kPa. Intensity values were normalized with respect to the value at atmospheric pressure (0 mmHg).

5.3.3 *Cycling ambient pressure at 4.2 MHz*

To determine if changes in subharmonic intensity were impacted by ambient pressure-induced microbubble destruction, $SHI_{PI\ .2}$ images of SonoVue were collected at a low acoustic pressure of 120 kPa while cycling ambient pressure between atmospheric pressure and increased

ambient pressure, p_{amb}, maintained over a period of time. **Figure 5.9**(a) shows the average measured subharmonic intensity at each stage of the pressure cycle, as a function of time, for p_{amb} = 0-140 mmHg. When p_{amb} = 0 mmHg (meaning ambient pressure is maintained at 0 mmHg for the whole 2 min duration), the subharmonic signal increases at a rate of 2.2 dB/min (discussed further in Section IV) and an overall increase of 4.4 dB is observed, which we use as the reference subharmonic intensity to determine if microbubble destruction occurred. For 0 mmHg $> p_{amb} \geq$ 80 mmHg, the subharmonic intensity increases by as much as 16 dB during pressurization (t = 1 min) and after depressurizing (t = 2 min) the subharmonic intensity returns to the reference subharmonic intensity (4.4 dB). For $p_{amb} >$ 80 mmHg, the subharmonic intensity increases by a smaller amount at t = 1 min relative to the subharmonic intensity during p_{amb} = 80 mmHg. In addition, for $p_{amb} >$ 100 mmHg, after depressurization (t = 2 min) the subharmonic intensity drops to a value that is lower than before pressurization (t = 0 min). The reduction in subharmonic intensity suggests that SonoVue experiences a permanent change at high ambient pressures (> 100 mmHg), most likely due to microbubble destruction and not due to a change in subharmonic sensitivity to ambient pressure.

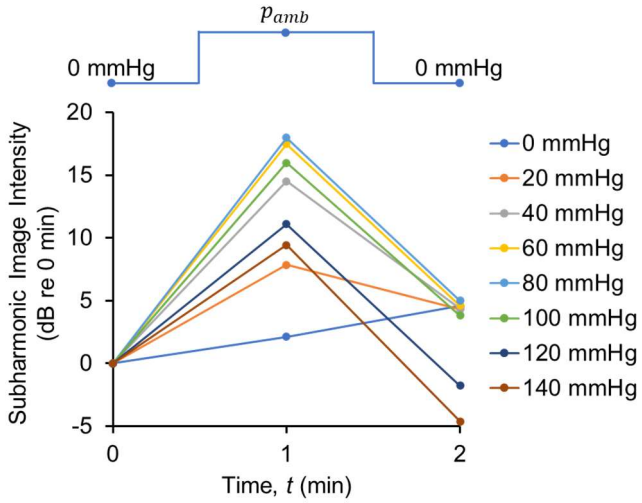

Figure 5.9*: Average image intensity of SonoVue as a function of time during prolonged ambient pressure cycling.*

A schematic of the applied ambient pressure (p_{amb}) as a function of time is shown above the plot. The ambient pressure was 0 mmHg (atmospheric pressure) at t = 0 min, increased to p_{amb} at t = 0.5 min, and decreased back to 0 mmHg at t = 1.5 min. The intensity values were normalized with respect to the value at t = 0 min. Images acquired with C5-1, 4.2 MHz, 18 cycles, pulse inversion, 120 kPa acoustic pressure)

5.4 DISCUSSION

In this study, we evaluated the effect of transmit frequency, bandwidth, pulsing scheme, and acoustic pressure on the subharmonic response of SonoVue microbubbles under ambient pressures of 0-140 mmHg. We covered a comprehensive range of imaging parameters for a total of 8 subharmonic imaging modes (**Table 5.2**) implemented on a clinical scanner and evaluated them in detail in vitro. We considered the subharmonic response during three transmit frequencies: 2.5 MHz (near resonance), 4.2 MHz (near twice resonance), and 7.0 MHz (above twice resonance). Transmitting at twice the resonance frequency resulted in the greatest change in subharmonic signal with ambient pressure, a 16 dB increase from 0-80 mmHg (+ 0.2 dB/mmHg) at 70 kPa acoustic pressure. High ambient pressures (> 100 mmHg) resulted in microbubble destruction that reduced subharmonic intensity, and not a change in subharmonic sensitivity.

5.4.1 Optimal subharmonic imaging mode for ambient pressure sensing for SonoVue

When transmitting near the resonance frequency ($SHI_{AM\ .5}$) with small number of cycles (broad bandwidth), little to no change in subharmonic intensity with ambient pressure was observed for all acoustic pressures with SonoVue [see **Figure 5.6**(a)**, Figure 5.7**(a)]. A small reduction in subharmonic intensity with ambient pressure (-0.05 dB/mmHg) was observed at low acoustic pressures (< 200 kPa), however, average spectra of RF data acquired at 170 kPa acoustic pressure [see **Figure 5.4**(a), **Figure 5.4**(b)] revealed a considerable overlap between the fundamental and subharmonic signals to the extent that they were not separable. Additionally, hydrophone measurements of the 2.5 MHz full amplitude pulse ($SHI_{2.5}$) showed that due to the wide bandwidth of the fundamental frequency, sound is directly transmitted at the subharmonic frequency [see **Figure 5.1**(b)], further confounding the UCA's response to ambient pressure. Our implementation of $SHI_{AM2.5}$ with pulses having only a few cycles was selected such that we could demonstrate the effect of the transmit bandwidth (**Table 5.1**) in order to draw useful comparisons. While studies with the commercially released subharmonic imaging mode (**Table 5.1**) often resulted in good correlation with ambient pressure, in-vitro studies with SonoVue [58], Sonazoid [31, 51, 59-61], and Definity [31, 51] driven near the resonance frequency have all found ambient pressure sensitivities near our measured sensitivity of -0.05 dB/mmHg with $SHI_{AM\ .5}$. Our results with $SHI_{AM2.5}$ simply say that the image intensity in our subharmonic mode decreased with increasing ambient pressure. However, the fact that we (in $SHI_{AM2.5}$) and other similar published

works (**Table 5.1**) used short pulses where the subharmonic component is not separable from the fundamental suggests that the observed ambient pressure sensitivity is not solely due to the subharmonic component. Additionally, in the studies referenced in **Table 5.1**, spectra of RF data are not provided to demonstrate and confirm the extent of subharmonic signal. Subharmonic imaging at the average resonance frequency may still be sensitive to ambient pressure changes, but a narrower transmit bandwidth would improve the detection of the subharmonic signal and enhance the sensitivity to ambient pressure.

Transmitting at twice the average resonance frequency and using pulses with long cycles ($SHI_{PI4.2}$) resulted in a significant increase in subharmonic intensity with ambient pressure for acoustic pressures less than 400 kPa with SonoVue [see **Figure 5.6**(b), **Figure 5.7**(b)]. The subharmonic change with ambient pressure was maximized at an acoustic pressure of 70 kPa, with a sensitivity of 0.20 dB/mmHg from 0-80 mmHg. The relationship of image intensity (subharmonic signal) with acoustic pressure agrees with prior works that have measured the subharmonic response of SonoVue at 3.0 MHz [58] and 4.0 MHz [62], however, we evaluated a more comprehensive range of acoustic and ambient pressure combinations in comparison to these studies. While previous studies have reported that the subharmonic generation threshold of lipid shelled microbubbles is dependent on both acoustic and ambient pressure [50, 58, 62], our results indicate that ambient pressures as low as 40 mmHg are sufficient to generate detectable subharmonic signal (dependent on the noise floor of the system) even at very low acoustic pressures (35 kPa). Our measured sensitivity is also slightly greater than recent in-vitro evaluations of SonoVue at 4 MHz with low acoustic pressures (120 kPa), where Nio, et al. [49] measured a sensitivity of 0.15 dB/mmHg from 0-75 mmHg, and Xu, et al. [62] measured a sensitivity of 0.16 dB/mmHg from 10-40 mmHg. Average spectra of RF data acquired at 70 kPa [see **Figure 5.4**(c), **Figure 5.4**(d)] showed a distinct subharmonic peak that increases with ambient pressure during both the full amplitude pulse ($SHI_{4.2}$) and after PI processing ($SHI_{PI4.2}$), and the reported image intensities are representative of subharmonic signal changes. We note that the subharmonic component is considered as an "even" harmonic, which PI detects while AM and AMPI detect nonlinear signal at all harmonic components but at a slightly lower level [28]. Small to negligible differences were observed between the nonlinear pulsing schemes at all acoustic pressures [see **Figure 5.8**], including the single pulse ($SHI_{4.2}$), suggesting that the narrow bandwidth (18 cycles at 4.2 MHz) used in these subharmonic modes was sufficient to separate the subharmonic and

fundamental components. The use of pulsing schemes may still offer some advantages by allowing the use of shorter pulses and improved spatial resolution. However, for our study we conservatively selected longer pulses to ensure good separation of the subharmonic component even without the use of a pulsing scheme. We also note that due to the dependence of ambient pressure sensitivity on acoustic pressure, the subharmonic response with AM and AMPI represents the combined subharmonic behavior across 2 acoustic pressures (half and full amplitude), while PI detects the subharmonic response from a single acoustic pressure. Therefore, the optimal subharmonic imaging mode that maximizes subharmonic signal change with ambient pressure was to transmit at twice the average resonance frequency, required longer than conventional imaging pulses (narrow transmit bandwidth), PI pulsing scheme ($SHI_{PI\ .2}$) and a low acoustic pressure of 70 kPa.

Subharmonic imaging above twice the resonance frequency with longer pulses ($SHI_{PI7.0}$) resulted in similar behavior to the $SHI_{PI\ .2}$ subharmonic mode, with subharmonic intensity increasing with ambient pressure at acoustic pressures < 400 kPa [see **Figure 5.6**(c), **Figure 5.7**(c)], and a distinct subharmonic peak observed in the average spectra of the RF data acquired at lower acoustic pressures (110 kPa) [see **Figure 5.4**(e), **Figure 5.4**(f)]. However, the detected change in subharmonic signal with ambient pressure (0-80 mmHg) was 0.12 dB/mmHg less with $SHI_{PI7.0}$ (0.08 dB/mmHg at 110 kPa) compared to $SHI_{PI4.2}$ (0.2 dB/mmHg at 70 kPa). One explanation for this reduced sensitivity may be due to the polydispersity of SonoVue, as the microbubbles that are at twice their resonance at 7 MHz, with an approximate radius of 0.75 μm [34], make up a smaller percentage of the total microbubble population compared to the average radius of 1.25 μm [37]. We also note that the receive processing of the imaging probe used for $SHI_{7.0}$ (eL18-4) is optimized for imaging depths of 1-4 cm, which may impact signal detection at our selected region of interest from 5-7 cm. Despite the reduced sensitivity, subharmonic imaging at 7 MHz still offers a viable method of detecting ambient pressure changes that can be useful for applications at shallow imaging depths such as interstitial fluid pressure measurements of breast cancer [63, 64].

5.4.2 Ambient pressure sensitivity of SonoVue

Figure 5.10 shows the subharmonic signal change with ambient pressure, referred to as sensitivity (dB/mmHg), as a function of acoustic pressure (calculated from the slopes observed in

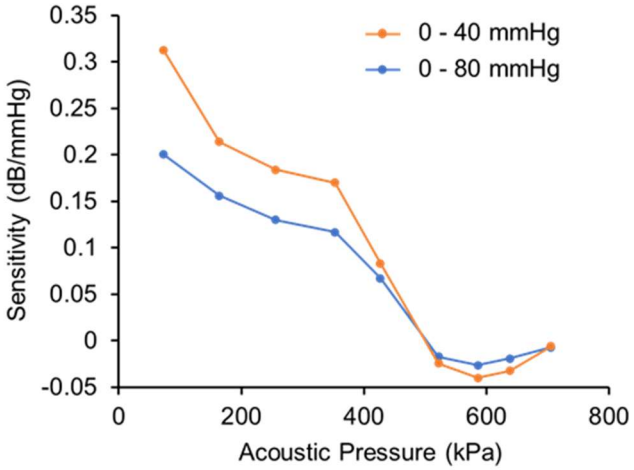

***Figure 5.10**: Average ambient pressure sensitivity as a function of acoustic pressure.*

Ambient pressure sensitivity is calculated from the change in subharmonic signal from 0-40 or 0-80 mmHg using the data presented in Fig. 7(b). Images acquired with C5-1, 4.2 MHz, 18 cycles, pulse inversion.

Figure 5.7(b)) with $SHI_{PI4.2}$. Sensitivity is shown for 2 ambient pressure ranges, 0-40 mmHg, which is the relevant pressure range for evaluating portal hypertension [65] and monitoring interstitial fluid pressure in solid tumors [66], and 0-80 mmHg, the relevant pressure range for evaluating pulmonary arteries and right heart chambers [67, 68]. SonoVue is sensitive to ambient pressure for acoustic pressures < 500 kPa and is maximized at 70 kPa with 0.31 dB/mmHg from 0-40 mmHg and 0.2 dB/mmHg from 0-80 mmHg. Similar to **Figure 5.7**(b), the sensitivity at 35 kPa is not shown in **Figure 5.10** due to no subharmonic signal detected from 0-20 mmHg. Our results also indicate that the optimal acoustic pressure for maximizing ambient pressure sensitivity with SonoVue (oscillating at twice the resonance frequency) is the minimum acoustic pressure (dependent on noise floor of scanner) needed to detect subharmonic signal at atmospheric pressure (70 kPa in this work). The increased sensitivity of SonoVue at lower acoustic pressures is an important consideration for clinical implementation of subharmonic imaging (**Table 5.1**) which has relied on an incident acoustic output algorithm to select patient specific acoustic pressures, typically during the "growth" phase of the subharmonic response [7]. However, due to the unique subharmonic response of SonoVue as a function acoustic pressure, confirmed with both our measurements [see **Figure 5.6**(b)] and in other in-vitro studies [58, 62], the acoustic output algorithm could be eliminated in favor of a constant, low acoustic pressure (< 200 kPa) that would offer ambient pressure sensitivity with SonoVue and avoid patient-specific calibration.

5.4.3 High ambient pressures results in microbubble destruction

After evaluation of subharmonic images ($SHI_{PI4.2}$) during prolonged ambient pressure cycling with SonoVue [see **Figure 5.9**], we observed that the high ambient pressures (> 100 mmHg) induce a permanent reduction in subharmonic signal, which we attribute to possible microbubble destruction due to static pressure and not a change in subharmonic sensitivity. When the chamber was not pressurized (p_{amb} = 0 mmHg) and observed for 2 minutes the subharmonic intensity increased by 2.2 dB/min to the reference intensity of 4.4 dB at t = 2 min. This time-dependence of the subharmonic response may be related to the diffusivity of the sulfur hexafluoride gas from SonoVue [37, 69] to the surrounding medium [70] and demonstrates the importance of comparing subharmonic intensities at the same time relative to when microbubbles were injected into the chamber. When the chamber was depressurized after low ambient pressures ($p_{amb} \leq$ 100 mmHg) the subharmonic intensity returned to the reference intensity (4.4 dB) indicating a nondestructive ambient pressure range exists from 0-100 mmHg. During high ambient pressures (p_{amb} > 100 mmHg) the overall subharmonic intensity was reduced, and after depressurizing (t = 2 min) the subharmonic intensity was below the reference intensity, decreased by 6 dB when p_{amb} was 120 mmHg and decreased by 9 dB when p_{amb} was 140 mmHg. Our results also agree with Nio, et al. [49] who reported similar descending subharmonic intensity at high ambient pressures (> 125 mmHg) with SonoVue and speculated that the decrease is due to microbubble buckling and destruction. This is important to consider when using subharmonic imaging in patients with severe heart disease, where ambient pressures can exceed 100 mmHg [3] and may require new techniques such as ultrafast imaging to measure dissolution time [47, 71]. The increase in subharmonic signal over time must also be considered for in-vivo work with SonoVue, as clinical implementation of subharmonic imaging (**Table 5.1**) currently utilizes continuous infusions for microbubble delivery which if paired with SonoVue may result in an ambient pressure sensitivity that changes over time. Therefore, subharmonic imaging techniques compatible with bolus injections should be developed to eliminate variation in ambient pressure sensitivity dependent on evaluation time.

5.4.4 Limitations of in-vitro evaluation

In this study we used a pressurized chamber placed in a water tank to evaluate the subharmonic response SonoVue and several subharmonic imaging modes. This allowed for direct

assessment of freshly prepared microbubbles covering a wide range of acoustic conditions to accurately quantify the change in subharmonic signal to ambient pressure. However, the simplicity of in vitro setups eliminates some factors that are present in-vivo. Microbubbles were injected directly from the prepared dilution into the chamber without first filtering the dilution to remove any large microbubbles, a function performed by the lungs in-vivo [72]. While the number of large bubbles only constitute a small percentage of the microbubble population [37, 38], the presence of these microbubbles could potentially influence the results in-vitro. Another factor was the absence of flow in our experimental setup, requiring a slow frame rate (0.33 Hz) to protect microbubbles from destruction during repeated scanning at the higher acoustic pressure. Still, our measurements of the subharmonic response of SonoVue as a function of acoustic pressure [see **Figure 5.6**(b)] indicate that sensitivity to ambient pressure is maximized at nondestructive acoustic pressures below the threshold for microbubble shell rupture (< 200 kPa) [see **Figure 5.10**] [39, 40]. By optimizing subharmonic imaging at low acoustic pressures, clinical implementation of $SHI_{PI\ .2}$ can be performed with real-time frame rates and does not require triggering methods (e.g., electrocardiogram triggering) that are necessary for high acoustic pressure techniques [43, 44].

Transmit beamforming is another important consideration, as the ambient pressure sensitivity is highly dependent on acoustic pressure. All subharmonic intensities described in this work represent the average intensity from the region of interest placed at image depths of 5-7 cm [see **Figure 5.2**(c)]. Comparing this region to the spatial pressure distribution of $SHI_{4.2}$ [see **Figure 5.1**(f)]**,** the 5-7 cm range corresponds to acoustic pressures within 60% (0-4 dB) of the maximum pressure delivered at 7 cm. However, microbubbles at shallower depths (2-5 cm) are exposed to lower acoustic pressures and will exhibit a different subharmonic response compared to microbubbles positioned near the maximum acoustic pressure [see 700 kPa images in **Figure 5.5**]. The dependence of subharmonic response on acoustic pressure presents a problem for clinical implementation of subharmonic imaging, as exact acoustic pressures cannot be known in-vivo. A potential solution is to select transmit beamforming that generates a more uniform acoustic pressure distribution such that ambient pressure sensitivity is uniform throughout the imaging plane. Additionally, the effect of attenuation, which is dependent on both imaging depth and transit frequency, must also be considered and may impact detected subharmonic signal during in-vivo evaluations.

5.5 Conclusion

In this study, we evaluated the effect of 3 different transmit frequencies (near resonance, twice resonance and greater than twice resonance), bandwidth, pulsing scheme, and acoustic pressure on the subharmonic response of SonoVue microbubbles under ambient pressures of 0-140 mmHg. Transmitting at twice the resonance frequency (4.2 MHz) results in the greatest change in subharmonic signal with ambient pressure, a 16 dB increase from 0-80 mmHg (+ 0.2 dB/mmHg) at 70 kPa acoustic pressure. This result is important because it eliminates the need for patient-specific acoustic pressures. SonoVue is also particularly sensitive to low ambient pressures (0-40 mmHg), relevant for monitoring IFP in solid tumors. Prolonged exposure to high ambient pressures (> 100 mmHg) resulted in microbubble destruction that impacts subharmonic intensity. The findings in this work provide evidence of the utility of SonoVue for ambient pressure sensing at low acoustic pressures.

5.6 Acknowledgements

This work was supported by NIH grant R01EB032655. SonoVue was generously supplied by Bracco (Bracco Suisse SA, Geneva, Switzerland).

5.7 References

[1] J. K. Dave *et al.*, "Noninvasive LV pressure estimation using subharmonic emissions from microbubbles," *JACC: Cardiovascular Imaging,* vol. 5, no. 1, pp. 87-92, 2012. doi: 10.1016/j.jcmg.2011.08.017.

[2] J. K. Dave *et al.*, "Subharmonic microbubble emissions for noninvasively tracking right ventricular pressures," *American Journal of Physiology-Heart and Circulatory Physiology,* vol. 303, no. 1, pp. H126-H132, 2012. doi: 10.1152/ajpheart.00560.2011.

[3] J. K. Dave *et al.*, "Non-invasive intra-cardiac pressure measurements using subharmonic-aided pressure estimation: proof of concept in humans," *Ultrasound in medicine & biology,* vol. 43, no. 11, pp. 2718-2724, 2017. doi: 10.1016/j.ultrasmedbio.2017.07.009.

[4] C. Esposito *et al.*, "Noninvasive evaluation of cardiac chamber pressures using subharmonic-aided pressure estimation with definity microbubbles," *Cardiovascular Imaging,* vol. 16, no. 2, pp. 224-235, 2023. doi:

[5] C. Esposito *et al.*, "Evaluation of intracardiac pressures using subharmonic-aided pressure estimation with sonazoid microbubbles," *Radiology: Cardiothoracic Imaging,* vol. 6, no. 1, p. e230153, 2024. doi: 10.1148/ryct.230153.

[6] J. K. Dave *et al.*, "Investigating the efficacy of subharmonic aided pressure estimation for portal vein pressures and portal hypertension monitoring," *Ultrasound in medicine & biology,* vol. 38, no. 10, pp. 1784-1798, 2012. doi: 10.1016/j.ultrasmedbio.2012.06.013.

[7] J. K. Dave *et al.*, "On the implementation of an automated acoustic output optimization algorithm for subharmonic aided pressure estimation," (in eng), *Ultrasonics,* vol. 53, no. 4, pp. 880-8, Apr 2013. doi: 10.1016/j.ultras.2012.12.010.

[8] J. R. Eisenbrey *et al.*, "Chronic Liver Disease: Noninvasive Subharmonic Aided Pressure Estimation of Hepatic Venous Pressure Gradient," *Radiology,* vol. 268, no. 2, pp. 581-588, 2013. doi: 10.1148/radiol.13121769.

[9] I. Gupta *et al.*, "Diagnosing Portal Hypertension with Noninvasive Subharmonic Pressure Estimates from a US Contrast Agent," *Radiology,* vol. 298, no. 1, pp. 104-111, 2021. doi: 10.1148/radiol.2020202677.

[10] F. Forsberg *et al.*, "Subharmonic and Endoscopic Contrast Imaging of Pancreatic Masses: A Pilot Study," *Journal of Ultrasound in Medicine,* vol. 37, no. 1, pp. 123-129, 2018. doi: 10.1002/jum.14310.

[11] B. Bozkurt *et al.*, "Universal definition and classification of heart failure: a report of the heart failure society of America, heart failure association of the European society of cardiology, Japanese heart failure society and writing committee of the universal definition of heart failure," *Journal of cardiac failure,* vol. 27, no. 4, pp. 387-413, 2021. doi: 10.1016/j.cardfail.2021.01.022.

[12] M. Arrigo *et al.*, "Acute heart failure," *Nature Reviews Disease Primers,* vol. 6, no. 1, p. 16, 2020. doi: 10.1038/s41572-020-0151-7.

[13] P. Ginès, A. Krag, J. G. Abraldes, E. Solà, N. Fabrellas, and P. S. Kamath, "Liver cirrhosis," *The Lancet,* vol. 398, no. 10308, pp. 1359-1376, 2021. doi: 10.1016/S0140-6736(21)01374-X.

[14] D. E. Kaplan *et al.*, "AASLD Practice Guidance on risk stratification and management of portal hypertension and varices in cirrhosis," *Hepatology,* vol. 79, no. 5, pp. 1180-1211, 2024. doi: 10.1097/HEP.0000000000000647.

[15] M. Humbert *et al.*, "2022 ESC/ERS Guidelines for the diagnosis and treatment of pulmonary hypertension: Developed by the task force for the diagnosis and treatment of pulmonary hypertension of the European Society of Cardiology (ESC) and the European Respiratory Society (ERS). Endorsed by the International Society for Heart and Lung Transplantation (ISHLT) and the European Reference Network on rare respiratory diseases (ERN-LUNG)," *European heart journal,* vol. 43, no. 38, pp. 3618-3731, 2022. doi: 10.1093/eurheartj/ehac237.

[16] S. Bousseau, R. S. Fais, S. Gu, A. Frump, and T. Lahm, "Pathophysiology and new advances in pulmonary hypertension," *BMJ medicine,* vol. 2, no. 1, p. e000137, 2023. doi: 10.1136/bmjmed-2022-000137.

[17] G. W. Hawryluk *et al.*, "Intracranial pressure: current perspectives on physiology and monitoring," *Intensive care medicine,* vol. 48, no. 10, pp. 1471-1481, 2022. doi: 10.1007/s00134-022-06786-y.

[18] M. M. Treggiari, N. Schutz, N. D. Yanez, and J.-A. Romand, "Role of intracranial pressure values and patterns in predicting outcome in traumatic brain injury: a systematic review," *Neurocritical care,* vol. 6, no. 2, pp. 104-112, 2007. doi: 10.1007/s12028-007-0012-1.

[19] Y. Chen *et al.*, "Right heart catheterization-related complications: a review of the literature and best practices," *Cardiology in Review,* vol. 28, no. 1, pp. 36-41, 2020. doi: 10.1097/CRD.0000000000000270.

[20] M. A. Al-Hijji *et al.*, "Safety and risk of major complications with diagnostic cardiac catheterization," *Circulation: Cardiovascular Interventions,* vol. 12, no. 7, p. e007791, 2019. doi: 10.1161/CIRCINTERVENTIONS.119.007791.

[21] A. S. Oseran, S. Ati, W. B. Feldman, S. Gondi, R. W. Yeh, and R. K. Wadhera, "Assessment of prices for cardiovascular tests and procedures at top-ranked US hospitals," *JAMA Internal Medicine,* vol. 182, no. 9, pp. 996-999, 2022. doi: 10.1001/jamainternmed.2022.2602.

[22] B. V. Scheer, A. Perel, and U. J. Pfeiffer, "Clinical review: complications and risk factors of peripheral arterial catheters used for haemodynamic monitoring in anaesthesia and intensive care medicine," *Critical care,* vol. 6, no. 3, p. 199, 2002. doi: 10.1186/cc1489.

[23] Y. Hai, W. Chong, J. R. Eisenbrey, and F. Forsberg, "Network meta-analysis: noninvasive imaging modalities for identifying clinically significant portal hypertension," *Digestive diseases and sciences,* vol. 67, no. 7, pp. 3313-3326, 2022. doi: 10.1007/s10620-021-07168-y.

[24] S. Parasuraman *et al.*, "Assessment of pulmonary artery pressure by echocardiography—a comprehensive review," *IJC Heart & Vasculature,* vol. 12, pp. 45-51, 2016. doi: 10.1016/j.ijcha.2016.05.011.

[25] J.-R. Ni *et al.*, "Diagnostic accuracy of transthoracic echocardiography for pulmonary hypertension: a systematic review and meta-analysis," *BMJ open,* vol. 9, no. 12, p. e033084, 2019. doi: 10.1136/bmjopen-2019-033084.

[26] S. Janda, N. Shahidi, K. Gin, and J. Swiston, "Diagnostic accuracy of echocardiography for pulmonary hypertension: a systematic review and meta-analysis," *Heart,* vol. 97, no. 8, pp. 612-622, 2011. doi: 10.1136/hrt.2010.212084.

[27] J. N. Amoore, "Oscillometric sphygmomanometers: a critical appraisal of current technology," *Blood pressure monitoring,* vol. 17, no. 2, pp. 80-88, 2012. doi: 10.1097/MBP.0b013e32835026b0.

[28] M. A. Averkiou, M. F. Bruce, J. E. Powers, P. S. Sheeran, and P. N. Burns, "Imaging methods for ultrasound contrast agents," *Ultrasound in medicine & biology,* vol. 46, no. 3, pp. 498-517, 2020. doi: 10.1016/j.ultrasmedbio.2019.11.004.

[29] W. T. Shi *et al.*, "Subharmonic imaging with microbubble contrast agents: initial results," *Ultrasonic imaging,* vol. 21, no. 2, pp. 79-94, 1999. doi: 10.1177/016173469902100201.

[30] W. Shi, F. Forsberg, J. Raichlen, L. Needleman, and B. Goldberg, "Pressure dependence of subharmonic signals from contrast microbubbles," *Ultrasound in Medicine & Biology,* vol. 25, no. 2, pp. 275-283, 1999/02/01/ 1999. doi: 10.1016/S0301-5629(98)00163-X.

[31] J. K. Dave *et al.*, "Noninvasive estimation of dynamic pressures in vitro and in vivo using the subharmonic response from microbubbles," (in eng), *IEEE Trans Ultrason Ferroelectr Freq Control,* vol. 58, no. 10, pp. 2056-66, Oct 2011. doi: 10.1109/tuffc.2011.2056.

[32] K. B. Bader and C. K. Holland, "Gauging the likelihood of stable cavitation from ultrasound contrast agents," *Physics in Medicine & Biology,* vol. 58, no. 1, p. 127, 2012. doi: 10.1088/0031-9155/58/1/127.

[33] Q. Wu *et al.*, "Challenges in classifying cavitation: Correlating high-speed optical imaging and passive acoustic mapping of cavitation dynamics," *The Journal of the Acoustical Society of America,* vol. 156, no. 5, pp. 3608-3620, 2024. doi: 10.1121/10.0034426.

[34] J. Chomas, P. Dayton, D. May, and K. Ferrara, "Nondestructive subharmonic imaging," *IEEE Transactions on Ultrasonics, Ferroelectrics, and Frequency Control,* vol. 49, no. 7, pp. 883-892, 2002. doi: 10.1109/TUFFC.2002.1020158.

[35] P. J. Frinking, N. de Jong, and E. I. Cespedes, "Scattering properties of encapsulated gas bubbles at high ultrasound pressures," *The Journal of the Acoustical Society of America,* vol. 105, no. 3, pp. 1989-1996, 1999. doi: 10.1121/1.426732.

[36] P. M. Shankar, P. D. Krishna, and V. L. Newhouse, "Subharmonic backscattering from ultrasound contrast agents," *The Journal of the Acoustical Society of America,* vol. 106, no. 4, pp. 2104-2110, 1999. doi: 10.1121/1.428142.

[37] J.-M. Gorce, M. Arditi, and M. Schneider, "Influence of Bubble Size Distribution on the Echogenicity of Ultrasound Contrast Agents: A Study of SonoVue™," *Investigative Radiology,* vol. 35, no. 11, pp. 661-671, 2000. doi:

[38] P. C. Sontum, "Physicochemical Characteristics of Sonazoid™, A New Contrast Agent for Ultrasound Imaging," *Ultrasound in Medicine & Biology,* vol. 34, no. 5, pp. 824-833, 2008/05/01/ 2008. doi: 10.1016/j.ultrasmedbio.2007.11.006.

[39] J. Sijl *et al.*, "Subharmonic behavior of phospholipid-coated ultrasound contrast agent microbubbles," *The Journal of the Acoustical Society of America,* vol. 128, no. 5, pp. 3239-3252, 2010. doi: 10.1121/1.3493443.

[40] P. Marmottant *et al.*, "A model for large amplitude oscillations of coated bubbles accounting for buckling and rupture," *The Journal of the Acoustical Society of America,* vol. 118, no. 6, pp. 3499-3505, 2005. doi: 10.1121/1.2109427.

[41] N. de Jong *et al.*, "“Compression-Only” Behavior of Phospholipid-Coated Contrast Bubbles," *Ultrasound in Medicine & Biology,* vol. 33, no. 4, pp. 653-656, 2007/04/01/ 2007. doi: 10.1016/j.ultrasmedbio.2006.09.016.

[42] P. J. A. Frinking, E. Gaud, J. Brochot, and M. Arditi, "Subharmonic scattering of phospholipid-shell microbubbles at low acoustic pressure amplitudes," *IEEE Transactions on Ultrasonics, Ferroelectrics, and Frequency Control,* vol. 57, no. 8, pp. 1762-1771, 2010. doi: 10.1109/TUFFC.2010.1614.

[43] S. R. Wilson, P. N. Burns, D. Muradali, J. A. Wilson, and X. Lai, "Harmonic hepatic US with microbubble contrast agent: initial experience showing improved characterization of

hemangioma, hepatocellular carcinoma, and metastasis," *Radiology,* vol. 215, no. 1, pp. 153-161, 2000. doi: 10.1148/radiology.215.1.r00ap08153.

[44] H. Becher, K. Tiemann, S. Kuntz-Hehner, H. Omran, and T. Schlosser, "Diagnostic impact of contrast echocardiography for assessment of left ventricular function and myocardial perfusion in patients with coronary artery disease," *European Heart Journal Supplements,* vol. 4, no. suppl_C, pp. C12-C21, 2002. doi: 10.1016/s1520-765x(02)90095-7.

[45] C. Tremblay-Darveau, R. Williams, and P. N. Burns, "Measuring Absolute Blood Pressure Using Microbubbles," *Ultrasound in Medicine & Biology,* vol. 40, no. 4, pp. 775-787, 2014/04/01/ 2014. doi: 10.1016/j.ultrasmedbio.2013.10.017.

[46] X. Qiao, Y. Wen, J. Yu, A. Bouakaz, Y. Zong, and M. Wan, "Noninvasive Pressure Estimation Based on the Subharmonic Response of SonoVue: Application to Intracranial Blood Pressure Assessment," *IEEE Transactions on Ultrasonics, Ferroelectrics, and Frequency Control,* vol. 69, no. 3, pp. 957-966, 2022. doi: 10.1109/TUFFC.2021.3138100.

[47] A. Bouakaz, P. J. A. Frinking, N. de Jong, and N. Bom, "Noninvasive measurement of the hydrostatic pressure in a fluid-filled cavity based on the disappearance time of micrometer-sized free gas bubbles," *Ultrasound in Medicine & Biology,* vol. 25, no. 9, pp. 1407-1415, 1999/11/01/ 1999. doi: 10.1016/S0301-5629(99)00109-X.

[48] T. Faez, G. Renaud, M. Defontaine, S. Calle, and N. de Jong, "Dynamic manipulation of the subharmonic scattering of phospholipid-coated microbubbles," *Physics in Medicine & Biology,* vol. 56, no. 19, p. 6459, 2011/09/20 2011. doi: 10.1088/0031-9155/56/19/018.

[49] A. Q. Nio *et al.*, "Optimal control of SonoVue microbubbles to estimate hydrostatic pressure," *IEEE Transactions on Ultrasonics, Ferroelectrics, and Frequency Control,* vol. 67, no. 3, pp. 557-567, 2019. doi: 10.1109/TUFFC.2019.2948759.

[50] R. H. Azami, F. Forsberg, J. R. Eisenbrey, and K. Sarkar, "Ambient Pressure Sensitivity of the Subharmonic Response of Coated Microbubbles: Effects of Acoustic Excitation Parameters," *Ultrasound in Medicine & Biology,* vol. 49, no. 7, pp. 1550-1560, 2023/07/01/ 2023. doi: 10.1016/j.ultrasmedbio.2023.02.019.

[51] H. Mayer *et al.*, "Investigation into the subharmonic response of three contrast agents in static and dynamic flow environments using a commercially available diagnostic ultrasound scanner," *Ultrasound in Medicine & Biology,* vol. 50, no. 11, pp. 1731-1738, 2024. doi: 10.1016/j.ultrasmedbio.2024.07.015.

[52] A. C. Larson *et al.*, "Contrast-enhanced subharmonic aided pressure estimation for assessment of intracranial pressure in vivo," *Pediatric Radiology,* vol. 53, no. 8, pp. 1640-1647, 2023/07/01 2023. doi: 10.1007/s00247-023-05637-2.

[53] H. Kuroda *et al.*, "Novel subharmonic-aided pressure estimation for identifying high-risk esophagogastric varices," *Journal of Gastroenterology,* vol. 60, no. 2, pp. 187-196, 2025/02/01 2025. doi: 10.1007/s00535-024-02161-4.

[54] S. B. Keller, P. S. Sheeran, and M. A. Averkiou, "Cavitation therapy monitoring of commercial microbubbles with a clinical scanner," *IEEE Transactions on Ultrasonics,*

Ferroelectrics, and Frequency Control, vol. 68, no. 4, pp. 1144-1154, 2020. doi: 10.1109/TUFFC.2020.3034532.

[55] D. R. Morel *et al.*, "Human pharmacokinetics and safety evaluation of SonoVue™, a new contrast agent for ultrasound imaging," *Investigative radiology,* vol. 35, no. 1, p. 80, 2000. doi:

[56] X. Qiao, Y. Wen, J. Yu, A. Bouakaz, Y. Zong, and M. Wan, "Noninvasive pressure estimation based on the subharmonic response of SonoVue: Application to intracranial blood pressure assessment," *IEEE Transactions on Ultrasonics, Ferroelectrics, and Frequency Control,* vol. 69, no. 3, pp. 957-966, 2021. doi: 10.1109/TUFFC.2021.3138100.

[57] C. P. Keravnou, C. Mannaris, and M. A. Averkiou, "Accurate measurement of microbubble response to ultrasound with a diagnostic ultrasound scanner," *IEEE Transactions on Ultrasonics, Ferroelectrics, and Frequency Control,* vol. 62, no. 1, pp. 176-184, 2015. doi: 10.1109/TUFFC.2014.006664.

[58] R. H. Azami, F. Forsberg, J. R. Eisenbrey, and K. Sarkar, "Acoustic response and ambient pressure sensitivity characterization of SonoVue for noninvasive pressure estimation," *The Journal of the Acoustical Society of America,* vol. 155, no. 4, pp. 2636-2645, 2024. doi: 10.1121/10.0025690.

[59] J. K. Dave *et al.*, "Subharmonic microbubble emissions for noninvasively tracking right ventricular pressures," (in eng), *Am J Physiol Heart Circ Physiol,* vol. 303, no. 1, pp. H126-32, Jul 2012. doi: 10.1152/ajpheart.00560.2011.

[60] I. Gupta, J. R. Eisenbrey, P. Machado, M. Stanczak, K. Wallace, and F. Forsberg, "On Factors Affecting Subharmonic-aided Pressure Estimation (SHAPE)," *Ultrasonic Imaging,* vol. 41, no. 1, pp. 35-48, 2019. doi: 10.1177/0161734618812083.

[61] J. K. Dave *et al.*, "Noninvasive estimation of dynamic pressures in vitro and in vivo using the subharmonic response from microbubbles," *IEEE transactions on ultrasonics, ferroelectrics, and frequency control,* vol. 58, no. 10, pp. 2056-2066, 2011. doi: 10.1109/TUFFC.2011.2056.

[62] G. Xu *et al.*, "Subharmonic Scattering of SonoVue Microbubbles Within 10–40-mmHg Overpressures In Vitro," *IEEE Transactions on Ultrasonics, Ferroelectrics, and Frequency Control,* vol. 68, no. 12, pp. 3583-3591, 2021. doi: 10.1109/TUFFC.2021.3101694.

[63] Y. Wang *et al.*, "Noninvasive Estimation of Tumor Interstitial Fluid Pressure from Subharmonic Scattering of Ultrasound Contrast Microbubbles," *Biosensors,* vol. 13, no. 5, p. 528, 2023. doi: 10.3390/bios13050528.

[64] V. G. Halldorsdottir *et al.*, "Subharmonic-aided pressure estimation for monitoring interstitial fluid pressure in tumors: Calibration and treatment with paclitaxel in breast cancer xenografts," *Ultrasound in medicine & biology,* vol. 43, no. 7, pp. 1401-1410, 2017. doi: 10.1016/j.ultrasmedbio.2017.02.011.

[65] E. Moitinho *et al.*, "Prognostic value of early measurements of portal pressure in acute variceal bleeding," *Gastroenterology,* vol. 117, no. 3, pp. 626-631, 1999. doi: 10.1016/S0016-5085(99)70455-5.

[66] A. Mohammadabadi *et al.*, "Pulsed focused ultrasound lowers interstitial fluid pressure and increases nanoparticle delivery and penetration in head and neck squamous cell carcinoma

xenograft tumors," *Physics in Medicine & Biology,* vol. 65, no. 12, p. 125017, 2020. doi: 10.1088/1361-6560/ab9705.

[67] H. W. Farber, A. J. Foreman, D. P. Miller, and M. D. McGoon, "REVEAL Registry: correlation of right heart catheterization and echocardiography in patients with pulmonary arterial hypertension," *Congestive heart failure,* vol. 17, no. 2, pp. 56-63, 2011. doi: 10.1111/j.1751-7133.2010.00202.x.

[68] M. McGoon and D. Miller, "REVEAL: a contemporary US pulmonary arterial hypertension registry," ed: European Respiratory Society, 2012.

[69] C. Greis, "Technology overview: SonoVue (Bracco, Milan)," *European radiology,* vol. 14, pp. P11-5, 2004. doi:

[70] E. Kanbar, D. Fouan, C. A. Sennoga, A. A. Doinikov, and A. Bouakaz, "Impact of Filling Gas on Subharmonic Emissions of Phospholipid Ultrasound Contrast Agents," *Ultrasound in Medicine & Biology,* vol. 43, no. 5, pp. 1004-1015, 2017/05/01/ 2017. doi: 10.1016/j.ultrasmedbio.2016.12.013.

[71] P. S. Epstein and M. S. Plesset, "On the stability of gas bubbles in liquid-gas solutions," *Journal of Chemical physics,* vol. 18, no. 11, pp. 1505-1509, 1950. doi: 10.1063/1.1747520.

[72] B. D. Butler and B. A. Hills, "The lung as a filter for microbubbles," *Journal of Applied Physiology,* vol. 47, no. 3, pp. 537-543, 1979. doi: 10.1152/jappl.1979.47.3.537.

CHAPTER 6. AMBIENT PRESSURE SENSITIVITY OF SONAZOID MICROBUBBLES AT RESONANCE FREQUENCY

Abstract

Subharmonic imaging for ambient pressure estimation is a noninvasive alternative to direct pressure catheter measurements that are currently used to diagnose multiple disease processes and monitor interstitial fluid pressure. Sonazoid, a microbubble contrast agent, is commonly used in subharmonic imaging due to its high sensitivity to ambient pressure. However, clinical implementations of subharmonic imaging employ frequencies below the resonance frequency of Sonazoid, requiring high acoustic pressure to generate subharmonic signal. We investigated transmitting long pulses (18 cycles) at the resonance frequency of Sonazoid microbubbles (4.2 MHz) and detecting the subharmonic component with narrow receive bandwidth in a pulse inversion scheme as a sensitive method to detect ambient pressure. We used an in-vitro pressure chamber with transparent acoustic windows and filled with Sonazoid microbubbles to vary the ambient pressure (0-140 mmHg) while collecting subharmonic images. We considered a range of acoustic pressures (70-700 kPa) to investigate the subharmonic response of Sonazoid above and below the acoustic pressure threshold of microbubble shell disruption. Native linearized image data were used to accurately measure the subharmonic signal in the images. During low acoustic pressures (< 200 kPa), we observed that the subharmonic response of Sonazoid can slightly increase with increasing ambient pressure. At high acoustic pressures (> 500 kPa) Sonazoid exhibits a slight negative sensitivity with ambient pressure, with a 4.6 dB decrease from 0-60 mmHg (-0.08 mmHg) at 640 kPa acoustic pressure. We also observed a significant difference in subharmonic responses of SonoVue and Sonazoid microbubbles driven at 4.2 MHz, with SonoVue exhibiting a higher sensitivity to ambient pressure for acoustic pressures < 400 kPa. The findings suggest that further investigation of Sonazoid in subharmonic imaging for ambient pressure sensing is necessary.

6.1 INTRODUCTION

Sonazoid (GE HealthCare, Oslo, Norway) a clinically approved contrast agent, is commonly used for subharmonic imaging studies (**Table *5.1***). Although Sonazoid shares a similar physiochemical structure to SonoVue (a phospholipid monolayer encapsulating sulfur hexafluoride gas [1, 2]), with a lipid monolayer (hydrogenated egg phosphatidyl serine) encapsulating an inert gas (perfluorobutane gas), Sonazoid exhibits a higher average resonance frequency, near 4 MHz [3, 4], and increased shell material stiffness compared to SonoVue [5, 6]. Despite both SonoVue and Sonazoid being lipid-shelled microbubbles, the differences in material and acoustic properties may result in subharmonic responses specific to each agent [7].

Most subharmonic imaging studies that use Sonazoid as an ambient pressure sensor drive the contrast agent at a transmit frequency of 2.5 MHz (**Table *5.1***), below its average resonance frequency. The selection of 2.5 MHz as the transmit frequency is often attributed to the in-vitro study by Dave, et al. [8], who evaluated the ambient pressure sensitivity of Sonazoid at a range of transmit frequencies (2.5-6.6 MHz) and acoustic pressures (0.35-0.6 MPa). The ambient pressure sensitivity of Sonazoid was optimized when driven at 2.5 MHz at 0.35 MPa acoustic pressure, however other transmit frequencies that were near resonance (4.4 MHz) or above resonance (5, 6.6 MHz) demonstrated similar sensitivities to ambient pressure (-0.07 dB/mmHg) during the same acoustic pressure. Wang, et al. [9] also evaluated the subharmonic response of Sonazoid when driven at its resonance frequency during an acoustic pressure range of 300-800 kPa, where 550 kPa was identified as the optimal acoustic pressure producing an ambient pressure sensitivity of -0.15 dB/mmHg. Notably, the studies by Halldorsdottir [8] and Wang [9] both used high acoustic pressures (> 200 kPa) that exceed the threshold for shell disruption and lipid shedding [10, 11]. Consequently, the subharmonic response of Sonazoid at low acoustic pressure (< 200 kPa) has yet to be explored, especially at higher transmit frequencies that may reduce the subharmonic threshold.

In this work we perform an initial study evaluating the change in subharmonic signal with ambient pressure of Sonazoid when driven near its resonance frequency. We considered a range of acoustic pressures (70-700 kPa) to investigate the subharmonic response of Sonazoid above and below the acoustic pressure threshold of microbubble shell disruption. Sonazoid was evaluated using the $SHI_{PI4.2}$ subharmonic mode (4.2 MHz, 18 cycles, pulse inversion), found to be the optimal mode with SonoVue in **Chapter 5**. A custom-built chamber pressurized to physiologically

relevant static ambient pressures (0-100 mmHg) was used to evaluate change in subharmonic signal with ambient pressure. We used Sonazoid diluted to concentrations equivalent to clinical doses. The microbubble solutions were constantly stirred and imaged at a slow frame rate (0.33 Hz) to minimize microbubble destruction during the experiments. Native linearized image data (with the logarithmic compression removed) were recorded and post-processed to measure changes in image intensity. The subharmonic signal change per unit ambient pressure is the key metric used to evaluate all the ultrasound parameters and allows for direct comparisons of the ambient pressure sensitivity of SonoVue and Sonazoid.

6.2 Material and Methods

6.2.1 Microbubble preparation

Sonazoid was reconstituted according to the manufacturer instructions, resulting in base concentrations of ~10^8 microbubbles/mL [12], and all measurements were completed within 3 hours of preparing the vial. Prior to each experiment, a new microbubble dilution was prepared by extracting a small volume from the vial, mixing in deionized water for 30 s, and then injecting into the chamber, resulting in a concentration of ~10^4 microbubbles/mL (same concentration used with SonoVue). The microbubble concentration was selected to be representative of clinical concentrations [13] when mixed in 5 L blood. To control for variation from different dilution times observed in literature [14], all experiments began 2 minutes from when agent was extracted from the starting vial.

6.2.2 Experimental protocol

To measure subharmonic signal change of Sonazoid with ambient pressure, we repeated the procedure of increasing acoustic pressure during static ambient pressures described in **Section 5.2.4** with the $SHI_{PI4.2}$ mode (**Table *5.2***). Briefly, the chamber [see **Figure 5.2**(a)] was set to a static ambient pressure between 0-100 mmHg, allowed to mix for 30s, and then the acoustic pressure was gradually increased. At each acoustic pressure, an image loop was recorded consisting of 5 frames captured at a frame rate of 0.33 Hz (once every 3 seconds) to minimize bubble destruction when evaluating the higher acoustic pressures. To avoid signal saturation at high acoustic pressures (> 400 kPa), the 2D analog gain of the scanner was reduced by 8 dB relative to the gain selected for subharmonic imaging at acoustic pressures less than 400 kPa. A new

microbubble dilution was used for each ambient pressure, with each experiment being completed within 10 minutes of extracting contrast agent from the starting vial. Native DICOM (linearized image data) were collected and post-processed with QLAB (Philips Healthcare, Bothell, WA, USA) using a region of interest [see **Fig. 5.2**(c)] spanning an image depth of 5-7 cm to measure linearized image intensity per frame. The average image intensity over 5 frames was calculated.

6.3 RESULTS

Figure 6.1 shows subharmonic images ($SHI_{PI4.2}$) of Sonazoid at acoustic pressures of 70, 430, and 700 kPa at ambient pressures of 0, 40, and 80 mmHg. We note that the images at an acoustic pressure of 70 kPa have an extra 2D gain of 8 dB compared to the images at 430 and 700 kPa. At all acoustic pressures, the image intensity when using Sonazoid shows little to no change with increasing ambient pressure. At 700 kPa, we observe a hyperechoic region from 6-9 cm, similar to subharmonic images with SonoVue at 700 kPa [see **Figure 5.5**], but the image brightness in shallower depths does not change with ambient pressure.

Figure 6.2 shows the average subharmonic image intensity as a function of acoustic pressure (**Figure 6.2**(a)) and as a function of ambient pressure (**Figure 6.2**(b)) for ambient pressures of 0-100 mmHg. **Figure 6.2**(a) shows that the subharmonic intensity gradually increases with acoustic pressure, and more rapidly increases when acoustic pressure > 500 kPa. Little to no

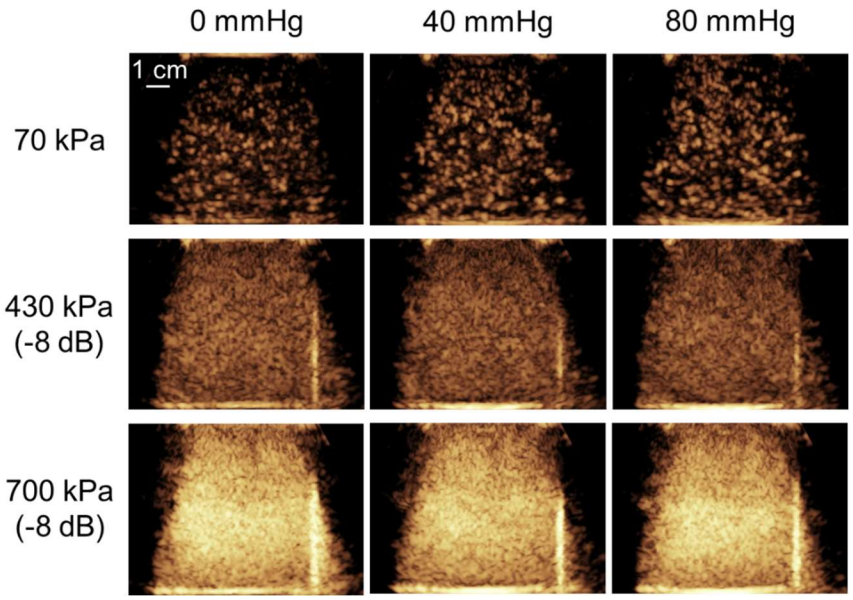

***Figure 6.1**: Subharmonic images of Sonazoid at 3 ambient pressures and 3 acoustic pressures. Images acquired with C5-1, 4.2 MHz, 18 cycles, pulse inversion.*

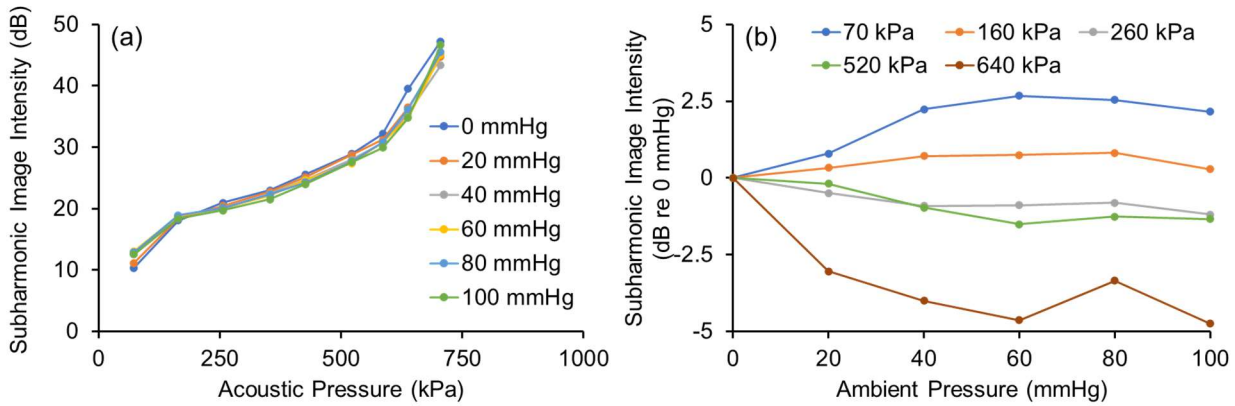

***Figure 6.2**: Average image intensity of Sonazoid as a function of (a) acoustic pressure, and (b) ambient pressure.*

Intensity values in (b) were normalized with respect to the value at atmospheric pressure (0 mmHg). Images acquired with C5-1, 4.2 MHz, 18 cycles, pulse inversion

change in subharmonic intensity is observed with increasing ambient pressure. **Figure 6.2**(b) further highlights the effects of ambient pressure, where at low acoustic pressure (< 200 kPa), Sonazoid increases in image intensity with increasing ambient pressure. The increase in image intensity with ambient pressure was maximized at the lowest acoustic pressure of 70 kPa, with a 2.7 dB increase at 60 mmHg and a sensitivity of 0.05 dB/mmHg from 0-60 mmHg. For acoustic pressures 200-500 kPa, Sonazoid was not found to be sensitive to ambient pressure changes in our in vitro experiments. At high acoustic pressures (> 500 kPa) Sonazoid exhibits a negative sensitivity with ambient pressure, maximized at 60 mmHg with a 4.6 dB decrease in intensity and a sensitivity of -0.08 mmHg from 0-60 mmHg.

6.4 Discussion

In this initial study, we considered a range of acoustic and ambient pressures for evaluating the subharmonic response of Sonazoid driven near its resonance frequency, with a special focus on low acoustic pressures. The subharmonic intensity of Sonazoid gradually increased with acoustic pressure [see **Figure 6.2**(a)]. During low acoustic pressures (< 200 kPa), the subharmonic response of Sonazoid slightly increases with increasing ambient pressure. A positive sensitivity with Sonazoid has not been observed in other studies (due to limited investigation of low acoustic pressures) and indicates that Sonazoid may also be considered for non-destructive subharmonic imaging. However, because the driving frequency is near the resonance frequency of Sonazoid, only a small percentage of the total bubble population (due to polydispersity of microbubble sizes

[4]) may be in the buckling regime to generate subharmonic signal. The small number of scatterers capable of generating subharmonic signal could explain the non-uniform appearance of Sonazoid at low acoustic pressures [see 70 kPa images in **Figure 6.1**] and the relatively weak subharmonic signal compared to the subharmonic response at higher acoustic pressures where subharmonic signal from microbubbles at resonance is dominant [15]. At high acoustic pressures (> 500 kPa) we measured the greatest ambient pressure sensitivity (-0.08 dB/mmHg) during 640 kPa acoustic pressure. Our results agree with Wang, et al. [9] who also observed a gradual increase in subharmonic signal from 300-800 kPa during a 16-cycle pulse at 4.4 MHz, and found an optimal acoustic pressure of 550 kPa for maximizing ambient pressure sensitivity (-0.15 dB/mmHg) over a smaller pressure range of 10-40 mmHg. Dave, et al. [8] measured a similar sensitivity (-0.06 dB/mmHg) when driving Sonazoid microbubbles with a 64-cycle, 4.4 MHz pulse during acoustic pressures greater than 500 kPa but also found Sonazoid was sensitive to ambient pressure from 300-500 kPa (where we observed no sensitivity). The difference in subharmonic behavior between our studies could be due to the longer pulse lengths (64 cycles vs 18 cycles in our study) used by Dave, et al. [8] which can exhibit increased ambient pressure sensitivity compared to subharmonic measurements with shorter pulse lengths [16].

The change in subharmonic signal with ambient pressure was also specific to the microbubble formulation, with SonoVue exhibiting a larger relative change in subharmonic signal compared to Sonazoid. Similar to **Figure 5.10** for SonoVue, **Figure 6.3** shows for Sonazoid the

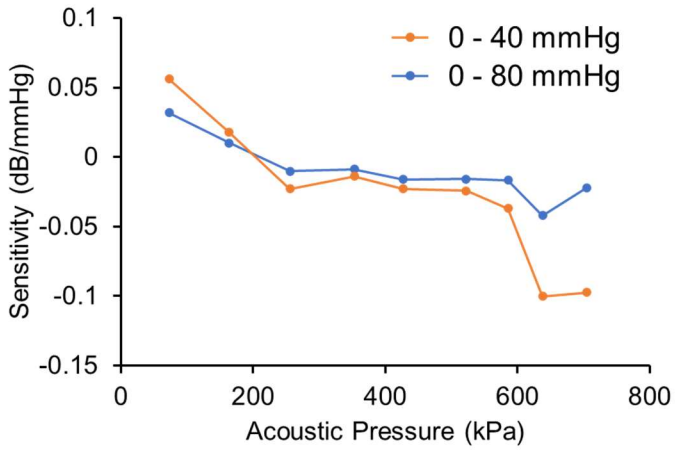

***Figure 6.3**: Average ambient pressure sensitivity as a function of acoustic pressure for Sonazoid. Ambient pressure sensitivity is calculated from the change in subharmonic signal from 0-40 or 0-80 mmHg using the data presented in **Figure 6.2**(b). Images acquired with C5-1, 4.2 MHz, 18 cycles, pulse inversion.*

ambient pressure sensitivity (dB/mmHg) as a function of acoustic pressure (calculated from the slopes observed in **Figure 6.2**(b)) measured with $SHI_{PI4.2}$. Sensitivity is shown for 2 ambient pressure ranges: 0-40 mmHg, which is the relevant pressure range for evaluating portal hypertension [17] and monitoring interstitial fluid pressure in tumors [18], and 0-80 mmHg, the relevant pressure range for evaluating pulmonary arteries and right heart chambers [19, 20]. **Figure 6.3** shows that Sonazoid exhibits a slight positive sensitivity to ambient pressure for acoustic pressures < 200 kPa, maximized at 70 kPa with +0.06 dB/mmHg from 0-40 mmHg. In comparison, SonoVue imaged with $SHI_{PI4.2}$ [see **Figure 5.10**] is sensitive to ambient pressure for acoustic pressures less than 500 kPa and is maximized at 70 kPa with +0.31 dB/mmHg from 0-40 mmHg. SonoVue exhibits a greater ambient pressure sensitivity since it is driven at twice its resonance frequency where most of the microbubble population is near the buckling regime generating a greater subharmonic signal magnitude relative to Sonazoid. Another consideration is the higher shell stiffness of Sonazoid which would resist the deformation necessary to transition to the buckled state, further limiting the subharmonic signal generation at low acoustic pressures [10]. The results of our study suggest that SonoVue offers a greater sensitivity to ambient pressure than Sonazoid when insonified at 4.2 MHz (twice the resonance frequency of SonoVue) with low acoustic pressures and is especially suited for applications such as evaluating portal hypertension where a smaller ambient pressure range (0-40 mmHg) is expected. Future studies should also consider implementing subharmonic imaging at twice the resonance frequency of Sonazoid (8.5 MHz) to directly compare the subharmonic response derived from buckling of both agents.

6.5 CONCLUSION

In this initial study, we evaluated the subharmonic response of Sonazoid microbubbles driven at the resonance frequency (4.2 MHz) under ambient pressures of 0-100 mmHg. We found that the subharmonic signal of Sonazoid can increase with ambient pressure during low acoustic pressures (< 200 kPa), with a small 2.5 dB increase from 0-80 mmHg (+ 0.03 dB/mmHg) at 70 kPa acoustic pressure. This result is important because non-destructive subharmonic imaging can also be performed with Sonazoid, and sensitivity may be further improved with transmit frequencies at twice the resonance frequency. We also observed a significant difference in subharmonic responses of SonoVue and Sonazoid driven at 4.2 MHz, with SonoVue exhibiting a

higher sensitivity to ambient pressure for acoustic pressures < 400 kPa. The findings in this work suggest the need for further investigation of Sonazoid at low acoustic pressures.

6.6 ACKNOWLEDGEMENTS

This work was supported by NIH grant R01EB032655. Sonazoid was generously supplied by GE HealthCare (GE HealthCare, Oslo Norway).

6.7 REFERENCES

[1] C. Greis, "Technology overview: SonoVue (Bracco, Milan)," *European radiology,* vol. 14, pp. P11-5, 2004. doi:

[2] J.-M. Gorce, M. Arditi, and M. Schneider, "Influence of Bubble Size Distribution on the Echogenicity of Ultrasound Contrast Agents: A Study of SonoVue™," *Investigative Radiology,* vol. 35, no. 11, pp. 661-671, 2000. doi:

[3] S. Kotopoulis *et al.*, "SonoVue® vs. Sonazoid™ vs. Optison™: Which Bubble Is Best for Low-Intensity Sonoporation of Pancreatic Ductal Adenocarcinoma?," *Pharmaceutics*, vol. 14, no. 1. doi: 10.3390/pharmaceutics14010098

[4] P. C. Sontum, "Physicochemical Characteristics of Sonazoid™, A New Contrast Agent for Ultrasound Imaging," *Ultrasound in Medicine & Biology,* vol. 34, no. 5, pp. 824-833, 2008/05/01/ 2008. doi: 10.1016/j.ultrasmedbio.2007.11.006.

[5] K. Sarkar, W. T. Shi, D. Chatterjee, and F. Forsberg, "Characterization of ultrasound contrast microbubbles using in vitro experiments and viscous and viscoelastic interface models for encapsulation," *The Journal of the Acoustical Society of America,* vol. 118, no. 1, pp. 539-550, 2005. doi: 10.1121/1.1923367.

[6] T. Faez, D. Goertz, and N. De Jong, "Characterization of Definity™ Ultrasound Contrast Agent at Frequency Range of 5–15 MHz," *Ultrasound in Medicine & Biology,* vol. 37, no. 2, pp. 338-342, 2011/02/01/ 2011. doi: 10.1016/j.ultrasmedbio.2010.11.014.

[7] H. Mayer *et al.*, "Investigation into the subharmonic response of three contrast agents in static and dynamic flow environments using a commercially available diagnostic ultrasound scanner," *Ultrasound in Medicine & Biology,* vol. 50, no. 11, pp. 1731-1738, 2024. doi: 10.1016/j.ultrasmedbio.2024.07.015.

[8] J. K. Dave *et al.*, "Noninvasive estimation of dynamic pressures in vitro and in vivo using the subharmonic response from microbubbles," *IEEE Trans Ultrason Ferroelectr Freq Control,* vol. 58, no. 10, pp. 2056-66, Oct 2011. doi: 10.1109/tuffc.2011.2056.

[9] Y. Wang *et al.*, "Noninvasive Estimation of Tumor Interstitial Fluid Pressure from Subharmonic Scattering of Ultrasound Contrast Microbubbles," *Biosensors,* vol. 13, no. 5, p. 528, 2023. doi: 10.3390/bios13050528.

[10] P. Marmottant *et al.*, "A model for large amplitude oscillations of coated bubbles accounting for buckling and rupture," *The Journal of the Acoustical Society of America,* vol. 118, no. 6, pp. 3499-3505, 2005. doi: 10.1121/1.2109427.

[11] J. Sijl *et al.*, "Subharmonic behavior of phospholipid-coated ultrasound contrast agent microbubbles," *The Journal of the Acoustical Society of America,* vol. 128, no. 5, pp. 3239-3252, 2010. doi: 10.1121/1.3493443.

[12] S. B. Keller, P. S. Sheeran, and M. A. Averkiou, "Cavitation therapy monitoring of commercial microbubbles with a clinical scanner," *IEEE Transactions on Ultrasonics, Ferroelectrics, and Frequency Control,* vol. 68, no. 4, pp. 1144-1154, 2020. doi: 10.1109/TUFFC.2020.3034532.

[13] P. Li *et al.*, "Pharmacokinetics of perfluorobutane after intra-venous bolus injection of Sonazoid in healthy Chinese volunteers," *Ultrasound in Medicine & Biology,* vol. 43, no. 5, pp. 1031-1039, 2017. doi: 10.1016/j.ultrasmedbio.2017.01.003.

[14] X. Qiao, Y. Wen, J. Yu, A. Bouakaz, Y. Zong, and M. Wan, "Noninvasive pressure estimation based on the subharmonic response of SonoVue: Application to intracranial blood pressure assessment," *IEEE Transactions on Ultrasonics, Ferroelectrics, and Frequency Control,* vol. 69, no. 3, pp. 957-966, 2021. doi: 10.1109/TUFFC.2021.3138100.

[15] J. Chomas, P. Dayton, D. May, and K. Ferrara, "Nondestructive subharmonic imaging," *IEEE Transactions on Ultrasonics, Ferroelectrics, and Frequency Control,* vol. 49, no. 7, pp. 883-892, 2002. doi: 10.1109/TUFFC.2002.1020158.

[16] K. S. Andersen and J. A. Jensen, "Ambient pressure sensitivity of microbubbles investigated through a parameter study," *The Journal of the Acoustical Society of America,* vol. 126, no. 6, pp. 3350-3358, 2009. doi: 10.1121/1.3242359.

[17] E. Moitinho *et al.*, "Prognostic value of early measurements of portal pressure in acute variceal bleeding," *Gastroenterology,* vol. 117, no. 3, pp. 626-631, 1999. doi: 10.1016/S0016-5085(99)70455-5.

[18] A. Mohammadabadi *et al.*, "Pulsed focused ultrasound lowers interstitial fluid pressure and increases nanoparticle delivery and penetration in head and neck squamous cell carcinoma xenograft tumors," *Physics in Medicine & Biology,* vol. 65, no. 12, p. 125017, 2020. doi: 10.1088/1361-6560/ab9705.

[19] H. W. Farber, A. J. Foreman, D. P. Miller, and M. D. McGoon, "REVEAL Registry: correlation of right heart catheterization and echocardiography in patients with pulmonary arterial hypertension," *Congestive heart failure,* vol. 17, no. 2, pp. 56-63, 2011. doi: 10.1111/j.1751-7133.2010.00202.x.

[20] M. McGoon and D. Miller, "REVEAL: a contemporary US pulmonary arterial hypertension registry," ed: European Respiratory Society, 2012.

CHAPTER 7. CONCLUSIONS

7.1 SUMMARY OF CONTRIBUTIONS

Ultrasound-mediated microbubble cavitation has been investigated in this thesis as a method of improving systemic drug uptake through modulation of the tumor microenvironment, in which the same clinical tools (ultrasound and microbubbles) used to identify solid tumors can also be used for treatment and subsequent monitoring. The unique tumor microenvironment of solid tumors, comprised of abnormal vasculature, desmoplasia within the extracellular matrix, and elevated interstitial fluid pressure (IFP) act as major barriers for delivery of systemic therapies. Through careful consideration of acoustic parameters, microbubble cavitation can induce localized biological effects that can overcome these barriers to drug delivery. We separately investigated the mechanical and thermal effects of microbubble cavitation therapy to elucidate how best to control these effects which can lead to improved systemic drug delivery. We also explored subharmonic imaging with microbubbles as a noninvasive strategy for measuring tumor IFP. The use of a clinical ultrasound system and commercial contrast agents throughout this thesis is intended to accelerate future translation efforts.

7.1.1 Cavitation therapy with a clinical scanner and real-time monitoring

In **Chapter 2** we designed and implemented pulses (1.67 MHz, 20-1000 cycles, 0.8-2.5 MPa, 5-100 ms pulse repetition time) suitable for microbubble cavitation with a phased array on a clinical scanner. The cavitation therapy setting was combined with imaging for better treatment guidance. We evaluated the cavitation activity *in vitro* with a comprehensive range of acoustic parameters (acoustic pressure, pulse repetition time, and pulse length) not previously covered to this extent by utilizing a novel perfusion phantom that consisted of microbubbles suspended in a gel phantom that has similar ultrasound properties as tissue. Passive cavitation detection (PCD) measurements found that the duration of inertial cavitation lasted for ~3-5 pulses during the first 100 ms of treatment. Similar cavitation activity was observed in our later *in vivo* studies (**Figure 3.9**(b) and **Figure 3.13**(b)), validating the in vitro work with the perfusion phantom as being representative of the microvascular network (capillary bed) of a tumor during the peak of a bolus injection of microbubbles. The findings in this *in vitro* evaluation informed the acoustic parameters selection for the subsequent *in vivo* studies discussed in **Chapter 3**.

In **Chapter 3** we successfully performed ultrasound cavitation treatments in animal tumor models *in vivo* delivered by the clinical system optimized in **Chapter 2** or a focused single element transducer and gained new insights on cavitation activity and changes to IFP resulting from cavitation therapy. Our setup was comprehensive, accurate, reliable, and included simultaneous real-time monitoring of cavitation treatments with PCD and contrast-enhanced ultrasound (CEUS) and provided comprehensive information of both cavitation activity and changes to tumor perfusion. CEUS captured spatial and temporal dynamics of transient tumor perfusion loss (TTPL) resulting from cavitation treatments. PCD confirmed accurate targeting of cavitation treatments and correlated with the extent of TTPL immediately after treatment. In our first study, we delivered cavitation treatments at 2 acoustic pressures (1.6, 2.2 MPa) with the clinical scanner that followed a protocol of 4 repeated treatments of 60s duration with alternating 5s on/off sonication. Pressure catheter measurements confirmed a significant reduction in IFP resulting from cavitation treatments that was similar between the 2 acoustic pressures used (1.6 and 2.2 MPa). All ultrasound conditions induced TTPL without significant tissue damage or hemorrhage. Cavitation treatments at 2.2 MPa caused near-complete cessation of flow, while cavitation treatments at 1.6 MPa gradually decreased TTPL. The significant perfusion disruption observed when the acoustic pressure was 2.2 MPa may impede drug transport of systemically delivered therapeutic agents. In another study, cavitation treatments at 3 acoustic pressures (1.2, 2.5, 4.0 MPa) were delivered by a focused, single element transducer following a protocol of a single, 1 s treatment and monitored by CEUS up to 60 minutes after treatment. TTPL immediately after treatments increased in severity with increasing acoustic pressure, where perfused area was partially disrupted (< 50% reduction in perfused area) when acoustic pressure was less than 2 MPa, while significant disruption (> 50% reduction in perfused area) was observed when acoustic pressure was above 2 MPa. Monitoring TTPL up to 60 minutes after a single 1 s treatment revealed that the majority of tumor perfusion recovered as soon as 5 minutes after treatment. In the case of high acoustic pressure (4.0 MPa) perfusion gradually degrades up to 60 minutes after treatment, possibly indicating some nonrecoverable vascular damage occurred. PCD measurements between the 2 treatment protocols also found similar results that inertial cavitation activity subsided after the first 1-20 transmitted pulses (depending on pulse repetition rate). The complimentary information provided by CEUS and PCD indicates that a single injection with a short treatment duration is sufficient for generating immediate TTPL and significant cavitation activity. Our measurements

of TTPL within the first hour after cavitation treatments also indicate that delaying subsequent cavitation treatments by at least 5 minutes (preferably longer) in this tumor model can increase the efficacy of treatments and may be used to further enhance systemic drug delivery.

7.1.2 Controlled hyperthermia with microbubble enhanced heating

In **Chapter 4**, we demonstrated control over the enhanced heat deposition during microbubble cavitation through careful selection of acoustic parameters and microbubble dosing. We evaluated temperature elevation in an ex-vivo porcine liver which maintains *in vivo* properties, used with and without machine perfusion to evaluate the effect of blood flow and perfusion on heat transfer in the liver. The measured temperature elevation in perfused and non-perfused porcine liver without microbubbles agreed with bioheat simulations. In non-perfused tissue, we defined 2 acoustic pressure regimes based on microbubble heating behavior. "Controlled" microbubble enhanced heating (BEH) occurs at low acoustic pressures ($\leq$ 1.2 MPa) when only injected microbubbles are inertially cavitating, but below the inertial cavitation threshold of residual air pockets trapped in the medium. "Uncontrolled" BEH occurs at high acoustic pressures (> 2 MPa) where both microbubbles and residual air pockets inertially cavitate, recognized by a plateau of temperature elevation due to intense cavitation shielding the focal area from further energy deposition. Thermocouple measurements also demonstrated that the heated area was larger when using microbubbles at all pressures. In the presence of perfusion, only local injections provided a sufficiently high concentration of microbubbles at the treatment location necessary for significant temperature enhancement to overcome the blood flow heat deposition. Little temperature enhancement was observed when systemic injections were used for microbubble delivery. While it may be possible to enhance heating with systemic injections, relevant for *in vivo* evaluations, we anticipate that the high microbubble concentrations required for significant heating would introduce acoustic shadowing that can shift the treatment location. Our findings suggest that we can combine the mechanical and thermal effects of cavitation therapy to modulate the tumor microenvironment and improve systemic drug delivery despite having investigated them separately in this thesis.

7.1.3 Subharmonic imaging to measure ambient pressure and IFP

In **Chapter 5** we evaluated SonoVue, a clinically available contrast agent that has not yet been used with clinical studies with subharmonic imaging, for ambient pressure sensing at low

acoustic pressures. We investigated a comprehensive range of ultrasound parameters, considering the effect of transmit frequency, bandwidth, pulsing scheme, and acoustic pressure on the subharmonic response of SonoVue under ambient pressures of 0-140 mmHg. A new subharmonic imaging mode was implemented on a clinical scanner. We show that transmitting at twice the resonance frequency of SonoVue, which lowers the acoustic pressure threshold for subharmonic signal generation, resulted in the greatest subharmonic signal change with ambient pressure. SonoVue was also particularly sensitive to ambient pressures of 0-40 mmHg, indicating SonoVue is well-suited for monitoring IFP in our subcutaneous model of HCC where IFP ranged from 0-15 mmHg (**Figure 3.15**). Some current commercially available implementations of subharmonic imaging use pulses with frequency near the resonance frequency of microbubbles and a small number of cycles. With these parameters, a considerable overlap between the fundamental and subharmonic signals exists to the extent that it is no longer possible to separate the subharmonic component. Our results demonstrate that improving the detection of the subharmonic component through careful selection of the transmit frequency and number of cycles can significantly enhance ambient pressure sensitivity. Additionally, we provided the first evidence that high ambient pressures (> 100 mmHg) resulted in microbubble destruction that reduced the subharmonic intensity. The findings in this work are significant as optimization at low acoustic pressures eliminates the need for patient specific calibrations used in existing clinical implementations of subharmonic imaging.

In **Chapter 6** we provided an initial investigation of the subharmonic response of Sonazoid with the subharmonic imaging mode created in **Chapter 5**. Sonazoid is a clinically available contrast agent, that has been investigated in the past for ambient pressure sensing. Our investigation addresses important gaps that existed in terms of the subharmonic response of Sonazoid. A small positive ambient pressure sensitivity with Sonazoid was observed at low acoustic pressures (< 200 kPa), indicating that Sonazoid may also be used for non-destructive subharmonic imaging but is much less sensitive to ambient pressure than SonoVue. Comparisons of the subharmonic response of SonoVue (**Chapter 5**) and Sonazoid (**Chapter 6**) when driven at 4.2 MHz revealed the differences between the microbubble formulations. SonoVue exhibited a greater ambient pressure sensitivity than Sonazoid, since most of the SonoVue microbubble population is driven at twice its resonance frequency (4.2 MHz) where microbubble shells enter a tensionless, buckled state. We hypothesized that Sonazoid may exhibit greater sensitivity to

ambient pressure when driven near twice its resonance frequency (8.5 MHz), which would enable comparison of microbubble buckling behavior between SonoVue and Sonazoid.

7.2 FUTURE DIRECTIONS

There are several interesting investigations that could follow considering the outcomes of this work. Although we demonstrated that cavitation therapy delivered with a clinical scanner can induce a reduction in tumor IFP, further optimization of ultrasound parameters may improve our understanding of the mechanisms of cavitation-induced IFP changes. Similar reduction in IFP was observed after 1.6 and 2.2 MPa cavitation treatments. At this point, we do not know if acoustic pressures less than 1.6 MPa may still reduce IFP. Further investigation of lower acoustic pressure (< 2 MPa) would also be of interest for studying drug extravasation and enhanced drug delivery since tumor perfusion is only partially disrupted at these pressures. Future in vivo studies may also consider measuring IFP, possibly with subharmonic imaging, and tumor perfusion at different stages of tumor growth in our HCC model to provide insights into tumor development. By balancing tumor perfusion loss and IFP with drug delivery new insights may be gained on cavitation induced changes to the tumor microenvironment.

The next step to our *ex vivo* evaluation of BEH is to evaluate these treatments *in vivo*. We hypothesized that BEH with systemic injections may also be suitable in hypervascular tumors, such as HCC, that can exhibit an early diversion of blood flow to the tumor and act to deliver a high concentration of microbubbles specific to the tumor. The subcutaneous HCC mouse model developed for **Chapter 3** offers an excellent opportunity to investigate BEH *in vivo*. Since microbubble cavitation can generate both thermal and mechanical effects, designing a study that investigates the biological effects of both microbubble cavitation effects is of great interest. A focused transducer can be used to deliver targeted cavitation treatments, programmed with acoustic conditions suitable for both BEH (high intensity) and generation of mechanical forces (low intensity). We note that while microbubble cavitation does not always enhance heat deposition (isolated mechanical effects), generation of BEH also indicates the generation of cavitation (stable or inertial) that can still induce mechanical forces (mechanical and thermal effects). Temperature measurements with a needle thermocouple or even MRI could be used to confirm temperature elevation with and without microbubbles. Similar readouts to our studies of cavitation therapy (PCD, CEUS, IFP) can also compliment this potential study by measuring cavitation activity and

biological mechanisms in response to heating treatments. An acute study with the animal model can allow for optimization of the relevant parameters for generating mild hyperthermia (≤ 10 ℃ temperature elevation) and enable future studies that investigate drug delivery enhancement with controlled BEH.

Finally, our results with subharmonic imaging also encourage the exploration of 2 major concepts: estimation of IFP and absolute pressure measurements. Subharmonic imaging may be used in the future to noninvasively monitor IFP changes in solid tumors following cavitation treatments. The subcutaneous HCC mouse model again offers an ideal environment to both deliver cavitation treatments and later evaluate IFP with pressure catheter measurements. Due to the small animal model, a high frequency linear probe is better suited for superficial imaging of subcutaneous tumors, which creates an excellent opportunity to implement subharmonic imaging at 8.5 MHz and study Sonazoid driven at twice its resonance its resonance frequency. Additionally, subharmonic imaging at low acoustic pressures (< 200 kPa) with SonoVue has not yet been studied *in vivo* and will offer valuable new insights on subharmonic imaging, including developing a new technique compatible with bolus injections. However, these measurements would still rely on pressure catheter measurements of tumor IFP to calibrate subharmonic signal to ambient pressure, therefore there is still a great need to develop a strategy for absolute pressure measurements. A promising solution is the inclusion of a second, low frequency (10-100 kHz) transducer that dynamically manipulates ambient pressure by a known amplitude in tandem with the high frequency (4-8 MHz) subharmonic imaging pulses [1]. While this dual-frequency technique has not been attempted *in vivo*, our animal water tank setup offers an opportunity to investigate the low frequency transducer as a secondary method for estimating IFP that can be later compared to pressure catheter measurements.

7.3 List of publications and presentations

7.3.1 Peer-reviewed publications

1. Krolak C., **De Koninck LH.**, Gu S., Wang YN., Powers JE., Averkiou M. "Tumor blood flow disruption: a controllable transient vascular reaction to ultrasound cavitation treatments." *[in prep]*
    - Chapter 3

2. Babu G., **De Koninck LH**., Rayner SG., de Jong N., Glenny RW., Averkiou MA. “A clinical perspective and review on the use of the subharmonic signal of ultrasound contrast agents for non-invasive pressure estimation” Ultrasound Med. Biol. *[in review]*
3. **De Koninck LH.**, Babu G., Powers JE., de Jong N., Averkiou MA. “Implementation of subharmonic imaging on a clinical scanner for optimal ambient pressure sensitivity with SonoVue microbubbles” IEEE Transactions on Ultrasonics, Ferroelectrics, and Frequency Control. *[in review]*
    - Chapter 5
4. Krolak C., **De Koninck LH.**, Gu S., Wang YN., Powers JE., Averkiou M. “Ultrasound cavitation therapy: inducing tumor drug delivery and blood flow changes with clinical ultrasound tools” J. Control. Release. *[in review]*
    - Chapter 3
5. **De Koninck LH.**, Vuong KS., Shin S., Powers JE., Averkiou MA. "Delivery of cavitation therapy with a modified clinical scanner: in vitro evaluation" IEEE Transactions on Ultrasonics, Ferroelectrics, and Frequency Control, 72 (3), 351-361 (2025).
    - Chapter 2
6. Juang EK., **De Koninck LH**., Vuong KS., Gnanaskandan A., Hsiao CT., Averkiou MA. “Controlled hyperthermia with high-intensity focused ultrasound and ultrasound contrast agent microbubbles in porcine liver” Ultrasound Med. Biol., 49 (8), 1852-1860 (2023).
    - Chapter 4
7. Keller SB., Lai TY, **De Koninck LH**., Averkiou MA. “Investigation of the phase of nonlinear echoes from microbubbles during amplitude modulation” IEEE Transactions on Ultrasonics, Ferroelectrics, and Frequency Control, 69 (3), 1032-1040 (2022).

7.3.2 Presentations at national and international conferences

1. **De Koninck LH.**, Babu G., Michaelis H., Powers J., de Jong N., Averkiou M. “Low MI pulse inversion subharmonic imaging implemented on a clinical scanner.” IEEE International Ultrasonics Symposium 2025 (poster presentation).
2. **De Koninck LH.**, Krolak C., Powers J., Averkiou M. “Simultaneous PCD and CEUS to monitor microbubble cavitation treatments in an animal tumor model.” 30th European Symposium on Ultrasound Contrast Imaging (poster presentation).
3. **De Koninck LH.**, Krolak C., Vuong K., Shin S., Powers J., Averkiou M. “Modulation of the tumor microenvironment with a modified clinical scanner.” IEEE International Ultrasonics Symposium 2024 (poster presentation).
4. **De Koninck LH.**, Krolak C., Vuong K., Powers J., Averkiou M. “Delivery of ultrasound cavitation therapy with a modified clinical scanner.” Acoustics 2023 Sydney (oral presentation).
5. **De Koninck LH.**, Juang E., Krolak C., Averkiou M. “Investigation of combined ultrasound cavitation treatment with contrast microbubbles and mild hyperthermia in porcine liver.” 22nd Annual International Symposium on Therapeutic Ultrasound (oral presentation, poster presentation, *student poster award*).
6. **De Koninck LH.**, Juang E., Vuong K., Gnanaskandan A., Averkiou M. “Targeted local hyperthermia with local and systemic injections of ultrasound contrast agents during HIFU.” 28th European Symposium on Ultrasound Contrast Imaging (poster presentation).
7. **De Koninck LH.**, Krolak C., Keller SB., Lai TY., Averkiou M. “Improved tissue signal suppression through phase segmentation during amplitude modulation with Sonazoid.” 27th European Symposium on Ultrasound Contrast Imaging (oral presentation).

7.4 REFERENCES

[1] S. Spiekhout, J. Voorneveld, N. de Jong, and J. G. Bosch, "Dual-Frequency Subharmonic Ultrasound Contrast Imaging for Non-Invasive Blood Pressure Measurement," *Ultrasound in Medicine & Biology,* vol. 51, no. 5, pp. 870-876, 2025/05/01/ 2025. doi: 10.1016/j.ultrasmedbio.2025.01.015.